HOKKAIDO UNIVERSITY

Title	Study on multi-timescale rheology of heterogeneous fluids by advancement of velocity-profiling-based rheometry
Author(s)	大家, 広平
Degree Grantor	北海道大学
Degree Name	博士(工学)
Dissertation Number	甲第15845号
Issue Date	2024-03-25
DOI	https://doi.org/10.14943/doctoral.k15845
Doc URL	https://hdl.handle.net/2115/94351
Type	doctoral thesis
File Information	Kohei_Ohie.pdf

Hokkaido University Collection of Scholarly and Academic Papers : HUSCAP

HOKKAIDO UNIVERSITY

DOCTORAL THESIS

Study on multi-timescale rheology of heterogeneous fluids by advancement of velocity-profiling-based rheometry

Author:
Kohei OHIE

Supervisor:
Prof. Yuji TASAKA

A thesis submitted in fulfillment of the requirements for the degree of Doctor of Philosophy

in the

Division of Energy and Environmental Systems
Graduate School of Engineering

February 19, 2024

HOKKAIDO UNIVERSITY

Abstract

Division of Energy and Environmental Systems
Graduate School of Engineering

Doctor of Philosophy

Study on multi-timescale rheology of heterogeneous fluids by advancement of velocity-profiling-based rheometry

by Kohei OHIE

Rheology is ubiquitous in both industry and nature. The rheology test is often performed as a quality evaluation in industry as the internal composition is reflected in the macroscopic rheological properties represented by viscosity and viscoelasticity. In recent years, data analysis such as the rheological properties reflecting tactile/texture sensations and sales data has been carried out in the development of new cosmetics and food products. Rheology plays an important role not only in industry but also in understanding the flow of magma, mineral, and petrochemical resources in nature. The demand for rheology evaluation from industry and academia has been expanding, and some representative examples are swallowing foods containing millimeter-sized ingredients and fluids containing bubbles and particles. These heterogeneous fluids cannot be measured by a standard torque-type rheometer, and the development of new tools that can access the rheology of these complex fluids is required. In addition, the rheological properties of these complex fluids change not only due to aging effects such as chemical reactions and phase separation but also depending on the amplitude and timescale of the applied shear deformation, so new measures are also required to comprehensively understand this multi-timescale rheology.

In this thesis, velocity-profiling-based rheometry is first introduced in Chapter 2. The standard torque-type rheometer assumes a constant shear rate in a submillimeter gap and indirectly evaluates the rheological properties by controlling the rotation speed and measuring the axial torque. This assumption is however not fully satisfied for complex fluids, and ultrasonic spinning rheometry (USR) has been developed to mitigate this shear localization problem. The concept of USR is that the rheological properties are reflected in the velocity information. The effective viscosity and viscoelasticity are indirectly evaluated from the experimentally measured velocity information via equations of fluid motion. Techniques and knowledge for improving the accuracy and precision of USR and further extensions of USR are additionally explained in this chapter. One of the strength points of rheometry based on the velocity information is its high applicability to complex fluids such as multi-phase fluids containing submillimeter dispersions. In addition, it can simultaneously evaluate shear-rate-dependent rheological properties such as shear-thinning and shear-thickening as the shear rate amplitude distributes in the radial direction in the cylindrical vessel. It is therefore possible to evaluate the shear rate dependence during non-equilibrium conditions such as phase separation of multi-phase fluids and chemical reactions. As representative examples of non-equilibrium conditions, phase separation of an oil-water mixture and hydrolysis of polysaccharide aqueous solutions with alpha-amylase are introduced in Chapter 3. The proposed K-n map

representation enables creating a data set of the time-resolved rheological properties of swallowing foods, and combined with medical knowledge, it has a high potential to be a quantitative indicator for evaluating food safety and palatability.

The rheological properties of non-Newtonian fluid change depending on the applied shear intensity and its unsteadiness such as oscillation frequency. Almost all the materials behave like liquids against a slow deformation, in contrast, behave like solids against a rapid deformation. In Chapter 4, a map representation called rheology mapping is introduced for comprehensively evaluating the dependence of viscoelasticity on both shear intensity and its unsteadiness. It is demonstrated with some typical polymer solutions; polyvinylpyrrolidone aqueous solutions as viscous dominant fluids, carboxymethyl cellulose aqueous solutions as shear-thinning fluids, and polyacrylamide aqueous solutions as viscoelastic fluids. Different map patterns are displayed for each solution, and it is expected to be a useful tool for characterizing polymer solutions and for constructing rheology models. In this chapter, the rheology mapping is further applied to investigate bubble suspension rheology. The addition of a small amount of bubble changes the original rheological properties of the dispersion medium, and it changes not only the flow behavior of food and chemical products but also the eruption pattern of volcanoes in nature. The map representation of the viscoelasticity theoretically obtained shows a holistic picture of the bubble suspension rheology. The effect of parallel combined steady and oscillatory shear on the viscoelasticity is further investigated using rheology mapping.

One of the characteristics of the rheometry based on the velocity information is that the velocity field can be reconstructed with the evaluated rheological properties. In Chapter 5, a reconstruction method for the velocity field is proposed and compared with experimental results. The rheological properties evaluated by the rheometry under steady and oscillatory shear conditions are applied to predict the one-directional laminar shear flow in a circular pipe. Comparison with the experimental data shows the reconstructability of the velocity field. In Chapter 6, The application of the inverse analysis, which is the basis of velocity-profiling-assisted rheometry, to the development of inline rheometry is finally introduced. Physical data such as velocity information in a pipeline is acquired, and rheological parameters are determined reversely so that the data satisfies the equations of fluid motion.

A series of these research projects have enabled the rheological evaluation of more complex fluids in muti-timescale and provided measures for understanding their dense information. It is expected that these tools will connect material development with fluid mechanics and be useful probes for understanding the flow of complex fluids.

Acknowledgements

I would like to express the deepest appreciation to Prof. Yuji Tasaka, my supervisor in these five years. He always listened to me enthusiastically and guided me in a better direction. Thanks to that, I was able to spend my days enjoying research and learning a lot, and most importantly, it was very much looking forward to sharing new ideas and findings at meetings with him. He also gave me many opportunities to collaborate with many companies and universities both domestically and internationally. Thanks to this, I was able to conduct research not only from an academic but also from an industrial perspective. I learned how to advance interdisciplinary development between fluid mechanics and other fields.

I am sincerely grateful to Prof. Yuichi Murai for always constructive advice and comments based on his wide knowledge on fluid engineering and physics. My interest in fluid mechanics began with a book he introduced to me when I was an undergraduate student. Even after I entered the laboratory, he talked about the significance and attractiveness of research on non-Newtonian fluids through examples in industries. Thanks to that, I was able to maintain a high level of motivation until today.

I would like to thank other laboratory staffs, Assist. Prof. Hyun Jin Park for his skillful advice on ultrasound technology, Assist. Prof. Yasufumi Horimoto for his fruitful comments on polymer rheology, Technician Emeritus Mr. Toshiyuki Sampo for his excellent technical assistance based on his many years of experience, Secretary Ms. Yui Miyazaki for her prompt and courteous response regarding travel expenses and equipment purchases.

I truly express my sincere gratitude to Dr. Taiki Yoshida, AIST and Dr. Daisuke Noto, The University of Pennsylvania. I strengthened my intension to go on the doctoral course as I experienced the interest of research activities through experiments and discussions with them. They always generously gave me skillful advice on ultrasound technology and image processing based on their wide knowledge and rich experience. In addition, it was very helpful to give me kind advice whenever I was worried about my research policy and future path.

I am deeply grateful to Assis. Prof. Haruko Chiba, Ms. Satomi Kumagai, and Ms. Yoko Ikeda, Hokkaido University Hospital for working with us on the food rheology project. Their advice and comments based on practical experience were very helpful in determining the direction of the project. I hope to continue to the collaboration and contribute to the development of food rheology on particularly swallowing foods for patients with dysphagia.

I sincerely express my appreciation to Prof. Masako Sugihara-Seki, Kansai University and Osaka University, and Prof. Naoto Yokoyama, Tokyo Denki University for providing us with some very interesting fluids and constructive discussions on the numerical prediction of the non-Newtonian fluid flows. These experiences have greatly motivated me to combine rheology and flow prediction.

I truly express my gratitude to Prof. Anne Juel, The University of Manchester for hosting me in Manchester and taking the time for the weekly meeting. I am also grateful to Dr. Claudio Fonte for his constructive advice based on his wide knowledge of rheology and non-Newtonian fluid mechanics. I am also very grateful to Dr. Elliott Sutton, and I learned a lot while conducting experiments and analysis together with him. The other members of the Physics of Fluids and Soft Matter Group also welcomed me warmly and I really enjoyed living in Manchester. It was a great experience to research fluid mechanics in the group for three months, and it has motivated me to remain in academia.

I am sincerely grateful to Prof. Peter Fischer, ETHZ for giving us important advice on rheology when he visited at Hokkaido University and whenever I met him at international conferences. When starting a new and challenging research project, his advice always led us in better direction.

I would like to express my gratitude to the dissertation committee members, Prof. Nobuyuki Oshima, Prof. Masao Watanabe, and Prof. Yoshiyuki Tagawa for their fruitful comments on my thesis.

Finally, I would like to give special thanks to, LFC students, my family and other personal supporters.

List of publications directly related to this thesis

[1] Ohie, K., Yoshida, T., Tasaka, Y., & Murai, Y., Flow Prediction of Complex Fluids in a Circular Pipe by Utilizing a Velocity-Profiling-Assisted Rheometer, *Industrial & Engineering Chemistry Research* 61(49), 18157-18164, 2022.

[2] Ohie, K., Yoshida, T., Tasaka, Y., Sugihara-Seki, M., & Murai, Y., Rheological characterization and flow reconstruction of polyvinylpyrrolidone aqueous solutions by means of velocity profiling-based rheometry, *Experiments in Fluids* 63(135), 1-13, 2022.

[3] Ohie, K., Chiba, H., Kumagai, S., Yoshida, T. & Tasaka, Y., A method for evaluating time-resolved rheological functionalities of fluid foods, *Journal of Texture Studies* 53(4), 444-452, 2022.

[4] Ohie, K., Yoshida, T., Tasaka, Y., & Murai, Y., Effective rheology mapping for characterizing polymer solutions utilizing ultrasonic spinning rheometry, *Experiments in Fluids* 63(40), 1-12, 2022.

[5] Ohie, K., Yoshida, T., Park, H.J., Tasaka, Y., & Murai, Y., Evaluation on time variation of effective viscosity by ultrasonic spinning rheometry (Application to separating oil-water mixture), *Transactions of the JSME (in Japanese)* 86(890), 1-13, 2020.

Sections. 1.1, 2.4, and 3.1 in this thesis partially include the content published in [5] Ohie *et al.*, *Transactions of the JSMS* 86(890), 2020. Sections 1.1 and 3.2 are reproduced in part from the content published in [3] Ohie *et al.*, *Journal of Texture Studies* 53(4), 2022. Sections 2.2 and 5.2 are reproduced in permission from [1] Ohie *et al.*, *Industrial & Engineering Chemistry Research* 61(49), 2022. Copyright 2022 American Chemical Society. Section 4.1 is reproduced in part from the content published in [4] Ohie *et al.*, *Experiment in Fluids* 63(40), 2022. Section 5.1 is reproduced in part from the content published in [2] Ohie *et al.*, *Experiments in Fluids* 63(135), 2022.

Contents

1 Introduction **1**
1.1 Background . . . 1
1.1.1 Role of rheology . . . 1
1.1.2 Limitations in the current rheology . . . 3
Oil-water mixtures in energy industry . . . 3
Swallowing foods for patients with dysphasia . . . 4
Polymer solutions in chemical industry . . . 4
Summary of the common problems . . . 5
1.1.3 Novel rheometry compled with velocity profiling . . . 5
1.2 Objectives . . . 6

2 Rheometry coupled with ultrasonic velocity profiling **9**
2.1 Ultrasonic velocity profiler (UVP) . . . 9
2.2 Rheological evaluation under steady shear . . . 11
2.3 Rheological evaluation under unsteady shear . . . 13
2.3.1 Phase analysis . . . 13
2.3.2 Linear viscoelastic analysis . . . 17
2.4 Technical note for USR . . . 22
Definition of shear rate . . . 22
Uncertainty caused by radial flow . . . 24
Precautions for DFT . . . 27
Polynomial fitting of the Fourier coefficients . . . 28
2.5 Further development of USR . . . 31
Methodology . . . 32
Robustness evaluation . . . 34
Experimental results of silicon oil . . . 37
Experimental results of carboxymethyl cellulose aqueous solution . . . 39
Application to suspensions of solid spherical particles . . . 40
Limitations of the method . . . 42

3 Time-resolved rheology in non-equilibrium conditions **47**
3.1 Separating oil-water mixture . . . 47
Separation process of the oil-water mixture . . . 47
Time variation of the effective viscosity . . . 48
Consideration . . . 50
3.2 K-n map for evaluating functionalities of fluid foods . . . 52
Role of rheology for better swallowing foods . . . 52
Materials . . . 53
Experimental setup and analytical procedures . . . 55
Experimental procedures . . . 55
Rheological properties of the original solutions . . . 56
Stability of the rheological properties after addition of amylase 56

Advantage of the functional evaluation by USR 58

4 Multi-timescale rheology **59**
4.1 Rheology mapping 59
4.1.1 Viscous dominant fluid (Polyvinylpyrrolidone) 60
Test materials 60
Viscosity-concentration function 61
Application of rheology mapping 62
Consideration from microscopic view 63
4.1.2 Shear-thinning fluid (Carboxymethyl cellulose) 64
Test materials 64
Application of rheology mapping 65
4.1.3 Viscoelastic fluid (Polyacrylamide) 67
Test materials 67
Application of rheology mapping 68
Consideration from microscopic view 69
4.2 Bubble suspension rheology 71
4.2.1 Review of bubble suspension rheology 71
4.2.2 Theoretical approach 72
4.2.3 Experimental verification 75
4.3 The effect of parallel combined steady and oscillatory shear 77
4.3.1 Theoretical approach 78
4.3.2 Discussion 81

5 Flow reconstruction and prediction **85**
5.1 Oscillatory shear flow between concentric cylinders 85
5.1.1 Theoretical background of the calculation 85
5.1.2 Validation of the reconstruction method 89
5.1.3 Technical note and further application to the CMC solution . . 91
5.2 Steady shear flow in a circular pipe 95
5.2.1 Test materials and rheological measurement 95
5.2.2 Flow prediction and experimental verification 98
Prediction protocol 98
Experimental setup for verification 98
Comparison of predicted and experimental results 99
Technical note and precision of pressure measurement 102
5.3 Oscillatory shear flow in a circular pipe 106
5.3.1 Test fluids and experimental setup 107
Basic characteristics of the test fluids 107
Measurement section attached into the circulating system . . . 107
5.3.2 Prediction scheme for a circular pipe flow 108
5.3.3 Results and discussion 112
Viscoelasticity evaluated by USR 112
Validation of the prediction scheme with experimental results 113

6 Inline rheometry for industrial applications **117**
6.1 Methodology 117
6.2 Validation of the method 119
6.2.1 Silicon oil 120
6.2.2 Carboxymethyl cellulose aqueous solution 121
6.3 Application example to food manufacturing processes 122

7 Concluding remarks and future perspectives **127**
7.1 Concluding remarks 127
(1) Advancement of the velocity-profiling-based rheometry . . 127
(2) Time-resolved rheology in non-equilibrium conditions . . . 127
(3) Multi-timescale rheology 128
(4) Application to flow reconstruction and prediction 129
(5) Further application to in-line rheometry 129
7.2 Epilogue and future perspectives 130

Bibliography **133**

Chapter 1

Introduction

1.1 Background

1.1.1 Role of rheology

The word "Rheology" was first used by Eugene Bingham about a centry ago. The prefix rheo comes from *rhein*, which means "flow" in Greek. Rheology is therefore literally a study of the flow of matter. It began with how to explain materials that behave intermediately between fluids and solids by combining the two major laws: Newton's law of viscosity and Hooke's law, which were respectively stated by Isaac Newton and Robert Hook in the 17th century. What is clear from this fact that these formulae for completely polar materials are incorporated in one discipline is how wide the scope of rheology is. The origin of the word *rhein* comes from the famous phase: *Panta rhei*, "Everything flows.", taking as the motto by Heraclitus. In this kind of meaning, nothing cannot be the scope of rheology.

There are two major directions of rheology research. One is the direction of utilizing rheological properties as an index for evaluating functionalities of materials. The properties represented by shear-rate-dependent viscosity, viscoelasticity, and yield stress appear as a comprehensive result of micro scale dynamics of polymer structures determined by chemical conditions such as molecular weight, concentration, pH, and temperature. The rheological properties are therefore utilized as a macro probe in material development, that is, as a tool for estimating the micro structures. The properties are also utilized for controlling quality of products in industries. The content composition of the products can be monitored indirectly by evaluating the rheological properties by creating a database of the correspondence between the composition and the properties in advance. The other direction is to use the rheological properties exactly as fluid characteristic parameters. They are utilized to predict the flow of non-Newtonian fluids and elucidate physics of fluids. The prediction of the flow by numerical simulation is conspicuous. Characteristic parameters in Maxwell model, Kelvin-Voigt model, Carreau-Yasuda model, etc. are experimentally identified, and the models are utilized in the computational fluid mechanics. Alternatively, in the elucidation of physical phenomena, the characteristic flow structures are explained in relation to spatial distributions of the properties. These two directions are not divided into different research fields but have achieved synergistic development.

The common and important step in both directions is to identify the rheological properties correctly. Only in the case that the properties of the bulk are evaluated accurately, we can proceed to the next step of discussing the internal structures or predicting the flow field as mentioned above. Torque-type rheometers are widely utilized in academic and industry to evaluate the rheological properties (Hyun et al., 2011). There are many types of device shapes such as parallel plates, cone and plate,

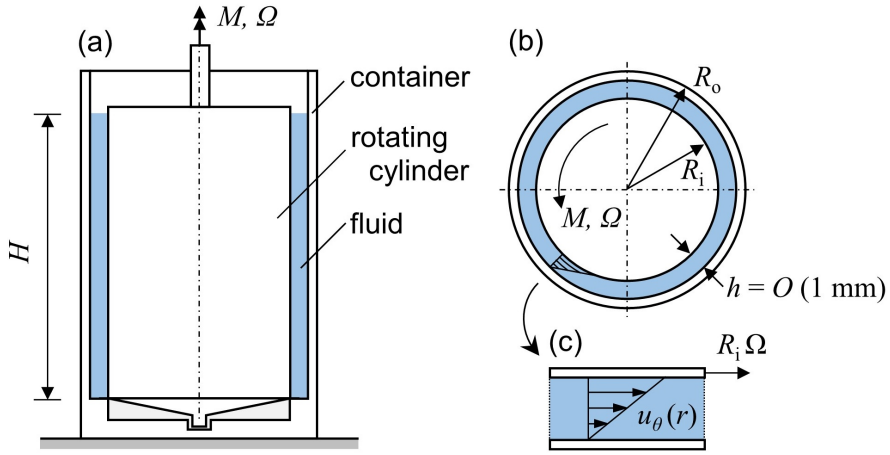


FIGURE 1.1: Schematics of cylinder viscometer: (a) Top view, (b) side view, and (c) ideal distribution of the flow velocity in the narrow gap between the rotating cylinder and container wall.

concentric double cylinders, but the principle adopted is the same for all of them. Here, the principle is explained for the cylindrical one (Irgens, 2014) as an example. Schematics of the rheometer is shown in Fig. 1.1. The test fluid is filled in the narrow gap between the inner and outer cylinders with radii of R_i and R_o. Assuming that the angular velocity is Ω and the viscosity of the fluid takes a constant under the flow, spatial distribution of the azimuthal velocity is approximated by

$$u_\theta(r) = \frac{R_\mathrm{o} - r}{R_\mathrm{o} - R_\mathrm{i}} R_\mathrm{i}\Omega, \tag{1.1}$$

when the gap distance $h = R_\mathrm{o} - R_\mathrm{i}$ is much smaller than the radii of the cylinders. Utilizing the velocity distribution, the shear rate in the azimuthal direction acting on the inner wall is derived as

$$\dot{\gamma}(r = R_\mathrm{i}) = \left|\left(\frac{\partial}{\partial r} - \frac{1}{r}\right) u_\theta(r = R_\mathrm{i})\right| = \frac{R_\mathrm{i}\Omega}{R_\mathrm{o} - R_\mathrm{i}}. \text{ (const.)} \tag{1.2}$$

Here, assuming that the axial torque is measured as M, the shear stress τ acting on the inner cylinder wall is derived as

$$\tau(r = R_\mathrm{i}) = \frac{M}{2\pi R_\mathrm{i}^2 H}. \tag{1.3}$$

Utilizing Eqs. 1.2, 1.3 and Newton's law of viscosity $\tau = \mu\dot{\gamma}$, where μ represents a viscosity coefficient of the fluid, the viscosity under the flow condition is also estimated. From the above, it is possible to estimate the viscosity of the fluid, shear rate, and shear stress by measuring the axial torque and the angular velocity. For other geometry types, the viscosity is also estimated basically in the same way assuming that the axial torque is proportional to the shear rate and viscosity. In addition, the shear rate dependent viscosity can be evaluated by varying the angular velocity or the geometric shape. The introduction of highly precised torque sensors has made it possible to evaluate the rheological properties over a wide range of the shear rate. It has made a great contribution to the development of rheology to date.

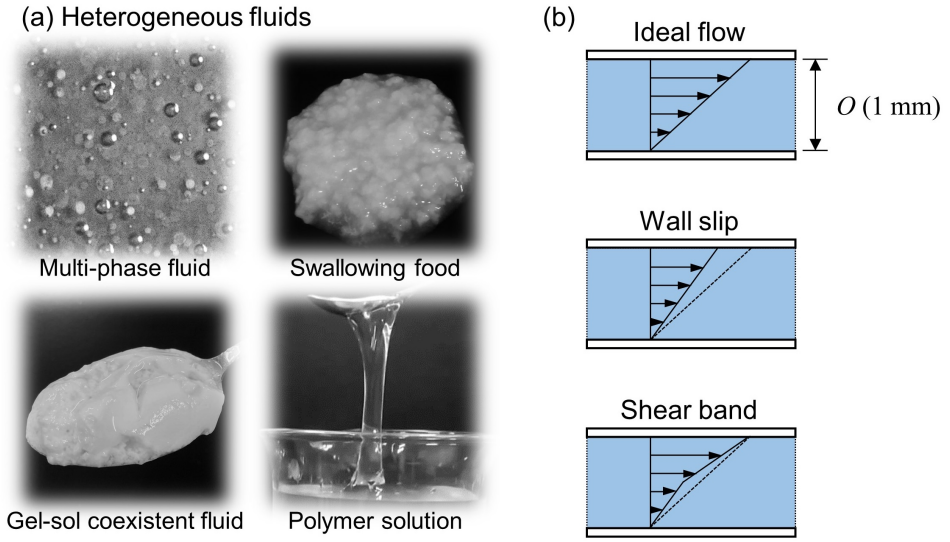


FIGURE 1.2: Limitations in the current rheometry: (a) Heterogeneous fluids which are impossible to evaluate by the torque-type rheometer, and (b) images of flow in the narrow gap of the rheometer. The ideal flow, wall slip, and shear band are shown in order from the above figure.

1.1.2 Limitations in the current rheology

The target fluids which require the rheological characterization are however quite complicated today. The torque-type rheometer is limited to fluids that are spatially and temporally homogeneous so that the shear rate is constant as shown in Eq. 1.1. The subjects described in detail below are far outside the applicable range of the current rheometer. The limitations are explained with specific examples here.

Oil-water mixtures in energy industry

Pipelines are utilized over the world as stable and economical ways of transporting crude oil. In such a fluid transportation system, the rheological properties of the working fluid are extremely important information in the design and management of the system, as described in the second direction of the rheology above. Generally, light crude oil is mined, and its viscosity can be evaluated with high accuracy by the torque tyepe rheometer. Many research results have been reported regarding the light crude oil (Rønningsen, 1992; Meriem-Benziane et al., 2012), contributing stable transport and storage. On the other hand, heavy crude oil has not been actively used as it is highly viscous and contains a lot of impurities, making it difficult to transport from oil fields to refineries. In recent years, the use of heavy crude oil has however attracted attention from the perspective of effective utilization of energy resources. At present, the possibility of the transportation has been found by means of reducing the viscosity by diluting or emulsifying (Hasan, Ghannam, and Esmail, 2010; Hart, 2014). However, such multi-phase fluids containing $O(1\ \mathrm{mm})$ dispersions close to the gap size of the rheometer are not covered by the torque type rheometer. The same issue applies not only to the diluted heavy crude oil but also to emulsion fuels, which are expected to protect the environment and improve fuel efficiency. A new method for evaluating the rheological properties of multiphase fluids is required.

Swallowing foods for patients with dysphasia

With the aging of the population, the annual deaths due to aspiration pneumonia in Japan is approximately 30,000, and the number of patients potentially suffering from aspiration disorders, dysphagia, is estimated to be one million. The eating process is exactly physics of fluids, and the contribution from rheology research is desperately required. There are two major approaches in the swallowing morphology study (Nishinari, 2003; Chen, 2009), where one is the measurement of the actual in-vivo swallowing process (Kumagai et al., 2009; Tashiro et al., 2010). The other is to evaluate the rhelogical properties of the fluid food and clarify the causal relationship with the swallowing process revealed in the in-vivo measurement. In fact, it was clarified about a half century ago that the swallowing process, as represented by the flow velocity in the pharynx, is closely related to the viscosity of the fluid food (Cutler, Morris, and Taylor, 1983; Houska et al., 1998). Regarding the former in-vivo measurement as mentioned above, not only aqueous solutions but also heterogeneous fluids such as rice porridge and gel dessert are included in the measurement targets, utilizing videofluorography and ultrasonic Doppler method. On the other hand, many researchers have pointed out the delay in the evaluation of the rheological properties (Nishinari, 2003; Kumagai and Kumagai, 2009), which is the other important direction as mentioned above. Even the viscosity of the rice porridge, which accounts for more than half the calories of the diet of patients with dysphagia, have not been evaluated. As with the oil-water mixture, the weakness of the torque-type rheometer for the heterogeneous fluids are exposed in practical applications. In addition, in the case of the fluid foods, it is also necessary to evaluate the timescale of the viscosity modification in the process of hydrolysis by amylase after mixing with saliva in the oral cavity. This is to ensure that the thickening effect of the swallowing food is retained until the moment of swallowing. At present, it is impossible to evaluate the rheological properties of fluids in such heterogeneous and non-equilibrium (transient) states.

Polymer solutions in chemical industry

Evaluating the rheology of polymer solutions is essential for applying functions of the solutions in material development, quality control of products, and optimal design of production lines. Polymer solutions exhibit various properties such as viscoelasticity, shear thinning/thickening characteristics, and yield stress. These macroscopic properties are exhibited as microstructures, which are uniquely formed based on chemical conditions such as the type of the solved polymer, its molecular weight, and concentration, change depending on both the degree of applied shear deformation and shear timescale represented by oscillation frequency. A thorough and informative discussion of the dependence of viscoelasticity on the shear strain and frequency was originally given by Pipkin (2012), classifying the properties into three characteristics: viscous, viscoelastic, and elastic. According to this concept, the variations in viscoelasticity can be displayed in a two-dimensional diagram representing Deborah and Weissenberg numbers (Reiner, 1964; Phan-Thien and Mai-Duy, 2013). This diagram is utilized for qualitative evaluations in arranging Lissarjous curves (Hyun et al., 2011), measured by the torque type rheometer (Ewoldt et al., 2007; Ewoldt, Hosoi, and McKinley, 2007). By quantitatively characterizing the shape of the Lissajous curves, it was succeeded to quantitatively map both the shear and frequency dependence in viscoelasticity (Ewoldt, Hosoi, and McKinley, 2008).

Although the quantitative map representation is extremely useful for characterizing polymer solutions and motivating development of optimal rheology models for numerical simulations (Larson and Desai, 2015), its range of application is still limited to specific polymer solutions showing ideal deformation/flow characteristics in the measurements of the torque type rheometer as shown in Fig. 1.2(b). The rheometer assumes the velocity profile as shown in Eq. 1.1 in the narrow gap filled with the test fluid and indirectly evaluate the rheological properties by measuring the axial torque and angular velocity. Previous studies however have so far suggested that entangled network structures in polymer solutions would induce elastic instability, shear history, shear banding, and wall-slip phenomena in the measurements of standard rheometers (Fischer, Wheeler, and Fuller, 2002; Sui and McKenna, 2007; Fardin et al., 2014). These cause spatial variations of shear rate in the narrow gap of the rheometer. Measurements conducted under the heterogeneous conditions cause bias errors in the determinations of the viscoelasticity (Mendes, Alicke, and Thompson, 2014; Saint-Michel et al., 2016).

Summary of the common problems

In the field of earth and planetary science as well, the viscoelastic effect of bubbles in magma and the effective viscosity modification due to the addition of solid particles have to be investigated to understand flows in nature, however, a powerful tool for measuring these rheological properties continues to be lacking. The current rheology measurements have reached their limits in a variety of research subjects from daily life to industry and nature, too many to mention here. The common problem regarding the oil-water mixtures, swallowing foods, and polymer solutions mentioned above is that the complexity of the fluid breaks down the important assumption in the measurement. It does not seem to have any meaning in the obtained rheological data, which are superposition of various phenomena such as friction between the dispersion and wall plate, shear localization between the gaps, and slippage at the interface. Another common problem is that even if it was possible to measure these complex fluids, the properties change over multiple time scales. It is not only depends on the amplitude and unsteadiness of the applied shear deformation, but also continues to change over time due to chemical reactions or phase separation even under the same applied condition. It is necessary to develop a new rheometer that solves all of these problems.

1.1.3 Novel rheometry compled with velocity profiling

The origin of the problems in the torque-type rheometer returns to the strong assumptions that the velocity distribution has to be Eq. 1.1, while many non-Newtonian fluids cause wall slip and shear band as shown in Fig. 1.2(b), in other cases, the dispersion is rubbed against the plate. A kind of paradigm shift has overcome the above problems with developing rheometries coupled with velocity profiling (Fardin et al., 2014; Gallot et al., 2013; Shiratori, Tasaka, and Murai, 2016). Unlike the principle of the torque-type rheometer, the flow velocity distribution in the gap is firstly measured for determining the actual shear deformation under the undesired deformation/flow conditions. There are various velocity measurement methods: ultrasonic velocity profiling (UVP) (Takeda, 1986; Takeda, 1995; Takeda, 2012; Tan et al., 2021), magnetic imaging velocimetry (Jarny et al., 2005), particle imaging velocimetry (Rodríguez-González et al., 2010). From the viewpoints of the dynamic range of

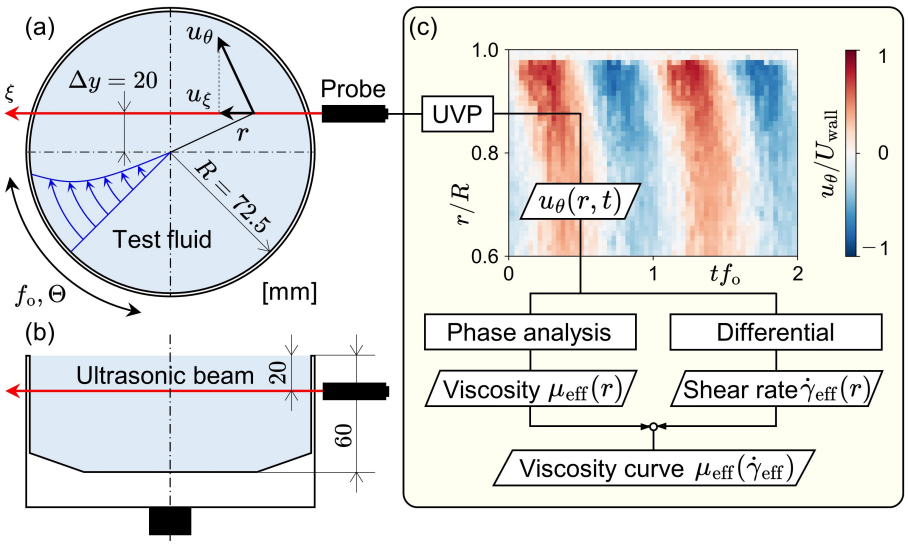


FIGURE 1.3: Overview of the velocity-profiling-based rheometry: (a) top view of the experimental apparatus and (b) side view, (c) analytical procedure of the phase analysis.

the velocity, measurement distance, scale of the facility, applicability to opaque fluids as almost all the non-Newtonian fluids are opaque, UVP is the most reasonable method satisfying these requirements in a well-balanced manner. A novel rheometry coupled with UVP, ultrasonic spinning rheometry (USR) has been developped in the last decade (Shiratori et al., 2013; Sakurai, Tasaka, and Murai, 2013; Tasaka, Kimura, and Murai, 2015; Tasaka et al., 2018; Yoshida, Tasaka, and Murai, 2017; Yoshida, Tasaka, and Murai, 2019b).

The concept of USR is to solve the equations of fluid motion as the rheological properties by substituting spatiotemporal velocity distributions of the oscillatory shear flow in a cylindrical open vessel as shown in Fig. 1.3. This is the opposite approach to computational fluid mechanics, which defines the properties firstly, solves the equation of fluid motion, and predicts the flow field. Based on the UVP measurement, USR has been established for a wide range of applications with complex fluids. Starting with developments for assuring the robustness of the analysis against the noise of the UVP measurement (Tasaka, Kimura, and Murai, 2015; Tasaka et al., 2018), successful stories of observing the complex properties of non-Newtonian fluids have been reported such as multi-phase fluids containing $O(1\ \mathrm{mm})$ size dispersions (Yoshida, Tasaka, and Murai, 2019a; Ohie et al., 2020), gel-sol coexistent fluids (Yoshida et al., 2018a; Yoshida, Tasaka, and Fischer, 2019), and viscoelastic polymer solutions (Yoshida, Tasaka, and Murai, 2019b; Yoshida, Tasaka, and Murai, 2019a). With USR as a core technology, the possibility of the above mentioned rheological characterization of the fluids in heterogeneous and non-equilibrium states has become realistic.

1.2 Objectives

The major objective of this thesis is to establish fundamental methodologies for rheological characterization of complex fluids in heterogeneous and non-equilibrium conditions. The obtained rheological properties are assured to be reversible for

reconstructing the original velocity field, which is an important characteristic to select or create constitutive equations in numerical simulation for predicting non-Newtonian fluid flows. This thesis mainly consists of five parts. First, the rheometry based on velocity information is further advanced. USR has some shortcomings and lacks in theoretical explanations, these are therefore cleared up in Chapter 2, and complete form of the rheometry is unveiled. As the second and third major contents, research projects that apply USR for rheological evaluation in heterogeneous and non-equilibrium conditions are summarized in Chapters 3 and 4. As the two directions of rheology research were mentioned at the beginning, the fourth major content is the application of the rheological properties identified by the velocity-profiling-based rheometry to flow prediction beyond just the rheological evaluation, and this is summarized in Chapter 5. The rheometry coupled with velocity profiling is basically based on an inverse problem approach, and this idea itself is applied for development of in-line rheometry in Chapter 6 as the last major content. The objectives and outline of each content are summarized below.

In Chapter 2, theoretical background of USR is explained. There are several analytical methods for USR, and phase analysis for evaluating the effective viscosity and linear viscoelastic analysis are introduced. The initial prototype of the USR was developed less than 10 years ago, and there are some shortcomings and a lack of some theoretical background. These issues are cleared up in this chapter and several techniques and knowledge cultivated during the development are recorded as technical notes of USR. Furthermore, to make USR more robust to rheological measurement of multi-phase fluids, a new method combined with torque measurement is unveiled.

As application of the velocity-profiling-based rheometry to heterogeneous and non-equilibrium conditions, the effective viscosity of the fluids whose rheological properties change over time is examined in Chapter 3. The oil-water mixture in the separation process is firstly targeted. While the water and the oil are separating in the vertical direction by the density difference, the effect of changes in the diameter and volume fraction of the water droplets on the effective viscosity of the mixture is monitored. The validity of the results are discussed by comparing with the theoretical formula. As another example of the fluids with time-varying rheological properties, the swallowing food mentioned above is examined. While many types of thickners are commercially available to thicken liquid foods properly, three aqueous solutions of thickeners are targeted as a first attempt. These have improved the stability against the saliva and ease of swallowing with each generation, but all of these characteristics are only evaluated qualitatively. The effective viscosity of these solutions after adding digestive enzyme is measured by USR, and the stability against the saliva and ease of swallowing are discussed. Through these two examples, the oil-water mixture and swallowing foods, applicability of the rheometry to heterogeneous and non-equilibrium conditions are indicated.

In order to evaluate viscoelasticity of the polymer solutions under various combinations of shear deformation and its timescale, an evaluation method termed rheology mapping is proposed in Chapter 4. The rheometry is utilized to resolve multi-time scale rheology. The map representation can comprehensively evaluate the dependence of viscoelasticiy on shear rate, strain, and oscillation frequency. It is applied to three typical types of polymer solutions to confirm the properties that have been recognized so far and to discover new properties. They are aqueous solutions of polyvinylpyrrolidone (PVP), carboxymehyl cellulose (CMC), and polyacrylamide, which are generally known as a Newtonian, shear thinning, and viscoelastic

fluids, respectively. With the torque-type rheometer, it was not possible to distinguish whether the evaluated property was material derived or geometrically dependent. It will be possible to break away from the current situation and discuss the essential combinations of the shear deformation and its timescale that modifies the viscoelasticity. The rheology mapping is a practical tool to investigate both shear rate and frequency dependent viscoelastic properties. As further application, rheology of dilute bubble suspensions is investigated. The comprehensive representation reveals the conditions where the viscosity increase/decrease occurs and the most prominent viscoelasticity appears.

One of the remarkable characteristics of the velocity-profiling-based rheometry is that the velocity field can be reconstructed with the identified rheological properties. In Chapter 5, a reconstruction method for the velocity field is proposed and compared with experimental results. The reversability and applicability of the rheometry to flow prediction are examined in this chapter. The rheological properties evaluated under steady and oscillatory shear conditions are applied to predict the one-directional laminar shear flow in a circular pipe. In Chapter 6, The application of the inverse analysis, which is the basis of velocity-profiling-assisted rheometry, to the development of inline rheometry is finally introduced. The in-line rheometry is applied to monitor transient pseudo manufacturing process of liquid foods, and time variations of shear-rate-dependent viscosity are quantified. Through these developments and demonstrations, it is indicated that the rheometry can be utilized not only for evaluation, but also as a practical tool for flow prediction and monitoring production processes, which will play major roles in industry as well.

Chapter 2

Rheometry coupled with ultrasonic velocity profiling

Theoretical background of rheometry coupled with ultrasonic velocity profiling is summarized in this chapter. The major concept of the rheometry is that the velocity profile of steady or unsteady shear flow is measured by an ultrasonic velocity profiler (UVP). The rheological properties represented by the effective viscosity and viscoelasticity are determined so that the measured velocity profile satisfies the equation of fluid motion. A general explanation of UVP is therefore given in § 2.1 first. Then, the velocity-profiling-based rheometry is introduced in § 2.2 and 2.3 under conditions of steady and unsteady shear, respectively. Technical note cultivated during these development are given in § 2.4. Finally, the most recent generation of velocity-profiling-assisted rheometry is presented in § 2.5.

2.1 Ultrasonic velocity profiler (UVP)

UVP is one of the most practical velocity measurement tools as much as optical visualization methods represented by particle image velocimetry (PIV) in the field of experimental fluid mechanics. It can obtain spatial and temporal distributions of velocity components of the direction of the measurement line. Spatial and temporal resolutions of UVP are $O(1\ \mathrm{mm})$ and $O(10\ \mathrm{msec})$. Dynamic range of the velocity is from $O(1\ \mathrm{mm/s})$ to $O(100\ \mathrm{mm/s})$ usually. Although the measurement is restricted in one line, the notable advantage is the applicability to opaque fluids, which is not covered by PIV while almost all the non-Newtonian fluids are opaque in food and chemical industries. This is why UVP is adopted for the velocity-profiling-based rheometry.

Measurement principles of UVP is specifically explained in the literature (Takeda, 1995; Takeda, 2012), brief explanation is therefore given here. Along the measurement line ξ, the ultrasonic transducer emits a pulse of ultrasonic waves whose fundamental frequency is f_0. The pulse is fully formed by $n(\geq 4)$ waves at least. When a particle exists on the measurement line, the pulse is reflected on the surface and comes back to the transducer as schematically shown in Fig. 2.1. The position ξ of the particle is determined by

$$\xi = \frac{c\tau}{2}, \tag{2.1}$$

where c and τ denote speed of sound in the test fluid and time-of-flight, that is, the total time it takes for the pulse to be emitted, reflected by the particle, and returned to the transducer. The frequency of the reflected ultrasonic pulse wave is modulated by Doppler shift frequency f_D. Assuming that the particle has the velocity component

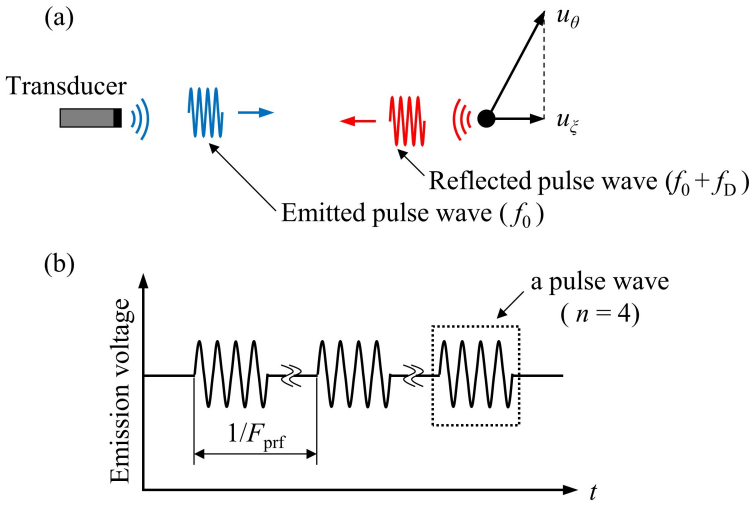


FIGURE 2.1: Measurement principle of UVP: (a) an ultrasonic pulse wave with the resonance frequency of f_0 is emitted from the transducer and reflected by a tracer particle, where the frequency of the returning pulse wave is modulated by f_D, and (b) schematic of the emission voltage.

u_ξ in the direction of the measurement line, the following relation is established:

$$u_\xi = \frac{cf_D}{2f_0}. \tag{2.2}$$

If the pulse could be measured as voltage fluctuations at the sampling frequency above $2(f_0 + f_D)$ taking into account Nyquist sampling theorem, u_ξ was obtained by determining f_D with spectrum analysis. Although possible today, no AD converter with such high temporal resolution $O(1\ \text{MHz})$ existed during the development of UVP in the 1980s. Therefore, pulse Doppler method is developed instead of recording the whole fluctuation of the pulse, which repeats pulse emission and echo reception. Since the principle must be the Doppler effect essentially, the details are omitted here and the available measurement ranges of the method are described next.

In the pulse Doppler method, a pulse wave is emitted N times to obtain an instantaneous velocity profile. Each of the N pulses is emitted in a certain waiting time $1/F_{\text{prf}}$, where F_{prf} represents a pulse repetition frequency. An emission of the pulse wave has to wait until the previous pulse wave comes back to the transducer, therefore, maximum depth of the velocity measurement P_{max} is limited to

$$P_{\text{max}} = \frac{c}{2F_{\text{prf}}}. \tag{2.3}$$

The condition $f_{\text{D}} < F_{\text{pfr}}/2$ should be satisfied according to Nyquist sampling theorem because a series of N pulse waves is measured with the sampling frequency F_{prf}. The measurable maximum velocity U_{max} is therefore limited to

$$U_{\text{max}} = \frac{cF_{\text{prf}}}{4f_0} \tag{2.4}$$

by considering both $f_D < F_{pfr}/2$ and Eq. 2.2. From Eqs. 2.3 and 2.4, there is a trade-off relation,

$$P_{max} \cdot U_{max} = \frac{c^2}{8 f_0}. \tag{2.5}$$

UVP Monitor model-Duo (Met-Flow, S.A., Switzerland), which is the main UVP device in this thesis, utilizes 8-bit digital signal processor, therefore, resolution of the velocity Δu_ξ is

$$\Delta u_\xi = \frac{U_{max}}{255}. \tag{2.6}$$

The pulse Doppler method requires N sets of emission and reception of the pulse wave to obtain an instantaneous velocity profile as mentioned before, therefore, the time resolution Δt is

$$\Delta t = \frac{N}{F_{prf}}. \tag{2.7}$$

The spatial resolution $\Delta\xi$ is defined by the width of the pulse wave as

$$\Delta\xi = n\frac{c}{f_0}, \tag{2.8}$$

where the term c/f_0 is a wavelength of the ultrasonic wave. A spatial resolution perpendicular to the measurement line is defined by the diameter of the pulse wave. In the cases of transducers with the resonance frequencies of 4 MHz and 2 MHz provided by Met-Flow, S.A., Switzerland, the active diameter is 5 mm and 10 mm, respectively.

2.2 Rheological evaluation under steady shear

Schematics and a photograph of the rheometer combined with an ultrasonic velocity profiler (UVP) are shown in Fig. 2.2(a), (b) and (c). The instrument consists of a fixed inner cylinder of R_{in} = 50 mm connected to an axial torque sensor (UTM III – 0.5Nm, Unipulse Co., Ltd., Japan) and an outer cylinder of R_{out} = 105 mm driven by a stepper motor with a constant rotation speed. Under this configuration, azimuthal one-directional flow is realized between the double concentric cylinders, as schematically shown in Fig. 2.2(b). The maximum shear rate realized in this prototype is $O(10^1\ s^{-1})$ with assumptions of a Newtonian fluid and maximum rotation speed of 50 rpm. This is lower than that of a standard torque-type rheometer because of being the wide gap between the double cylinders. Expansion of the shear rate range is possible to $O(10^2\ s^{-1})$ by narrowing the gap and increasing the maximum rotation speed of the stepping motor. A stepped cylinder is suspended by three stainless rods from the base and placed under the inner cylinder to insulate the influence of secondary flow, that is, end effects induced by the bottom of the outer cylinder. Neither the stepped cylinder nor rods are in contact with the inner cylinder, so the torque sensor measures axial torque that is caused solely by simple shear stress acting on the inner cylinder wall. This is an improvement over the velocity profiling-assisted rheometer described in previous studies (Derakhshandeh, Vlassopoulos, and Hatzikiriakos, 2012; Shiratori et al., 2015; Shiratori, Tasaka, and Murai, 2016), which simply consisted of inner and outer cylinders. This experimental apparatus is, nevertheless, a prototype and therefore has some shortcomings, such as its large size and the fact that the inner cylinder is also filled with the test fluid. Large amount of test sample is required comparing with a standard torque-type rheometer. This size problem can

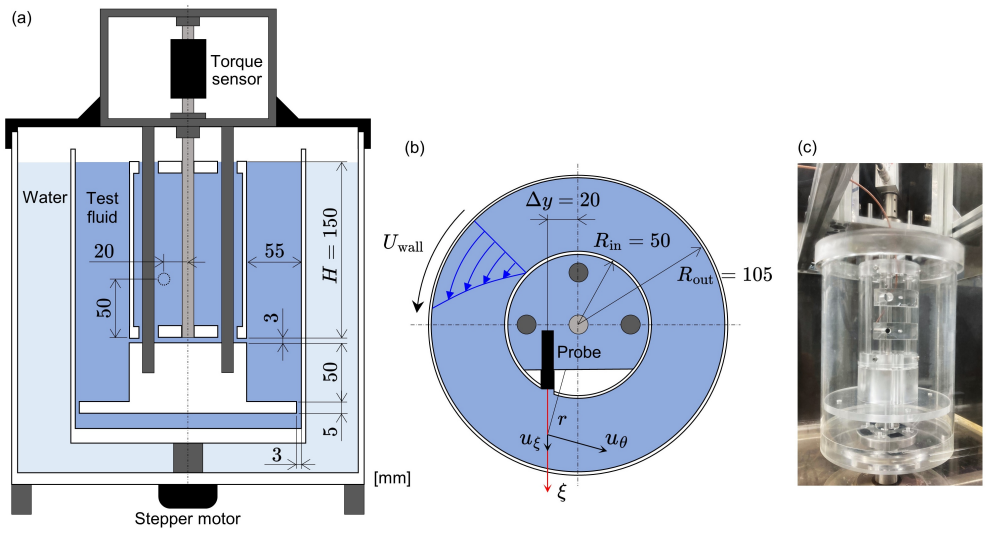


FIGURE 2.2: Schematics of a rheometer combined with ultrasonic velocity profiling for evaluating shear-rate-dependent rheological properties of complex fluids: (a) vertical cross-sectional view, (b) horizontal cross-sectional view at the height of the ultrasonic probe, and (c) photograph of rheometer taken from the side, in which the test fluid and surrounding water are not present for better visibility. Unit of length: mm.

be solved by minimizing the height and gap-size; the amount of a test fluid will be reduced to 500 mL, which will be improved in the next version.

The ultrasonic probe of an UVP (UVP Duo monitor, MetFlow SA, Switzerland) is horizontally inserted into the inner cylinder at an off-axis position of Δy = 20 mm to capture the azimuthal velocity profile $u_\theta(r,t)$. Frequency of the ultrasonic wave and the active diameter of the probe are 4 MHz and 5 mm. As shown in Fig. 2.2(b), the UVP captured spatiotemporal distribution of velocity components in the propagation direction of the ultrasonic waves. Spatial resolution of the UVP is approximately 1 mm in the propagation direction and its temporal resolution is O(10 ms). The UVP measurement volume is therefore a cylinder with a diameter of 5 mm and height of 1 mm. The higher the emission frequency is, the better spacial resolution UVP has, but the ultrasonic pulse is attenuated more. For example, clay suspensions with volume fraction of 30 wt.% can be measured by a low emission frequency 2 MHz transducer: application range of the velocity-profiling-assisted rheometer is wide. Assuming that flow in the gap is axisymmetric and dominates in the azimuthal direction, $u_\xi(\xi,t)$ is uniquely converted to $u_\theta(r,t) = (r/\Delta y)u_\xi(\xi,t)$. When the outer cylinder rotates with a constant azimuthal velocity U_{wall}, spatial distributions of simple shear rate are obtained from the averaged velocity profile $\bar{u}_\theta(r)$ as:

$$\dot{\gamma}(r) = \left(\frac{d}{dr} - \frac{1}{r}\right)\bar{u}_\theta(r). \tag{2.9}$$

Synchronously with the UVP measurement, the torque sensor measures the time variation of the axial torque $T(t)$ acting on the inner cylinder. Shear stress acting on the inner cylinder is therefore obtained from the time-averaged axial torque T as:

$$\tau_{\text{wall}} = \frac{T}{2\pi R_{\text{in}}^2 H}, \tag{2.10}$$

where H is height of the inner cylinder, as shown in Fig. 2.2(a). Considering conservation of angular momentum, the spatial profile of shear stress is derived as

$$\tau(r) = \tau_{\mathrm{wall}} \left(\frac{R_{\mathrm{in}}}{r} \right)^2 . \tag{2.11}$$

Shear-rate-dependence of shear stress $\tau(\dot{\gamma})$, generally called a flow curve, was obtained by combining Eqs. 2.9 and 2.11. For improving precision of the evaluation, dozens of flow curves are obtained by increasing rotation speed of the outer cylinder gradually. Average shear stress at each $\dot{\gamma}$ is evaluated in the range from $\dot{\gamma} - \Delta\dot{\gamma}$ to $\dot{\gamma} + \Delta\dot{\gamma}$ with $\Delta\dot{\gamma} = 1\ \mathrm{s}^{-1}$, and corresponding standard deviations are also evaluated, which therefore also reflects precision of the shear rate calculated from the velocity data obtained by the UVP measurement.

A standard torque-type rheometer assumes a constant shear rate in its narrow gap. In cases of some polymer solutions, the evaluated rheological properties include bias errors caused by shear-localization problems. The velocity-profiling-assisted rheometer mitigates these problems and enables robust evaluation of complex fluids, including high-molecular-weight polymer solutions and heterogeneous materials.

2.3 Rheological evaluation under unsteady shear

The rheometry coupled with UVP under unsteady shear conditions were proposed by Shiratori et al. (2015). They measured the spin-up flow in an open cylindrical vessel, and the resulting spatiotemporal velocity distribution was measured using UVP or particle velocity profiling. Tasaka, Kimura, and Murai (2015) further proposed rheometry in sinusoidally oscillatory shear flow, which only utilizes velocity information, called ultrasonic spinning rhometry (USR). The phase analysis is the pioneering methodology of USR, and it evaluates the effective viscosity from the phase delay of the oscillatory shear flow propagating from the outer wall to the central axis, which is explained in § 2.3.1. For accessing more specific rheological properties, linear viscoelastic analysis was developed using the Maxwell model as the constitutive equation. The idea is that the velocity information captured by UVP is substituted in the equation of fluid motion, and the viscosity coefficient and elastic modulus are locally evaluated so that the velocity distribution satisfies the equation. This method is summarized in § 2.3.2.

2.3.1 Phase analysis

Schematic of the experimental setup used in the phase analysis and linear viscoelastic analysis is shown in Fig. 2.3. An acrylic cylindrical vessel with radius of $R = 77$ mm is filled with a test fluid. The vessel is put in a water bath for temperature control and propagation of ultrasonic waves in the UVP measurement. An ultrasonic transducer is installed horizontally and off-axis Δy away from the central axis of the vessel to capture the azimuthal velocity $u_\theta(r,t)$. The vessel is sinusoidally oscillated by a stepping motor with the oscillation frequency of f_o and the rotation angle of Θ. The velocity at the wall is hence given as $u_{\mathrm{wall}}(t) = U_{\mathrm{wall}}\sin(\omega_\mathrm{o} t)$ with $\omega_\mathrm{o} = 2\pi f_\mathrm{o}$ and $U_{\mathrm{wall}} = 2\pi f_\mathrm{o} R\Theta$. The oscillatory shear flow propagating from the cylindrical wall toward the central axis is measured by UVP, which can get the velocity distribution $u_{\tilde{\xi}}(\tilde{\xi},t)$ as denoted in § 2.1. Assuming that the flow in the vessel is axially symmetric and dominated in the azimuthal direction, the velocity captured by UVP

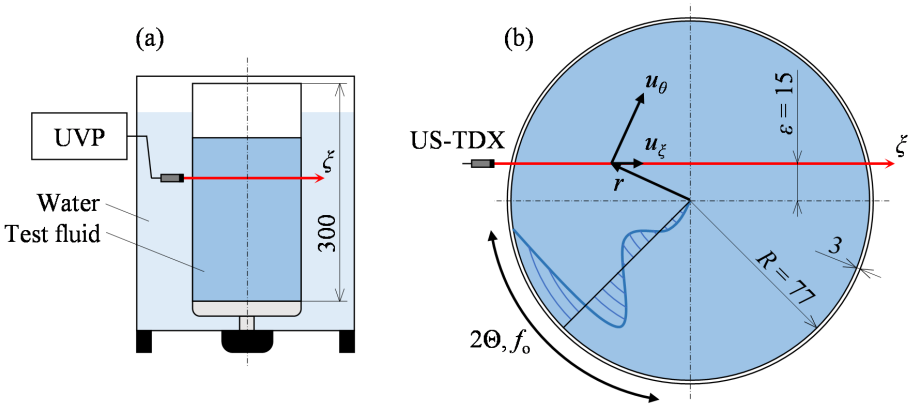


FIGURE 2.3: Schematic diagrams of the experimental setup for capturing spatiotemporal velocity distributions of oscillatory shear flows by the ultrasonic velocity profiler: (a) side view and (b) top view. Dimensions in [mm]

is uniquely converted as $u_\theta = (r/\Delta y)u_\xi$. Under these flow assumptions, symmetrical velocity distributions are obtained at the near and far sides from the ultrasonic probe. The results do not change regardless of which side is used for the analysis, but it should be noted that when using an ultrasonic probe with high emission frequency, for example 8 MHz, radially coarse-grained data is obtained for the velocity distribution on the far side due to the expansion of the ultrasonic pulse. In addition, if the attenuation of the ultrasonic waves is significant, as in the case of multi-phase fluids, only the velocity distribution in the near side is obtained. Given these considerations, the advantage of using the velocity distribution on the near side may be greater, but the advantage of using the far side is that multiple reflections within the acrylic wall can be avoided, and the velocity distribution up to the vicinity of the wall can be obtained.

The phase analysis focuses on the phase lag of the oscillatory shear flow propagating from the side wall toward the central axis of the vessel. The phase lag function $\phi(r)$ is obtained by descrete Fourier transform as

$$\phi(r) = \arg\left[\hat{u}_\theta(r, \omega = \omega_o)\right], \tag{2.12}$$

where the hat symbol represents Fourier transform operation. The DFT is defined as

$$\hat{u}_\theta(r, \omega = 2\pi k\Delta f) = \frac{2}{N}\sum_{n=0}^{N-1} u_\theta\left(r, \frac{nT}{N}\right)\exp\left(-ik\frac{2\pi}{N}n\right)(k = 0, 1, ..., N-1), \tag{2.13}$$

where N and T denote number of temporal profiles and total measurement time $N\Delta t$. Considering the characteristic of DFT, coefficient in Eq. 2.13 is $2/N$ not $1/N$, which will be specifically explained in § 2.4. The frequency resolution Δf is determined as $\Delta f = 1/N\Delta t = 1/T$, where Δt is the temporal resolution of UVP. Empirically, when the viscosity of a test fluid is low such as pure water, the fluid cannot track the oscillatory motion of the cylindrical wall, and there will be a considerable phase lag between the fluid near the wall and that near the central axis of the vessel. On the other hand, for the highly viscous fluid such as honey, the fluid inside the vessel immediately follows the oscillatory motion of the wall, and there will be almost no phase lag between the fluid near the wall and that near the central axis. What is clear

from these experiments is that the radial gradient of the phase lag function, $d\phi/dr$ reflects the local viscosity. This is the principle in the phase analysis.

Assuming the flow in the cylindrical vessel is axially symmetric and that radial flow is negligible, the flow field satisfies Cauchy's equation of motion, that is, conservation of angular momentum,

$$\rho \frac{\partial u_\theta}{\partial t} = \left(\frac{\partial}{\partial r} + \frac{2}{r} \right) \tau, \tag{2.14}$$

where ρ and τ represent density of the fluid and shear stress. As for a Newtonian fluid, Newton's law of viscosity $\tau = \mu\dot{\gamma}$ is established, where $\dot{\gamma}$ represents shear rate calculated in the cylindrical coordinate as

$$\dot{\gamma}(r,t) = \left(\frac{\partial}{\partial r} - \frac{1}{r} \right) u_\theta(r,t). \tag{2.15}$$

Substituting Eq. 2.15 to Newton's law of viscosity and Eq. 2.14, the following equation is obtained,

$$\frac{\partial u_\theta}{\partial t} = \nu \left(\frac{\partial^2 u_\theta}{\partial r^2} + \frac{1}{r}\frac{\partial u_\theta}{\partial r} - \frac{u_\theta}{r^2} \right), \tag{2.16}$$

where ν represents kinematic viscosity of the fluid. With two boundary conditions, $u_\theta(r = R, t) = U_{\mathrm{wall}} \sin(2\pi f_\mathrm{o} t)$ and $u_\theta(r = 0, t) = 0$, the analytical solution of Eq 2.16 is obtained as

$$u_\theta(r,t) = U_{\mathrm{wall}} A_\mathrm{N}(r;\nu) \sin[\omega_\mathrm{o} t + \phi_\mathrm{N}(r;\nu)]. \tag{2.17}$$

Specifications of the derivation are described in the literature (Tasaka, Kimura, and Murai, 2015). The phase lag $\phi_\mathrm{N}(r;\nu)$ is calculated as

$$\phi_\mathrm{N}(r;\nu) = \tan^{-1}\left[\frac{\Phi(R)\Psi(r) - \Phi(r)\Psi(R)}{\Phi(R)\Phi(r) + \Psi(R)\Psi(r)} \right], \tag{2.18}$$

$$\Phi(r) = \sum_{m=0}^{\infty} \frac{2^m}{m!(m+1)!} \left(\frac{kr}{2} \right)^{2m+1} f_m, f_m = \begin{cases} (-1)^{(m+2)/2} & m = \text{even number} \\ (-1)^{(m+1)/2} & m = \text{odd number} \end{cases}, \tag{2.19}$$

$$\Psi(r) = \sum_{m=0}^{\infty} \frac{2^m}{m!(m+1)!} \left(\frac{kr}{2} \right)^{2m+1} g_m, g_m = \begin{cases} (-1)^{m/2} & m = \text{even number} \\ (-1)^{(m+1)/2} & m = \text{odd number} \end{cases}. \tag{2.20}$$

In these equations, k is defined as $k = \sqrt{\omega_\mathrm{o}/2\nu}$. In the phase analysis, all the rheological properties including viscosity and viscoelasticity are represented by an effective Newtonian viscosity ν_{eff}, which satisfies the following condition,

$$\frac{d\phi(r)}{dr} = \frac{d\phi_\mathrm{N}(r;\nu = \nu_{\mathrm{eff}})}{dr}. \tag{2.21}$$

As $d\phi_\mathrm{N}(r;\nu)/dr$ monotonically decreases with respect to ν at each radial position, ν_{eff} is obtained uniquely at each r. Determining ν_{eff} at each radial position, spatial variation of the effective viscosity $\nu_{\mathrm{eff}}(r)$ is obtained. Regarding the representative shear rate at each radial position, the effective value of $\dot{\gamma}(r,t)$ in the time direction, $\dot{\gamma}_{\mathrm{eff}}(r)$ is used, which is also explained in § 2.4.

As demonstration of the phase analysis, results of silicon oil (Shin-Etsu Chemical

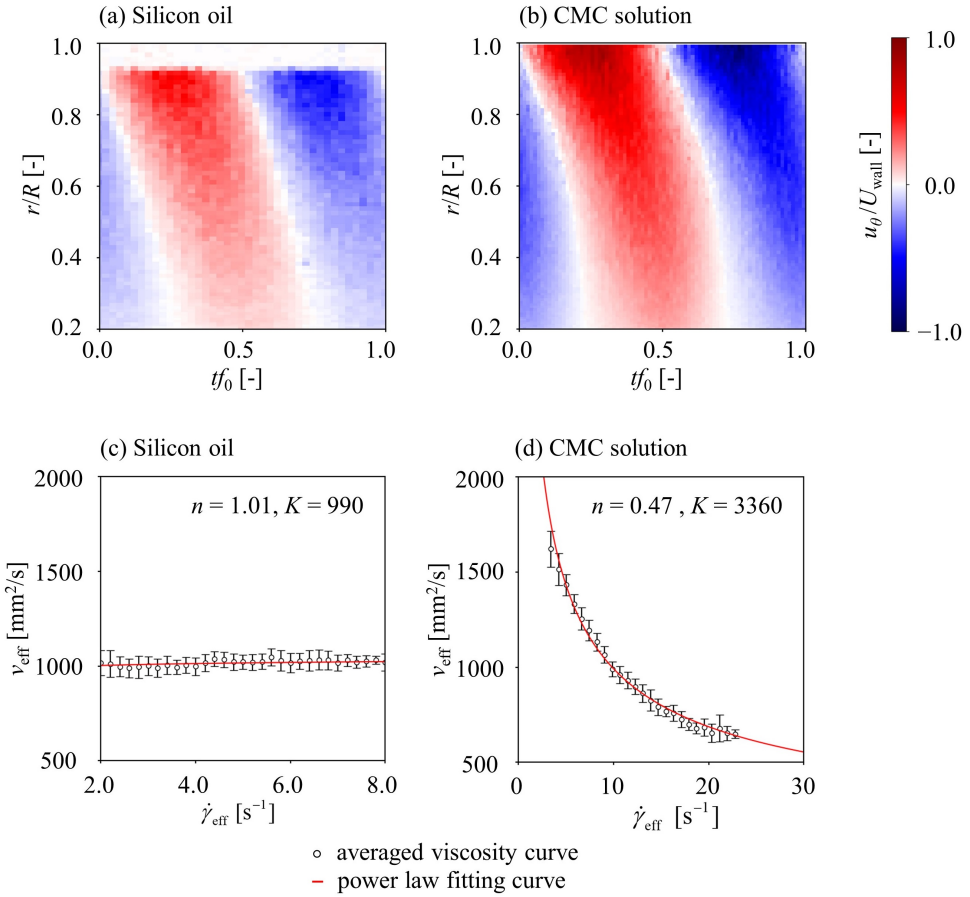


FIGURE 2.4: Demonstrations of the phase analysis: Spatiaotemporal distributions of the azimuthal velocity $u_\theta(r,t)$ for (a) 1000 cSt silicon oil (Newtonian fluid) and (b) carboxymethl cellulose (CMC) 1.0 wt.% aqueous solution at 25 °C. The oscillation frequency is f_o and the rotation amplitudes are $\Theta = 5\pi/6$ rad for the silicon oil and $\Theta = \pi$ rad for the CMC solution. The effective viscosity curves are obtained by the phase analysis for (c) the silicon oil and (d) the CMC solution, respectively. The error bars indicate standard deviations.

Co. Ltd., Japan) with the kinematic viscosity of 100 cSt and carboxymethyl cellulose (CMC) 1.0 wt.% aqueous solution (Molecular weight: 2.0×10^6 g/mol, Daicel Miraizu Co. Ltd., Japan) are introduced here. The formar and latter ones are respectively well known as Newtonian fluid and shear thinning fluid (Kulicke et al., 1996; Benchabane and Bekkour, 2008). Both of the experiments were conducted at 25°C, and fine spherical particles (CHP20P, Mitsubishi Chemical Co. Ltd., Japan) are added to the fluids as the tracer particles of the UVP measuremnt. Density of the particles is almost the same to that of the fluids, and mean diameter is in the range of 75 – 150 μm. In the UVP measurement, 2 MHz and 4 MHz ultrasonic transducers were utilized respectively for the silicon oil and the CMC solution as ultrasonic waves are considerably attenuated in the silicon oil. The oscillation parameters were set as $f_o = 0.5$ Hz, $\Theta = 5\pi/6$ rad for the silicon oil and $\Theta = \pi/$ rad for the CMC solution.

Time variations of instantaneous radial profile $u_\theta(r,t)$ are shown in Fig. 2.4. The axes show the normalized elapse time and radial position with the contours representing the measured velocity in the azimuthal direction. These spatiotemporal

distributions show that the oscillatory shear flow driven by the cylindrical wall (r/R = 1.0) propagates toward the central axis with a time delay (diagonal patterns on the distribution) and attenuation (lowering in the velocity amplitude away from the wall). When comparing the phase lag of the silicon oil and the CMC solution, that of the former is almost straight, meaning that the fluid is Newtonian. Regarding the latter, the spatial derivative of the phase lag becomes smaller toward the central axis. This means that the fluid has relatively low viscosity near the wall and high viscosity near the central axis. Viscosity curves of the fluids are also shown in Fig. 2.4. The graphs show the shear rate dependent viscosity $\nu_{\mathrm{eff}}(\dot{\gamma}_{\mathrm{eff}})$ obtained by the phase analysis. As for the silicon oil, the viscosity takes a constant value regardless of $\dot{\gamma}_{\mathrm{eff}}$, meaning that the fluid is Newtonian. On the other hand, the viscosity of the CMC solution monotonically decreases as $\dot{\gamma}_{\mathrm{eff}}$ increases, that is, the shear thinning characteristic emerges.

2.3.2 Linear viscoelastic analysis

Almost all the materials express not only viscous but also elastic behaviour. Linear viscoelastic analysis introduced here decomposes contributions of viscosity and elasticity to the shear stress, which is an effective tool for better understanding viscoelastic characteristics of the materials. Linear and non-linear viscoelastic properties mean here whether the stress response includes higher harmonics or not. The linear viscoelastic analysis targets the fluids that response sinusoidal shear stress against the sinusoidal shear deformation. The analysis assumes that the flow in the cylindrical vessel satisfies Cauchy's equation of motion as shown in Eq 2.14. The following Maxwell model is introduced as a constitutive equation to decompose viscous and elastic contributions to the shear stress while the phase analysis utilizes Newton's law of viscosity,

$$\tau + \frac{\mu_{\mathrm{e}}}{E_{\mathrm{e}}}\frac{\partial \tau}{\partial t} = \mu_{\mathrm{e}}\left(\frac{\partial u_\theta}{\partial r} - \frac{u_\theta}{r}\right), \tag{2.22}$$

where μ_{e} and E_{e} represent viscosity coefficient and elastic modulus. Note that μ_{e} and E_{e} are parameters defined in Eq. 2.22, and are constants that relate the shear rate and stress profiles for one oscillation cycle. These parameters are allowed to change depending on the applied shear intensity and frequency. As an useful indicator to quantify viscoelasticity, phase difference of viscoelasticity δ is introduced as

$$\tan\delta = \frac{E_{\mathrm{e}}}{\mu_{\mathrm{e}}\omega_{\mathrm{o}}}, \tag{2.23}$$

where $\delta = \pi/2$ rad stands for a pure viscous fluid, $\delta = 0$ rad for a pure elastic material, and $0 < \delta < \pi/2$ rad for a viscoelastic material. The optimal set of μ_{e} and E_{e} is uniquely determined by directly substituting the experimentally obtained $u_\theta(r,t)$ to Eqs. 2.14 and 2.22 in theory. It is however difficult because of the measurement noise of UVP particularly in differential operations. DFT is therefore performed to u_θ with respect to t for removing the measurement noise and extracting only the dominant frequency component. Performing DFT to Eqs. 2.14 and 2.22,

$$i\omega\rho\hat{u}_\theta = \left(\frac{\partial}{\partial r} + \frac{2}{r}\right)\hat{\tau}, \tag{2.24}$$

$$\hat{\tau} + i\omega\frac{\mu_{\mathrm{e}}}{E_{\mathrm{e}}}\hat{\tau} = \mu_{\mathrm{e}}\left(\frac{\partial}{\partial r} - \frac{1}{r}\right)\hat{u}_\theta, \tag{2.25}$$

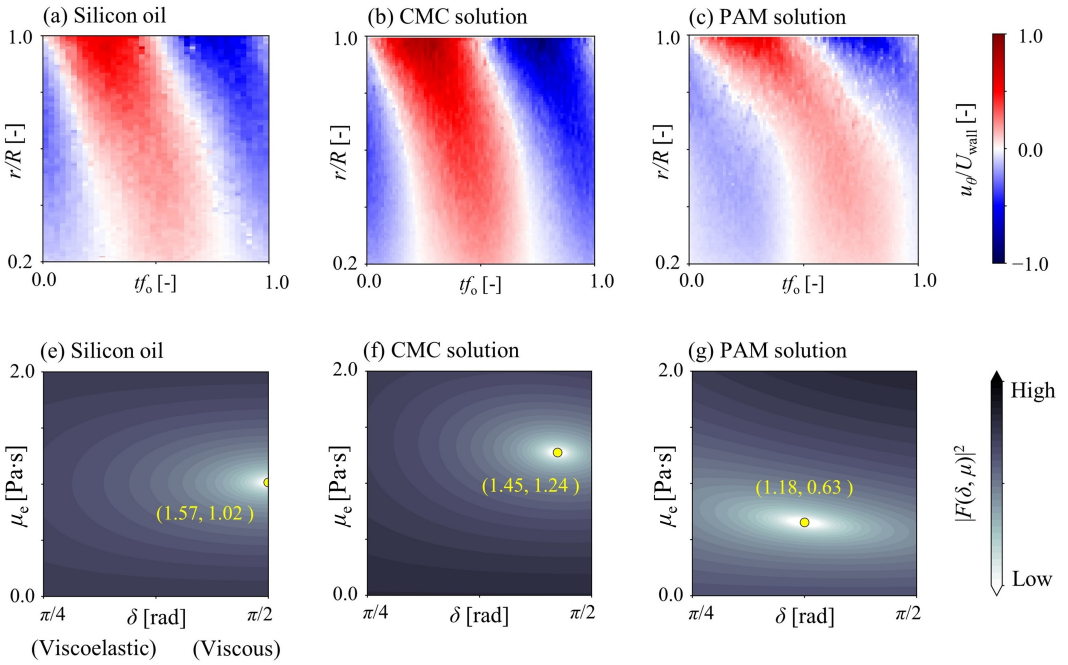


FIGURE 2.5: Demonstrations of the linear viscoelastic analysis: Spatiotemporal distributions of the azimuthal velocity $u_\theta(r,t)$ for (a) 1000 cSt silicon oil, (b) the CMC 1.0 wt.% and (c) the PAM 1.0 wt.% aqueous solutions, where the oscillation parameters are f_o = 0.5 Hz and $\Theta = \pi$ rad. Distributions of the cost function F at r/R = 0.6 for (a) the silicon oil, (b) the CMC, and (b) the PAM solutions.

are derived, where the hat symbol represents DFT operation. The cost function is defined as residual of both sides in Eq. 2.24.

$$F(\mu_e, \delta; r) = \left| i\omega\rho\hat{u}_\theta - \left(\frac{\partial}{\partial r} + \frac{2}{r}\right)\hat{\tau}\right|^2_{\omega=\omega_o}, \tag{2.26}$$

where $\hat{\tau}$ is obtained by the following calculation,

$$\hat{\tau}(r,\omega) = \mu_e \sin^2\delta\,[Re(r,\omega) + iIm(r,\omega)], \tag{2.27}$$

$$Re(r,\omega) = \frac{\partial}{\partial r}\mathrm{Re}[\hat{u}_\theta] - \frac{1}{r}\mathrm{Re}[\hat{u}_\theta] + \left(\frac{\partial}{\partial r}\mathrm{Im}[\hat{u}_\theta] - \frac{1}{r}\mathrm{Im}[\hat{u}_\theta]\right)\cot\delta, \tag{2.28}$$

$$Im(r,\omega) = \frac{\partial}{\partial r}\mathrm{Im}[\hat{u}_\theta] - \frac{1}{r}\mathrm{Im}[\hat{u}_\theta] - \left(\frac{\partial}{\partial r}\mathrm{Re}[\hat{u}_\theta] - \frac{1}{r}\mathrm{Re}[\hat{u}_\theta]\right)\cot\delta. \tag{2.29}$$

Solving optimization problems based on the cost function at each r, $\mu_e(r)$ and $\delta(r)$ are obtained. As one of the optimization algorithms, particle swarm optimization (Banks, Vincent, and Anyakoha, 2007) was adopted in the code. On of the advantages to use δ instead of E_e is to narrow the searching area of the rheological variables in the optimization problems. The elastic modulus takes from zero to infinity while δ is from 0 to $\pi/2$ rad. It should be noted that μ_e and δ vary depending on r in the case of non-Newtonian fluids as the amplitude of shear rate takes $O(10^1\ \mathrm{s}^{-1})$ on the cylindrical wall and gradually decreases to $O(10^{-1}\ \mathrm{s}^{-1})$ toward the central axis of the vessel.

As demonstration of the linear viscoelastic analysis, results of the silicon oil, the CMC 1.0 wt.% solution, and polyacrylamide (PAM) 1.0 wt.% aqueous solution (Molecular weight: 1.3×10^7 g/mol, MT AquaPolymer Co. Ltd., Japan) are introduced here. The PAM solution is well known as a viscoelastic fluid (Kulicke and Porter, 1980; Lewandowska, 2007). All the experiments were conducted at 25°C. As for the UVP measurement, the tracer particles (CHP 20P) were added to the fluids. The transducer with the emission frequency of 2 MHz was used for the silicon oil and that of 4 MHz was used for the aqueous solutions. The oscillation parameters were set as $f_o = 1.0$ Hz and $\Theta = \pi$ rad.

Time variations of instantaneous radial profile of the azimuthal velocity $u_\theta(r,t)$ are shown in upper panels in Fig. 2.5. Compared with the distributions in the silicon oil and the CMC solution, that of the PAM solution is clearly different. The oscillatory shear flow propagates without any phase lag near the central axis ($r/R < 0.4$), showing that the PAM solution has a yield stress. Distributions of the cost function at $r/R = 0.6$ as a representative example are shown in the lower panels in Fig. 2.5. All the distributions are uni-modal, meaning that the viscoelasticity is uniquely determined at each r. As for the silicon oil firstly, the viscosity is evaluated as $\mu_e = 1.02$ Pa·s, which is almost the same to the catalog value of 0.97 Pa·s. The phase difference of viscoelasticity is evaluated as $\delta = 1.57$ rad, which is almost the same to $\delta = \pi/2$ rad, meaning that the silicon oil is a purely viscous fluid. The silicon oil is generally recognized as a Newtonian fluid, and these results testify the validity of the linear viscoelastic analysis. As for the CMC solution, it is evaluated as a viscoelastic fluid. The CMC solution tends to attract attention for its shear-thinning characteristic, but it can be seen that it also has weak viscoelasticity. As for the PAM solution, it can be seen that the PAM solution has stronger viscoelasticity than the CMC solution. In this way, the linear viscoelastic analysis enables a quantitative discussion of the viscoelasticity of polymer solutions. This viscoelasticity is however the result under the limited condition of the shear rate at $r/R = 0.6$ and $f_o = 0.5$ Hz. In fact, the viscoelasticity of polymer solutions changes variously depending on the shear deformation and its timescale represented by shear rate, strain, and oscillation freuquency. Comprehensive evaluation of viscoelasticity with USR is proposed in § 4.1 later.

The linear viscoelastic analysis uses the Maxwell model as a constitutive equation, and the viscosity coefficient and elastic modulus are optimally determined at eaqch radial position so that the velocity distribution satisfies the Cauchy's equation of motion. This Maxwell model is therefore has a much higher degree of freedom to characterize the linear viscoelasticity, and compared here with the original Maxwell model, fractional Maxwell model, and upper convected Maxwell model, which are often used simple models for characterizing viscoelasticity. The first comparison is done with the original Maxwell model, which relates the shear stress τ and shear strain γ as

$$\tau + \frac{V}{G}\frac{d\tau}{dt} = V\frac{d\gamma}{dt} \tag{2.30}$$

with the viscosity coefficient V and elastic modulus G. Fourier transform is performed on Eq. 2.30 to know the frequency response of the shear stress when the sinusoidal shear deformation is applied,

$$\hat{\tau} + i\omega\frac{V}{G}\hat{\tau} = i\omega V\hat{\gamma}. \tag{2.31}$$

Complex viscosity is defined as $G^* = \hat{\tau}/\hat{\gamma}$, which is useful rheological property for

understanding both amplitude and phase relations of the shear rate and stress. It is also expressed as $G^* = G' + iG''$ with the storage modulus G' and loss modulus G''. Solving Eq. 2.31 regarding $\hat{\tau}/\hat{\gamma}$, the complex viscosity is obtained as

$$G^*(\omega) = \frac{G(V\omega)^2 + iG^2(V\omega)^2}{G^2 + (V\omega)^2}. \tag{2.32}$$

Assuming that $G^*(\omega)$ is obtained with a rheometer, G and V are determined, for example, by fitting the experimentally obtained $G'(\omega)$ and $G''(\omega)$ with Eq. 2.32 in real and imaginary parts, respectively. Essentially, the Maxwell model used in USR allows V and G to change depending on ω and also shear rate, it is therefore clear that the USR one can perfectly fit the experimental data and can characterize variety of frequency and shear rate dependent viscoelasticity, rather than the original Maxwell model with the fixed parameters regardless of the applied frequency and shear rate. Basically, the same thing can be said about the fractional and upper convected Maxwell models. However, the strengths of these models are demonstrated when trying to characterize the frequency dependent viscoelasticity with a small number of parameters, these models and hence their derivation of complex viscosity are summarized below.

The fractional Maxwell model describes the relation of shear stress σ and shear rate γ as

$$\sigma + \frac{\mathbb{V}}{\mathbb{G}} \frac{d^{\alpha-\beta}\sigma}{dt^{\alpha-\beta}} = \mathbb{V} \frac{d^{\alpha}\gamma}{dt^{\alpha}}, \tag{2.33}$$

with the first and second quasiproperties $\mathbb{V}$ and $\mathbb{G}$ with units of [Pa s^{α}] and [Pa s^{β}], respectively, and α and β are fractional derivative orders, where $0 < \beta < \alpha < 1$. This model includes two fractional mechanical elements in series, where the fractional components behaves like between a spring and a damper. Note that the ultimate conditions of $\alpha \to 1$ and $\beta \to 0$ corresponds to the original Maxwell model. Caputo derivative for fractional differentiation is defined as

$${}_a^C D_t^{\alpha} f(t) = \frac{1}{\Gamma(n-\alpha)} \int_a^t (t-t')^{n-\alpha-1} f^{(n)}(t') dt' \tag{2.34}$$

with $n-1 < \alpha \leq n$ and this operation assures linearity regarding given functions $f(t)$, $g(t)$, and a constant b as

$${}_a^C D_t^{\alpha} [bf(t) + g(t)] = b\, {}_a^C D_t^{\alpha} f(t) + {}_a^C D_t^{\alpha} g(t). \tag{2.35}$$

The fractional operations included in Eq. 2.33 correspond to Caputo derivative with $a = 0$ as

$$\frac{d^{\alpha}}{dt^{\alpha}} f(t) \equiv {}_0^C D_t^{\alpha} f(t). \tag{2.36}$$

These differential operations have the following properties in the Fourier space,

$$\mathcal{F}\left[\frac{d^{\alpha}}{dt^{\alpha}} f(t); \omega\right] = (i\omega)^{\alpha} \hat{f}(\omega). \tag{2.37}$$

Therefore, Eq. 2.30 is easily transformed in the Fourier space as

$$\hat{\sigma} + (i\omega)^{\alpha-\beta} \frac{\mathbb{V}}{\mathbb{G}} \hat{\sigma} = (i\omega)^{\alpha} \mathbb{V} \hat{\gamma}, \tag{2.38}$$

and the complex viscosity $G^* = \hat{\sigma}/\hat{\gamma}$ is derived as

$$G^*(\omega) = \frac{\mathbb{V}(i\omega)^\alpha \, \mathbb{G}(i\omega)^\beta}{\mathbb{V}(i\omega)^\alpha + \mathbb{G}(i\omega)^\beta}. \tag{2.39}$$

Regarding $(i^\omega)^\alpha$ and $(i\omega)^\beta$, principal values are adopted, that is, $i^\alpha = \cos(\alpha\pi/2) + i\sin(\alpha\pi/2)$ and $i^\beta = \cos(\beta\pi/2) + i\sin(\beta\pi/2)$. The elastic modulus G' and loss modulus G'' are thus derived as

$$\begin{aligned} G'(\omega) &= \mathrm{Re}\,[G^*(\omega)] \\ &= \frac{\mathbb{V}\omega^\alpha(\mathbb{G}\omega^\beta)^2\cos(\alpha\pi/2) + (\mathbb{V}\omega^\alpha)^2\mathbb{G}\omega^\beta\cos(\beta\pi/2)}{(\mathbb{V}\omega^\alpha)^2 + (\mathbb{G}\omega^\beta)^2 + 2\mathbb{V}\omega^\alpha\mathbb{G}\omega^\beta\cos[(\alpha-\beta)\pi/2]}, \end{aligned} \tag{2.40}$$

$$\begin{aligned} G''(\omega) &= \mathrm{Im}\,[G^*(\omega)] \\ &= \frac{\mathbb{V}\omega^\alpha(\mathbb{G}\omega^\beta)^2\sin(\alpha\pi/2) + (\mathbb{V}\omega^\alpha)^2\mathbb{G}\omega^\beta\sin(\beta\pi/2)}{(\mathbb{V}\omega^\alpha)^2 + (\mathbb{G}\omega^\beta)^2 + 2\mathbb{V}\omega^\alpha\mathbb{G}\omega^\beta\cos[(\alpha-\beta)\pi/2]}. \end{aligned} \tag{2.41}$$

This model can well describe the linear viscoelastic property of aqueous biopolymer and food biopolymer solutions (Jaishankar and McKinley, 2014).

The upper convected Maxwell model is one of the simplest constitutive equations used in computational fluid mechanics for viscoelastic fluids. It describes the relation of the extra stress tensor τ and shear rate tensor $\dot{\gamma} = \nabla v + (\nabla v)^T$ with the velocity vector v as

$$\tau + \lambda_1 \overset{\triangledown}{\tau} = \mu_0 \dot{\gamma}, \tag{2.42}$$

where λ_1 is a relaxation time and μ_0 is a viscosity coefficient. The symbol of the inverted triangle represents the upper convected time derivative defined as

$$\overset{\triangledown}{\tau} = \frac{d\tau}{dt} + v \cdot \nabla\tau - (\nabla v)^T \cdot \tau - \tau \cdot \nabla v. \tag{2.43}$$

Confinement of the flow in one-direction, that is, $v = [v_1,\ 0,\ 0]$ yields the following three equations from Eq. 2.42 as

$$\tau_{11} + \lambda_1 \frac{d\tau_{11}}{dt} = 0, \tag{2.44}$$

$$\tau_{12} + \lambda_1 \left(\frac{d\tau_{12}}{dt} - \dot{\gamma}_{12}\tau_{11} \right) = \mu_0 \dot{\gamma}_{12}, \tag{2.45}$$

$$\tau_{22} + \lambda_1 \left(\frac{d\tau_{22}}{dt} - 2\dot{\gamma}_{12}\tau_{12} \right) = 0, \tag{2.46}$$

with $\dot{\gamma}_{12} = \partial v_1/\partial x_1$. Assuming t is large enough so that τ_{11} converges to zero based on the Eq. 2.44, Eqs. 2.45 and 2.46 become

$$\tau_{12} + \lambda_1 \frac{d\tau_{12}}{dt} = \mu_0 \dot{\gamma}_{12}, \tag{2.47}$$

$$\tau_{22} + \lambda_1 \left(\frac{d\tau_{22}}{dt} - 2\dot{\gamma}_{12}\tau_{12} \right) = \mu_0 \dot{\gamma}_{12}. \tag{2.48}$$

Eq. 2.47 is exactly the form of the original Maxwell model. In response to the explanation of USR, questions are often raised about how it differs with the other Maxwell models, and the answer derived here is that the viscoelastic model used in USR covers all the above in the linear region.

2.4 Technical note for USR

Several techniques and knowledge are required to accurately and precisely evaluate the rheological properties by USR. Here, the points to be noted from the experimental procedures to the analysis are summarized as technical notes of USR.

Definition of shear rate

Yoshida et al. (2018a) proposed a method to obtain a spatial distribution of representative shear rate based on a spatiotemporal distribution of shear rate. In the method, the distribution $\dot{\gamma}(r,t)$ is firstly calculated by Eq. 2.15 utilizing a discretetized equation. At each radial position, $\dot{\gamma}(r,t)$ is fitted in the time direction by the least squares method utilizing the following function,

$$\dot{\gamma}(r_i,t) = a_i \sin\left[2\pi f_o (t - b_i)\right] + c_i, \tag{2.49}$$

where a_i, b_i, and c_i are fitting parameters at the radial position r_i. Spatial variations $a(r)$, $b(r)$, and $c(r)$ are obtained by performing the fitting at all the radial positions. Then, the spatial variation of the representative shear rate $\dot{\gamma}_{\mathrm{eff}}$ is derived as

$$\dot{\gamma}_{\mathrm{eff}}(r) = \frac{1}{\sqrt{2}} a(r). \tag{2.50}$$

The distribution $\dot{\gamma}_{\mathrm{eff}}$ is essentially equivalent to a distribution of the effective value of the shear rate profile at each radial position,

$$\dot{\gamma}_{\mathrm{eff}}(r) = \sqrt{\frac{1}{T}\int_0^T \dot{\gamma}^2(r,t)dt}, \tag{2.51}$$

where T denotes a measurement time.

Tasaka et al. (2018) proposed a method to obtain a spatial distribution of representative shear rate based on Fourier coefficients. In the method, real and imaginary parts of velocity intensity at dominant frequency $\omega_o = 2\pi f_o$ are required. The spatial distribution of the representative shear rate $\dot{\gamma}_{\mathrm{max}}(r)$ is defined as

$$\dot{\gamma}_{\mathrm{max}}(r) = \sqrt{\left[\left(\frac{d}{dr} - \frac{1}{r}\right)\mathrm{Re}(r)\right]^2 + \left[\left(\frac{d}{dr} - \frac{1}{r}\right)\mathrm{Im}(r)\right]^2}, \tag{2.52}$$

with $\mathrm{Re}(r) = \mathrm{Re}[\hat{u}_\theta(r, \omega = \omega_o)]$ and $\mathrm{Im}(r) = \mathrm{Im}[\hat{u}_\theta(r, \omega = \omega_o)]$.

The difference of the two ways for evaluating representative shear rate is discussed here. Assuming that the azimuthal velocity distribution is given as $u_\theta(r,t) = A(r)\sin\left[\omega_o t + \alpha(r)\right]$, $\dot{\gamma}_{\mathrm{max}}$ is obtained as

$$\begin{aligned}\dot{\gamma}_{\max}(r) &= \sqrt{\left[\left(\frac{d}{dr}-\frac{1}{r}\right)\mathrm{Re}(r)\right]^2+\left[\left(\frac{d}{dr}-\frac{1}{r}\right)\mathrm{Im}(r)\right]^2} \\ &= \sqrt{\left[\left(\frac{d}{dr}-\frac{1}{r}\right)a(r)\cos\alpha(r)\right]^2+\left[\left(\frac{d}{dr}-\frac{1}{r}\right)a(r)\sin\alpha(r)\right]^2} \\ &= \sqrt{\left[\frac{da(r)}{dr}-\frac{a(r)}{r}\right]^2+\left[a(r)\frac{d\alpha(r)}{dr}\right]}. \end{aligned} \tag{2.53}$$

Spatiotemporal distribution of the shear rate of the assumed velocity profile is derived as

$$\begin{aligned}\dot{\gamma}(r,t) &= \left(\frac{\partial}{\partial r}-\frac{1}{r}\right)u_\theta(r,t) \\ &= \left(\frac{\partial}{\partial r}-\frac{1}{r}\right)a(r)\sin\left[\omega_o t+\alpha(r)\right] \\ &= \sqrt{\left[\frac{da(r)}{dr}-\frac{a(r)}{r}\right]^2+\left[a(r)\frac{d\alpha(r)}{dr}\right]}\sin\left[\omega_o t+\alpha(r)+\beta(r)\right], \end{aligned} \tag{2.54}$$

where $\beta(r)$ is defined as

$$\tan\beta(r) = a(r)\frac{d\alpha(r)}{dr}\Big/\left[\frac{da(r)}{dr}-\frac{a(r)}{r}\right]. \tag{2.55}$$

Comparing Eq. 2.53 and Eq. 2.54, $\dot{\gamma}_{\max}(r)$ corresponds to the spatial variation of the maximum shear rate at each radial position. There is a linear relationship between $\dot{\gamma}_{\mathrm{eff}}$ and $\dot{\gamma}_{\max}$ as,

$$\dot{\gamma}_{\mathrm{eff}}(r) = \frac{1}{\sqrt{2}}\dot{\gamma}_{\max}(r). \tag{2.56}$$

Features of the two methods for calculating the representative shear rate are discussed from the view point of robustness against the measurement noise of UVP. First, in the calculation of $\dot{\gamma}_{\mathrm{eff}}$ and $\dot{\gamma}_{\max}$, each analysis is devised to reduce the influence of the noise. As for the former one, band pass filter around the oscillation frequency f_o is utilized against $u_\theta(r,t)$. As for the $\dot{\gamma}_{\max}$, $\mathrm{Re}(r)$ and $\mathrm{Im}(r)$ in Eq. 2.52 are locally fitted by a polynomial function. The detail are described later.

The robustness is evaluated using the analytical solution (Eq. 2.17), to which artificially generated UVP noise is added. Firstly, velocity in the vessel in stationary condition is measured to roughly investigate characteristics of the measurement noise of UVP. The vessel is filled with 500 mm^2/s silicon oil with the tracer particles (CHP 20P). Histogram of the noise is shown in Fig. 2.6 (a). The sampling number is 10^2 (spatial) $\times$ 10^4 (temporal) = 10^6. Assuming that the histogram follows white noise and Gaussian distribution, the mean value and standard deviation are estimated to be 0.0 mm/s and 1.2 mm/s (3σ = 3.6 mm/s).

Spatiotemporal velocity distribution is calculated by the analytical solution previously shown in Eq. 2.17. The oscillation parameters were set as f_o = 1.0 Hz and $\Theta = \pi/2$ rad. The white on Gaussian noise is linearly added to the velocity distribution at each spatiotemporal point. Based on this artificially noise-added velocity distribution, $\dot{\gamma}_{\mathrm{eff}}$ and $\dot{\gamma}_{\max}$ are calculated. Spatial variations of the relative error of $\dot{\gamma}_{\mathrm{eff}}$ and $\dot{\gamma}_{\max}$ against each true one are shown in Fig. 2.6 (b) and (c). Comparing

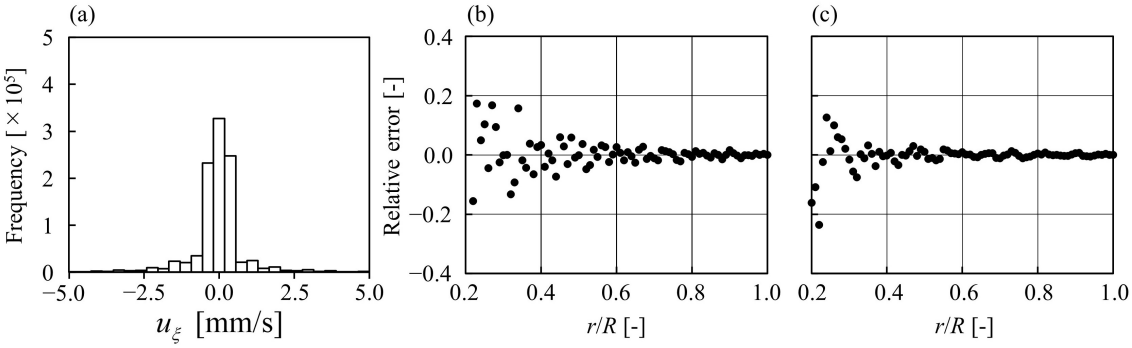


FIGURE 2.6: Robustness evaluation of the two method for calculating the spatial variation of the representative shear rate: (a) Histogram of the measurement noise of UVP in a stationary condition, and spatial variations of relative error of (b) $\dot{\gamma}_{\mathrm{eff}}$ and (c) $\dot{\gamma}_{\mathrm{max}}$ for each true value.

these two graphs it is obvious that $\dot{\gamma}_{\mathrm{max}}$ is more robust than $\dot{\gamma}_{\mathrm{eff}}$ against the measurement noise. This is because $\dot{\gamma}_{\mathrm{max}}$ is calculated after fitting the Fourier coefficients $\mathrm{Re}(r)$ and $\mathrm{Im}(r)$ by the polynomial function, while $\dot{\gamma}_{\mathrm{eff}}$ is calculated after the band pass filter processing. The extraction of $\mathrm{Re}(r)$ and $\mathrm{Im}(r)$ from the velocity intensity spectrum is essentially equivalent to band pass filtering process, therefore, $\dot{\gamma}_{\mathrm{max}}$ has undergone two times noise suppression processes. This is the reason for the higher precision of $\dot{\gamma}_{\mathrm{max}}$ than $\dot{\gamma}_{\mathrm{eff}}$.

Uncertainty caused by radial flow

Supposing that a cylindrical container with upper and lower bottoms is filled with a fluid and the rotation speed is increased. At the boundary layer on the upper and lower bottoms the centrifugal force exceeds the pressure gradient, and an outward flow in the radial direction occurs. Along with this, the fluid inside the vessel is transported to the boundary layer to satisfy the continuity of the fluid, and an axial flow occurs (Benton and Clark Jr, 1974). A secondary flow (meridian plane flow) is generated in the container. It is considered that such flow occurs in the cylindrical vessel used in USR. Conventional torque rheometers cause uncertainty in rheological evaluations due to the collapse of the Couette flow assumption. Similarly, in USR, the generation of the radial flow makes it impossible to apply the equation of motion (Eq. 2.14) and also the velocity conversion formula that assumes one directional flow, that is, $u_\theta = (r/\Delta y)u_\xi$ is no longer valid. There is a concern that the accuracy of the rheological evaluation in the undesirable state will decrease. Therefore, the average velocity field on the vertical cross section of the vessel is measured with UVP, and the effect of the radial flow on the evaluation of the effective viscosity is investigated here.

Silicon oil with kinematic viscosity of $1000\,\mathrm{mm}^2/\mathrm{s}$, which is a Newtonian fluid, was used as the test fluid. In the phase analysis, when the target is a Newtonian fluid, the effective viscosity matches with its kinematic viscosity. Fine spherical particles (Mitsubishi Chemical Co., Ltd., CHP 20P, diameter 75 – 150 μm, specific density to the silicon oil 1.03) were suspended as the tracer particles for the UVP measurement, and the test fluid was filled to the liquid level $z = 125$ mm from the bottom of the vessel. The oscillation parameters were set as $f_o = 1.0$ Hz and $\Theta = \pi/2$ rad. When the ultrasonic transducer is installed at $\Delta y = 0$ mm, u_ξ obtained by UVP is directly replaced by the radial velocity component u_r. First, the ultrasonic transducer

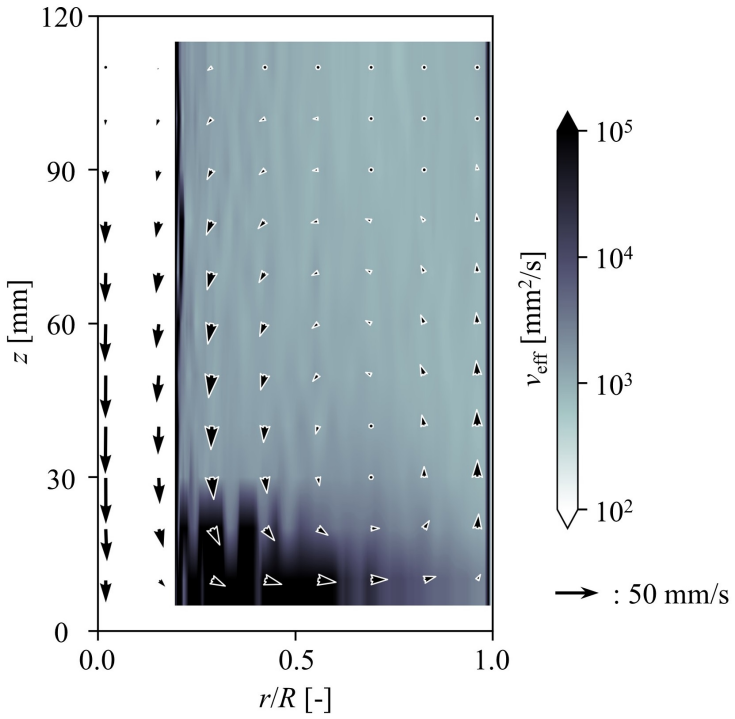


FIGURE 2.7: Effect of radial flow on evaluation of the effective viscosity (1000 mm^2/s silicon oil, f_o = 1.0 Hz, $\Theta = \pi/2$ rad): Vectors and color contour indicate time averaged velocity field and the effective viscosity calculated by the phase analysis.

(frequency: 2 MHz, diameter: 10 mm) was installed at a height of z = 10 mm for the velocity measurement, and then Δz = 10 mm was shifted in the vertical direction and the measurement was performed again. By repeating this until z = 110 mm, the velocity distribution $u_r(r,z,t)$ at which the spatial resolution in the vertical direction is Δz can be obtained. Here, it is assumed that the axially symmetry of the flow field is satisfied ($\partial/\partial\theta = 0$). The continuity equation for in-compressible fluids in the cylindrical coordinate system is

$$\frac{\partial u_z}{\partial z} + \frac{1}{r}\frac{\partial}{\partial r}(ru_r) + \frac{1}{r}\frac{\partial u_\theta}{\partial \theta} = 0. \tag{2.57}$$

Considering the time average (operation symbol: $\bar{}$) on both sides of Eq. 2.57 and assuming axially symmetric flow, the following equation is obtained,

$$\frac{\partial \bar{u}_z}{\partial z} + \frac{1}{r}\frac{\partial}{\partial r}(r\bar{u}_r) = 0. \tag{2.58}$$

Utilizing Eq. 2.58, the experimentally obtained velocity distribution $u_r(r,z)$, and the boundary condition $\bar{u}_z(r, z = 0) = 0$, the time averaged distribution $\bar{u}_z(r,z)$ is estimated. The averaged velocity field in the vertical section of the vessel is shown in Fig. 2.7. The vector diagram is appropriately thinned out for viewing. It can be seen that the averaged flow field also has a meridian flow in the oscillatory rotation too. It was estimated that an axial flow of up to 50 mm/s was generated near the axis. Since the phase analysis utilizes the velocity information of $r/R > 0.4$ in which the measured velocity is sufficiently large compared to the velocity resolution of UVP,

this axial flow is not a problem, but the ultrasonic transducer should be installed at the certain distance or more from the bottom surface of the vessel.

The effective viscosity ν_{eff} in the undesirable meridian flow is evaluated. The ultrasonic transducer was installed at $\Delta y = 15$ mm, and the position in the vertical direction was increased by $\Delta z = 10$ mm as in the previous case of $\Delta y = 0$ mm for capturing the radial flow, and velocity was measured. Since the measurement line is installed at the position of $\Delta y = 15$ mm, velocity distribution is not obtained in the region of $r/R < \Delta y/R \approx 0.2$. Therefore, the region with the information of ν_{eff} is $0.2 < r/R < 1.0$. The phase analysis was performed on the obtained velocity distribution. The results are shown as color contours in Fig. 2.58. Near the bottom of the vessel ($0 < z < 30$ mm), ν_{eff} is evaluated higher than the kinematic viscosity of the silicon oil, 1000 mm^2/s. The region is within the range of the viscous layer thickness $\delta_{\mathrm{v}} = \sqrt{2\nu/f_{\mathrm{o}}} = 45$ mm on the bottom surface of the vessel, and the influence of the oscillatory flow propagating from the bottom surface cannot be ignored. In the horizontal cross section in the viscous layer, the flow almost similar to rigid body rotation occurred, that is, $d\phi/dr \approx 0$, and ν_{eff} was overestimated. On the other hand, in the region of $30 < z < 120$ mm , a radial flow of $O(1$ mm/s) occurs, but the measured effective viscosity matches the kinematic viscosity of the silicon oil. Since the advection term in the Navier-Stokes equation is ignored in USR, the effect of momentum transport by the advection is added to the effective viscosity. However, as a result of evaluation from the experimental data, the order of the advection term is about one hundreadth of the inertial term in the radial flow of about $O(1$ mm/s), which is sufficiently negligible. This is considered to be the reason why the accuracy of the effective viscosity was maintained in the region of $30 < z < 120$ mm. In the region, a flow in the vertical direction of about $O(1$ mm/s) is also generated, but this also does not affect the accuracy of the effective viscosity for the same reason as the radial flow. Moreover, since the azimuthal velocity is about $O(100$ mm/s), the assumption of the one-directional flow holds, and the flow field in the vessel can be assumed as a simple shear flow. Based on the above, in order to guarantee the accuracy of the effective viscosity evaluated by USR, it is necessary to install the UVP measurement line sufficiently away from the viscous layer on the bottom surface of the vessel. Even if the transducer is set at an appropriate height, radial flow may occur due to the Weissenberg effect, and in such cases the USR is not applicable. Before measuring the velocity distribution u_θ, it is therefore necessary to install the ultrasonic transducer at $\Delta y = 0$ mm and confirm that the radial flow can be sufficiently ignored. Also, when the ultrasonic transducer is too close to the liquid level, the UVP will capture the fluctuating movement of the gas-liquid interface due to the expansion of the ultrasonic pulse wave. The transducer therefore must be at least twice its diameter away from the liquid surface. As a result of evaluating the effective viscosity at $z = 10$ mm according to these notations, the relative error of ν_{eff} was about 10% or less in this demonstration.

There may be cases where samples are expensive and cannot be prepared in large quantities. In such cases, the recently developed portable type USR (P-USR) is effective (Yoshida, Ohie, and Tasaka, 2022). A tank is filled with a test fluid, and a cylindrical container with a special top end shape, which was designed not to generate secondary flow, is placed in the fluid. The ultrasonic transducer for the UVP measurement is embedded in the cylinder, and these are sinusoidally oscillated for making the axially symmetric and azimuthal flow in the cylinder. As the container has no bottom surface, and the top surface is composed of non-axisymmetric rods, the generation of the secondary flow is insulated, which realizes accurate rheological evaluation.

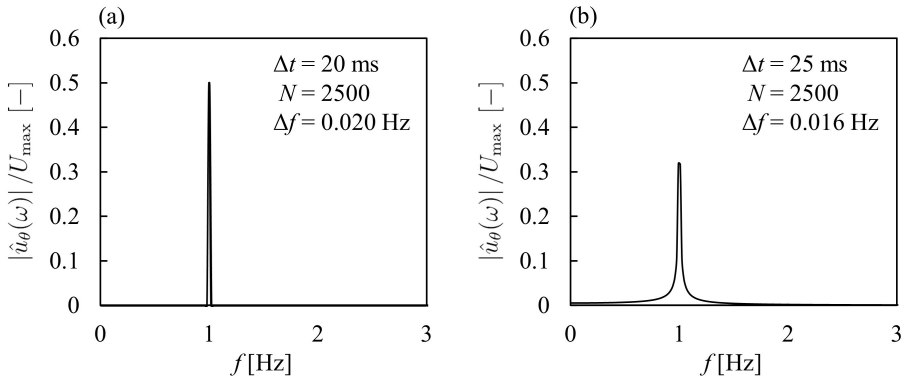


FIGURE 2.8: Precautions of DFT for preventing lower estimation of the velocity intensity when the definition of Eq. 2.59 is used: (a) Correspondence between the velocity intensity obtained by DFT and the actual velocity intensity, and (b) spectrum leakage under the undesirable condition $f_o \neq n\Delta f$.

Precautions for DFT

In the phase analysis and linear viscoelastic analysis, the velocity distribution is Fourier transformed to extract the velocity intensity and phase information of the oscillation frequency component. There are two points to be aware of when operating DFT. The first one is about correspondence between the velocity intensity obtained by DFT and the actual velocity intensity. Assuming that the velocity profile at a radial position is given as $u_\theta(t) = U_{\text{wall}} \sin(2\pi f_o t)$, the velocity intensity spectrum obtained by DFT is shown in Fig. 2.8 (a) when the following definition of DFT is used,

$$\hat{u}_\theta(r, \omega = 2\pi k\Delta f) = \frac{1}{N}\sum_{n=0}^{N-1} u_\theta\left(r, \frac{nT}{N}\right)\exp\left(-ik\frac{2\pi}{N}n\right)(k = 0, 1, ..., N-1), \tag{2.59}$$

which is different definition with Eq. 2.13. In the equation above, N and T denote number of temporal profiles and total measurement time $N\Delta t$. The frequency resolution Δf is determined as $\Delta f = 1/N\Delta t = 1/T$, where Δt is the temporal resolution of UVP. The intensity at the oscillation frequency f_o is just the half of the maximum velocity U_{wall}, according to one of the characteristics of DFT,

$$\begin{aligned} |\hat{u}_\theta(\omega)|_{\omega=2\pi f_o} &= \frac{1}{T}\int_0^T U_{\max}\sin(2\pi f_o t)\cdot\sin(2\pi f_o t)dt \\ &= \frac{U_{\max}}{2}. \end{aligned} \tag{2.60}$$

Therefore, only extracting the real and imaginary components of the velocity intensity spectrum at the dominant frequency leads to lower estimation of $\dot{\gamma}_{\max}$, and this is why the former definition of DFT (Eq. 2.13) is used in the USR analysis.

The second notation is about frequency resolution Δf in the velocity intensity spectrum obtained by DFT. When an oscillation frequency f_o is not integer multiple of Δf, i.e. $f_o \neq n\Delta f$ (n : natural number), spectrum leakage occurs and the velocity intensity at the dominant frequency is estimated lower than its original one, causing lower estimation of $\dot{\gamma}_{\max}$. The frequency resolution Δf is defined as $\Delta f = 1/N\Delta t$, where N and Δt represent the number of temporal profiles and time resolution of

the UVP measurement. The parameter set N and Δt should be well examined to meet $f_o = n\Delta f$ before starting the velocity measurement.

When performing the UVP measurement to meet the above conditions, it maybe necessary to worsen the temporal resolution. There is also a way to use data fitting using a sine wave function without using DFT. Against the spatial and temporal velocity profile $u_\theta(r,t)$, the data fitting is done at each radial position using the function,

$$u_\theta(r,t) = A(r)\sin[\omega_o t + \phi(r)], \tag{2.61}$$

where the velocity amplitude $A(r)$ and the phase lag $\phi(r)$ are determined at each radial position based on, for example, least squares method. Although this fitting approach is useful, frequency analysis of the velocity profile is still necessary for assuring the linear viscoelasticity.

Polynomial fitting of the Fourier coefficients

In addition to the above precautions, polynomial fitting against the spatial profiles of the Fourier coefficients are required to assure the precision of USR. The first is the division of the velocity distribution in the time direction. For example, when the number of measurement profiles is 10,000 in the time direction, the linear viscoelastic analysis using all the velocity information will yield only one set of viscosity and delta curves. As the measurement noise of UVP is the white on Gaussian noise as revealed by Yoshida et al. (2018b), steep noise may be added in rare cases over the long measurement time. The noise has a considerable effect on the velocity intensity and the phase at the dominant frequency, and worsen the accuracy of the linear viscoelastic analysis. However, it cannot be determined whether the estimated rheological properties are affected by the noise as there is only the one set of viscosity and delta curves. To avoid this problem, the velocity distribution of 10,000 profiles should be cut out, for example, every 200 profiles as ideally shown in Fig. 2.9. The linear viscoelastic analysis is performed for each of the velocity distributions of 200 profiles, and the sets of viscosity and delta curves are obtained. By shifting the window for extracting the velocity distribution, for example, every 50 profiles in the time direction, a total $(10,000-200)/50+1 = 197$ sets of viscosity and delta curves can be obtained. By plotting them on a two-dimensional histogram, whose horizontal axis is $\dot{\gamma}_{\mathrm{eff}}$ and vertical axis is μ_e or δ, the variance of the evaluated results can be grasped. It is possible to judge whether the evaluated properties are statistically meaningful. Furthermore, the set of μ_e, δ, and $\dot{\gamma}_{\mathrm{eff}}$ evaluated in the interval of the velocity distribution to which the strong noise is added can be excluded as they distribute far from the mode curve of the histogram. For example, a 97% confidence interval is taken for each direction of μ_e, δ, and $\dot{\gamma}_{\mathrm{eff}}$. By reducing the profile from 10,000 to 200 profiles, the precision of the linear viscoelastic analysis itself decreases a little, but the overall accuracy becomes much better when the number of viscosity and delta curves is increased.

The second point to be noted is the spatial derivatives of the Fourier coefficients. When evaluating the effective viscosity, viscoelasticity, and effective shear rate, the spatial derivatives of the Fourier coefficients are required for the analysis. Even though the dominant frequency component is extracted by DFT, undesirable fluctuations originated from the noise are still contained in the spatial distributions of the velocity intensity and the phase as described in the operation for cutting out the velocity distribution above. It may be possible to utilize discrete equations in the case of the phase analysis as it is up to the first derivative of the Fourier coefficients, but

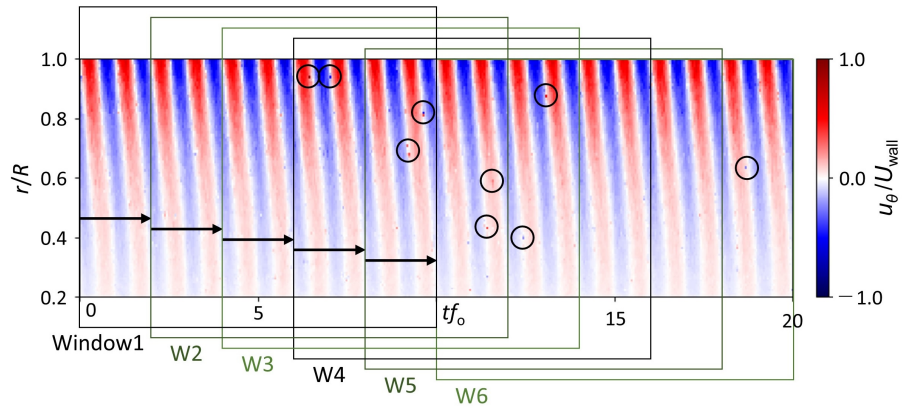


FIGURE 2.9: Division of the velocity distribution to improve the precision of the analysis: The circles represent the rarely added steep noise.

in the linear viscoelastic analysis, the noise is amplified in the discrete calculations as it includes the second derivative. Polynomial fitting is therefore utilized for the spatial distributions of the Fourier coefficients. When there is no sharp change in the spatial distributions of the velocity intensity and the phase, polynomial fitting may be utilized for the entire space at once. For example, in the case of Newtonian fluids, accurate results are obtained by polynomial fitting on fifth order polynomials (Tasaka et al., 2018). This fitting method has been improved to a local polynomial fitting. The original polynomial fitting is performed on $2N + 1$ points before and after including a certain radius position r_i, and the value of the Fourier coefficient and its derivatives are determined at r_i utilizing the regression function. By shifting the radial position and performing the same operations, the spatial distribution of the Fourier coefficient and its derivative values can be finally obtained, which the original undesirable fluctuations are removed. The advantage over the fitting to the entire space at once is that the local polynomial fitting can respond to sudden changes in rheological properties inside the cylindrical vessel. Which methods to utilize should be decided after observing the spatial distributions of the velocity intensity and the phase. Regarding the local polynomial fitting, the following gives guidelines for the optimum degree of the polynomial and number of neighboring points are given.

The results of the linear viscoelastic analysis when the degree of the local polynomial fitting and the number of neighboring points are changed are shown in Fig. 2.10 and 2.11. The test fluid is the 1000 cSt silicon oil, which was also utilized earlier, and the oscillation parameters are $f_o = 1.0$ Hz and $\Theta = \pi/2$ rad. The least squares method is utilized for the fitting. The results of the analysis should match $\mu_e = 0.97$ Pa $\cdot$ s and $\delta = \pi/2$ rad, as shown by the dotted lines in the figures. By comparing the analytical result with the correct values, the optimum order and the number of neighboring points can be determined. Regarding the viscosity curves first, the bottom row in Fig. 2.10 is the result when the number of neighboring points is 5. Both the accuracy and precision are extremely poor at any order polynomial. The low number of neighboring points is almost the same situation as when utilizing the discrete equations, and the addition of the undesired fluctuations caused by the noise to one or two of the five points greatly affects the accuracy and precision of the analysis. In the case of the middle row in Fig. 2.10 where the number of neighboring points is

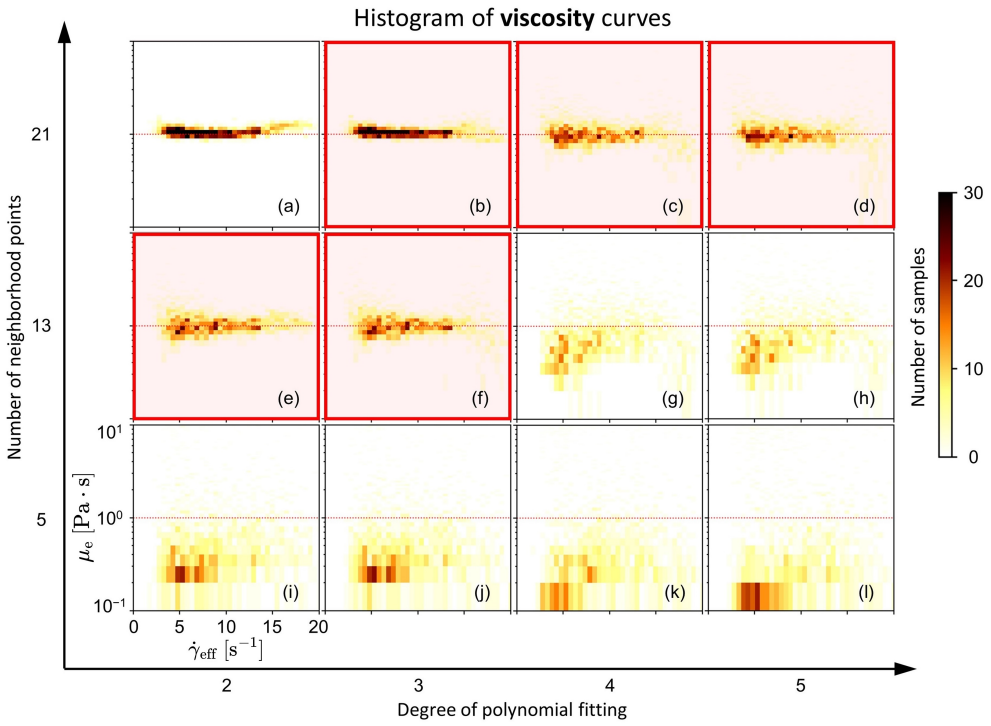


FIGURE 2.10: Histograms of the viscosity curves under different degree of polynomial fitting and number of neighboring points for the fitting: The test fluid is 1000 cSt silicon oil, which is generally known as a Newtonian fluid. The oscillation parameters are f_o = 1.0 Hz and $\Theta = \pi/2$ rad.

increased to 13, the accuracy is sufficiently guaranteed although there is standard deviations of about $O(0.01\ \mathrm{Pa \cdot s})$ in the case of the second and third order polynomials. The accuracy is still poor for the fourth and fifth order polynomials. This is because the fitting corresponds to the undesired fluctuations in the spatial distributions of the Fourier coefficients, that is, it is considered to be due to over-fitting. In the upper row in Fig. 2.10, when the number of neighboring points is 21, the accuracy and precision are sufficiently maintained by any polynomial with degree of 3 or more. As for the case of the second order polynomial, the accuracy deteriorates at the high shear rate regime because the degree of freedom of the fitting shape is too low, which is only a parabola. Regarding the histograms of the delta curves in Fig. 2.11, it is confirmed that the effects of the degree and the number of neighboring points on the accuracy and precision of the analysis are almost the same as that of the histograms of the viscosity curves. At first glace, the histograms in the lower and middle rows seem to have a concentrated distribution at $\delta = \pi/2$ rad under all conditions. However, the conditions (g)-(l) were excluded from the optimal conditions for the analysis as the evaluated values are distributed throughout the histogram, and in particular, the distribution is also concentrated at $\delta = 0$ rad . From the above, the optimum degree and number of neighboring points for the local polynomial fitting are 13 points for second and third order polynomials and 21 points for fourth and fifth order polynomials. It should be noted here that one of the advantages of USR is that can locally evaluate rheological properties in the cylindrical vessel. Therefore, when there is a steep change in the spacial distributions of the velocity intensity and

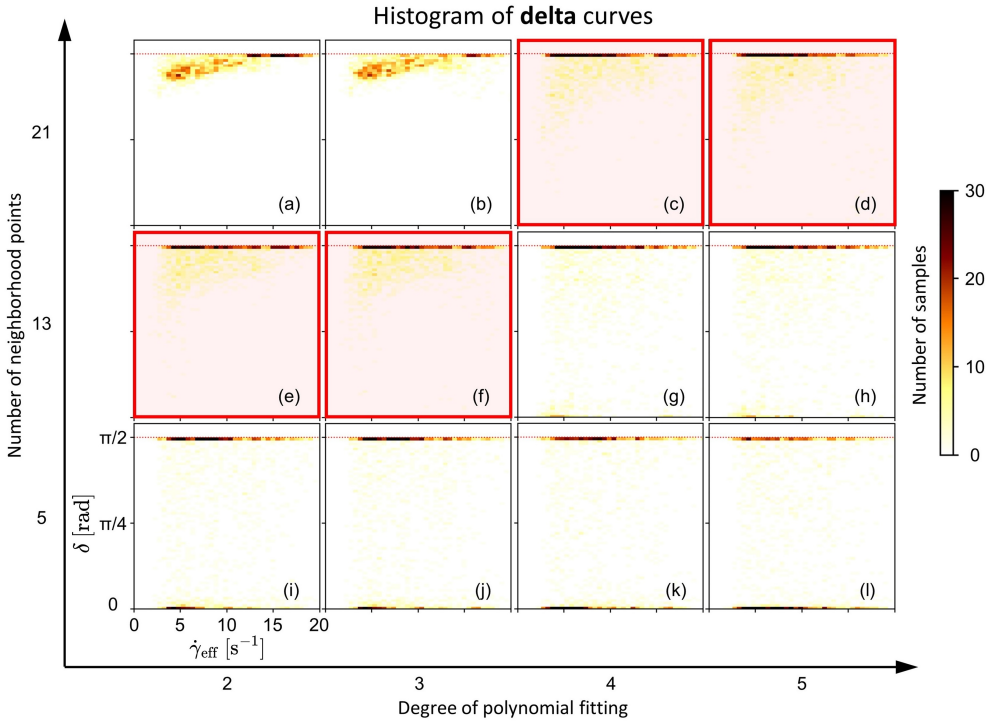


FIGURE 2.11: Histograms of the delta curves under different degree of polynomial fitting and number of neighboring points for the fitting: The test fluid is 1000 cSt silicon oil, which is generally known as a Newtonian fluid. The oscillation parameters are f_o = 1.0 Hz and Θ = $\pi/2$ rad.

the phase, the second or third order polynomials with the small number of neighboring points is desirable. As a method for further improving the local polynomial fitting, the local polynomial fitting weighted by Gaussian distribution has been utilized recently in USR, but the details are omitted. The precision can be improved as much as possible depending on devices as USR itself has high accuracy.

2.5 Further development of USR for exploring bulk rheology of multi-phase fluids

This thesis mainly summarizes research projects using the above three rheometries. In parallel to these projects, further improvements to USR have also been made, and the most recent generation of velocity-profiling-assisted rheometry is presented here. USR is still a developing method that has been improved in recent years and has some shortcomings. The major drawback is taking the spatial second derivative to calculate the cost function for the optimization problem also mentioned in the previous section describing the polynomial fitting. As the Cauchy's equation of motion includes the spatial derivative of the stress (Eq 2.14), which includes the shear rate in the Maxwell model (Eq. 2.22), it is therefore inevitable to calculate the second derivative of the velocity intensity. The measurement noise of the UVP is amplified by the operation. Previously, there was an example of USR measuring a particle suspension (Yoshida, Tasaka, and Murai, 2019a), and an ad-hoc approach was taken to obtain statistical mean values in the radial direction. However, this is limited to fluids without shear-rate-dependent properties, and the advantage of the

local evaluation is lost. There is also an example of measuring particle suspensions using phase analysis (Tasaka, Kimura, and Murai, 2015) in USR. The results showed that the effective viscosity increased with an increase in particle volume fraction. Although the tendency was consistent with the theory, systematic errors were confirmed. In addition, although the viscosity coefficient and elastic modulus of the Maxwell model are determined at each radial position, the spatial gradient of these properties is neglected in the cost function. Inaccuracy arises when abrupt changes of the properties in the radial direction occur. To solve this problem regarding the robustness against the measurement noise of UVP, a more robust method in oscillatory shear flows is proposed, which combines the idea of noise reduction using Fourier space used in USR and torque measurement.

Methodology

The rheometer proposed here mainly consists of coaxial cylinders, where the outer cylinder is sinusoidally oscillated, and the inner cylinder is fixed to a torque sensor for measuring the wall shear stress acting on the inner cylinder surface. UVP (Takeda, 1986; Takeda, 2012) measures the one-directional azimuthal flow in the gap, and the radial derivative of the velocity gives a shear rate at each radial position. Based on Cauchy's equation of motion, namely, momentum conservation law, the corresponding shear stress is obtained at each radial position from the velocity information and the wall shear stress as a boundary condition, and hence the relation of the shear rate and stress is obtained. This section gives specifications of the experimental setup and theoretical background.

The rheometer proposed here mainly consists of coaxial cylinders, where the outer cylinder is sinusoidally oscillated, and the inner cylinder is fixed to a torque sensor for measuring the wall shear stress acting on the inner cylinder surface. UVP measures the one-directional azimuthal flow in the gap, and the radial derivative of the velocity gives a shear rate at each radial position. Based on Cauchy's equation of motion, namely, momentum conservation law (Eq. 2.14), the corresponding shear stress is obtained at each radial position from the velocity information and the wall shear stress as a boundary condition, and hence the relation of the shear rate and stress is obtained. Specifications of the experimental setup and theoretical background is given below.

The experimental setup is shown in Fig. 2.12. The inner cylinder with radius of $R_{\mathrm{in}} = 50$ mm and height of $H = 150$ mm is connected to a torque sensor (UTM III, 0.5 Nm, Unipulse Co., Ltd., Japan) mounted in the base as shown in Fig. 2.12 (a) and (b). The outer cylinder with a $R_{\mathrm{out}} = 105$ mm radius is connected to a stepping motor, and the wall velocity is given as $u_{\mathrm{wall}}(t) = U_{\mathrm{wall}}\sin(\omega_{\mathrm{o}} t)$, where $U_{\mathrm{wall}} = 2\pi f_{\mathrm{o}} R_{\mathrm{out}}\Theta$. The control parameters are the oscillation frequency f_{o} and rotation angle Θ, where the outer cylinder rotates in the range of 2Θ. The stepped disk is independently mounted below the inner cylinder with the three stainless rods, cutting off the oscillatory shear flow propagating from the bottom. The inner cylinder therefore receives the one-directional azimuthal flow propagating from the outer cylinder wall, realizing accurate rheological evaluation (Ohie et al., 2022b).

The measurement example by the torque sensor is shown in Fig 2.13 (a) with symbols behind. The test fluid is silicon oil (KF-96-3,000cs, Shin-Etsu Chemical Co., Ltd., Japan), which exhibits Newtonian viscosity in the range of shear rate examined. The oscillation parameters are $f_{\mathrm{o}} = 0.5$ Hz and $\Theta = 2\pi/3$ rad. The torque sensor outputs a voltage value corresponding to the applied axial torque with a conversion coefficient $k = 0.05$ Nm/V. The voltage is acquired with a data acquisition

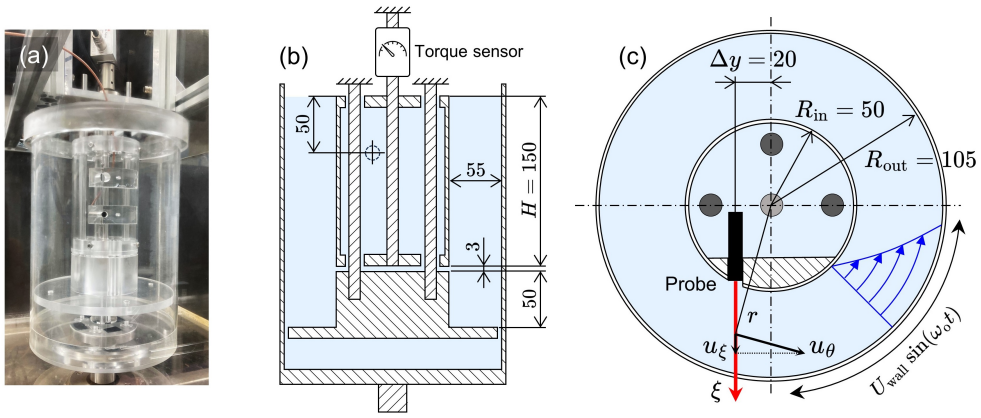


FIGURE 2.12: Overview of a torque rheometer coupled with an ultrasonic velocity profiler: (a) photograph of the experimental setup taken from the side, (b) vertical cross-sectional view through the central axis, and (c) horizontal cross-sectional view at the height of the ultrasonic probe. In figure (a), the test fluid and surrounding water for temperature control are absent, making the internal structures more visible.

device (USB-6341, National Instruments) with a time resolution of 1 ms. As shown in Fig. 2.13 (a), the measured voltage has an off-set value, the data is therefore fitted with $V(t) = A_v \sin(\omega_o t + \phi_v) + V_0$ for extracting the dominant frequency component, corresponding to the cylinder oscillation. As shown in Fig. 2.13 (b), excluding this off-set value, the voltage $V(t)$ is converted to the wall shear stress acting on the inner cylinder as

$$\tau_{\text{wall}}(t) = A_{\tau\text{wall}} \sin(\omega_o t + \phi_{\tau\text{wall}}), \tag{2.62}$$

where the amplitude is obtained as $kA_v/2\pi R_{\text{in}}^2 H$ and the phase delay is as same as ϕ_v.

Synchronously with the torque measurement, the one-directional azimuthal flow in the gap is measured by UVP, where the ultrasonic transducer is inserted in the inner cylinder at a height of 50 mm from the liquid surface (see Fig. 2.13 (b)). In the measurement by UVP, the velocity component in the direction of the propagating ultrasonic waves, $u_\xi(\xi, t)$, is obtained as shown in Fig. 2.13 (c). The transducer is therefore installed with an off-axis of $\Delta y = 20$ mm, otherwise the velocity captured by UVP is always zero along the measurement axis ξ. With this assumption of the one-directional flow, the azimuthal velocity is obtained as $u_\theta(r, t) = (r/\Delta y) u_\xi(\xi, t)$, where the converted velocity distribution is shown in Fig. 2.13 (d). For eliminating the measurement noise of UVP and extracting only the dominant frequency component, the temporal profile of the azimuthal velocity is fitted with a sine function at each radial position by the least squares method, and hence the velocity distribution is represented as

$$u_\theta(r, t) = A_u(r) \sin[\omega_o t + \phi_u(r)]. \tag{2.63}$$

There is a near field region in front of the transducer, where the ultrasonic pulse is generated and fully developed. Strictly, it is preferable to keep the transducer and the inner cylinder surface several centimeters apart. In this setup, the velocity profile was obtained in the near-field as the transducer is in the direct contact with the liquid. If the velocity profile is not obtained in the near-field, improvements in the setup are required such as inserting the transducer into the inner cylinder more

and filling the cavity with gel for ultrasound propagation.

Compared with a standard torque rheometer, the gap size is wider, hence the shear rate amplitude distributes in radial direction and obtained as

$$\begin{aligned}\dot{\gamma}(r,t) &= \left(\frac{\partial}{\partial r}-\frac{1}{r}\right)u_\theta(r,t)\\ &= A_{\dot{\gamma}}(r)\sin[\omega_o t+\phi_{\dot{\gamma}}(r)],\end{aligned} \tag{2.64}$$

where the amplitude and phase delay are derived by substituting Eq. 2.63 to Eq. 2.64 as

$$A_{\dot{\gamma}}(r)=\sqrt{\left[\left(\frac{\mathrm{d}}{\mathrm{d}r}-\frac{1}{r}\right)A_u\right]^2+\left(A_u\frac{\mathrm{d}\phi_u}{\mathrm{d}r}\right)^2}, \tag{2.65}$$

$$\phi_{\dot{\gamma}}=\tan^{-1}\left[A_u\frac{\mathrm{d}\phi_u}{\mathrm{d}r}\Big/\left(\frac{\mathrm{d}}{\mathrm{d}r}-\frac{1}{\mathrm{d}}\right)A_u\right]. \tag{2.66}$$

Regarding the shear stress distribution $\tau(r,t)$, the axially symmetric and one-directional flow satisfies Cauchy's equation of motion, which was previously presented in Eq. 2.14. Fourier transform is performed on Eq. 2.14 to extract only the dominant frequency component, and Eq. 2.24. Now focusing on the dominant frequency component $\omega=\omega_o$ and separating Eq. 2.24 to real and imaginary parts with $\hat{u}_\theta(r,\omega=\omega_o)=R_u(r)+iI_u(r)$ and $\hat{\tau}(r,\omega=\omega_o)=R_\tau+iI_\tau$, it is rewritten as

$$-\omega_o\rho I_u=\left(\frac{\mathrm{d}}{\mathrm{d}r}+\frac{2}{r}\right)R_\tau, \tag{2.67}$$

$$\omega_o\rho R_u=\left(\frac{\mathrm{d}}{\mathrm{d}r}+\frac{2}{r}\right)I_\tau. \tag{2.68}$$

Note that the Fourier coefficients R_u and I_u are obtained from the measured velocity by UVP as $R_u=A_u\cos\phi_u$ and $I_u=A_u\sin\phi_u$, therefore, $R_\tau(r)$ and $I_\tau(r)$ are uniquely obtained from Eqs. 2.67 and 2.68 with the measured wall shear stress by the torque sensor as boundary conditions, $R_\tau(r=R_{\mathrm{in}})=A_{\tau\mathrm{wall}}\cos\phi_{\tau\mathrm{wall}}$ and $I_\tau(r=R_{\mathrm{in}})=A_{\tau\mathrm{wall}}\sin\phi_{\tau\mathrm{wall}}$. The shear stress is also expressed as

$$\tau(r,t)=A_\tau(r)\sin[\omega_o t+\phi_\tau(r)], \tag{2.69}$$

with $A_\tau=\sqrt{R_\tau^2+I_\tau^2}$ and $\phi_\tau=\tan^{-1}(I_\tau/R_\tau)$. Finally, the storage and loss moduli are obtained as

$$G'=\frac{A_\tau}{A_\gamma}\cos\delta, \tag{2.70}$$

$$G''=\frac{A_\tau}{A_\gamma}\sin\delta, \tag{2.71}$$

with $A_\gamma=A_{\dot{\gamma}}/\omega_o$ and $\delta=\pi/2-(\phi_{\dot{\gamma}}-\phi_\tau)$. The phase of viscoelasticity δ is an useful indicator, where $\delta=\pi/2$ rad represents purely viscous, $\delta=0$ rad means elastic, and the intermediate values indicate that the fluid has viscoelasticity. We name this velocity-profiling-assisted rheometry, VPAR.

Robustness evaluation

Robustness of the proposed rheometry against the measurement noise of UVP is evaluated in this section. As representative examples, Newtonian and Maxwell fluids are selected, and exact solutions of their oscillatory shear flows are analytically

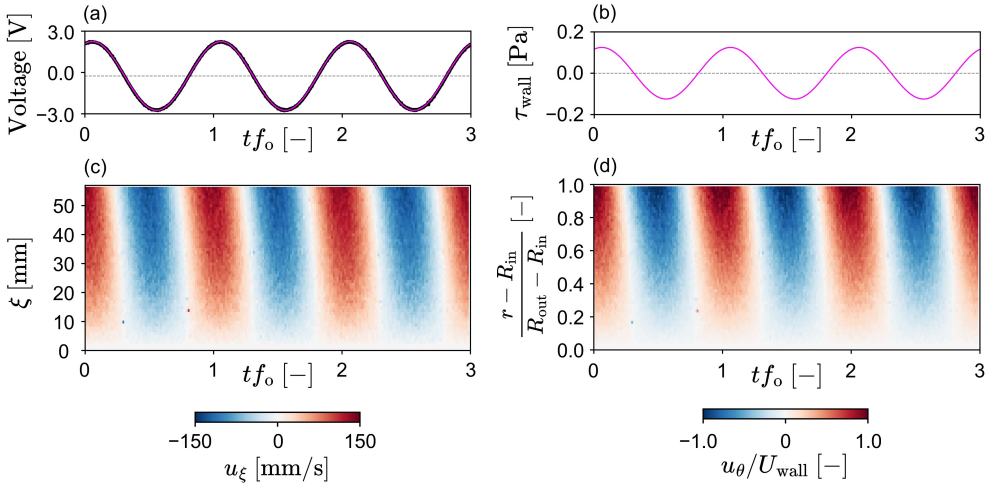


FIGURE 2.13: Synchronous measurement results of the silicon oil by the torque sensor and ultrasonic velocity profiler (UVP) when the oscillation parameters are given as $f_o = 0.5$ Hz and $\Theta = 2\pi/3$ rad: (a) temporal profile of the measured voltage by the torque sensor, (b) temporal profile of the wall shear stress converted from that of the voltage, (c) spatial and temporal distribution of the velocity u_ξ captured by UVP, and (d) converted azimuthal velocity u_θ.

derived first. The UVP-like artificial noise is added on the velocity distribution. Accuracy and precision of the rheometry is evaluated in comparison with the original USR. As shown in Fig. 2.13 (a) and (c), noise intensity of the axial torque is negligible against that of the velocity profiles, measurement noise of the axial torque was not take into account in the robustness evaluation.

One of the most simple constitutive equations expressing the viscoelasticity is Maxwell model previously presented by Eq. 2.22 with viscosity coefficient μ_e and elastic modulus E_e, where the shear rate $\dot{\gamma}$ is defined by Eq. 2.64 in the cylindrical coordinate. Assuming that "Maxwell fluid" which obeys the Maxwell model is filled in the gap between the double concentric cylinders, the oscillatory shear flow can be mathematically obtained by solving Eq. 2.24 with boundary conditions of $u_\theta(r = R_{in}, 0) = 0$ and $u_{wall}(t) = U_{wall}\sin(\omega_o t)$. The derivation starts with applying Fourier transform on Eq. 2.22, and the stress $\hat{\tau}$ is obtained such that

$$\hat{\tau}(r,\omega) = \mu_e \sin^2\delta \left(1 - \frac{i}{\tan\delta}\right)\left(\frac{\partial}{\partial r} - \frac{1}{r}\right)\hat{u}_\theta(r,\omega) \tag{2.72}$$

with $\tan\delta = E_e/\mu_e\omega$. Substituting $\hat{\tau}(r, \omega = \omega_o)$ to Eq 2.24, the following Bessel differential equation is obtained as

$$\left[\frac{d^2}{dr^2} + \frac{1}{r}\frac{d}{dr} + \left(\beta^2 - \frac{1}{r^2}\right)\right]\hat{u}_\theta(r, \omega = \omega_o) = 0, \tag{2.73}$$

where the constant β is defined as

$$\beta^2 = \frac{\rho\omega}{\mu_e}\left(\frac{1}{\tan\delta} - i\right)\Bigg|_{\omega=\omega_o}. \tag{2.74}$$

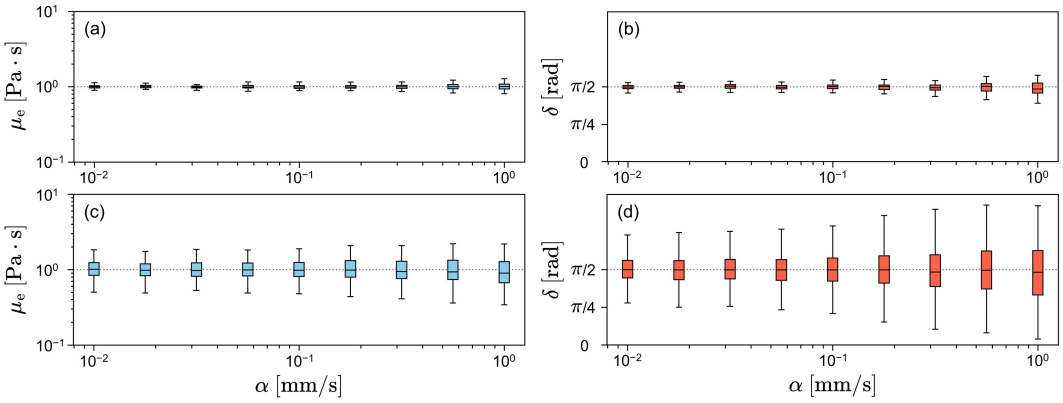


FIGURE 2.14: Robustness evaluation of the velocity-profiling-assisted rheometry (VPAR) in a case of Newtonian fluid with $\mu_e = 1.0$ Pa · s: Evaluation results of VPAR for (a) viscosity coefficient μ and (b) phase of viscoelasticity δ under different noise intensities α, and evaluation results of the conventional USR for (c) viscosity coefficient and (d) phase of viscoelasticity. The dotted lines in figures (a) and (c) indicate $\mu_e = 1.0$ Pa · s and those in (b) and (d) show $\delta = \pi/2$ rad. The oscillation parameters are $f_o = 0.5$ Hz and $\Theta = 2\pi/3$ rad. The evaluated μ and δ at the normalized radial position of $(r - R_{in})/(R_{out} - R_{in}) = 0.7$ are shown with box plots.

Through the separation of variables in time and space, the exact solution of Eq. 2.73 is derived as

$$u_\theta(r,t) = U_{wall}\,\mathrm{Im}\left[\frac{J_1(\beta r)Y_1(\beta R_{in}) - J_1(\beta R_{in})Y_1(\beta r)}{J_1(\beta R_{out})Y_1(\beta R_{in}) - J_1(\beta R_{in})Y_1(\beta R_{out})}e^{i\omega_o t}\right]. \tag{2.75}$$

The functions J_1 and Y_1 are first-order Bessel function of the first and second kind, respectively.

As noise-model of the UVP measurement considered from experimental results, Yoshida et al. (2018b) proposed the following formula,

$$u_{err}(u_\xi) = n_1(0, \alpha|u_\xi|) + n_2(0, \sigma^2_{min}), \tag{2.76}$$

where α and σ^2_{min} represent a noise amplitude coefficient and the lowest noise level. These terms respectively mean measurement noise depending on the velocity intensity and noise caused by its resolution as the UVP utilized in the experiment (UVP monitor model Duo, Met-Flow SA, Switzerland) uses an 8-bit digital signal processor. The functions n_1 and n_2 generate random numbers following a Gaussian distribution with the mean as the first argument and the variance as the second argument. Strictly speaking, σ_{min} depends on the maximum velocity set in the UVP software. It is chosen as $\sigma^2_{min} = 10$ mm^2/s^2 following the value identified by Yoshida et al. (2018b) because the maximum velocity in this study is $O(10^2$ mm/s), the same range as the previous research. This UVP-like artificial noise with different conditions of α is added to the velocity distribution (Eq. 2.75), and the resulting distributions are analyzed with VPAR and USR.

For a Newtonian fluid with $\mu_e = 1.0$ Pa · s and $\delta = \pi/2$ rad, the evaluated μ_e and δ at $(r - R_{in})/(R_{out} - R_{in}) = 0.7$ are shown in Fig. 2.14, where the oscillation parameters are $f_o = 0.5$ Hz and $\Theta = 2\pi/3$ rad. The fluid density was set as 1000 kg/m^3. For each condition of α, the noise-added velocity distributions were generated one thousand

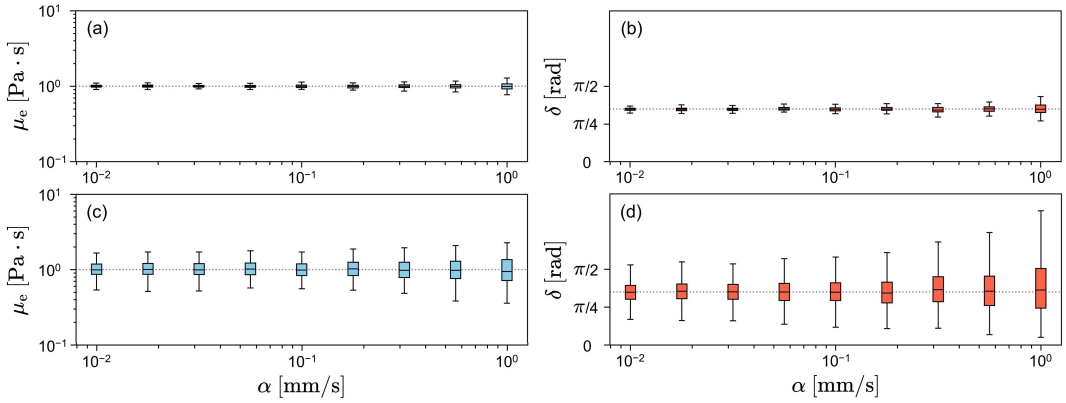


FIGURE 2.15: Robustness evaluation of VPAR in a case of Maxwell fluid with μ_e = 1.0 Pa·s and $\delta = 0.7\pi/2$ rad: Evaluation results of VPAR for (a) viscosity coefficient μ_e and (b) phase of viscoelasticity δ under different noise intensities α, and evaluation results of the conventional USR for (c) viscosity coefficient and (d) phase of viscoelasticity. The dotted lines in figures (a) and (c) corresponds to μ_e = 1.0 Pa·s and those in (b) and (d) represent $\delta = 0.7\pi/2$ rad. The oscillation parameters are f_o = 0.5 Hz and $\Theta = 2\pi/3$ rad. The evaluated μ_e and δ at the normalized radial position of $(r - R_{in})/(R_{out} - R_{in}) = 0.7$ are shown with box plots.

times independently, and the results are shown with box plots, where Fig. 2.14 (a) and (b) are those obtained by VPAR and Fig. 2.14 (c) and (d) are those done by USR. The accuracy is assured in both methods, but the data variance differs by about ten times, showing a clear difference in precision. The same robustness evaluation is also done for a Maxwell fluid with μ_e = 1.0 Pa·s and $\delta = 0.7\pi/2$ rad as shown in Fig. 2.15. As with the results of Newtonian fluid, VPAR accurately works to evaluate both μ_e and δ with higher precision than USR. In contrast, the variance enlarges in USR above $\alpha = 10^{-1}$ mm/s both in Newtonian and Maxwell fluids. This is because the maximum velocity $u_{\tilde{\zeta}}$ at the radial position is $O(10^2$ mm/s), and the variance $\alpha|u_{\tilde{\zeta}}|$ becomes $O(10$ mm^2/s$^2)$ at maximum, which starts to exceed the same order of $\sigma^2_{min}(= 10$ mm^2/s). Silicon oil is often used as dispersion medium because it has a wide variety of viscosity depending on the molecular weight and stable electric characteristics in experiments using suspensions. The noise intensity α of this fluid is evaluated as $O(10^{-1}$ mm/s) even in single phase state (Yoshida et al., 2018b). As the noise intensity increases in multi-phase flows, the superiority of VPAR over USR is more emphasized in measuring multi-phase flows.

Experimental results of silicon oil

The rheometer is applied to three kinds of fluids to show the accuracy and applicability of VPAR for evaluating multi-phase fluids as bulk rheology. The first one is silicon oil, which is a typical Newtonian fluid. The second one is a carboxymethyl cellulose (CMC) aqueous solution, which is known as shear-thinning and viscoelastic fluid. The last one is suspensions of solid spherical particles with diameter of $O(100\ \mu$m), which is out of applicable ranges of the standard rheometer, to show the applicability of VPAR for evaluating multi-phase fluids as bulk rheology.

The silicon oil (KF-96-3,000cs, Shin-Etsu Chemical Co., Ltd., Japan) with a density of $\rho = 967$ kg/m^3 was chosen as a typical Newtonian fluid. The double cylinders

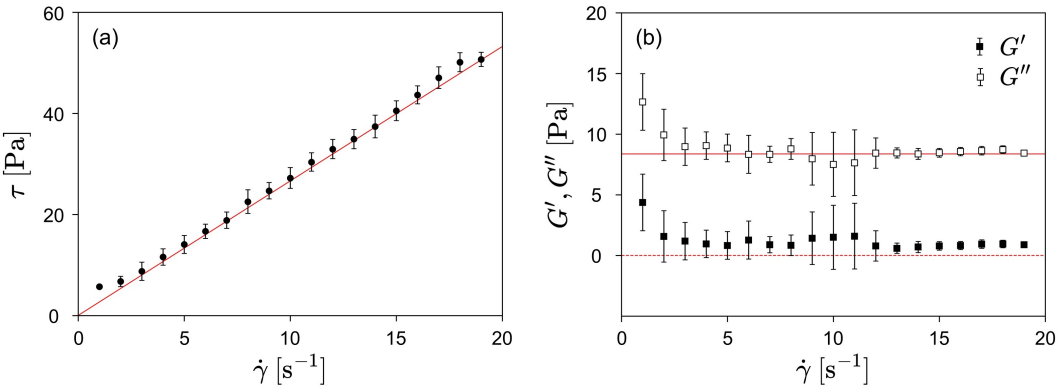


FIGURE 2.16: Measurement results of the silicon oil by VPAR with the oscillation frequency of f_o = 0.5 Hz: (a) shear stress amplitude τ against the applied shear rate $\dot{\gamma}$, where the solid line represents a flow curve of a Newtonian fluid with the viscosity coefficient of the catalog value 2.66 Pa·s, and (b) elastic modulus G' and loss modulus G'' as functions of $\dot{\gamma}$. The symbols indicate mean value at each shear rate and error bars show standard deviations. In figure (b), solid and dashed lines indicate the catalog value of the silicon oil, G'' = 8.34 Pa and G' = 0 Pa.

were installed in a water bath for temperature control, and it was kept at 26.5 ± 0.5°C during the experiment. The viscosity coefficient at this temperature is μ = 2.66 Pa·s as the catalog value. The ultrasonic probe with a resonance frequency of 2 MHz (Met-Flow SA, Switzerland) was used, and the speed of sound was measured as c = 1004 m/s in the preliminary experiment. As tracer particles for the UVP measurement, a total of 5 g of flow beads (CL-2507, Sumitomo Seika Chemicals Co., Ltd., Japan) with a density of 0.92 g/mL and mean diameter of 180 μm was added to 9 L silicon oil. The resulting volume fraction of the tracer particles is 0.056%, which is negligible enough to ignore modification of the effective viscosity. The oscillation parameters were f_o = 0.5 Hz and the amplitude Θ was increased from $\pi/6$ to π rad.

The obtained velocity distributions and temporal profiles of the axial torque were analyzed by VPAR. The shear rate amplitude $A_{\dot{\gamma}}$ and the shear stress amplitude A_τ are denoted as $\dot{\gamma}$ and τ in the following, which are more similar notations. The amplitude of shear stress as a function of shear rate is shown in Fig 2.16, where the plots are experimental results and the solid line corresponds to a Newtonian fluid with μ = 2.66 Pa·s. Excluding the plot at the lowest shear rate, there is a good agreement between the experimental results and the catalog value. A representative viscosity obtained using a function of $\tau(\dot{\gamma}) = \mu\dot{\gamma}$ and least squares method is evaluated as 2.73 Pa·s, where the relative error against the catalog value is 2.6%. The stress is also decomposed to G' and G'' as shown in Fig. 2.16 (b). The solid and dashed lines represent $G'' = \mu\omega_o$ with μ = 2.66 Pa·s and G' = 0 Pa. It can be confirmed that G'' is much higher than G' by one order in the entire shear rate range, showing that the silicon oil is a viscous dominant fluid. In the calculation of the mean values and standard deviations in Fig. 2.16, all the experimental data were included. The error bars around $\dot{\gamma} = 10^1$ s^{-1} are relatively large, but a more accurate evaluation will be possible by removing abnormal values using box plots like the ones in Fig. 2.14 and 2.15.

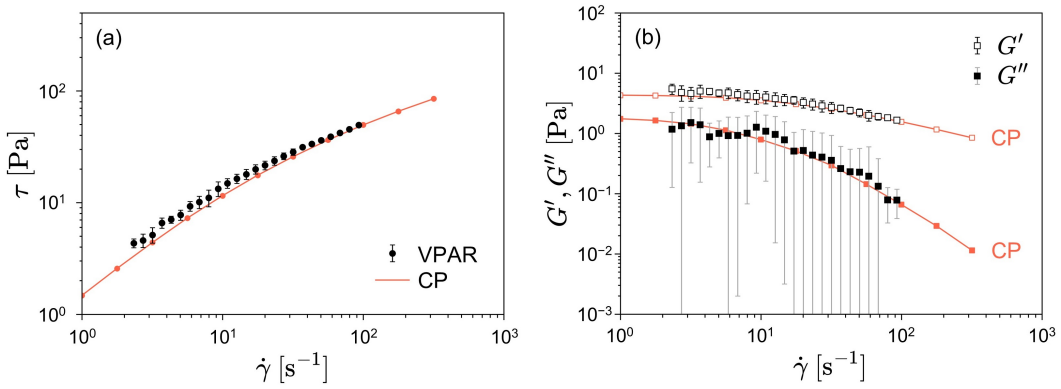


FIGURE 2.17: Measurement results of the carboxymethyl cellulose (CMC) 1.2 wt.% aqueous solution by VPAR with the oscillation frequency of f_o = 0.5 Hz: (a) shear stress amplitude τ against the applied shear rate amplitude $\dot{\gamma}$, and (b) shear rate dependent elastic modulus G' and loss modulus G''. The symbols represent mean values at each shear rate with error bars showing standard deviations. The solid lines are obtained in a strain sweep test by a standard torque-type rheometer with a cone-plate (CP) geometry in the same condition of the oscillation frequency.

Experimental results of carboxymethyl cellulose aqueous solution

The second test fluid is carboxymethyl cellulose (CMC) aqueous solution (CMC1190, Daicel Miraizu Co., Ltd., Japan), which is known as a shear-thinning and viscoelastic fluid (Ghannam and Esmail, 1997; Benchabane and Bekkour, 2008). The molar weight of CMC1190 is 8.2×10^5 and the concentration was 1.2 wt.%. A total of 5 g of the tracer particles (CHP20/P120, Mitsubishi Chemical Co., Ltd., Japan) with a density of 1.01 g/mL and a diameter of 75 – 150 μm was added to 9 L of the aqueous solution for the UVP measurement. The temperature was kept at 25.0°C during the experiment. The oscillation parameters are f_o = 0.5 Hz and Θ from $\pi/6$ to $5\pi/3$ rad. The dependence of the shear stress amplitude on the shear rate is evaluated by VPAR as shown in Fig. 2.17 (a). The plots indicate mean value with error bars for standard deviations. The gradient of the curve gradually decreases, showing a shear-thinning characteristic. The CMC solution with the tracer particles removed was also measured with a standard torque-type rheometer (Anton Paar MCR702e) with a cone-plate (CP) geometry with a diameter of 50 mm and a slope of 1°. The result of the strain sweep test with the oscillation frequency of 0.5 Hz is shown in Fig. 2.17 (a) with a solid line, showing a good agreement with the results obtained with VPAR. The stress was decomposed to G' and G'' as shown in Fig. 2.17 (b). It can be seen that the gap between the curves of G' and G'' widens as the shear rate increases, changing from viscoelastic to purely viscous. This characteristic is often observed in the CMC solution and many kinds of polymer solutions (Ohie et al., 2022a). The results obtained with VPAR are in perfect agreement with the standard rheometer as shown in Fig. 2.17 (b), reinforcing the validity of the proposed method.

Compared with the conventional USR, the advantage of this method lies in its robustness against the measurement noise and its wider range of the shear rate amplitude that can be realized in the apparatus. As the conventional USR did not have an inner cylinder, the flow field is close to almost rigid rotation for high viscous fluid, and the shear rate is essentially zero. In contrast, applying a non-slip condition on

the inner cylinder, at least the shear rate is roughly estimated as $U_{\mathrm{wall}}/(R_{\mathrm{out}} - R_{\mathrm{in}})$, where the maximum shear rate can be further extended by reducing the gap width. As the current USR ignores the radial gradient terms of the viscosity coefficient and elastic modulus, it is not permissible to use this approach to narrow the gap for creating a steep shear rate distribution, that is, a steep distribution of the rheological properties in the gap.

Application to suspensions of solid spherical particles

The suspensions of solid spherical particles were finally measured to demonstrate the applicability of VPAR to the rheology of multi-phase fluids in unsteady shear flows. As suspended solid spherical particles, UBK535 (Mitsubishi Chemical Co., Ltd., Japan) with a density of 1.27 g/mL and mean diameter of 220 μm were used, where the high-viscous silicon oil (KF-96-3000cs, Shin-Etsu Chemical Co., Ltd., Japan) was selected as dispersion medium to suspend the solid particles. The terminal velocity is estimated by Stokes' law to be 0.2 mm/min, and the experimental time for each condition of volume fraction is about 10 min, so the sedimentation of the particles can be neglected. Totally 9 L of the pure silicon oil was filled in the double concentric cylinders, and it was measured by VPAR. Then the fluid was collected in another bucket, and 100 g of the particles was added. The bucket was put in a vacuum chamber to remove small bubbles, and the suspension was stirred with an impeller for 15 min to distribute the particles uniformly. The suspension was brought back from the bucket to the cylinder for the measurement by VPAR. This process was continued four times, and the resulting volume fraction is 0.8%, 1.7%, 2.6%, and 3.4% as shown in Fig. 2.18 (a). The speed of sound was also measured with a 2 MHz ultrasonic probe, and the results are summarized in Fig. 2.18 (b). As the volume fraction increases, the speed of sound also increases because the proportion of solids increases as the entire suspension.

The results of the suspensions measured by VPAR are shown in Fig. 2.19. The symbols are mean values with error bars indicating standard deviations. The solid line shows a flow curve with $\mu_0 = 2.73$ Pa$\cdot$s, which is the viscosity of the pure silicon oil identified with VPAR. The symbols lie straight, passing through the origin at each condition. Although it is not included in the graph, even when it is decomposed into G' and G'', plateau profiles as like Fig. 2.16 (b) were obtained under all the volume fractions, showing that the suspensions behave as viscous dominant fluids in unsteady shear flows. In addition, the gradient of the lines gradually increases in higher volume fraction, indicating that the addition of solid spherical particles increases the viscosity of suspensions. As a representative value, the viscosity coefficient at $\dot{\gamma} = 10$ s^{-1}, which is the middle shear rate in the graph, was calculated at each volume fraction, and summarized in Fig. 2.20 with symbols showing mean values and error bars indicating standard deviations. When the fluid is purely viscous, that is, $\delta = \pi/2$ rad in Eq. 2.22, μ_{e} corresponds the kinematic viscosity μ, the vertical axis is therefore noted as μ. The error bars in the horizontal direction show the uncertainty of the volume fraction. As the previous experimental procedures described, the suspension was transferred from the cylindrical vessel to the bucket or vice versa to increase the volume fraction. The amount of the silicon oil lost was about 160 mL for each time. The uncertainty of the volume fraction was evaluated from this amount. In Fig. 2.20, a statistically significant monotonic increases against

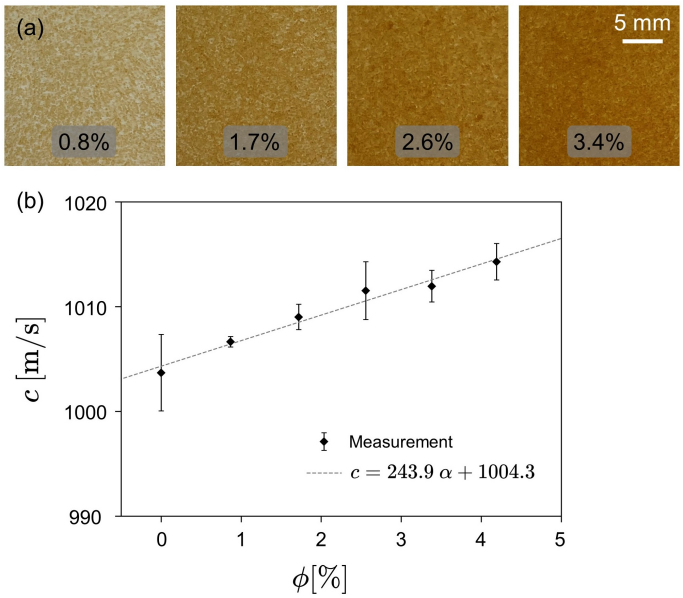


FIGURE 2.18: (a) Photographs of the suspensions of the solid spherical particles with different volume fractions, where the suspensions were filled in acrylic cylinders with diameter of 34 mm and photos were taken from the side, (b) modification of speed of sound measured with a 2 MHz ultrasonic probe, where the symbols represent the average values and dashed line is a regression curve based on least squares method against the measurement data.

the volume fraction is confirmed. Regarding the suspension rheology of solid spherical particles, Einstein (1906) proposed the following formula to evaluate the effective viscosity μ_{eff} as

$$\mu_{\text{eff}} = \mu_0 \left(1 + \frac{5}{2}\phi\right). \tag{2.77}$$

(Guth, 1938) semi-empirically further developed the formula to cover semi-dilute regime including a higher order term as

$$\mu_{\text{eff}} = \mu_0 \left(1 + 2.5\phi + 14.1\phi^2\right). \tag{2.78}$$

The solid line in Fig. 2.20 shows the effective viscosity evaluated by the Guth and Gold formula with $\mu_0 = 2.73$ Pa · s, agreeing with the measurement results of $\phi < 3\%$. The suspension with the volume fraction of 1.7% was also measured by a standard torque-type rheometer (Anton Paar MCR702e) with a plate-plate geometry, however, agreement with the Guth and Gold formula was not confirmed as described in the next paragraph. The results of the VPAR reinforces the validity of the proposed method and its applicability to exploring the rheology of multi-phase fluids. The symbol with the highest volume fraction deviates from the semi-empirical formula. This is attributed to limitations regarding the UVP measurement denoted explicitly in the next section.

A standard torque-type rheometer with a plate-plate geometry was tentatively applied to the suspension with volume fraction of 1.7%. Diameter of the plate is 50 mm and the gap size is 1 mm. Steady shear test was conducted to be compared with the semi-empirical formula denoted by Eq. 2.78. The silicon oil was measured

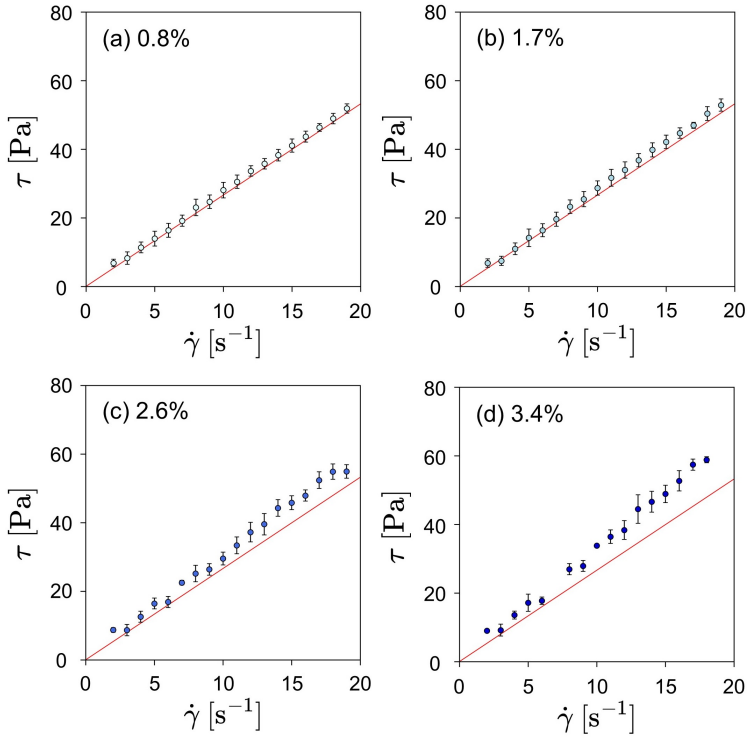


FIGURE 2.19: Measurement results of the suspensions of solid spherical particles with diameter of 220 μm for different volume fractions of (a) 0.8%, (b) 1.7%, (c) 2.6%, and (d) 3.4%. The symbols are mean values obtained by VPAR and error bars represent standard deviations. The solid line corresponds to a flow curve of a Newtonian fluid with the viscosity coefficient of 2.73 Pa · s, which is identified with VPAR by measuring the silicon oil as the dispersion medium suspending the solid particles.

three times and the suspension five time, where an individual sample was replaced for each measurement. The temperature of the plate was kept at 25.0°C during all the measurement. The viscosity curves in steady shear are shown in Fig. 2.21. The solid line in the figure shows the mean value in the entire shear rate, 2.83 Pa · s. In the case of the silicon oil, the viscosity almost matches the catalog value at 25.0°C, 2.91 Pa · s, with a difference of 2.8%. Viscosity of the suspension increases against that of the silicon oil. The dashed line shows the effective viscosity 2.96 Pa · s estimated by Eq. 2.78 with μ_0 = 2.83 Pa · s, but the results measured by the rheometer deviate from this value in lower shear rate range. The dotted line corresponds to the viscosity increase with the volume fraction of 6.2% as reference.

Limitations of the method

The rheometer is based on torque measurement and UVP. The velocity profile of the test fluid in the gap has to be obtained accurately by UVP at first. In the UVP measurement, a cylindrical ultrasonic pulse is emitted in the direction of ξ as shown in Fig. 2.12 (c). Its active diameter is about 10 mm and thickness is O(1 mm), and UVP essentially outputs the balk-averaged velocity in this spatial resolution. The dispersion size, therefore, has to be smaller than this volume, and usually is O(1 mm) at maximum. In the previous section, the suspensions of solid spherical particles with

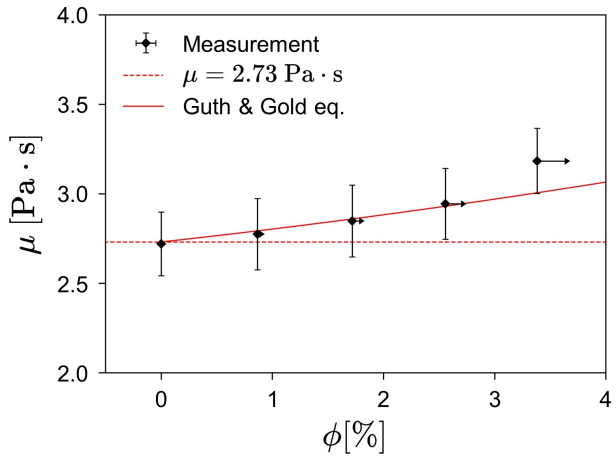


FIGURE 2.20: Viscosity coefficient as a function of volume fraction. The viscosity is evaluated at $\dot{\gamma} = 10\ \mathrm{s}^{-1}$, which is the middle shear rate in Fig. 2.19. The symbols indicate mean values at the shear rate and error bars show standard deviations. The dashed line is the viscosity of the dispersion media $\mu_0 = 2.73$ Pa·s, which was identified with VPAR. The solid line is the effective viscosity calculated by the semi-empirical formula proposed by Guth (1938). The arrows indicate uncertainty of the volume fraction caused by the loss of silicon oil in the process of adding the particles to increase volume fraction.

a diameter of 220 μm were measured by the ultrasonic transducer with a resonance frequency of 2 MHz, and the upper limitation of the volume fraction was 3 % when the dispersion media is silicon oil. This limitation of the volume fraction is also mentioned in the previous research using UVP (Tasaka, Kimura, and Murai, 2015). This limitation was determined in this paper by comparison with the theoretical equation for suspensions of solid spherical particles. However, when investigating the rheology of multi-phase fluids having unknown rheological properties, it is necessary to know the measurable distance in advance. One of the easiest way is to measure the velocity profile of rigid body rotation in an open cylindrical container. In the measurable range from the transducer, the velocity component captured by UVP u_ξ becomes $\Omega\Delta y$ with the angular velocity of Ω. In addition, for measuring a suspension with higher volume fractions, other transducers with lower resonance frequency are potential candidates for weakening attenuation of ultrasonic waves, or the optical approach is also one of the prominent candidate (Noto et al., 2023).

The measurable ranges of shear rate, viscosity, and oscillation frequency are mentioned here. As for the oscillation frequency, the time resolution of UVP is $O(10\ \mathrm{ms})$, it is therefore limited to $O(1\ \mathrm{Hz})$ at the maximum currently. Regarding the measurable ranges of viscosity and shear rate, numerical experiments were performed assuming a Newtonian fluid with different frequencies of 0.1, 0.2, 0.5, 1.0, and 2.0 Hz. The fluid density is assumed to be $\rho = 1000\ \mathrm{kg/m^3}$ here and the same geometry with the experimental apparatus is introduced. The velocity resolution of UVP is usually $\Delta u_\xi = O(1\ \mathrm{mm/s})$, corresponding to $\Delta u_\theta = O(10\ \mathrm{mm/s})$. The wall velocity U_{wall} has to be larger than this value. The spatiotemporal velocity distribution is obtained by Eq. 2.75 with given U_{wall} tentatively ranging from $U_{\mathrm{min}} = 100$ mm/s to $U_{\mathrm{max}} = 1000$ mm/s and μ ranging from 10^{-1} to 10^3 Pa·s. The minimum and maximum shear rates realized in the gap are determined under different μ, and they are summarized in Fig. 2.22 with solid lines. The resolution of the torque sensor attached

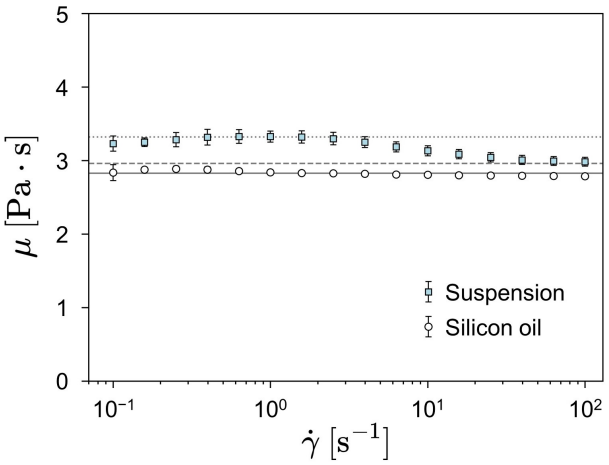


FIGURE 2.21: Viscosity curves of the silicon oil and suspension with the volume fraction of 1.7% measured by a standard torque-type rheometer. The solid line shows the viscosity of 2.83 Pa · s, which is a mean value of the open circles in the entire shear rate range. The dashed and dotted lines are effective viscosities estimated by Eq. 2.78 with μ_0 = 2.83 Pa · s for 1.7% and 6.2%, respectively.

to the inner cylinder is $O(10^{-3}$ Nm). Therefore, the oscillatory shear flow induced on the outer cylinder surface has to reach the inner cylinder. The wall shear stress has to be large enough so that the converted axial torque exceeds the resolution of the sensor as shown in Fig. 2.22 with dashed lines.

As shown in Fig. 2.22, for each oscillation frequency condition, there is a region that extends directly up and one that extends to the lower right on the graph, with a specific viscosity as a boundary. This boundary drops with decreasing frequency. The thickness of the viscous layer on the outer cylinder is estimated by the Stokes' first problem as $\delta_v = \sqrt{2\mu/\omega_o\rho}$. When the thickness of viscous layer exceeds the gap distance, $R_{out} - R_{in}$, the minimum and maximum shear rates are roughly estimated as $U_{min}/(R_{out} - R_{in}) = O(10^0$ s$^{-1})$ and $U_{max}/(R_{out} - R_{in}) = O(10^1$ s$^{-1})$, respectively, corresponding to the region extending directly up in Fig. 2.22. In contrast, the minimum and maximum shear rates are approximately U_{min}/δ_v and U_{max}/δ_v at $\delta_v < R_{out} - R_{in}$, corresponding to the region extending to the lower right in Fig. 2.22. The viscosity satisfying $\delta_v = R_{out} - R_{in}$ decreases for lower oscillation frequency condition, the boundary between the two regions hence shifts down as the frequency decreases. In addition, the maximum shear rate U_{max}/δ_v for a given viscosity therefore increases with the frequency increasing.

The measurable frequency and shear rate ranges in Fig. 2.22 are relatively narrow comparing with a standard torque-type rheometer. These limitations can be improved by changing the gap size and torque sensor. The maximum oscillation frequency and the measurable minimum shear rate are also depends on the time and velocity resolutions of the UVP measurement. The development of a high-resolution ultrasonic velocity profiler is an important future work not only for exploring the rheology of multi-phase fluids in wider ranges but also as a fluid measurement tool. The shear rate ranges realized in the current VPAR, however, are the most interesting but difficult conditions when it comes to probing the rheology of multi-phase fluids. For example, the viscoelasticity of dilute bubble suspensions has been investigated in steady shear flows (Rust and Manga, 2002) and small amplitude oscillatory shear

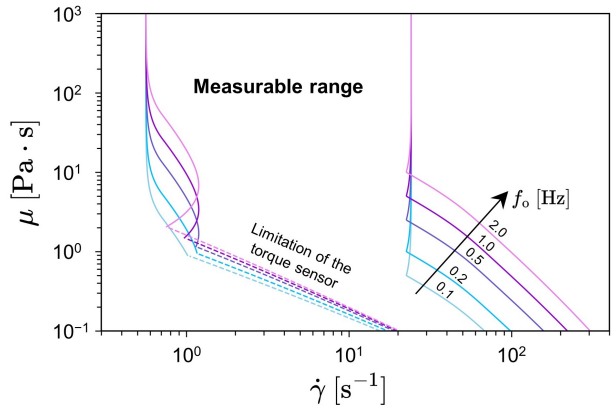


FIGURE 2.22: Measurable ranges of shear rate and viscosity of the proposed rheometry. The solid lines indicate minimum and maximum shear rates under different oscillation frequencies, whereas the dashed lines show the minimum shear rate determined by the resolution of the torque sensor attached to the apparatus. The performance of UVP assumed here is that the time and velocity resolutions are $O(10\,\mathrm{ms})$ and $O(1\,\mathrm{mm/s})$, respectively.

flows (Llewellin, Mader, and Wilson, 2002), while the viscoelastic properties with the bubble deformation involved have not been elucidated experimentally. Using a silicon oil with the viscosity coefficient of 5 Pa·s and suspended bubbles with diameter of 1 mm can realizes unsteady shear flows accompanying the bubble deformation, which will be investigated in future work as well as oil-water mixtures and suspensions of poly-dispersed and anisotropic particles.

Chapter 3

Time-resolved rheology of complex fluids in non-equilibrium conditions

As demonstrated in the previous chapter, one of the strength points of the rheometry based on the velocity information is its high applicability to complex fluids such as multi-phase fluids containing millimeter size dispersions. In addition, it can simultaneously evaluate shear rate dependent rheological properties such as shear-thinning and shear-thickening as the shear rate amplitude distributes in the radial direction in the cylindrical vessel. It is therefore possible to evaluate the shear-rate-dependence during non-equilibrium conditions such as phase separation of multi-phase fluids and chemical reactions. As representative examples of non-equilibrium conditions, phase separation of an oil-water mixture and hydrolysis of polysaccharide aqueous solutions with α-amylase are introduced in § 3.1 and 3.2, respectively.

3.1 Separating oil-water mixture

The time variation of the effective viscosity of the mixture of pure water and 1000 cSt silicon oil is examined. The silicon oil in which fine spherical particles (CHP 20P) were suspended, and pure water were filled in the vessel at a volume ratio of 10:1 to a liquid level height of z = 140 mm. The mixture was stirred at 120 rpm for 1 minute using a spatula. As a result, a group of water droplets with a diameter of $O(0.1 - 1.0$ mm$)$ was formed in the silicon oil solvent. Since a mixer and surfactant were not used, the emulsion was not in a stable state, and the droplets accumulated on the bottom surface of the vessel over time due to the difference in the specific densities of the silicon oil and water. The specific gravity of the silicon oil is 0.97. After the stirring, the state of the mixture such as the diameter and number of droplets on the measurement line of UVP changes with time as the water and oil separated each other. Afterd letting it stand for about 10^3 min, it was confirmed that the silicon oil and water were separated into two layers in the vertical direction. Only the silicon oil was present on the measurement line finally. The transient changes in the effective viscosity associated with the separation of the oil-water mixture are evaluated, and the results are discussed.

Separation process of the oil-water mixture

The separation of the oil-water mixture is explained here. Water droplets with a diameter of $O(0.1 - 1.0$ mm$)$ were formed by stirring. Immediately after that, droplets with a relatively large diameter existed and the number of density of the droplets

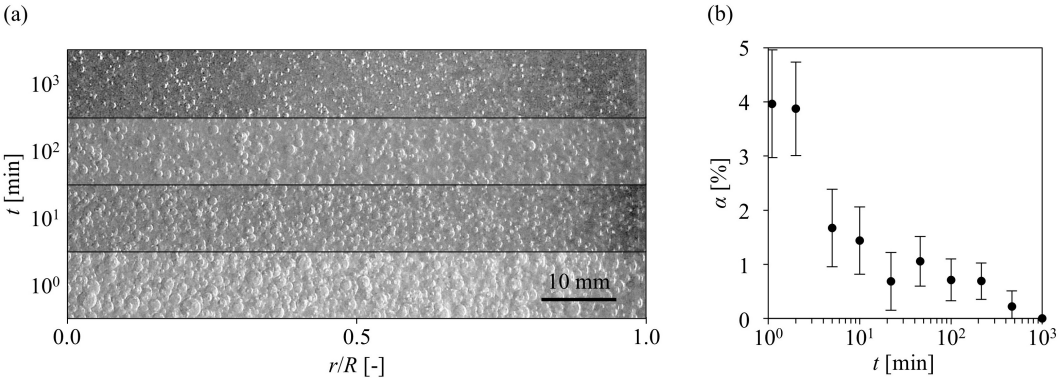


FIGURE 3.1: Temporal change of the oil-water mixture: (a) Gray-scale pictures taken from side of the vessel, and (b) temporal change of the volume fraction α of the droplets in the measurement line with 3σ error bars

was high, so the ultrasonic waves used in UVP were considerably attenuated, and velocity information inside the vessel could not be obtained. Furthermore, in USR, the size of the droplet has to be smaller than the measurement volume of UVP in order to consider the oil-water mixture as a continuum. Therefore, after the stirring, the mixture was allowed to stand for 15 min for reducing the number density of the droplets. It was confirmed that the ultrasonic wave was transmitted to the inside, and this moment is defined as time t = 0 min. At time t =1, 2, 5, 10, 22, 46, 100, 215, 262, 1000 min, the oscillation of the vessel and velocity measurement were performed for 100 sec. The oscillation parameters were selected as f_o = 0.5 Hz and Θ = 5 $\pi/6$ rad. The vessel was kept to stand for 1000 min through the experiment except time to the velocity measurement. In addition, as the solvent silicon oil has a high viscosity of 1000 mm^2/s , the convection effect of the droplets due to the secondary flow are sufficiently small to be ignored, and it is considered that the droplets were uniformly dispersed in the radial direction. The vessel was photographed from the side in order to grasp the multi-phase state at each time. Figure 3.1(a) shows images cut out only on the measurement line. From the visualized images, it can be seen that the diameter and number density of the droplets existing on the measurement line decrease with the passage of time. Immediately before the velocity measurement at each time, a small amount of the mixture on the measurement line was collected with a dropper. After collecting the mixture, they were allowed to stand in test tubes for several days and separated into two layers completely. The masses of the silicon oil and water were measured and converted to the volume fraction α as shown in Fig. 3.1(b). In the graph, 3σ error bars are displayed as the uncertainty of the volume fraction measurement. The void fraction α decreases with the passage of time.

Time variation of the effective viscosity

Spatiotemporal distributions of the velocity are shown in Fig. 3.2, where Fig. 3.2(a), (b), and (c) respectively show distributions at measurement time 1, 22, 1000 min. Velocity distribution near the side wall $r/R > 0.9$ was not obtained due to the co-reflections of the ultrasonic pulse inside the acrylic wall on the front side. This regime is removed for the phase analysis. From these distributions, it is confirmed that the degree of the phase lag increases over time, which qualitatively means that

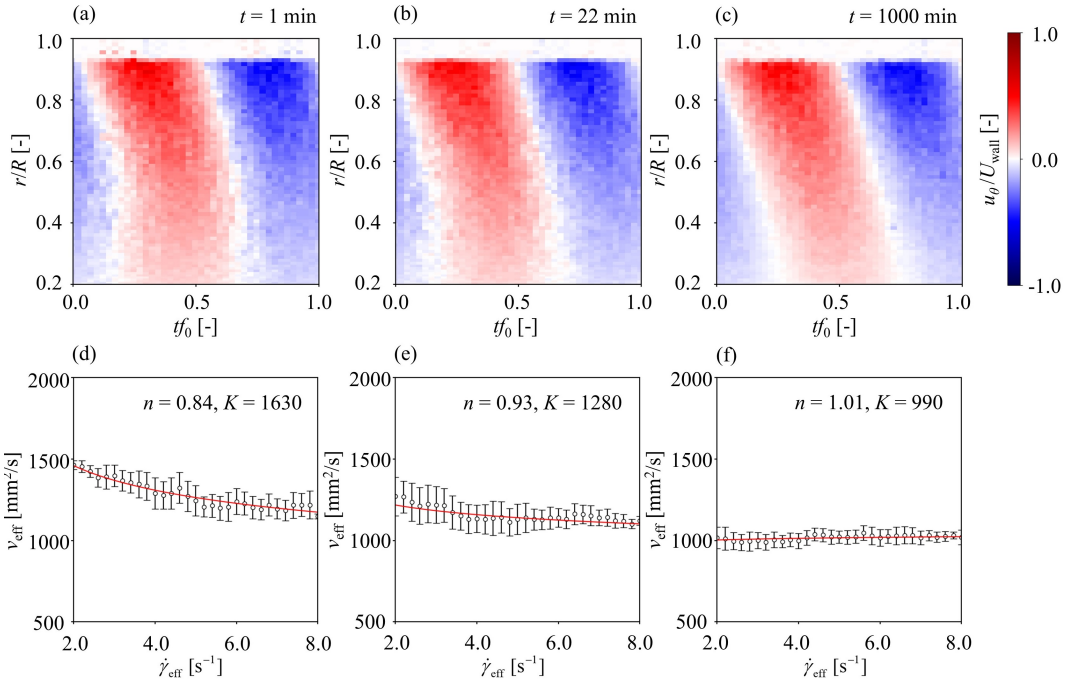


FIGURE 3.2: Measurement results of the oil-water mixture: (a)-(c) Spatiotemporal distributions of the azimuthal velocity at elapsed times, 1, 22, 1000 min, respectively, and (d)-(f) time-averaged viscosity curves obtained by the phase analysis and power law fitting curve, where error bars represent standard deviation

the effective viscosity increases over time. The phase analysis was adopted to the velocity distributions and the effective viscosity curves are obtained as shown in Fig. 3.2(d), (e), and (f). In the analysis, velocity distributions at the radial range $0.4 < r/R < 0.9$ were utilized so that the velocity intensity is sufficiently larger than the velocity resolution of UVP. The vertical axis of the graphs shows kinematic viscosity as the analysis evaluates viscosity as the effective kinematic viscosity. The density difference between the oil-water mixture with the volume fraction 5% of the water droplets (effective density: 996.8 kg/m^3) and the silicon oil single phase (density: 967.2 kg/m^3) is extremely small, about 1.5 kg/m^3. Therefore, the effect of the density variation on the kinematic effective viscosity can be ignored. In Fig. 3.2(d) and (e), shear-thinning property (ν_{eff} decreases as $\dot{\gamma}_{\mathrm{eff}}$ increases.) is confirmed, while ν_{eff} takes 1000 mm^2/s in Fig. 3.2(f) , which is the catalog value of the silicon oil.

All the viscosity curves at each measurement time are summarized in Fig. 3.3(a). The figure shows time variation of the viscosity curves, which is impossible to be obtained with ordinary torque type rheometers. Shear-thinning property is confirm ed up to $t = 10^2$ min, while it is completely lost and the fluid behaves as Newtonian at $t = 10^3$ min. In order to quantify the degree of the shear-thinning property, power law fitting is applied to the viscosity curves as,

$$\nu_{\mathrm{eff}} = K\dot{\gamma}_{\mathrm{eff}}^{n-1}. \tag{3.1}$$

The flow consistency index K and the power law constant n are determined by the least squares method. Newtonian and shear thinnig fluids correspond to $n = 1$ and $0 < n < 1$, respectively. The closer n is to zero, the greater $\dot{\gamma}_{\mathrm{eff}}$ depenedence of ν_{eff}, that is, the greater shear thinning property the fluid has. Figure 3.3(b) shows the results

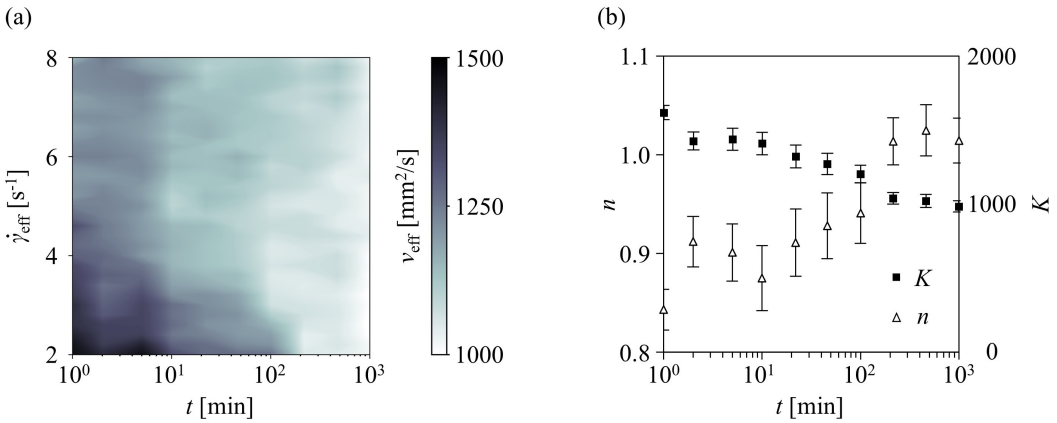


FIGURE 3.3: Time-resolved evaluation of the effective viscosity of the separating oil-water mixture: (a) Time variation of the viscosity curves and (b) time variation of the power law fitting parameters, where error bars represent standard deviation.

of the power law fitting. The power law index n converges to 1 over time. This means that the mixture changes from shear-thinning to Newtonian fluid. As for the flow consistency index K, it decreases monotonically over time, and it matches the kinematic viscosity of the silicon oil 1000 mm^2/s at $t = 10^3$ min, which is a reasonable result as the mixture has returned to the silicon oil single phase at the time. These temporal variations of n and K are due to changes in the multiphase state such as the diameter and void fraction of the droplets on the measurement line of UVP. In the next paragraph, it is verified based on previous studies whether the above results, in which the shear-thinning and effective visocosity decrease due to the multi-phase state.

Consideration

Studies on the effective viscosity of fluids containing dispersions began with fluids containing a small amount of fine solid particles (Einstein, 1906), and have been conducted theoretically and experimentally by Mooney (1951), Frankel and Acrivos (1970), Pal (2001), Rust and Manga (2002), Llewellin, Mader, and Wilson (2002) and so on. Choi and Schowalter (1975) derived the constitutive equation for a fluid containing a large number of deformable and immiscible droplets (i.e. an emulsion). From this equation, Han and King (1980) derived a formula to evaluate the effective viscosity coefficient μ_{eff} of the emulsion under steady shear flow. Under the condition that the viscosity coefficient of the dispersion medium μ_{s} is sufficiently larger than the viscosity coefficient of the dispersion μ_{d}, the equation is simplified as

$$\eta = \frac{1 + (6Ca/5)^2 (1 + 20\alpha/3) (1 + 4\alpha)}{1 + (6Ca/5)^2 (1 + 20\alpha/3)^2} \left(1 + \alpha + \frac{5}{2}\alpha^2\right), \tag{3.2}$$

where η is the relative viscosity defined as $\eta = \mu_{\mathrm{eff}}/\mu_{\mathrm{s}}$. Capillary number Ca is a dimensionless number representing the deformation rate of the dispersion of diameter d, which is defined as the ratio of viscous shear stress $\mu\dot{\gamma}$ to surface tension σ,

$$Ca = \frac{\mu d\dot{\gamma}}{\sigma}. \tag{3.3}$$

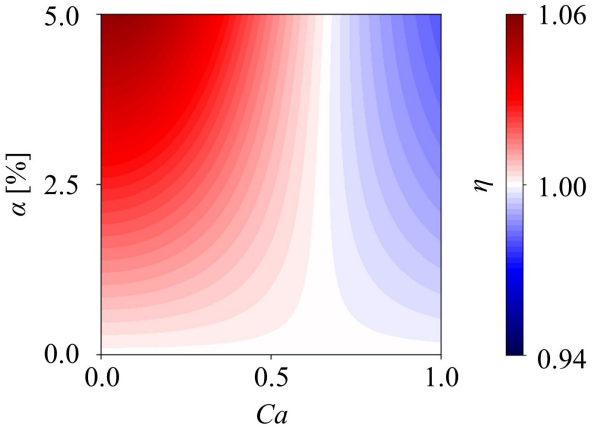


FIGURE 3.4: Relative viscosity η estimated by the formula given by Choi and Schowalter (1975) against each Capillary number Ca and volume fraction α.

When $Ca > 1$, the viscous shear stress around the droplet is more dominant than the surface tension, and the droplet is accompanied by large deformation. Under the condition of $Ca < 1$, the surface tension exceeds the viscous shear stress, and the droplet is only minutely deformed.

In the experiment, the condition $\alpha < 5.0\%$ and $Ca \approx O(0.1)$ is satisfied, and the distribution of η evaluated by Eq. 3.3 in the range is shown in Fig. 3.4. From the figure, it is confirmed that an increase in the Ca number decreases η, and an increase in α increases η. It can be interpreted that the decrease in flow resistance on a micro-scale due to the deformation of the droplet reduces the effective viscosity, and the promotion of momentum transport by increasing the volume fraction of the droplet increases the effective viscosity. The tendency of shear-thinning and effective viscosity to decrease as the droplet diameter and volume fraction decreases, which was observed in the experiment, is consistent with the previous studies. On the other hand, when $10^0 < t < 10^1$ min, the effective viscosity increased by 40% even though the volume fraction was about 4%. This point cannot be obviously explained from the Eq. 3.2, which states that the effective viscosity increases up to about the volume fraction.

From the viewpoint of the dynamics of water droplets, the following two are considered as the factors causing the difference between the experimental results and the theory by Choi and Schowalter (1975). One is the increase in the effective volume fraction α_{eff} due to the accumulation (cluster) of the droplets. It is known that when a cluster occurs, the effective volume fraction of the dispersion increases ($\alpha_{\text{eff}} > \alpha$) by immobilizing the solvent layer on the cluster (Lewis and Nielsen, 1968). As Fig. 3.1(a) is an image taken from the side of the vessel and integrated in the depth direction, it is impossible to directly confirm the accumulation of droplets, but it is possible that the droplets accumulated due to the oscillatory shear flow or when the droplets fall to the bottom of the vessel. Numerical simulations by Chang and Powell (1993) have revealed that small-diameter droplets tend to accumulate in large-diameter droplets, especially when the droplets diameters are not uniform as in the experiment. The second possible factor that caused a difference between the experimental result and the theory regarding the increase in the effective viscosity is that the effective viscosity evaluation was performed in the oscillatory shear flow. In most previous studies including Eq. 3.2, the deformation of the dispersion

and flow field are premised on the steady state, and there are few cases where they are applied to the unsteady state. When the deformation of the dispersions and the flow field are unsteady, the interaction between the dispersions may increase, and it is considered that the effective viscosity is evaluated higher than that evaluated in Eq. 3.2. Further studies are needed theoretically and experimentally for the evaluation of the rheological properteis in the unsteady shear flow. Another possible factor is that the phase analysis represents viscosity and viscoelasticity with the effective viscosity. Evaluating viscoelasticity using the velocity-profiling-assisted rheoemter proposed in § 2.5 is also future work.

3.2 K-n map for evaluating functionalities of fluid foods

Role of rheology for better swallowing foods

To investigate the rheological properties that an ideal swallowed food should have to prevent aspiration, it is necessary to investigate the dynamics of the swallowed food *in vivo* and identify a causal relationship with the rheological properties of foods evaluated *in vitro* (Wood, 1968; Shama and Sherman, 1973; Cutler, Morris, and Taylor, 1983; Hutchings and Lillford, 1988; Houska et al., 1998; Nakauma et al., 2011). In recent years, the development of *in vivo* methods of measurement has been remarkable, as represented by video fluorography (Palmer and Hiiemae, 1997; Takahashi et al., 2002; Bangyeekhan, Leelamanit, and Tekasakul, 2013; Zhu, Mizunuma, and Michiwaki, 2014; Qazi et al., 2020) and ultrasonic pulse Doppler methods (Nagatoshi et al., 2001; Hasegawa et al., 2005; Hasegawa, Nakazawa, and Kumagai, 2008; Kumagai and Kumagai, 2009; Moritaka and Nakazawa, 2009; Tashiro et al., 2010; Gao and Kohyama, 2014; Qazi et al., 2020), which have enabled detailed access to the behavior of the bolus in the swallowing process.

In vitro methods of measurement are technically far behind these *in vivo* methods. Most swallowed foods are in heterogeneous and non-equilibrium conditions, which makes it extremely difficult to evaluate the rheological properties, such as viscoelasticity and shear-rate-dependent viscosity, with the conventional torque-type rheometers widely used in academic and industrial fields (Matsumoto, 1978; Nishinari, 2003; Kumagai and Kumagai, 2009; Tashiro et al., 2010). Even though there are several practical methods for quantitatively characterizing the rheological properties (Ewoldt, Hosoi, and McKinley, 2008; Wagner et al., 2017), it should be noted that target fluids are limited only in homogeneous and equilibrium states.

There are three main difficulties in *in vitro* evaluations caused by the heterogeneous and non-equilibrium conditions. The first problem is that wall-slip and shear-banding phenomena occur frequently in the measurements of functional swallowed foods, such as gel-sol coexistent fluids, using torque-type rheometers (Fischer, Wheeler, and Fuller, 2002; Sui and McKenna, 2007; Fardin et al., 2014). Under the wall-slip and shear-banding phenomena, the standard torque-type rheometers cannot be used to distinguish whether the evaluated rheological properties originate from the properties of the swallowed foods themselves or are superimposed phenomenon from the wall-slip and shear banding (Mendes, Alicke, and Thompson, 2014; Saint-Michel et al., 2016). The second problem is the limited use of ordinary rheometers with heterogeneous fluids. Swallowed foods, such as porridge containing dispersions with millimeter size and yogurt, in which gel and sol states coexist, cannot fit in the narrow gap of the rheometers, and there is an increasing demand in the food and medical fields to be able to evaluate the rheology of such complex fluids. The last problem regarding the non-equilibrium conditions may be the most

difficult of the three. Considering digestive enzyme in saliva decomposes the starch contained in many swallowed foods with a concomitant reduction in viscosity, the time variation of rheological properties represented by shear-rate-dependent viscosity has to be evaluated (Chen, 2009; Kumagai and Kumagai, 2009). A standard rheometer evaluates the viscosity under one fixed shear rate at a time; therefore, such temporal evaluations take an enormous amount of time and are often impossible to perform.

To meet the diverse demands for evaluating the rheological properties of swallowed foods, USR is a potential candidate. USR has been used to investigate millibubble/solid particle suspensions (Sakurai, Tasaka, and Murai, 2013; Tasaka, Kimura, and Murai, 2015; Yoshida, Tasaka, and Murai, 2019a), an oil-water mixture (Ohie et al., 2020), porridge (Tasaka et al., 2021), and gel-sol coexistent fluids (Yoshida, Tasaka, and Murai, 2017; Yoshida et al., 2018a; Yoshida, Tasaka, and Fischer, 2019). In addition to its applicability to the analysis of complex fluids, USR can be used to evaluate the shear-rate-dependent viscosity as the shear rate is $O(10^1\ \mathrm{s}^{-1})$ near the cylindrical wall of the vessel and $O(10^{-1}\ \mathrm{s}^{-1})$ near the central axis, which fall in the shear rate range required for evaluating the rheological properties of swallowed foods (Shama and Sherman, 1973; Kumagai et al., 2009; Tashiro et al., 2010). It is therefore possible to evaluate the effect of chemical reactions, or the time variation of multi-phase states, on the shear-rate-dependent viscosity, indicating that USR may solve the third problem related to swallowed foods in the non-equilibrium condition. The time variation of the viscosity curve can theoretically be evaluated on a time scale of $O(1\ \mathrm{s})$.

Herein, a method for evaluating rheological properties, especially variations over time, is proposed using USR. Aqueous solutions mixed with starch-based, guar gum-based, or xanthan gum-based thickeners were used as test fluids. These thickeners are classified as first, second, and third generation additives, respectively, for use in a dysphagia diet (Matsuo et al., 2020). The starch-based thickener is classified as the first generation, and it has been regarded as a problem that the viscosity decreases due to hydrolysis by amylase. The guar gum-based thickener is classified as the second generation, and the viscosity is sustained even though the amylase is mixed. The xanthan gum-based thickener classified as the third generation has further improved swallowability and flavor (Ueha et al., 2014). The time variation of the flow curves of these solutions after being mixed with alpha-amylase was evaluated by USR, and the rheological properties of the thickeners from each generation were quantitatively characterized.

Materials

Three types of commercial food thickeners were used: starch-based (Tromeline, Nutri Co. Ltd., Japan), guar gum-based (Hightoromeal, Foodcare Co. Ltd., Japan), and xanthan gum-based (Softia S, Nutri Co. Ltd., Japan). Three concentrations of each thickener in pure water were used, as summarized in Table 3.1. The solution with the lowest concentration of the starch-based thickener was difficult in the USR measurement to capture the time variation of shear thinning property with converting sufficient range of the shear rate due to the low viscosity. More than the specified amount was therefore added as shown in the parenthesis in Table 3.1. The specified amount was dissolved in 1 L of pure water with stirring with a spatula at room temperature of 25°C. Nine test solutions were degassed with a vacuum pump and then stored at room temperature for a day. As tracer particles for the UVP measurements, a small amount of styrene spherical particles (MCI GEL CHP20/P120, Mitsubishi Chemical

TABLE 3.1: Amount of the three thickeners added to 100 mL of pure water. The solution of the starch-based thickener was so low in viscosity that it could not be measured by USR, therefore, 3.8 g was added instead of 2.4 g.

Thickener \ Conc.	Low (L)	Middle (M)	High (H)
Starch-based (I)	2.4 g (3.8 g)	4.7 g	7.1 g
Guar gum-based (II)	1.5 g	2.2 g	2.7 g
Xanthan gum-based (III)	1.0 g	2.0 g	3.0 g

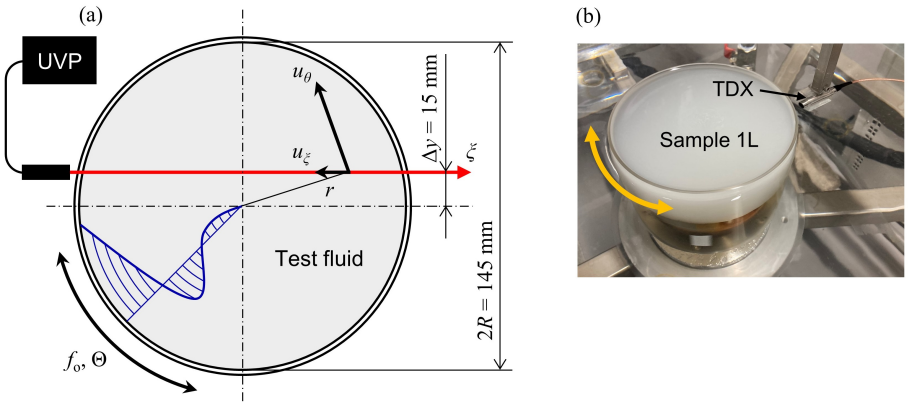


FIGURE 3.5: Experimental setup of USR for capturing the spatiotemporal velocity distribution in an oscillating cylindrical vessel: (a) schematic top view and (b) photograph of the setup, where a cylindrical vessel was installed in a water bath for the UVP measurements and temperature control

Co. Ltd., Japan), with a mean diameter and density of 75 – 150 μm and 1.01 g/mL, were added to all the solutions. As 5 g of the tracer particles was added in 1 L of each solution, the volume fraction of the particles was ϕ = 0.05%. Based on the theoretical formula of the effective viscosity proposed by Einstein (1906), increase rate of the viscosity caused by the particles with volume fraction of ϕ is roughly estimated by $5\phi/2$. In this experiment, the increase rate is estimated by 0.125%, and changes in the rheological properties can be sufficiently small to be ignored. For simplicity of notation, each solution is represented by a Greek numeral and an uppercase letter denoting the generation of the thickener and the concentration, respectively (see Table 3.1).

In the viscosity stability test, alpha-amylase (FUJIFILM Wako Pure Chemical Co. Ltd., Japan) was used. First, 0.1 g of alpha-amylase powder was dissolved in 200 mL of pure water, then 2 mL of this amylase solution was added to 1 L of the thickened solution. The total amount of the amylase powder added was 1 ppm. This amount of amylase is almost as specified by the stability test method of thickeners determined by the Consumer Affairs Agency of Japan. The method of mixing the amylase solution and the thickened solution is specifically explained later.

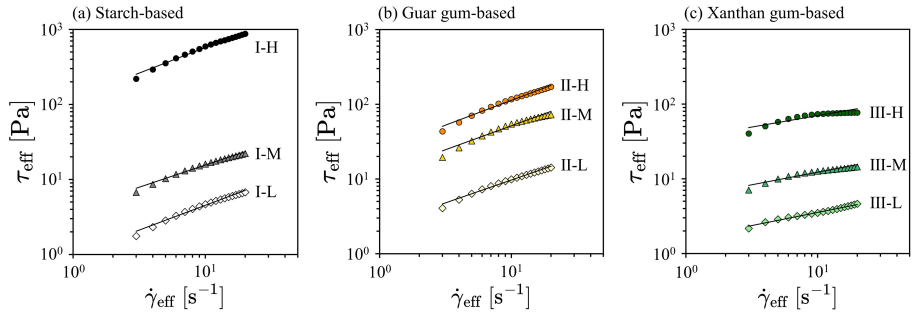


FIGURE 3.6: Flow curves obtained by USR for aqueous solutions of (a) starch-based, (b) guar gum-based, and (c) xanthan gum-based thickeners at 25 ∘C, where the oscillation parameters were set at f_o = 1.0 Hz and $\Theta = \pi/2$ rad. The symbols represent the types of solution and concentration, L, M, H for low, middle and high concentrations, respectively. Solid lines are the fitting results of the power law model.

Experimental setup and analytical procedures

Regarding the rheological measurement by USR, the experimental setup of USR is schematically shown in Fig. 3.5. An acrylic cylindrical vessel (radius: R = 72.5 mm; thickness: 2 mm; and height: 60 mm) filled with a test fluid was installed in the center of a water bath for the UVP measurement and temperature control. The vessel was driven by a stepping motor as the velocity of the cylindrical wall takes a sine wave (see § 2.3). The phase analysis of USR was adopted for evaluating the shear-rate-dependent effective viscosity $\mu_{\mathrm{eff}} = \rho\nu_{\mathrm{eff}}$. Flow curve $\tau_{\mathrm{eff}}(\dot{\gamma}_{\mathrm{eff}})$ is also obtained by the integral operation on $d\tau_{\mathrm{eff}} = \mu_{\mathrm{eff}} d\dot{\gamma}_{\mathrm{eff}}$ with a boundary condition of $\tau_{\mathrm{eff}}(\dot{\gamma}_0) = \tau_0 = \mu_{\mathrm{eff}}(\dot{\gamma}_0)\dot{\gamma}_0$, where τ_{eff} is the effective shear stress. In this thesis, numerical integration is performed with $\dot{\gamma}_0 = 3\ \mathrm{s}^{-1}$, which is the minimum shear rate on the viscosity curve $\mu_{\mathrm{eff}}(\dot{\gamma}_{\mathrm{eff}})$ evaluated by USR. In this definition of differential viscosity, the power law exponent n never takes a negative value even in the limited range of the shear rate.

Experimental procedures

The shear-rate-dependent rheological properties of the original solutions was investigated by USR before the addition of amylase. The cylindrical vessel was filled with each of the 1 L solutions, and the temperature of the solution was controlled at 25°C by a thermostatic chamber. The USR measurements were conducted with the oscillation parameters: f_o = 1.0 Hz and $\Theta = \pi/2$ rad to obtain the viscosity curves. Following the USR measurements of the original solutions, the stability after the addition of amylase was evaluated at the same temperature for the I, II – H, and III – H solutions. II and III solutions rarely react with amylase, so only the II – H and III – H solutions were evaluated as representative solutions. To allow the solution and the amylase to be mixed sufficiently, 200 mL of the solution was withdrawn from the vessel to a beaker and was stirred quickly and thoroughly with 2 mL of the amylase solution with a spatula for approximately 10 s. The solution was put back to the vessel and the whole solution was similarly stirred. Immediately after that, the oscillation of the vessel and the UVP measurements were performed for the USR test in 20 min. The spatiotemporal velocity profile was extracted every 10 s, and a flow curve was obtained for each time point.

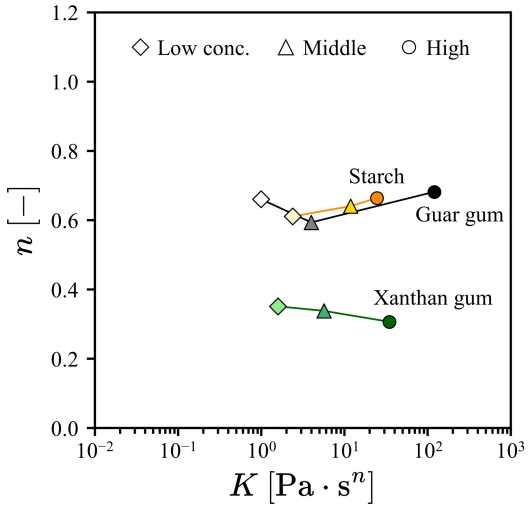


FIGURE 3.7: $K-n$ diagram converted from the flow curves in Fig. 3.6. The symbols represent the concentration of thickener.

Rheological properties of the original solutions

The flow curves obtained by USR before adding the amylase are shown in Fig. 3.6, where the axes represent the effective shear rate $\dot{\gamma}_{\mathrm{eff}}$ and the effective shear stress τ_{eff} in logarithmic scale. For quantitatively characterizing shear-rate-dependence of the rheological properties, power law fitting $\tau_{\mathrm{eff}} = K\dot{\gamma}_{\mathrm{eff}}^{n}$ was applied to the flow curves, where K and n represent the consistency index and power law exponent. The conditions of $n < 1$, $n = 1$, and $1 < n$ correspond to pseudo-plastic, Newtonian, and dilatant fluids, respectively. The shear-thinning property becomes more dominant as the value for n decreases. The fitting based on the model was conducted against each flow curve in Fig. 3.6 using the least squares method. The fitting is in good agreement in the experimental results. The obtained parameters were plotted on the typical $K-n$ space as shown in Fig. 3.7, which was originally proposed for practically characterizing shear-rate-dependence of viscosity and elasticity (Wagner et al., 2017). The symbols of different concentrations are connected for better visibility. For the starch and guar gum-based solutions, n takes almost the same value regardless of the concentration, meaning that there was little difference in the shear-thinning properties of these solutions before addition of amylase. The guar gum-based thickener, classified as the second generation thickener, had a better thickening effect per unit mass than the starch-based thickener, classified as the first generation thickener, because the K value of the $II-H$ (2.2 g per 100 mL) solution was larger than that of the $I-M$ (4.7 g per 100 mL) solution. The plotted points for the xanthan gum solutions were located at the far lower of the graph compared with the starch and guar gum solutions. Therefore, the xanthan gum solution has remarkable shear thinning property, which is tentatively a better condition for swallowing food (Nishinari et al., 2011; Nishinari et al., 2019).

Stability of the rheological properties after addition of amylase

The temporal changes of the flow curves after being mixed with amylase are shown in Fig 3.8. The symbols represent the elapsed time after the addition. For the starch-based solutions, the flow curves lowered over time as shown in Fig. 3.8(a),

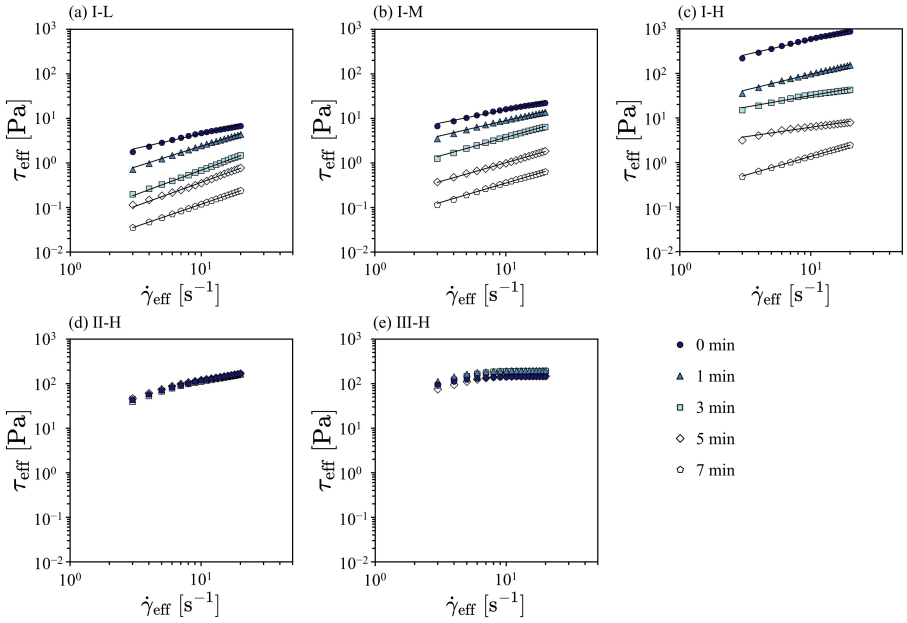


FIGURE 3.8: Instantaneous flow curves obtained by USR for the (a) I – L, (b) I – M, (c) I – H, (d) II – H, (e) III – H solutions at 25°C, where the oscillation parameters were f_o = 1.0 Hz and $\Theta = \pi/2$ rad. The symbols represent the elapsed time after being mixed with the amylase.

(b), and (c). Seven minutes after the addition of the amylase, the effective shear stress/viscosity of the starch-based solutions decreased to less than one-hundredth of the original values. In contrast, the flow curves of the II – H and III – H solutions were maintained over 7 min, indicating that the second and third generation thickeners were not affected by the amylase. Preliminary experiments indicated that the reaction proceeded uniformly in the vessel regardless of the radial position having a different shear rate amplitude. This is because the oscillatory shear flow in the vessel was under laminar conditions, where the stirring capacity was weaker than the turbulent conditions.

For quantitatively characterizing instantaneous shear-rate-dependence of the rheological properties, the power law fitting was applied to the flow curves, and the obtained parameters were plotted on the $K - n$ space as shown in Fig. 3.9. The shape of the symbols indicates the elapsed time after being mixed with the amylase, and the circles represent the time just before the addition. The symbols for different solutions with different concentrations are connected by lines for better visibility of the time variations. For the II – H and III – H solutions, the position of the plotted parameters does not change over time, indicating that mixing with amylase does not modify the rheological properties. The plot of the starch solutions (I), however, monotonically moved to the left with time elapsed. In addition, n approaches unity (Newtonian fluid) over time as an overall tendency. These indicate that the amylase changes the starch-based solutions to like pure water, increasing the risk of aspiration (Nagatoshi et al., 2001; Hasegawa et al., 2005; Kumagai et al., 2009; Tashiro et al., 2010).

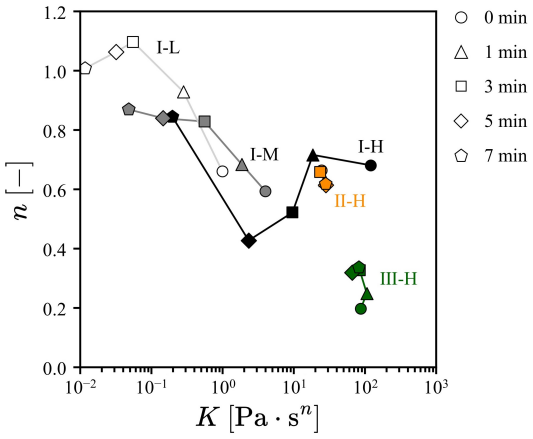


FIGURE 3.9: $K - n$ diagram converted from the viscosity curves in Fig. 3.8. The symbols represent the elapsed time after being mixed with amylase. The notions of I, II, III are for starch, guar gum, and xanthan gum-based solutions, and L, M, H are for low, middle, and high concentrations, respectively.

Advantage of the functional evaluation by USR

Food materials are generally in heterogeneous and exhibit markedly different properties depending on timescale, and these represent a vast majority of the real foods (Wagner et al., 2017; Nishinari et al., 2019). The changes in the polysaccharide aqueous solutions mentioned above over a period of several minutes may be able to be measured with a standard torque-type rheometer. However, the notable advantage of USR is its high applicability to heterogeneous fluids. The evaluation method base on USR will be applied to create a database of complex fluids, such as multi-phase and gel-sol coexistent fluids represented by porridge and yogurt, in which USR has a great advantage over ordinary torque-type rheometers. A data set of the time-resolved rheological properties of swallowed foods can be constructed on the $K - n$ space. In particular, porridge, which accounts for more than half of the calories in Japanese hospital food, loses its viscosity through hydrolysis. At what time the rheological properties of porridge decrease can be evaluated using the developed method. This method can assess how long the addition of a thickener can extend the time sustaining the original properties. In addition, *in vivo* measurements are required in parallel with these evaluations through the $K - n$ diagram for elucidating the area where safe swallowing food is in. The last thing to emphasize in this section is that a food bolus is subjected to not only shear but also extensional flows during swallowing process. Elongational and yielding properties also provide important insights on the dynamics of food bolus represented by cohesiveness (Nishinari et al., 2019; Hadde and Chen, 2019; Ross et al., 2019; Tobin et al., 2020). Combining extensional viscosity and yield stress measurements in addition to the evaluation by the present USR will lead better understanding bolus dynamics of heterogeneous foods in non-equilibrium conditions.

Chapter 4

Multi-timescale rheology

Rheological properties of non-Newtonian fluid change depending on the applied shear intensity but also its unsteadiness such as oscillation frequency. Almost all the materials behave like liquids against a steady shear, in contrast, solids against a rapid deformation. In § 4.1, rheology mapping is introduced for comprehensively evaluating dependence of viscoelasticity on both shear intensity and its unsteadiness. It is demonstrated with some typical polymer aqueous solutions. In § 4.2, the rheology mapping is further applied to rheology of dilute bubble suspensions in unsteady shear flows. The effect of parallel combined steady and oscillatory shear on the viscoelasticity is also investigated using the rheology mapping.

4.1 Rheology mapping

Nevel map representation termed rheology mapping is proposed for comprehensively evaluating the dependence of viscoelasticity on applied shear deformation and shear timescale represented by the oscillation frequency. Basic concept for the mapping is firstly explained with some ideal examples. The mapping is applied to three typical kinds of polymer solutions. They are polyvinylpyrrolidone (PVP) in § 4.1.1, carboxymethyl cellulose (CMC) in § 4.1.2, and polyacrylamide (PAM) in § 4.1.3, which are well known as a viscous dominant, shear thinning, viscoelastic fluid, respectively. In the end of each section, considerations associating the macroscopic rheological properties with microscopic dynamics of polymer coils are denoted.

The USR makes it possible to evaluate the viscoelasticity with shear rate dependence even with fixed oscillation parameters (f_o, Θ), because of the radial distributions of the shear rate amplitudes in the cylindrical vessel. The frequency dependence of the viscoelasticity can then be evaluated effectively by step-wise increases in the oscillation frequency f_o. The maximum angle of rotation Θ corresponding to a f_o is set so that the maximum wall velocity U_{wall} is a constant under all of the f_o conditions. The following rheology mapping is proposed as a method to disassemble the complex data in the information of the viscoelasticity obtained by the above series of experimental operations. The viscosity coefficient μ_e and phase difference δ are summarized by contours on a two-dimensional map in which the axes correspond to f_o and the effective shear rate $\dot{\gamma}_{eff}$, respectively (Fig. 4.1). Note that μ_e and E_e are constants that characterize the amplitude ratio and phase relationship of the shear rate and stress for one oscillation period, and are not defined by the instantaneous shear rate and stress. These are however allowed to change depending on the shear rate amplitude and frequency. The relation $\dot{\gamma}_{eff} = 2\pi f_o \gamma_{eff}$ holds along $\dot{\gamma}_{eff}$, f_o and the effective shear strain γ_{eff}. The group of contour curves of γ_{eff} matches a group of straight lines passing through the origin of the map. A contour approaches

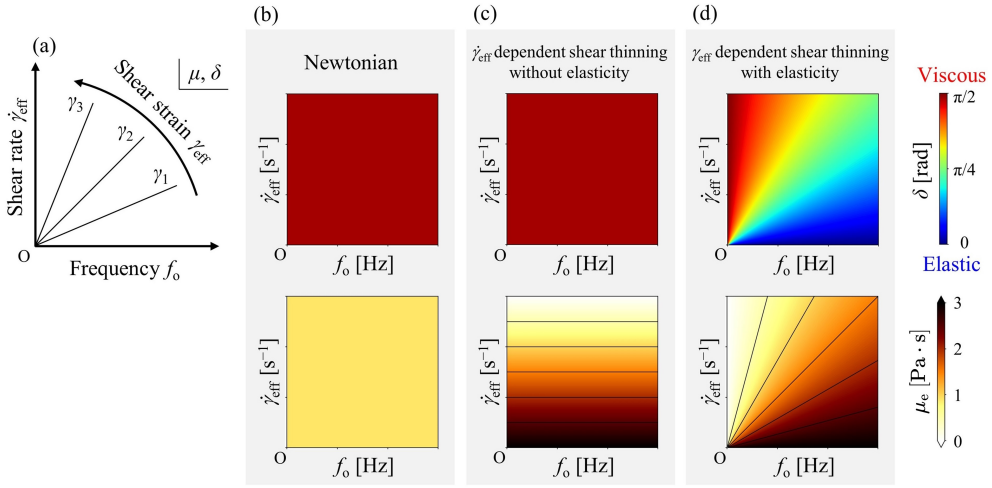


FIGURE 4.1: The concept of the rheology mapping for evaluating the dependence of viscoelasticity on shear rate $\dot{\gamma}_{\mathrm{eff}}$, strain γ_{eff}, and frequency f_o: (a) Definition of each axis, and three ideal examples showing simplified rheological properties as (b) Newtonian, (c) shear thinning without elasticity, and (d) γ_{eff}-dependent shear thinning with elasticity.

the vertical axis as γ_{eff} increases. The map therefore is a comprehensive expression of the dependence of the viscoelasticity on $\dot{\gamma}_{\mathrm{eff}}$, γ_{eff}, and f_o. In the map, the vertical axis given by the present rheology mapping is $\dot{\gamma}_{\mathrm{eff}}$, while the Pipkin diagram (Pipkin, 2012) adapts strain amplitude and frequency for the axes.

For ease of understanding the rheology mapping, three ideal examples showing simplified rheological properties as Newtonian, shear-thinning without and with elasticity are considered and presented in Fig. 4.1(b)-(d). The first example showing a Newtonian viscosity will be represented as a monochrome in both the map representations of δ and μ_e as shown in Fig. 4.1(b). The second example showing shear-thinning without elasticity is represented as colored map patterns in Fig. 4.1(c). The monochrome in the map of δ means that the fluid is purely viscous regardless of the values of $\dot{\gamma}_{\mathrm{eff}}$, γ_{eff}, and f_o, while the color variations in the map representing μ_e expresses shear-thinning characteristic. The third example showing shear-thinning with elasticity is represented as the colored map patterns in Fig. 4.1(d). In this ideal case, viscoelasticity varies from elastic to viscous essentially as γ_{eff} increases. The color variations in the map representation of μ_e expresses the γ_{eff}-dependent shear-thinning characteristic. In this way, the dependence of viscosity and degree of viscoelasticity can be directly and comprehensively identified.

4.1.1 Viscous dominant fluid (Polyvinylpyrrolidone)

Test materials

Polyvinylpyrrolidone (PVP) aqueous solutions (Molecular weight: 3.6×10^5 g/mol, Tokyo Chemical Industry Co. Ltd., Japan) with different concentrations from 4 wt.% to 20 wt.% in increments of 2 wt,% were chosen as test fluids. The solutions have been reported to be Newtonian in steady shear flow, while viscoelasticity emerges in oscillatory shear flow depending on applied shear rate and frequency (Seo, Kang, and Lee, 2014). Dependence of viscosity on the concentration and boundary between

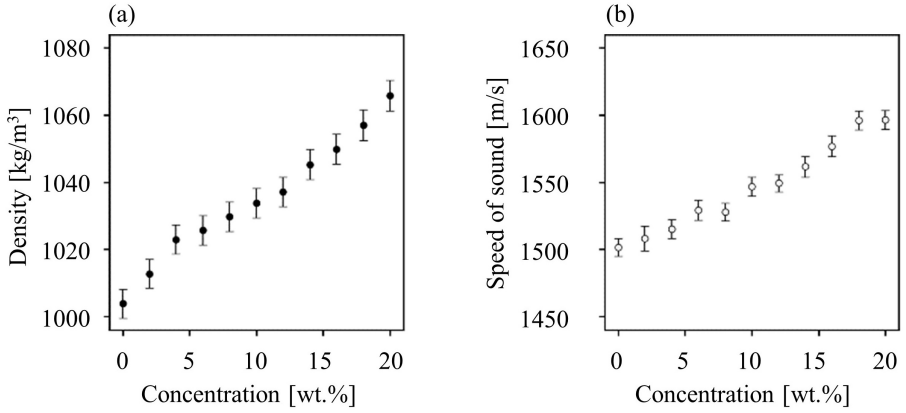


FIGURE 4.2: Basic properties of the PVP aqueous solutions with different concentrations: (a) Dnesity and (b) speed of sound.

the conditions where the solutions behave viscous or viscoelastic, are revealed by the present rheology mapping.

Fine spherical particles (density: 1/01 g/mL, diameter: 75 – 150 μm, CHP 20P, Mitsubishi Chemical Co. Ltd., Japan) were mixed a little to the solutions as tracer particles for the UVP measurement. Temperature of the solutions was kept at 25°C in all the experiments by thermostatic chamber. The dependence of fluid density and speed of sound v_s on the concentration was preliminary measured, which is necessary parameter for the UVP measurement. They monotonically increase with the concentration as shown in Fig. 4.2. Therefore, bulk modulus K, which is calculated by $K = \rho {v_s}^2$ also increases monotonically with the concentration. The solutions hence become solidity with increasing the concentration.

Viscosity-concentration function

Dependence of the effective viscosity on the concentration is firstly revealed by the phase analysis in an oscillatory shear flow with a low oscillation frequency regarding a nearly steady shear flow. Spatiotemporal velocity distribution obtained by the UVP measurement is shown in Fig. 4.3, where the oscillation parameters are $f_o = 0.5$ Hz and $\Theta = \pi$ rad. Horizontal and vertical axes represent the oscillation period and the normalized radial position. It is confirmed that oscillatory shear flow propagates from the wall toward center of the vessel, accompanying a phase lag. With increasing the concentration, radial slope of the phase lag decreases and thickness of viscous layer on the wall increases, meaning that the effective viscosity μ_{eff} increases with the concentration. The radial range where the velocity intensity is sufficiently large compared to the velocity resolution of UVP is utilized for the following phase analysis.

Results of the phase analysis on the velocity distributions are shown in Fig. 4.4(a). All the effective viscosity curves are horizontal and monotonically shift up with increasing the concentration. The solutions are therefore assumed as Newtonian whose viscosity is uniquely determined by the concentration in the low frequency oscillatory shear flow. To investigate the relation between the viscosity and concentration more specifically, representative viscosity μ_{rep} is defined as the average value of the viscosity curve for each concentration and summarized in Fig. 4.4(b). The

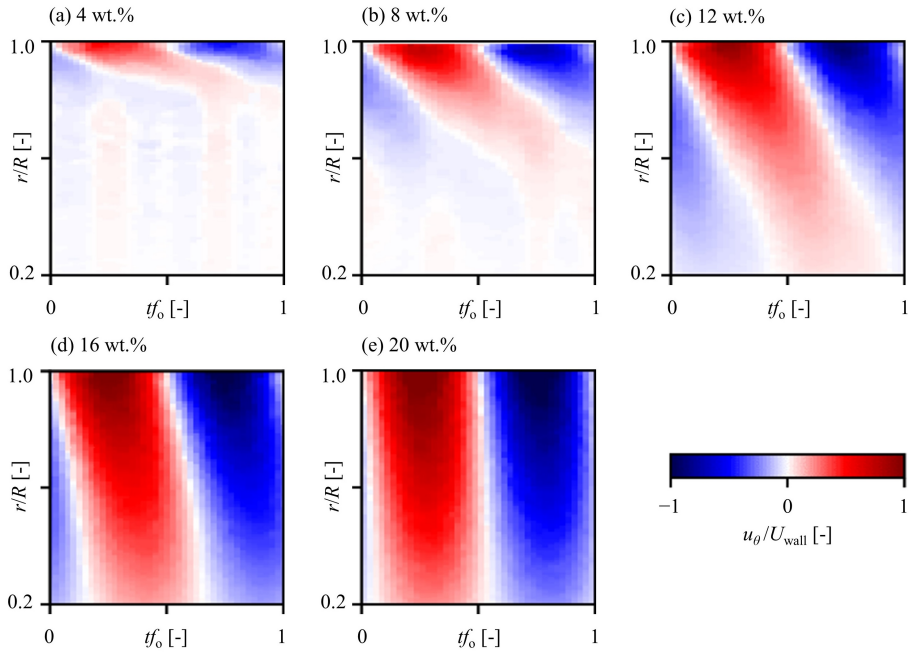


FIGURE 4.3: Spatiotemporal velocity distributions obtained by UVP for PVP aqueous solutions with different concentrations, where oscillation parameters are given as f_o = 0.5 Hz and $\Theta = \pi$ rad.

plots completely regress to Martin equation (Macosko, 1994), an empirical equation correlating the viscosity coefficient μ with the concentration c,

$$\frac{\mu - \mu_s}{\mu_s c} = [\mu]\exp\left(K_M c[\mu]\right), \tag{4.1}$$

where μ_s represents viscosity coefficient of the solvent. For the PVP solutions, μ_s is equivalent to viscosity coefficient of pure water at 25°C, 0.89 Pa·s. Parameters $[\mu]$ and K_M are intrinsic viscosity and Martin's coefficient, which depend on the polymer-solvent system. The fitting result based on the least squares method, they are estimated as $[\mu]$ = 2.16 wt.% and K_M = 0.12. Comparing with other typical polymer solutions such as carboxymethyl cellulose, which are generally known as shear thinning fluids (Benchabane and Bekkour, 2008; Kulicke and Porter, 1980), molecular weight of the PVP solution is less than half. It is therefore considered that the PVP solutions are difficult to form shear induced structures and the viscosity does not have shear rate dependence in the low frequency oscillatory shear flows. Since the internal structure can be modeled easily and reasonably, it seems to be in good agreement with Martin equation and theoretical formulae.

Application of rheology mapping

Rheology mapping was applied to the solutions for comprehensively evaluating the viscoelasticity with respect to applied shear deformation and shear timescale. Results of the solutions with three concentrations are representatively shown in Fig.4.5. Upper three panels indicate distribution of viscosity coefficient μ_e and lower ones do distribution of the phase difference of viscoelasticity δ. Firstly as for the 8 wt.% solution, viscosity is almost Newtonian for f_o < 1.0 Hz as shown in Fig. 4.5(a). On the other hand, for the opposite condition f_o > 1.0 Hz , μ_e monotonically decreases

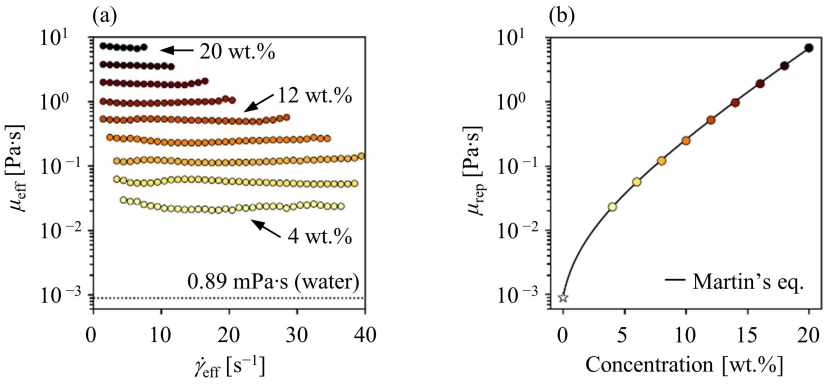


FIGURE 4.4: Phase analysis for the PVP aqueous solutions with different concentrations, where oscillation parameters are f_o = 0.5 Hz and $\Theta = \pi$ rad: (a) Effective viscosity curves and (b) relation between concentration and representative viscosity μ_{rep}.

as $\dot{\gamma}_{\mathrm{eff}}$ increases, indicating shear-thinning property. The distribution in Fig. 4.5(b) shows that there is a clear boundary between viscous and viscoelastic regions indicated by the dotted line. Elasticity completely disappears when a certain shear rate is applied to the solution for each f_o as deformability of polymer coils or entanglements of them contributing elasticity is yielded. As for the 12 wt.% and 16 wt.% solutions, shear-thinning properties remarkably emerges for $f_o > 2.0$ Hz as shown in Fig. 4.5(b) and (c), which is higher frequency than that for the 8 wt.% solution. Furthermore, degree of the shear-thinning is weakening when comparing with that of 8 wt.% solution. As for the δ distributions in Fig. 4.5(d)-(f), boundaries between viscous and viscoelastic regions shift to lower $\dot{\gamma}_{\mathrm{eff}}$ and higher f_o directions on the map. The PVP solutions approach Newtonian as the concentration increases.

Consideration from microscopic view

Possible explanations for the macroscopic rheological properties revealed by the current rheology mapping are given here associating with microscopic dynamics of polymer coils. The solutions with all the concentrations are regarded as Newtonian fluid in the low frequency oscillatory shear flow as revealed, while shear-thinning property gradually emerges as f_o increases. It is remarkable at higher frequency than 1.0 Hz for the 8 wt.% and 2.0 Hz for the 16 wt.%. Main factors of shear-thinning property are shear induced structures such as stretch and orientation of polymer coils dissolved in water, making fluid resistance lower in microscopic view. In oscillatory shear whose timescale $1/f_o$ is longer than relaxation time of the polymer coils, the structures are difficult to be established as stretched polymer coils restore the original state in one oscillation cycle. On the other hand, in the opposite condition, stretched polymer coils enter the next oscillation cycle without sufficient time to restore the original state. As a result, the polymer coils stay stretched for a longer period than that in the previous conditions. Boundaries of f_o between Newtonian and shear thinning are 1.0 Hz and 2.0 Hz for 8 wt.% and 16 wt.%, therefore relaxation time of these fluids are estimated to be $1/(1.0\ \mathrm{Hz}) = 1.0$ s and $1/(2.0\ \mathrm{Hz}) = 0.5$ s, respectively. This is the exact opposite of general knowledge that the relaxation time increases with the concentration. A possible explanation is that polymer coils do not form complex entanglements, but rather form contraction as the concentration increases. In addition, one considerable reason for weakening shear thinning property

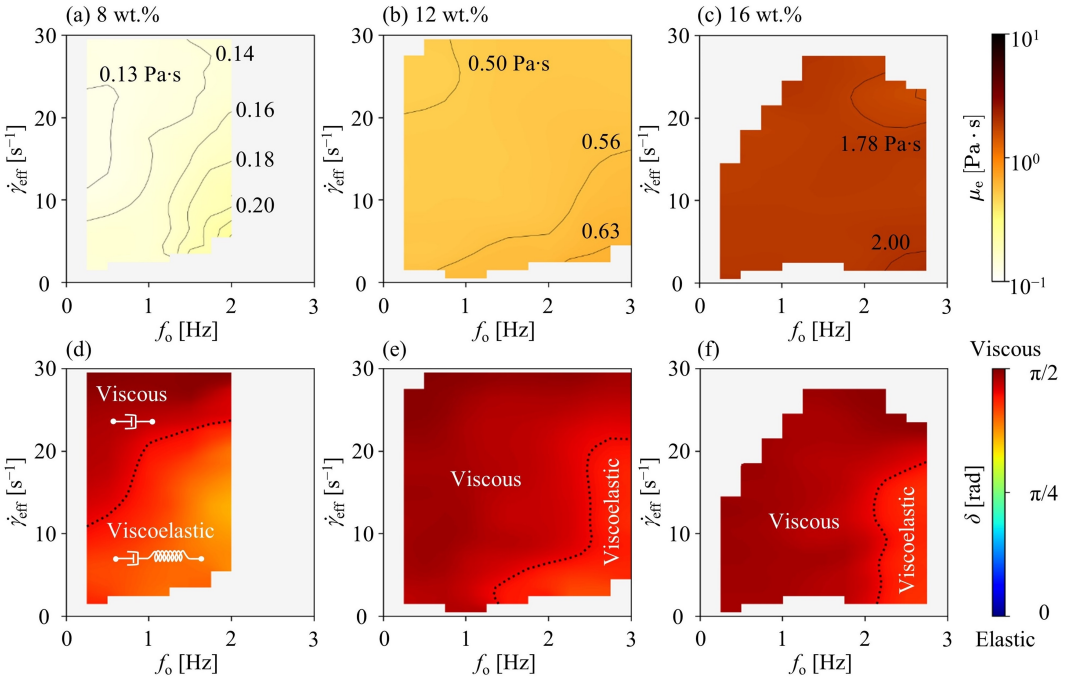


FIGURE 4.5: Rheology mapping for the PVP solutions with different concentrations: Upper and lower panels respectively indicate the distribution of the viscosity coefficient μ and phase differences δ.

with increasing the concentration is that the shear induced structures of polymer coils are difficult to be established as the polymer coils are strongly restrained to each other under increased number of the contracted coils. In three lower panels in Fig. 4.5, boundaries between viscous and viscoelastic regions are clearly shift to higher f_o and lower $\dot{\gamma}_{\mathrm{eff}}$ directions. In the PVP solution with the low concentration 8 wt.%, deformability of the coils and entanglements of them contributes elasticity in wide area on the map. On the other hand, viscoelasticity disappears as the concentration increases, meaning that the thickening effect by the increased number of polymer coils is more dominant than the elasticity.

4.1.2 Shear-thinning fluid (Carboxymethyl cellulose)

Test materials

The second test fluids are carboxymehyl cellulose (CMC) aqueous solution (Daicel Miraizu Co. Ltd., Japan, Molecular weight: 2.0×10^6 g/mol), which are widely used as a thickener in cosmetics and pharmaceuticals. The rheological properties of the solution have been evaluated by standard torque-type rheometers in many reports (Benchabane and Bekkour, 2008; Kulicke and Porter, 1980; Ghannam and Esmail, 1997), and the efficacy of the measurements has also been examined by visualizing the flow in the narrow gap of a rhemeter (Yoshida, Tasaka, and Murai, 2019b). The CMC solution is generally known as purely viscous and shear thinning fluid. In the present study, CMC aqueous solutions in three different concentrations (0.5, 1.0 and 1.5 wt.%) are examined to investigate how variations of the concentration are represented by the rheology mapping. The properties identified in the previous studies will be detailed with the map, and additional characteristics discovered in the comprehensive evaluation will be discussed. In the experiments, small amounts

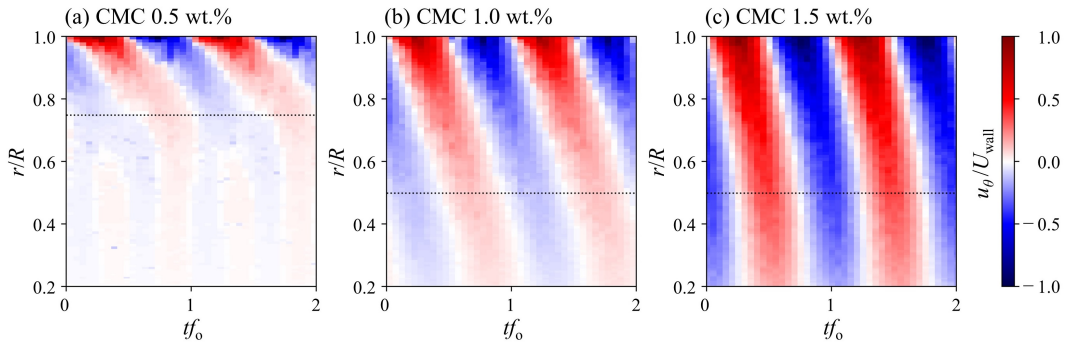


FIGURE 4.6: Spatiotemporal velocity distributions obtained by UVP for the CMC solutions with different concentrations: (a) 0.5 wt.%, (b) 1.0 wt.%, and (c) 1.5 wt.%, for the set oscillation parameters of f_o = 1.0 Hz and $\Theta = \pi/2$ rad.

of fine spherical particles (CHP20P, Mitsubishi Chemical Co. Ltd., Japan), of density 1.01 g/mL and mean diameter 75 – 150 μm, are mixed a little into the test fluids as tracer particles for the UVP measurements. The added particles have weak chemical reactivity so as not to affect the rheological properties.

Application of rheology mapping

The CMC solutions with different concentrations (0.5, 1.0, 1.5 wt.%) were prepared in the cylindrical vessel. For the different frequencies f_o applied to the vessel, the flow velocity distributions were measured by the UVP, and the rheological properties were evaluated with the procedures of the USR. At the oscillation parameters (f_o = 1.0 Hz and $\Theta = \pi/2$ rad, U_{wall} = 760 mm/s), Fig. 4.6 indicates the time variations of instantaneous radial profile of u_θ. The axes show the cycle periods of the oscillation and the normalized radial coordinates, while the contours represent the measured velocity in the azimuthal direction. These spatiotemporal distributions show that the oscillatory shear flow driven by the cylindrical wall (r/R = 1.0) propagates toward the central axis with a time delay (diagonal patterns on the distribution) and attenuation (lowering in the velocity amplitude away from the wall). For the 0.5 wt.% CMC solution the flow is established at $r/R > 0.75$, as the thickness of a viscous layer at the cylinder wall. The degree of the time delay and attenuation decreases as the CMC concentration increases: The viscosity increases as the concentration increases.

The rheological properties of the CMC solutions were examined for different concentrations (0.5, 1.0, 1.5 wt.%) following the procedures of the USR as explained before. The radial range for the rheological evaluation is indicated by the dotted lines in Fig. 4.6, where the distinct velocity fluctuations due to the cylinder oscillation is obtained by the UVP. The results of the rheology mapping for the CMC solutions are summarized in Fig. 4.7. The upper and lower panels respectively indicate the phase lag δ and the viscosity coefficient μ_e, represented by the contour. Since the thickness of viscous layer is too small to evaluate the properties considering the spatial resolution of the UVP, the rheological evaluations are limited to within 1.0 and 2.0 Hz in the 0.5 and 1.0 wt.% solutions, respectively.

The phase lag δ in the 0.5 wt.% case in Fig. 4.7(a) shows a purely viscous behavior at the $f_o < 0.5$ Hz range and changes to viscoelastic fluid at the opposite condition.

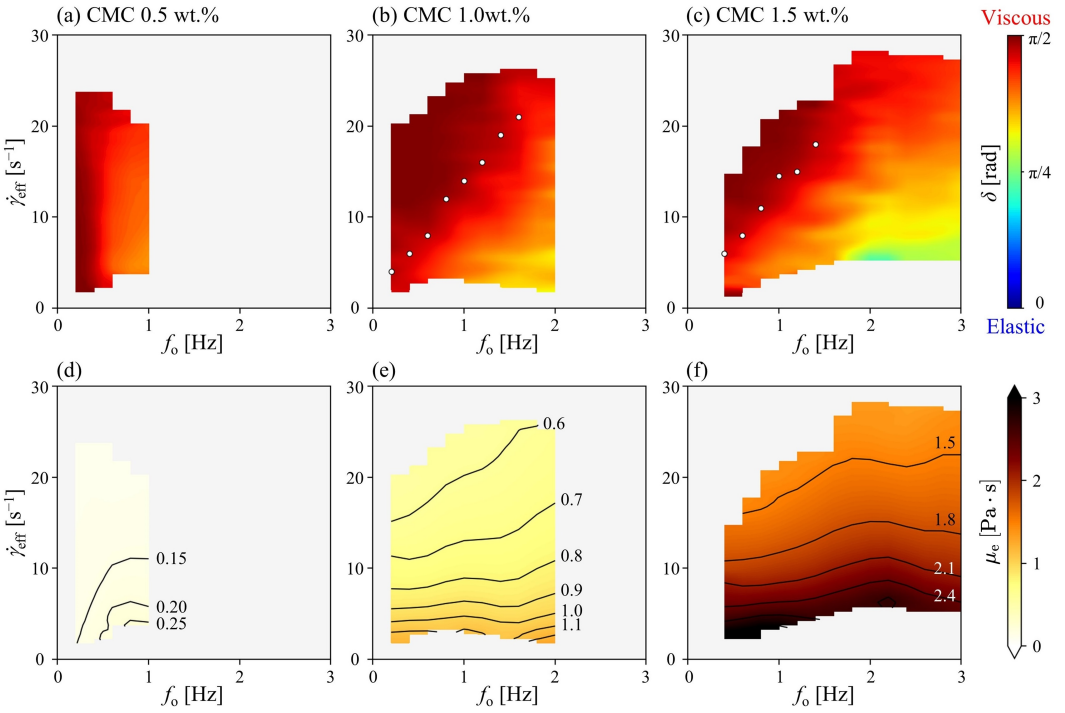


FIGURE 4.7: Rheology mapping for CMC solutions with different concentrations: (a)-(c) and (d)-(f) indicate the distribution of phase differences δ and viscosity coefficients μ_e, respectively. White dots in (b) and (c) represent the critical shear rate $\dot{\gamma}_{eff,c}$ at each oscillation frequency f_o.

In Fig. 4.7(d), μ_e assumes a constant value at the lowest frequency f_o = 0.2 Hz, representing a Newtonian-like fluid behavior, and shear-thinning characteristic emerges weakly as f_o increases.

At the higher concentrations, 1.0 and 1.5 wt.%, δ widely varies depending on f_o and $\dot{\gamma}_{eff}$. The CMC solutions are generally seen as purely viscous fluids, but the results also express the elasticity as depending on f_o and $\dot{\gamma}_{eff}$. White dots superimposed on the panels in Figs. 4.7(b) and (c) represent the critical shear rates $\dot{\gamma}_{eff,c}$, showing $\delta \approx \pi/2$ rad at each f_o. The critical shear rates are re-plotted in Fig. 4.8 with the standard deviations. These plots form a straight line passing through the origin of the map, corresponding to a contour line for the effective shear strain γ_{eff}. The critical shear strains determined by the least squares method are $\gamma_{eff,c}$ = 210% and 206% at the 1.0 and 1.5 wt.% concentrations, respectively without any significant difference between the two values. The solutions completely lose elasticity when γ_{eff} exceeds $\gamma_{eff,c}$.

Focusing on the distributions of μ_e for the 1.0 and 1.5 wt.% solutions as shown in Fig. 4.7(e) and (f), the shear-thinning characteristic is confirmed at any f_o. It is notable that the contour lines of μ_e are generally horizontal meaning that the viscosity strongly depends on $\dot{\gamma}_{eff}$, and not on γ_{eff} and f_o. These remarkable characteristics will be discussed later with the results of the polyacrylamide aqueous solutions denoted in the following section.

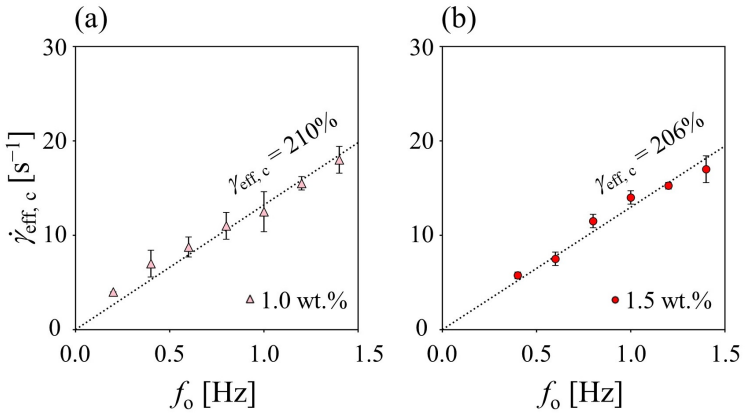


FIGURE 4.8: Deviation of the critical shear rate $\dot{\gamma}_{\mathrm{eff,c}}$ at various oscillation frequencies f_o for CMC solutions with different concentrations: (a) 1.0 wt.% and (b) 1.5 wt.%; the error bars indicate standard deviations and the dotted lines are the regression curves $\dot{\gamma}_{\mathrm{eff,c}} = 2\pi f_o \gamma_{\mathrm{eff,c}}$ for determining the critical shear strain $\gamma_{\mathrm{eff,c}}$.

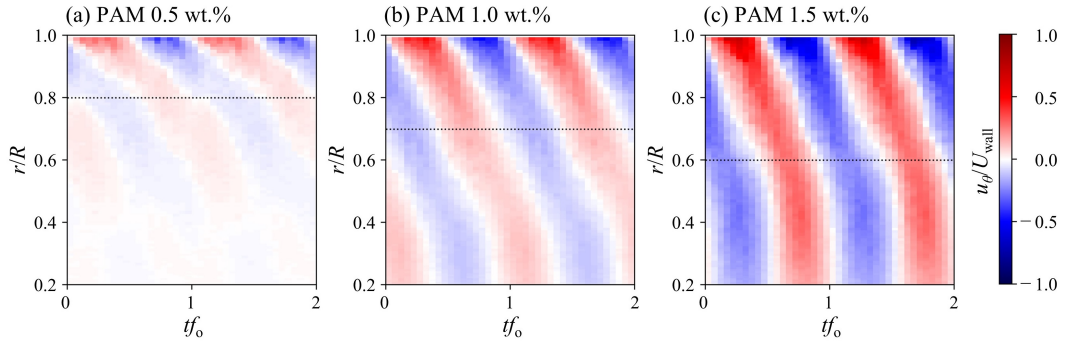


FIGURE 4.9: Spatiotemporal velocity distributions obtained by the UVP measurement in PAM solutions with different concentration: (a) 0.5 wt.%, (b) 1.0 wt.%, and (c) 1.5 wt.%, for the set parameters, f_o = 1.0 Hz and $\Theta = \pi/2$ rad.

4.1.3 Viscoelastic fluid (Polyacrylamide)

Test materials

The third test fluids are polyacrylamide (PAM) aqueous solution (MT AquaPolymer Co. Ltd., Japan, Molecular weight: 1.3×10^7 g/mol). The molecular weight is 6.5 times that of the CMC. The PAM solution is generally regarded as viscoelastic and shear-thinning fluid (Lewandowska, 2007; Ghannam and Esmail, 1998). In the PAM solution, shear banding occurs even inside the narrow gap of standard rheometers. Careful attention therefore must be paid to the specifics of the measurements, to ensure that inaccuracies in the evaluated viscoelasticity are accounted for. On the other hand, USR is useful with such complex fluids as it determines actual profiles of shear rates in the evaluation of viscoelasticity. As with the CMC solutions, PAM aqueous solutions with three different concentrations (0.5, 1.0 and 1.5 wt.%) are examined here. Similar to the previous PVP and CMC aqueous solutions, a small amount of fine spherical particles (CHP 20P) are suspended for the UVP measurements.

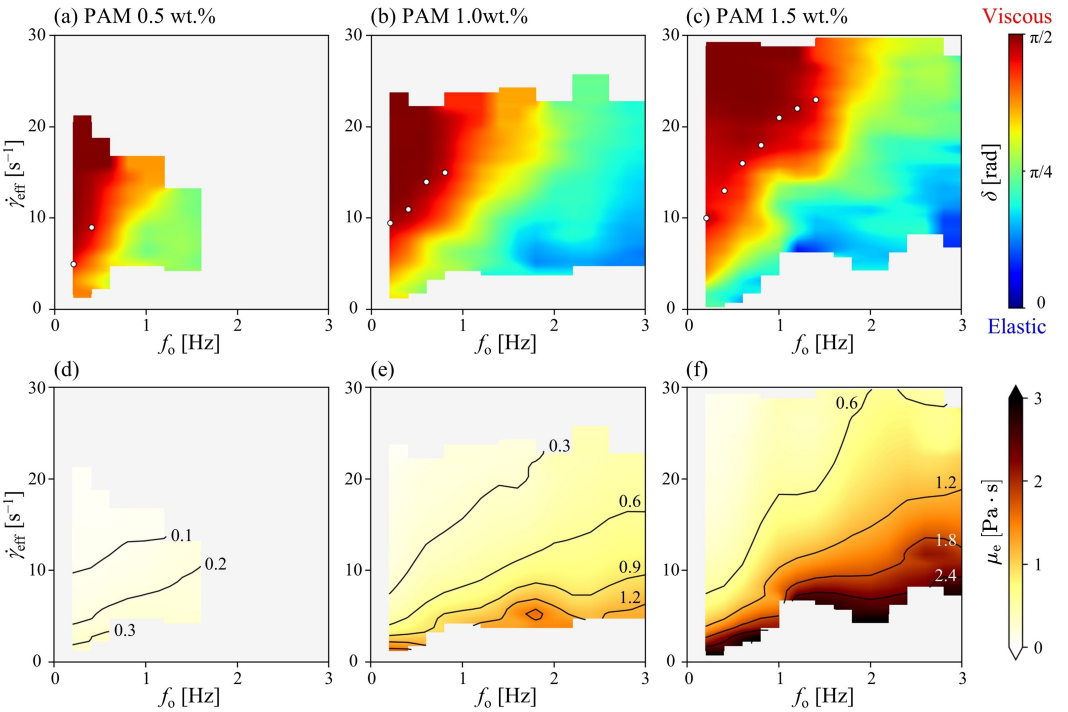


FIGURE 4.10: Rheology mapping for PAM solutions with different concentrations: (a)-(c) and (d)-(f) indicate distributions of the phase difference δ and viscosity coefficient μ_e, respectively. White dots in (a)-(c) represent the critical shear rate $\dot{\gamma}_{\mathrm{eff,c}}$ at each oscillation frequency f_o.

Application of rheology mapping

The PAM solutions with different concentrations (0.5, 1.0, 1.5 wt.%) are examined. The spatiotemporal velocity distributions were measured as shown in Fig. 4.9, where the oscillation parameters are representatively given as f_o = 1.0 Hz and $\Theta = \pi/2$ rad. Compared with the distributions in the CMC solutions in Fig. 4.6, those of the PAM solutions are clearly different. The oscillatory shear flow propagates without any phase lag near the central axis as shown in Fig. 4.3(b) and (c), showing that the solutions are subject to a yield stress. The radial range for the rheological evaluation is indicated by the dotted horizontal lines in Fig. 4.3, at which the solutions display fluidity, and distinct velocity fluctuations driven by the cylinder oscillations are obtained by the UVP.

The results of the rheology mapping with the PAM solutions are shown in Fig. 4.10. In the 0.5 wt.% solution, viscoelasticity clearly appears at the $f_o > 0.8$ Hz range in Fig. 4.10(a), while the CMC solution with the same concentration is viscous with weak elasticity as shown in Fig. 4.7(a). Focusing on the distribution of μ_e in Fig. 4.10(d), the shear-thinning characteristics appear at all f_o values, and there are no Newtonian regions like those observed in the CMC solution with the same concentration.

In the 1.0 and 1.5 wt.% solutions in Fig. 4.10(b) and (c), the measurable range in f_o is widened because of the increased apparent viscosity of the solutions. In these two solutions, the dominant region of elasticity is wider than that of the 0.5 wt.% solution at the $f_o > 1.0$ Hz range. It must be noted that δ approaches $\pi/2$ rad (i.e. purely viscous) as the effective shear strain γ_{eff} increases. Although the PAM solution is generally known as a viscoelastic fluid, it changes to purely viscous with

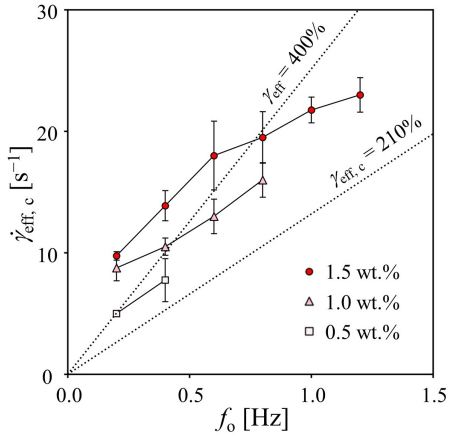


FIGURE 4.11: Deviation of the critical shear rate $\dot{\gamma}_{\mathrm{eff,c}}$ at each oscillation frequency f_{o} for PAM solutions with different concentrations, error bars indicate standard deviations. The lower dotted line represents the critical shear strain $\gamma_{\mathrm{eff,c}}$ = 210% evaluated in the CMC solutions (Fig. 4.8).

increasing γ_{eff}. As also mentioned in Sec. 4.1.2, the viscoelasticity shifts from viscous to elastic in a wide range of the map. The critical shear rates $\dot{\gamma}_{\mathrm{eff,c}}$ in Fig. 4.10(a)-(c) are re-plotted in Fig. 4.11 with the standard deviations. The graph shows that $\dot{\gamma}_{\mathrm{eff,c}}$ increases as the concentration increases. Compared with the $\dot{\gamma}_{\mathrm{eff,c}}$ of the CMC solutions as shown in Fig. 4.8, that of the PAM solutions assumes larger values with around 400% (Fig. 4.11).

Focusing on the distributions of μ_{e} for the 1.0 and 1.5 wt.% solutions in Fig. 4.10(e) and (f), the pattern of the contour lines is very different from that of the CMC solutions in Fig. 4.7(e) and (f). While that of the CMC solutions is horizontal, that of the PAM solutions can be regarded as forming a group of lines which almost all pass through the origin, corresponding to a group of contour lines for γ_{eff}. The viscosity of the PAM solutions therefore strongly depends on γ_{eff}.

Consideration from microscopic view

The rheological properties displayed by the rheology mapping are discussed here in association with the microscopic dynamics of polymer coils. For the 0.5 wt.% CMC solution in Fig. 4.7(d), the $\dot{\gamma}_{\mathrm{eff}}$ dependence of μ_{e} clearly shifts from Newtonian towards shear-thinning at around f_{o} = 0.5 Hz. The major causes of the shear thinning characteristics in polymer solutions are generally explained by shear induced structures such as disentanglement, stretch, or increases in the orientation of the polymer coils in the direction of the shear (Schramm et al., 1994; Krishnan, Deshpande, and Kumar, 2010; Rao, 2013). The 0.5 wt.% concentration CMC solution is estimated to be in a semi-dilute non-entangled regime (Benchabane and Bekkour, 2008), that is, the dispersed polymer coils in the water are individually dispersed without contact each other. Under oscillatory shear flows, the difference between the timescale of the oscillatory shear flow t_{f} (i.e. reciprocal of the oscillation frequency f_{o}) and the major relaxation time t_{r} of the polymer coil would determine the characteristic shift from a Newtonian to a non-Newtonian regime. When t_{f} is shorter than t_{r}, the dispersed polymer coils always keep stretched, due to insufficient relaxation during a single

oscillation cycle. The degree of the stretch affects the flow resistance viewed microscopically according to Dunstan, Hill, and Wei (2004). The shear-thinning characteristics observed at the range of $f_o > 0.5$ Hz in Fig. 4.7(d) may then be considered as a result of the stretching of the dispersed polymer coils, whose degree of the stretching depends on $\dot{\gamma}_{eff}$. Under the opposite condition ($t_f > t_r$), the viscosity coefficient is not dependent on $\dot{\gamma}_{eff}$ due to insufficient stretching of the polymer coil, that is, the shear induced structure is not maintained throughout the oscillation cycle. As the result, the 0.5 wt.% concentration CMC solution has Newtonian regime in the region of $f_o < 0.5$ Hz in Fig. 4.7(d). These considerations are also supplemented by the results shown in Fig. 4.7(a), indicating the clear boundary between purely viscous and viscoelastic at $f_o = 0.5$ Hz.

With higher concentrations of the CMC solutions (1.0 and 1.5 wt.%), shear-thinning characteristic emerges at all the f_o conditions. As the concentration increases, polymer coils become overlapped (Graessley, 1980), and form enhanced segments of polymer coils, accompanying increased relaxation times of the segments. The boundary between the Newtonian and shear thinning regimes suggested at 0.5 Hz in Fig. 4.7(d), therefore, shifts to the lower frequency side, and no Newtonian regime is observed in Figs. 4.7(e) and (f). In addition to the shear-thinning characteristic observed at all f_o, it is notable that the viscosity of the CMC solutions with 1.0 and 1.5 wt.% concentrations strongly depends on $\dot{\gamma}_{eff}$ as mentioned in Sec. 4.1.2. It was experimentally confirmed that orientation and distortion of a polymer coil vary depending on the applied shear rate and that this causes the shear-thinning characteristic in steady shear flows (Dunstan, Hill, and Wei, 2004). This also holds for the oscillatory shear flow and the viscosity of the CMC solutions depend most strongly on $\dot{\gamma}_{eff}$, and less or not on γ_{eff} and f_o as shown in Figs. 4.7(e) and (f). In addition, it is notable that the 1.0 and 1.5 wt.% concentration CMC solutions have almost the same critical shear strain as shown in Fig. 4.8. This means that the polymer coil yields or entanglement of them is resolved, and elasticity does not develop when γ_{eff} approaches $\gamma_{eff,c}$. As the concentration increases, the number of entanglements between polymer coils increases and greater stress is required to disentangle the structures (Kulicke et al., 1996). It must be noted, however, that the shear strain required for the disentanglement does not depend on the concentration as shown by the results in Fig. 4.8. This is a new finding, and one that can be read from the novel representations by the rheology mapping in Figs. 4.7(b) and (c).

For the 0.5 wt.% concentration PAM solution, shear-thinning characteristic is confirmed at all the f_o conditions as shown in Fig. 4.10(d), while the CMC solution with the same concentration shows the clear shift from Newtonian to shear-thinning characteristic at $f_o = 0.5$ Hz as shown in Fig. 4.7(d). Molecular weight of the PAM is 6.5 times that of the CMC, polymer coils in the 0.5 wt.% PAM solution therefore have longer relaxation times than those of the 0.5 wt.% CMC solution. The boundary between the Newtonian and shear-thinning regimes shifts to the lower frequency side than $f_o = 0.5$ Hz and no Newtonian regime is observed. As for the δ distribution shown in Fig. 4.10(a), δ takes lower values than that of the CMC solutions in Fig. 4.10(a)-(c) at each f_o and $\dot{\gamma}_{eff}$. Viscoelasticity is more pronounced in the PAM solution. When the molecular weight increases, the elastic effect of the entanglement and the polymer coil itself is stronger than the thickening effect of the number of polymer coils.

With more concentrated PAM solutions (1.0 and 1.5 wt.%), it is notable that μ_e decreases as γ_{eff} increases. This trend is also observed in the δ distributions as shown in Figs. 4.10(e) and (f). The strong dependence of μ_e and δ on γ_{eff} can be understood as an effect of the disentanglement of the polymer coils from the applied γ_{eff}. Strongly

entangled polymer coils cause elasticity and high viscosity. Entanglements of polymer coils are gradually disentangled according to the applied γ_{eff}, and elasticity and viscosity decrease, closely depending on γ_{eff}. The main factor in the shear-thinning of the CMC solutions is considered to be the orientation of single polymer coils as mentioned. However, for these two PAM solutions, the remaining entanglements do not allow single polymer coils to orient alone, and the disentanglement of the polymer coils may be surmised to be the dominant factor in the shear-thinning characteristics here. Based on the experiments conducted by Kulicke and Porter (1980) comparing steady and dynamic shear viscosities of PAM solutions, they considered that shear strain, not frequency, is responsible for disentangling the polymer coils. The increasing δ and decreasing μ_e as γ_{eff} increases would therefore quantitatively support their deduction. In addition, $\dot{\gamma}_{\text{eff,c}}$ increases with the concentration as shown in Fig. 4.11. It is considered that not only the overlap between the polymers increases as the concentration increases, but also a stronger entanglement is formed. As the result, yield and disentanglement of the polymer coils are less likely to occur, and $\dot{\gamma}_{\text{eff,c}}$ is increased with the concentration.

4.2 Bubble suspension rheology

The rheology mapping is a practical tool to investigate both shear rate and frequency dependent viscoelastic properties. In this section, rheology of dilute bubble suspensions is investigated as application of the rheology mapping.

4.2.1 Review of bubble suspension rheology

Bubbly flows are ubiquitous in both industry and nature. Addition of a small amount of bubbles changes the original rheological properties of the dispersion medium, and it changes not only the flow behavior of food and chemical products, but also the eruption pattern of volcanoes in nature (Llewellin and Manga, 2005). Bubble suspension rheology is therefore important to understand and predict these flow structures, and it has a century-long history originating with the well-known Einstein equation (Einstein, 1906):

$$\eta = 1 + b\phi, \tag{4.2}$$

where η is the relative viscosity and ϕ is the volume fraction. For a dilute suspension of solid spherical particles in steady shear flow, $b = 5/2$ (Einstein, 1906), and $b = 1$ for spherical bubbles in steady shear flow (Taylor, 1932). In the case of emulsion, which is a suspension of immiscible droplets, constitutive equations taking into account the deformation of the dispersion and its unsteadiness have been proposed for dilute (Frankel and Acrivos, 1970) and non-dilute (Choi and Schowalter, 1975) conditions. Han and King (1980) applied these constitutive equations to steady simple shear flow, and obtained formula for evaluating the effective viscosity of emulsion. Rust and Manga (2002) modified this formula for bubble suspensions and systematized in dilute conditions η as a function of ϕ and the capillary number Ca:

$$\eta = 1 + \frac{1 - (12/5)Ca^2}{1 + [(6/5)Ca]^2}\phi, \tag{4.3}$$

where $Ca = \lambda_r \dot{\gamma}_0$ with relaxation time of the suspended bubble λ_r and bulk shear rate applied to the suspension $\dot{\gamma}_0$. The validity of this equation has been confirmed by recent advanced experiments (Morini et al., 2019; Mitrou et al., 2023). Llewellin,

Mader, and Wilson (2002) further investigated the viscoelastic properties under small-amplitude oscillatory shear and proposed a constitutive equation in the form of the Jeffery model,

$$\boldsymbol{S} + \frac{6}{5}\lambda_{\mathrm{r}}\frac{\mathrm{d}\boldsymbol{S}}{\mathrm{d}t} = \mu_0\left(1+\phi\right)\boldsymbol{d} + \mu_0\frac{6}{5}\lambda_{\mathrm{r}}\left(1-\frac{5}{3}\phi\right)\frac{\mathrm{d}\boldsymbol{d}}{\mathrm{d}t}, \tag{4.4}$$

where μ_0 is the dynamic viscosity of the dispersion Newtonian medium, $\boldsymbol{S}$ and $\boldsymbol{d}$ are the deviatoric stress tensor and rate of deformation tensor defined by $\boldsymbol{d} = \left[\nabla\boldsymbol{u} + (\nabla\boldsymbol{u})^{\mathrm{T}}\right]/2$ with the bulk velocity of the suspension $\boldsymbol{u}$. Mitrias et al. (2017) performed direct numerical simulation and obtained consistent results with experiments in the dilute regime. Summarizing the progress in bubble suspension rheology, the steady shear viscosity is generalized by Eq. (4.3), and the viscoelastic properties for $Ca \ll 1$ are given by the Jeffery model (4.4). Both equations were originally derived from a constitutive tensor equation for a dilute emulsion theoretically obtained by Frankel and Acrivos (1970). Strictly, the applicable range of the original equation is restricted for small bubble deformation and weakly time-dependent flow. However, experimental and numerical simulation results indicate that this restriction allows highly deformable bubbles and unsteady shear flows.

In this section, the former (§ 4.2.2) was devoted to provide the last piece of the puzzle, namely, the viscoelasticity under conditions involving bubble deformation was elucidated based on the Frankel and Acrivos (1970) equation including both time derivative terms and nonlinear terms related to the bubble deformation. By using the rheology mapping, holistic picture of the bubble suspension rheology is presented. The latter part (§ 4.2.3) shows experimental verification of the above theoretical work. Measurement example of a dilute bubble suspension examined by USR is introduced. In addition, comparison of the wall shear stress predicted from the theoretically derived rheological properties and axial torque experimentally measured under unsteady shear flow in a Taylor–Couette system is demonstrated. The good agreement between the results intensified the validity of the theoretical work and indicated that the shear flows of bubble suspensions are predictable for the diverse applications mentioned above.

4.2.2 Theoretical approach

The original tensor equation theoretically derived by Frankel and Acrivos (1970) with assuming that the viscosity of the dispersion is negligible against that of the dispersion medium is expressed as

$$\begin{aligned}\boldsymbol{S} + \frac{6}{5}\lambda_{\mathrm{r}}\frac{\mathcal{D}\boldsymbol{S}}{\mathcal{D}t} &= -p\boldsymbol{I} + 2\mu_0\left(1+\phi\right)\left(\boldsymbol{d} + \frac{6}{5}\lambda_{\mathrm{r}}\frac{\mathcal{D}\boldsymbol{d}}{\mathcal{D}t}\right)\\ &+ \left(\frac{\mu_0^2 a}{\sigma}\right)\phi\left[-\frac{32}{5}\frac{\mathcal{D}\boldsymbol{d}}{\mathcal{D}t} + \frac{48}{35}\mathrm{S_d}(\boldsymbol{d}\cdot\boldsymbol{d})\right].\end{aligned} \tag{4.5}$$

The operations $\mathcal{D}/\mathcal{D}t$ and $\mathrm{S_d}$ denote the Jaumann derivative and the symmetric traceless part of the tensor to which it applies,

$$\frac{\mathcal{D}\boldsymbol{S}}{\mathcal{D}t} = \frac{\partial\boldsymbol{S}}{\partial t} + \boldsymbol{u}\cdot\nabla\boldsymbol{S} - \boldsymbol{\omega}\cdot\boldsymbol{S} + \boldsymbol{S}\cdot\boldsymbol{\omega}, \tag{4.6}$$

$$\mathrm{S_d}\left(\boldsymbol{d}\cdot\boldsymbol{d}\right) = \frac{1}{2}\left[\boldsymbol{d}^2 + (\boldsymbol{d}^{\mathrm{T}})^2 - \frac{2}{3}\mathrm{tr}(\boldsymbol{d}^2)\boldsymbol{I}\right]. \tag{4.7}$$

In the above equations, $\boldsymbol{\omega}$ is the vorticity tensor defined by $\boldsymbol{\omega} = \left[\nabla \boldsymbol{u} - (\nabla \boldsymbol{u})^{\mathrm{T}}\right]/2$ and $\boldsymbol{I}$ is an identity matrix. The parameters a, and σ are the bubble radius and surface tension of the dispersion medium, respectively, giving the relaxation time $\lambda_{\mathrm{r}} = \mu_0 a/\sigma$. Here, we assume that unsteady simple shear, $d_{12} = d_{21} = \dot{\gamma}(t)$, is applied to the suspension, and the following two equations are derived from Eq. (4.5),

$$N_{\mathrm{I}} + \frac{6}{5}\lambda_{\mathrm{r}}\left(\frac{dN_{\mathrm{I}}}{dt} + 2\dot{\gamma}\tau_{12}\right) = \frac{12}{5}\mu_0\lambda_{\mathrm{r}}\left(1 - \frac{5}{3}\phi\right)\dot{\gamma}^2, \tag{4.8}$$

$$\tau_{12} + \frac{6}{5}\lambda_{\mathrm{r}}\left(\frac{d\tau_{12}}{dt} - \frac{1}{2}\dot{\gamma}N_{\mathrm{I}}\right) = \mu_0\left(1+\phi\right)\left(\dot{\gamma} + \frac{6}{5}\lambda_{\mathrm{r}}\frac{d\dot{\gamma}}{dt}\right) - \frac{16}{5}\mu_0\lambda_{\mathrm{r}}\phi\frac{d\dot{\gamma}}{dt}, \tag{4.9}$$

where $N_{\mathrm{I}} = \tau_{22} - \tau_{11}$, the first normal stress difference. The dimensions of the relations are reduced by the characteristic shear rate, $\dot{\gamma}_{\mathrm{eff}}$, and the angular oscillation frequency, ω_{o}, where $\dot{\gamma}(t) = \sqrt{2}\dot{\gamma}_{\mathrm{eff}}\sin(\omega_{\mathrm{o}}t)$. The representative shear stress is given by $\mu_0\dot{\gamma}_{\mathrm{eff}}$. Substituting $\dot{\gamma} = \dot{\gamma}_{\mathrm{eff}}\dot{\gamma}^*$, $\tau_{12} = \mu_0\dot{\gamma}_{\mathrm{eff}}\tau^*$, $N_{\mathrm{I}} = \mu_0\dot{\gamma}_{\mathrm{eff}}$, and $t = t^*/\omega_{\mathrm{o}}$ to Eqs. (4.8) and (4.9), the relations are expressed as

$$N_{\mathrm{I}}^* + \frac{6}{5}\left(Cd\frac{\mathrm{d}N_{\mathrm{I}}^*}{\mathrm{d}t^*} + 2Ca\dot{\gamma}^*\tau^*\right) = \frac{12}{5}Ca\left(1 - \frac{5}{3}\phi\right)\dot{\gamma}^{*2}, \tag{4.10}$$

$$\tau^* + \frac{6}{5}\left(Cd\frac{\mathrm{d}\tau^*}{\mathrm{d}t^*} - \frac{1}{2}Ca\dot{\gamma}^*N_{\mathrm{I}}^*\right) = \left(1+\phi\right)\dot{\gamma}^* + \frac{6}{5}Cd\left(1 - \frac{5}{3}\phi\right)\frac{\mathrm{d}\dot{\gamma}^*}{\mathrm{d}t^*}, \tag{4.11}$$

where an asterisk indicates a non-dimensional variable. In addition to the volume fraction ϕ, the dimensionless parameters describing the stress response are $Ca = \lambda_{\mathrm{r}}\dot{\gamma}_{\mathrm{eff}}$ and the dynamic capillary number $Cd = \lambda_{\mathrm{r}}\omega_{\mathrm{o}}$ representing the unsteadiness of the flow. The usual capillary number is the product of the viscosity coefficient and the representative velocity divided by the surface tension, but here the product of the effective shear rate and the bubble radius is used instead of the representative velocity. Note that Eqs. (4.3) and (4.4) are derived from the set of Eqs (4.10) and (4.11) assuming steady shear ($Cd = 0$) and negligible bubble deformation ($Ca = 0$), respectively.

Here, the viscoelastic properties are discussed based on Eqs. (4.10) and (4.11). The relative viscosity η is defined as the amplitude of τ^* divided by that of $\dot{\gamma}^*$. The phase difference α of $\tau^*(t^*)$ against $\dot{\gamma}^*(t^*)$ indicates the conditions of the viscoelasticity, namely, the phase of the viscoelasticity $\delta = \pi/2 - \alpha$ rad, where $\pi/2$ rad represents a purely viscous fluid, while $\delta = 0$ rad means that the material is purely elastic. For intermediate δ values, $0 < \delta < \pi/2$ rad, the fluid exhibits viscoelasticity. The phase δ is also given by $\tan\delta = G''/G'$, where G' and G'' are storage and loss moduli, respectively.

Under different combinations of ϕ, Ca, and Cd, the corresponding η and δ are obtained by numerically solving the set of Eqs. (4.10) and (4.11). They are shown in Fig. 4.12 in the form of rheology maps, which are comprehensive expression of viscoelasticity proposed by Ohie et al. (2022a) and also demonstrated in § 4.1. The modulations of both η and δ intensify as ϕ increases. For the η distributions, the maximum value of $\eta = 1 + \phi$ (Taylor, 1932) occurs at $Ca = 0$ and $Cd = 0$, and it monotonically concentrically decreases in the higher Ca and Cd directions. Ultimately, η converges to $\eta = 1 - 5\phi/3$, which was also reported by Mackenzie (1950). Although the viscosity decrease and increase intensify at higher ϕ, the critical curve for $\eta = 1$ seems to be universal regardless of ϕ. Under steady shear ($Cd = 0$), the critical capillary number of $Ca = \sqrt{5/12} \simeq 0.65$ is obtained from Eq. (4.3). Under small-amplitude

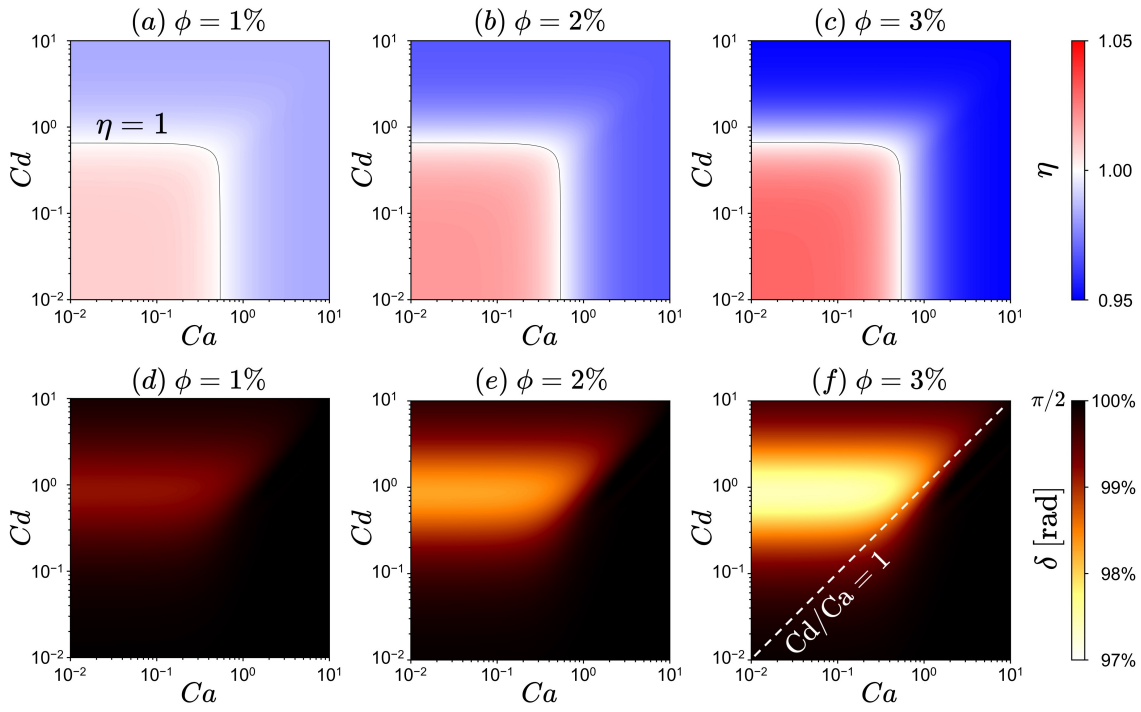


FIGURE 4.12: Viscoelasticity of dilute bubble suspensions. Relative viscosities (η) at volume fractions (ϕ) of (a) 1%, (b) 2%, and (c) 3%. Phases of the viscoelasticity (δ) at volume fractions of (d) 1%, (e) 2%, and (f) 3%.

oscillatory shear ($Ca \ll 1$), the relative viscosity derived from Eq. (4.11) is

$$\eta = 1 + \frac{1 - (12/5)Cd^2}{1 + [(6/5)Cd]^2}\phi, \tag{4.12}$$

where the terms on the same scale as $O(\phi^2)$ were ignored in the derivation. Note that this equation has the same form as Eq. (4.3), and the critical dynamic capillary number is also $Cd = \sqrt{5/12} \simeq 0.65$. The increase or decrease in the viscosity therefore depends on whether Ca or Cd exceeds this critical value.

The δ distributions have minimum points at approximately $Ca \ll 1$ and $Cd \sim 1$ as shown in Figs. 4.12(d)–(f). Assuming small-amplitude oscillatory shear ($Ca \ll 1$), from Eq. (4.11), δ is

$$\delta = \frac{\pi}{2} - \tan^{-1}\frac{(16/5)Cd\phi}{(1+\phi) + [1 - (5/3)\phi][(6/5)Cd]^2}. \tag{4.13}$$

The minimum point is determined to satisfy $\partial\delta/\partial Cd = 0$. Under the dilute condition, it is given by

$$Cd = \frac{5}{6}\sqrt{\frac{1+\phi}{1-(5/3)\phi}} \sim 1. \tag{4.14}$$

The viscoelastic properties are most pronounced at this point, and δ monotonically increases toward other areas, converging to that of a purely viscous fluid. This means that the bubble suspension has the most prominent viscoelasticity when the timescale of the shear deformation is the same as the relaxation time of the bubble.

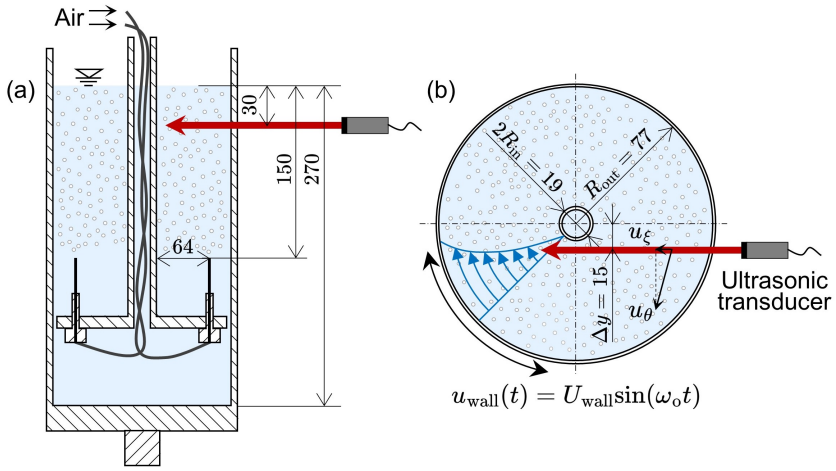


FIGURE 4.13: Experimental setup for ultrasonic spinning rheometry (USR): (a) cross section of the setup and (b) top view of the double cylinders. Fine bubbles are generated by four needles mounted on the acrylic plate. The outer cylinder is surrounded by water for temperature control and propagation of ultrasonic waves.

One of the advantages of the map representation is that the dependence of the viscoelasticity on the shear rate, strain, and oscillation frequency can be simultaneously determined. As shown by the dashed line in Fig. 4.12(f), the distributions of δ have a boundary at $Cd/Ca = 1$, where the shear strain is exactly unity. Therefore, the bubble suspension loses viscoelasticity when the shear strain is larger than this critical value regardless of Ca and Cd.

4.2.3 Experimental verification

Theoretically or empirically derived constitutive equations have usually been evaluated by rheological measurements. However, existing techniques have difficulties with bubble suspensions. A standard torque-type rheometer with a cone and plate geometry is the first candidate for bubble suspensions, but the maximum size of the dispersion usually has to be smaller than 10 μm; hence, it is not practical for bubble suspensions. Other candidates are parallel plates and concentric cylinders, but it is challenging to remove the bubble-rise effect (Pal, 2003) and edge effect in the cylinder, respectively. The parallel plate was previously used by Llewellin, Mader, and Wilson (2002) for small-amplitude oscillatory shear ($Ca \ll 1$), but it is not applicable for $Ca = O(1)$ because the shear rate amplitude has a radial profile. Another potential approach is falling sphere viscometry (Murai and Oiwa, 2008), but it has three-dimensional flow around the sphere, not simple shear flow.

As the most promising method for bubble suspensions, viscoelastic analysis by ultrasonic spinning rheometry (USR) (Tasaka et al., 2018) is introduced here. An example of measurement of a dilute bubble suspension with $\phi = 1.3\%$ and $a = 0.8$ mm suspended in Newtonian silicon oil (KF-96-3,000cs, Shin-Etsu Chemical Co., Ltd., Japan, $\mu_0 = 2.90$ Pa$\cdot$s, $\sigma = 21$ mNm) is shown in Fig. 4.14. The oscillation frequency of the vessel 2.0 Hz gives $Cd = 1.4$, and the shear rate range from 0 to 20 s^{-1} corresponds to Ca from 0 to 2.2. Based on Fig. 4.12(a), the relative viscosity is approximately unity, starting viscosity reduction. The solid line in Fig. 4.14(b) shows the flow curve of $\tau_{eff} = \mu_0\dot{\gamma}_{eff}$, and most of the points are close to or below this line.

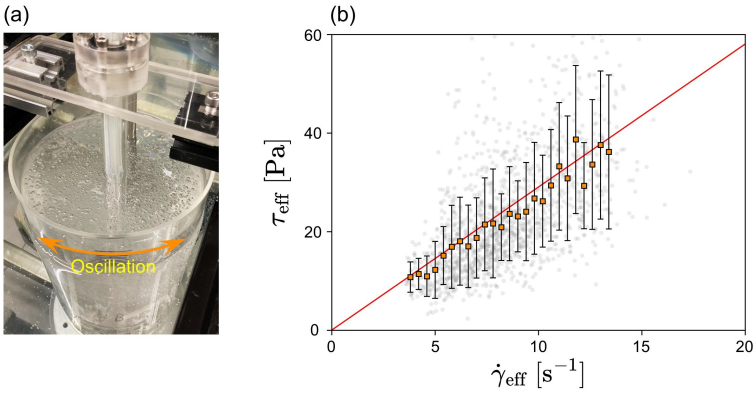


FIGURE 4.14: Viscoelastic analysis of the bubble suspension by ultrasonic spinning rheometry (USR). (a) Experimental setup. (b) Flow curve evaluated by USR, where the dark plots are the average values of the data points shown in the background and the error bars indicate the standard deviation. The solid line shows the flow curve of $\tau_{\mathrm{eff}} = \mu_0 \dot{\gamma}_{\mathrm{eff}}$.

Therefore, the experimental result obtained by USR is statistically consistent with the theoretical value, although the raw data are highly scattered. In the field of suspension rheology, the two disciplines of theory and experimentation with novel tools have made great contributions to clarifying the physics of the rheological properties (Tapia et al., 2022). To experimentally investigate the bubble suspension rheology in more detail, further improvement of USR with respect to the measurement noise is important future work.

Now, application of the theoretical work to flow prediction is demonstrated. The Taylor–Couette geometry was chosen as a typical geometry, and the wall shear stress acting on the inner cylinder was compared between the prediction and experimental results. The experimental setup mainly consisted of a fixed inner cylinder connected to a torque sensor (UTM III 0.5 Nm, Unipulse Co., Ltd., Japan) and an outer cylinder driven by a stepping motor, as shown in Figs. 4.15(a) and (b). The radii of the cylinders were $R_{\mathrm{out}} = 105$ mm and $R_{\mathrm{in}} = 50$ mm, with the corresponding gap size of 55 mm. Controlling the outer cylinder motion by the stepping motor to $u_{\mathrm{wall}}(t) = U_{\mathrm{eff}} \sin(\omega_{\mathrm{o}} t)$, the test fluid in the gap was subjected to one-directional oscillatory shear, which was dominant in the azimuthal direction. Highly viscous silicon oil (KF-96-5,000cs, Shin-Etsu Chemical Co., Ltd., Japan, $\mu_0 = 4.86$ Pa$\cdot$s, $\sigma = 21$ mNm) as a Newtonian fluid was filled in the cylinder, and fine bubbles were generated by the four fine needles mounted on the stepped disk. The representative bubble radius a was determined to be $a = 0.6$ mm, and the volume fraction was $\phi = 1.1\%$. The amplitude of the axial torque was measured under different U_{wall} and ω_{o}. T_b represents the torque amplitude for the bubble suspension, and T_0 represents that for the pure silicon oil.

Here, the specifications of the bubble generation method in double concentric cylinders are explained. An acrylic plate was fixed to the inner cylinder, which was independent of the outer cylinder, as shown in Figs. 4.13(a) and 4.15(a). Four fine needles were mounted on the plate, and air was distributed by four pumps through silicon tubes located in the inner cylinder. Before starting the measurement in the oscillatory shear flow, the outer cylinder was rotated with a constant velocity of approximately 6 rpm, and fine bubbles with almost the same diameter (≤ 2 mm) were

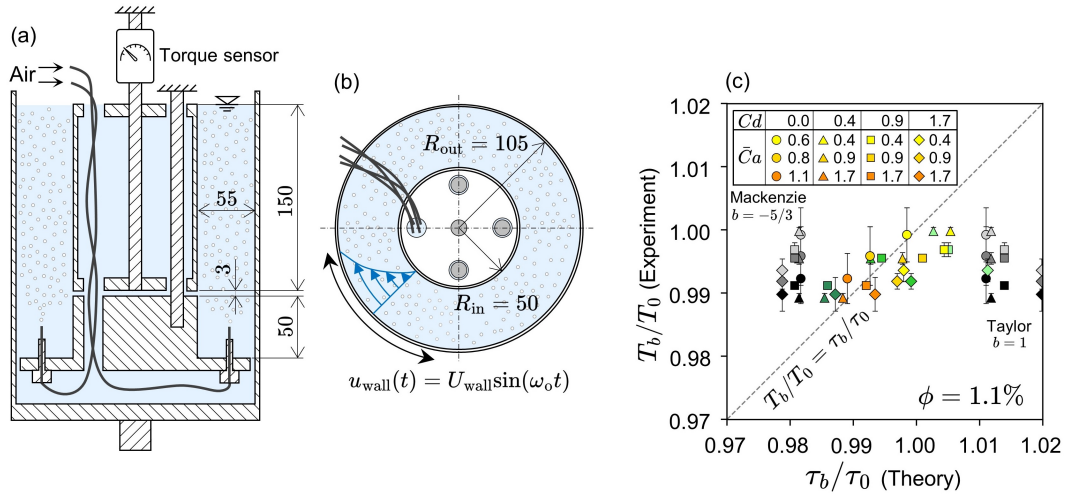


FIGURE 4.15: Experimental verification of the theory: (a) cross section of the experimental setup, (b) top view of the double cylinders, and (c) comparison of the experimentally measured torque ratio and theoretically evaluated wall shear stress ratio. The orange symbols are based on the viscoelasticity. The green and black symbols are predicted by Eqs. (4.3) and (2.77) with $b = 1$ and $-5/3$.

generated in the silicon oil. Before starting the measurement, impellers were used to gently stir the suspension to evenly disperse the bubbles in the gap. The resulting volume fractions were 1.3% and 1.1% in 3,000 and 5,000 cSt silicon oil, respectively. Histograms of the bubble diameters are shown in Fig. 4.16. The De Brouchere average diameter, which is the ratio between the fourth and third moments of the size distribution, recently proposed by Mitrou et al. (2023), was used as the representative radius a to calculate both the capillary and dynamic capillary numbers. The resulting diameters were $2a = 1.66$ and 1.15 mm, as shown by the dashed lines in Fig. 4.16. These values correspond to the diameters at which the cumulative volume fractions were approximately 50%, as shown by the plus symbols in Fig. 4.16.

The velocity field of the oscillatory shear flow between the double cylinders was reconstructed based on the rheology map shown in Fig. 4.12 along with the method proposed by Ohie et al. (2022c) and also explained in § 5.1, and the wall shear stress ratio τ_b/τ_0 was obtained. A comparison of the ratios from experiment and theory is shown in Fig. 4.15(c), where $\bar{C}a$ is the bulk capillary number defined as $\bar{C}a = \lambda_r U_{wall}/(R_{out} - R_{in})$. At each Cd, the corresponding ratio decreased as $\bar{C}a$ increased. The prediction was also conducted with Eqs. (4.2) and (4.3), but those based on the viscoelasticity showed the best agreement. This result verified the theoretical work in § 4.2.2 generalizing the viscoelasticity of a dilute bubble suspension, and it indicates the applicability of the constitutive equation for predicting the diverse shear flows in industry and nature.

4.3 The effect of parallel combined steady and oscillatory shear on dilute bubble suspensions

Bubbly flows are ubiquitous both in industry and nature. There is a variety of flows containing bubbles such as chemical industries, maritime transportation, rivers, and magma flows. These flows are often not only in steady shear or oscillatory shear

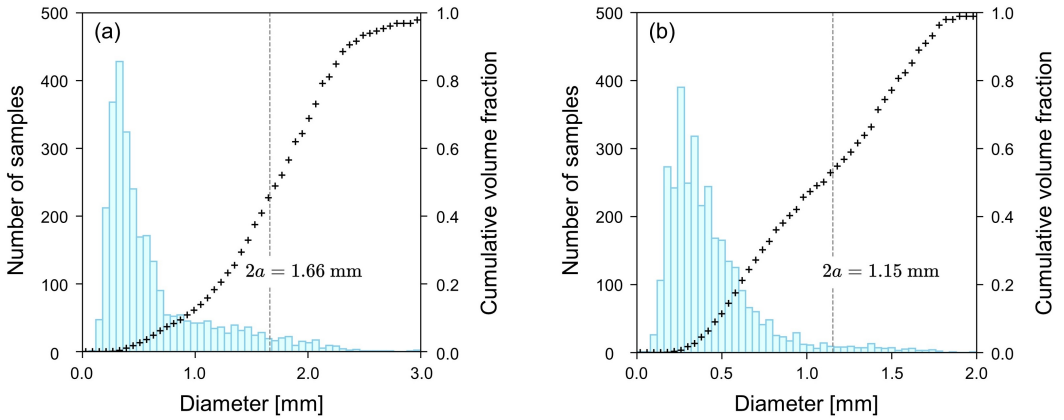


FIGURE 4.16: Histograms of the generated bubble diameters in (a) 3,000 and (b) 5,000 cSt silicon oil. The dashed lines correspond to the De Brouchere average diameters, and the plus symbols indicate the cumulative volume fractions.

consisting of a single frequency component, but also a combination of these. For example, when microbubbles are injected into the boundary layer on the bottom of a ship, the bubble suspension in the turbulent flow may undergo a background non-zero steady shear and superimposed oscillatory shear driven by turbulent fluctuations. When magma containing bubbles ascends through a conduit, steady shear is dominantly applied to the bubble suspension, but as the diameter of the conduit is not always constant, there are acceleration and deceleration of the ascending velocity, and pulsatile shear is superimposed. The effect of parallel combined steady and oscillatory shear on the viscoelasticity of bubble suspensions is therefore important to know for understanding bubbly flows. In this section, multi-timescale rheology is further explored by using the constitutive equation derived in § 4.2 and rheology mapping.

4.3.1 Theoretical approach

Assume that the following parallel combined steady and oscillatory shear is applied to a dilute bubble suspension,

$$\dot{\gamma}(t) = \dot{\Gamma}_0 + \dot{\gamma}_0 \dot{\gamma}^*(t) \tag{4.15}$$

with the shear rate amplitudes of a steady component $\dot{\Gamma}_0$ and an oscillatory component $\dot{\gamma}_0$. For example, when a sinusoidal shear is superimposed to $\dot{\Gamma}_0$, the normalized shear rate $\dot{\gamma}^*$ is given as $\dot{\gamma}^*(t) = \sqrt{2}\sin(\omega_o t)$ with an angular frequency ω_o. In theory, the stress response $\tau(t)$ can be obtained by substituting Eq. 4.15 to Eq. 4.8 and 4.9, and the same ones are rewritten below,

$$N_I + \frac{6}{5}\lambda_r\left(\frac{dN_I}{dt} + 2\dot{\gamma}\tau\right) = \frac{12}{5}\mu_0\lambda_r\left(1 - \frac{5}{3}\phi\right)\dot{\gamma}^2, \tag{4.16}$$

$$\tau + \frac{6}{5}\lambda_r\left(\frac{d\tau}{dt} - \frac{1}{2}\dot{\gamma}N_I\right) = \mu_0(1+\phi)\left(\dot{\gamma} + \frac{6}{5}\lambda_r\frac{d\dot{\gamma}}{dt}\right) - \frac{16}{5}\mu_0\lambda_r\phi\frac{d\dot{\gamma}}{dt}. \tag{4.17}$$

The dimensions of these relations are reduced by the two characteristic shear rate $\dot{\Gamma}_0$, $\dot{\gamma}_0$, and the angular frequency ω_o. The representative shear stress is tentatively given

as $\mu_0\sqrt{\dot{\Gamma}_0^2+\dot{\gamma}_0^2}$. Substituting $\dot{\gamma}=\dot{\Gamma}_0+\dot{\gamma}_0\dot{\gamma}^*$, $\tau=\mu_0\sqrt{\dot{\Gamma}_0^2+\dot{\gamma}_0^2}\tau^*$, $N_\mathrm{I}=\mu_0\sqrt{\dot{\Gamma}_0^2+\dot{\gamma}_0^2}N_\mathrm{I}^*$, and $t=t^*/\omega_\mathrm{o}$ to each terms of Eq. 4.16,

$$N_\mathrm{I}=\mu_0\sqrt{\dot{\Gamma}_0^2+\dot{\gamma}_0^2}N_\mathrm{I}^*, \tag{4.18}$$

$$\frac{6}{5}\lambda_\mathrm{r}\left(\frac{dN_\mathrm{I}}{dt}+2\dot{\gamma}\tau\right)=\frac{6}{5}\mu_0\sqrt{\dot{\Gamma}_0^2+\dot{\gamma}_0^2}\left[\lambda_\mathrm{r}\omega_\mathrm{o}\frac{dN_\mathrm{I}^*}{dt^*}+2\lambda_\mathrm{r}(\dot{\Gamma}_0+\dot{\gamma}_0\dot{\gamma}^*)\tau^*\right], \tag{4.19}$$

$$\frac{12}{5}\mu_0\lambda_\mathrm{r}\left(1-\frac{5}{3}\phi\right)\dot{\gamma}^2=\frac{12}{5}\mu_0\lambda_\mathrm{r}\left(1-\frac{5}{3}\phi\right)\left(\dot{\Gamma}_0+\dot{\gamma}_0\dot{\gamma}^*\right)^2, \tag{4.20}$$

are obtained. Three non-dimensional parameters are defined as $Ca'=\lambda_\mathrm{r}\dot{\Gamma}_0$, $Ca''=\lambda_\mathrm{r}\dot{\gamma}_0$, and $Cd=\lambda_\mathrm{r}\omega_\mathrm{o}$. In the parallel combined flows, two capillary numbers are required to describe the amplitudes of steady component Ca' and oscillatory component Ca'' with the dynamic capillary number Cd. Substituting Eqs. 4.18, 4.19 and 4.20 to Eq. 4.16, the following non-dimensionalized equation is obtained,

$$N_\mathrm{I}^*+\frac{6}{5}Cd\frac{dN_\mathrm{I}^*}{dt^*}+\frac{12}{5}\left(Ca'+Ca''\dot{\gamma}^*\right)\tau^*=\frac{12}{5}\left(1-\frac{5}{3}\phi\right)\frac{\left(Ca'+Ca''\dot{\gamma}^*\right)^2}{\sqrt{Ca'^2+Ca''^2}}. \tag{4.21}$$

Regarding Eq. 4.17 in the same procedure, each term is modified as

$$\tau=\mu_0\sqrt{\dot{\Gamma}_0^2+\dot{\gamma}_0^2}\tau^*, \tag{4.22}$$

$$\frac{6}{5}\lambda_\mathrm{r}\left(\frac{d\tau}{dt}-\frac{1}{2}\dot{\gamma}N_\mathrm{I}\right)=\frac{6}{5}\mu_0\sqrt{\dot{\Gamma}_0^2+\dot{\gamma}_0^2}\left[\lambda_\mathrm{r}\omega_\mathrm{o}\frac{d\tau^*}{dt^*}-\frac{1}{2}\lambda_\mathrm{r}\left(\dot{\Gamma}_0+\dot{\gamma}_0\dot{\gamma}^*\right)N_\mathrm{I}^*\right], \tag{4.23}$$

$$\mu_0\left(1+\phi\right)\dot{\gamma}=\mu_0\left(1+\phi\right)\left(\dot{\Gamma}_0+\dot{\gamma}_0\dot{\gamma}^*\right), \tag{4.24}$$

$$\frac{16}{5}\mu_0\lambda_\mathrm{r}\left(1-\frac{5}{3}\phi\right)\frac{d\dot{\gamma}}{dt}=\frac{16}{5}\mu_0\left(1-\frac{5}{3}\phi\right)\dot{\gamma}_0\lambda_\mathrm{r}\omega_\mathrm{o}\frac{d\dot{\gamma}^*}{dt^*}, \tag{4.25}$$

and substituting these to Eq. 4.17, the following non-dimensionalized equation is obtained,

$$\begin{aligned}\tau^*+\frac{6}{5}\left[Cd\frac{d\tau^*}{dt^*}-\frac{1}{2}\left(Ca'+Ca''\dot{\gamma}^*\right)N_\mathrm{I}^*\right] &= \left(1+\phi\right)\frac{Ca'+Ca''\dot{\gamma}^*}{\sqrt{Ca'^2+Ca''^2}} \\ &+ \frac{6}{5}\left(1-\frac{5}{3}\phi\right)\frac{Ca''Cd}{\sqrt{Ca'^2+Ca''^2}}\frac{d\dot{\gamma}^*}{dt^*}.\end{aligned} \tag{4.26}$$

Here, the viscoelastic properties are derived based on Eqs. 4.21 and 4.26. Under different combinations of Ca', Ca'', and Cd, $\dot{\gamma}(t^*)=\sqrt{2}\sin(t^*)$ is substituted to these two equations, and the corresponding shear stress $\tau^*(t^*)$ is numerically obtained with the periodic boundary condition of $\tau^*(t^*=0)=\tau^*(t^*=\pi/2)$. The numerical solutions are presented in Fig. 4.17 with gray symbols behind. It can be seen that under all the conditions, the stress response is the superposition of a steady and sinusoidal components. As the stress is normalized by $\mu_0\sqrt{\dot{\Gamma}_0^2+\dot{\gamma}_0^2}$, the stress profile shifts up and its amplitude decreases as Ca' increases. Furthermore, the stress profile shifts down and its amplitude enlarges as Ca'' increases. The solid lines in Fig. 4.17 are the fitting results on the numerical solutions based on the least squares method with

$$\tau^*(t^*)=\bar{\tau}^*+\tilde{\tau}^*\sin(t^*+\alpha), \tag{4.27}$$

where $\bar{\tau}^*$ is an average stress, $\tilde{\tau}^*$ is an stress amplitude, and α is a phase difference

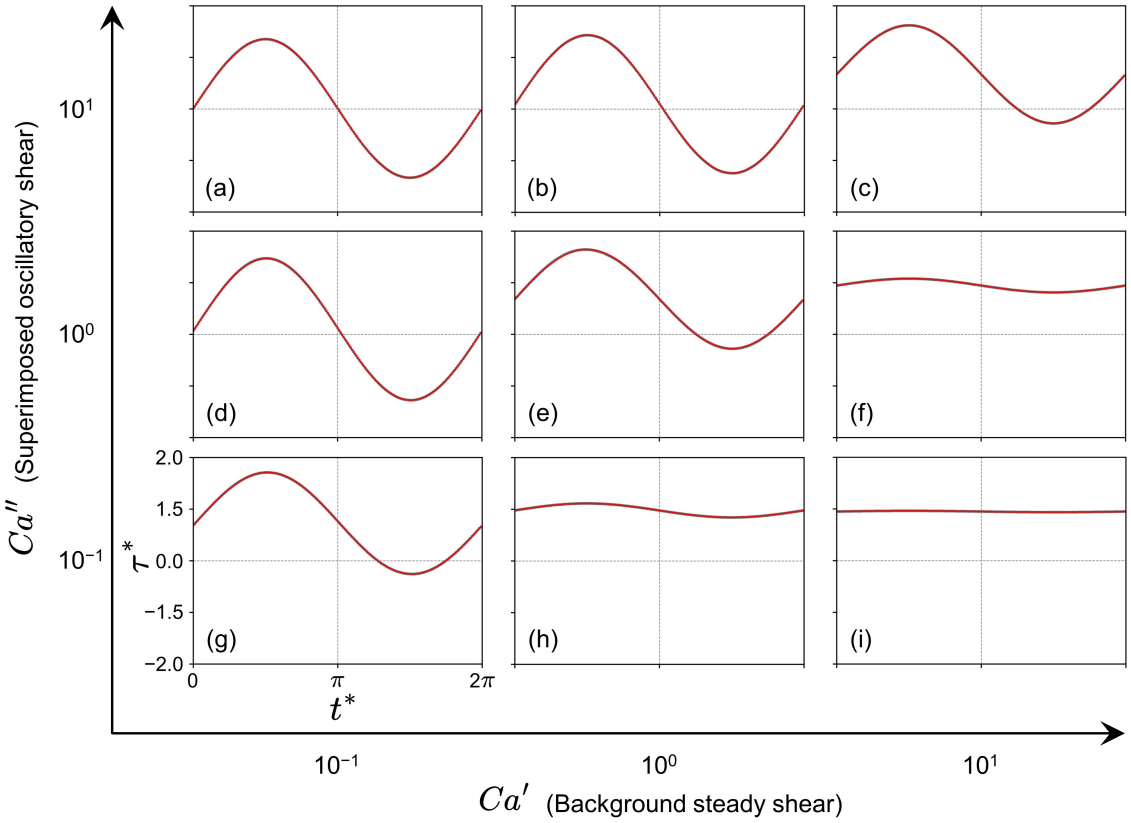


FIGURE 4.17: Temporal profiles of the normalized shear stress τ^* against the normalized elapsed time t^* in $Cd = 10^0$ and all the combinations of $Ca' = 10^{-1}, 10^0, 10^1$ and $Ca'' = 10^{-1}, 10^0, 10^1$. The volume fraction is $\phi = 3\%$. The gray symbols behind are the numerical solutions and the red lines are the fitting results based on the least squares method with Eq. 4.27.

between $\dot{\gamma}^*(t^*)$ and $\tau^*(t^*)$. The phase of viscoelasticity δ is defined as $\pi/2 - \alpha$, where $\delta = \pi/2$ rad represents a purely viscous fluid, while $\delta = 0$ rad means that the material is purely elastic. For intermediate values, the fluid exhibits viscoelasticity.

The definition of viscosity in such parallel combined steady and oscillatory shear is not obvious. Returning to the usual definition that viscosity is stress divided by shear rate, one possible idea in the parallel combined flow is to use two types of viscosity, where the ratio of stress divided by shear rate is calculated for both steady and pulsate components, respectively. Remembering that the stress is normalized with $\mu_0\sqrt{\dot{\Gamma}_0^2 + \dot{\gamma}_0^2}$, the relative viscosity η' and η'' regarding the background steady component and superimposed oscillatory component is respectively derived as

$$\eta' = \frac{1}{\mu_0}\frac{\mu_0\sqrt{\dot{\Gamma}_0^2 + \dot{\gamma}_0^2}\,\bar{\tau}^*}{\dot{\Gamma}_0} = \frac{\sqrt{Ca'^2 + Ca''^2}}{Ca'}\,\bar{\tau}^*, \tag{4.28}$$

$$\eta'' = \frac{1}{\mu_0}\frac{\mu_0\sqrt{\dot{\Gamma}_0^2 + \dot{\gamma}_0^2}\,\tilde{\tau}^*}{\sqrt{2}\dot{\gamma}_0} = \frac{\sqrt{Ca'^2 + Ca''^2}}{\sqrt{2}Ca''}\,\tilde{\tau}^*. \tag{4.29}$$

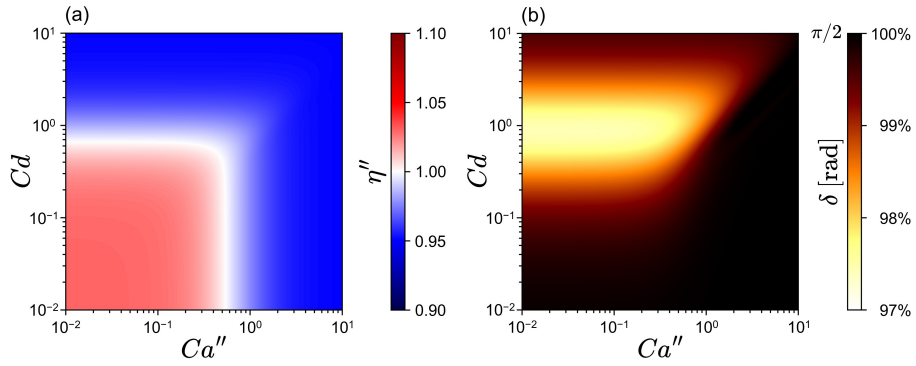


FIGURE 4.18: Viscoelasticity of dilute bubble suspensions with the volume fraction of $\phi = 3\%$ and $Ca' = 10^{-2}$: (a) relative viscosity η' and (b) phase of viscoelasticity δ.

4.3.2 Discussion

The viscoelasticity is evaluated under different conditions for Ca'' and Cd when the steady component is sufficiently small ($Ca' = 10^{-2}$) first to verify the validity of the series of formula expansion and numerical solutions as shown in Fig. 4.18. Comparing Fig. 4.18(a) and 4.12(c), 4.18(b) and 4.12(f), they match perfectly, and the validity was confirmed. Figure 4.19(a)–(i) show the viscoelasticity with the volume fraction of $\phi = 3\%$ under the parallel combined steady and oscillatory shear flows under different conditions for Ca' and Ca'' in $Cd = 10^{-1}$, 10^{0}, and 10^{1}. The amount of information is extremely large, these graphs are explained in order to starting from the distributions of η' in Fig. 4.19(a)–(c). In these three panels, steady shear is dominant when $Ca'' = 10^{-2}$, so the η' distributions on the horizontal axis follow Eq. 4.3 under any Cd condition, and the critical capillary number $Ca' \simeq 0.65$ is also confirmed. When oscillatory shear is superimposed, that is, when looking at the η' distribution in the higher Ca'' direction, η' monotonically decreases. This means that the momentum transport itself in the mean flow is modulated by the addition of oscillatory shear. A further noteworthy point in these three maps is that under conditions below the critical Ca' number, as Cd increases, the boundary that turns from viscosity increase (red area) to viscosity decrease (blue area) shifts in the higher Ca'' direction. The bulk shear strain in the oscillatory shear is given as $\dot{\gamma}_0\omega_o$, that is, Ca''/Cd. Therefore, even under the same Ca'', the larger Cd the smaller the bubble deformation, keeping more spherical shape. The closer the bubble is to a spherical shape, the more the streamline of the flow is distorted and the viscous dissipation increases, resulting in an increase in the effective viscosity. The viscosity η'' defined in the pulsation component is shown in the middle panels in Fig. 4.19. Under the condition that Ca' is sufficiently small ($Ca = 10^{-2}$), that is, the η'' distribution on the vertical axis matches Eq. 4.12. When parallel applying background shear, that is, focusing on the higher Ca' direction, the viscosity η'' monotonically decreases. When the bubble deforms due to an increase in Ca', it essentially provides a slip condition between the dispersion media and reduces the oscillatory shear propagating.

Finally, the distribution of the phase of viscoelasticity δ is shown in Fig. 4.19(g)–(i). The bubble suspension exhibits viscoelasticity as there is a time difference between the deformation applied in the suspension and the bubble deformation response. When the timescale of the applied shear deformation (unsteadiness) is longer than the relaxation time of the bubble ($Cd \ll 1$), the bubble deformation

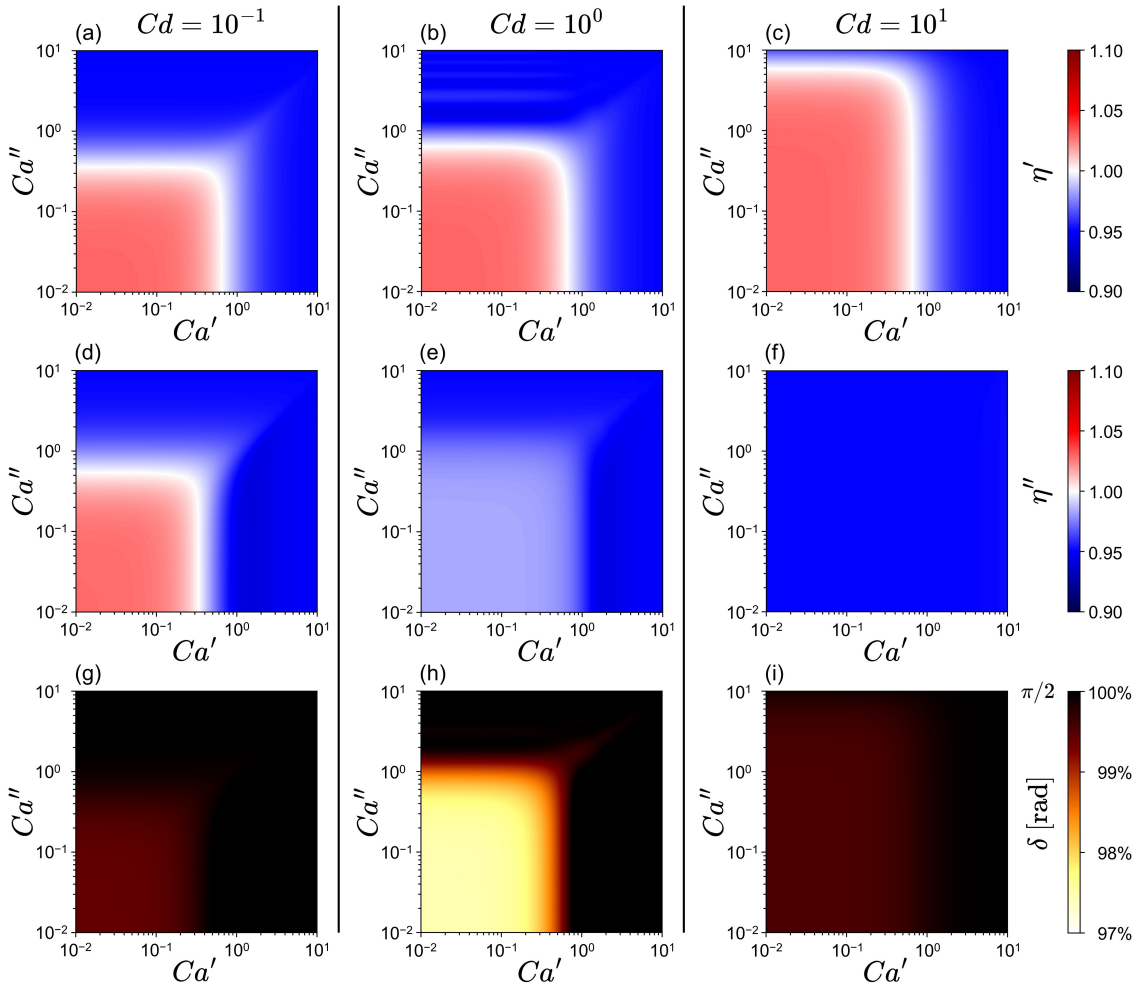


FIGURE 4.19: Viscoelasticity of dilute bubble suspensions with the volume fraction of ϕ = 3% under parallel combined steady and oscillatory shear flows: (a)–(c) relative viscosity η' defined in the background steady shear, (d)–(f) relative viscosity η'' defined in the parallel combined oscillatory shear, and (g)–(i) phase of viscoelasticity δ in the conditions of $Cd = 10^{-1}$, 10^{0}, and 10^{1}.

can transit to an equilibrium state corresponding to the applied shear rate, showing a purely viscous response. In contrast, when the applied oscillation is faster than the relaxation time ($Cd \gg 1$), the bubble deformation cannot follow it at all and the suspension behaves like a purely viscous fluid. It was indicated in § 4.2 that the viscoelasticity is maximized when the timescale of the applied shear deformation is as same as the relaxation time and when the bubble keeps near the spherical shape where the restoring force of the bubble due to surface tension is strongest. In Fig. 4.19(g)–(i), under the condition of $Ca'' = 10^{-2}$, the flow is dominated with the oscillatory shear and the δ distribution on the vertical axis correspond to Fig. 4.18(b) at each Cd condition. When the background steady shear is applied, δ monotonically decreases toward higher Ca' direction, converging to purely viscous ($\delta = \pi/2$ rad). The background shear forces the bubble to deform from the spherical shape where it can exhibit the most prominent viscoelasticity. The phase of viscoelasticity δ therefore decreases toward higher Ca' direction and converges to purely viscous response.

It is clear from Fig. 4.19 that the rheological properties in parallel combined flows cannot be extrapolated from the viscosity curve evaluated under steady shear or the viscoelasticity evaluated under oscillatory shear, except when mean or pulsating flow is dominant and unless the physics of the dispersion is fully understood. This experience also leads to the concept of data-driven rheology proposed at the end of this thesis.

Chapter 5

Flow reconstruction and prediction

One of the strength points of the velocity-profiling-based rheometry is that the velocity profile can be reconstructed by the identified rheological properties. The obtained rheology data therefore is highly reliable to be used in flow prediction or for selecting appropriate constitutive equations. In this chapter, the oscillatory shear flow in the cylindrical coordinate is reconstructed from the viscoelasticity evaluated by USR and compared with experimental results in § 5.1. As simple application examples of flow prediction, applications to predicting steady and pulsating flows in a circular pipe are introduced in § 5.2 and 5.3.

5.1 Oscillatory shear flow between concentric cylinders

The ultimate goal of this series of research is to predict the flow of complex fluids in industrially practical geometries for a circular pipe and more complex geometries. As a fundamental and important step that must be solved before the application, it is necessary to establish a method for reconstructing the velocity field that assures consistency with the experimentally evaluated rheological properties. A reconstruction method is proposed to incorporate the viscoelasticity data evaluated by USR into the numerical calculation of the flow reconstruction. An oscillatory shear flow generated between double concentric cylinders as shown in Fig. 5.1 is targeted as a basic flow field. This is a typical geometry for evaluating the performance of flow prediction (Shiratori, Tasaka, and Murai, 2016) and also famous for Couette inverse problem (Krieger, 1968). The boundary conditions are given as

$$u(r = R_{\mathrm{in}}, t) = 0, \tag{5.1}$$

$$u(r = R_{\mathrm{out}}, t) = U_{\mathrm{wall}} \sin(\omega_{\mathrm{o}} t), \tag{5.2}$$

where R_{in} = 26 mm and R_{out} = 77 mm are the radii of the inner and outer cylinders. The PVP solution examined in § 4.1 is targeted on first, and the flow field is reconstructed when the non-Newtonian characteristic evaluated by the rheology mapping is taken into consideration. The flow field is also calculated when the PVP solution is assumed to be a Newtonian fluid as is generally recognized. By comparing these two results with experiments in the double concentric cylinders, the performance of the proposed calculation method directly incorporating the viscoelasticity data is evaluated.

5.1.1 Theoretical background of the calculation

Viscoelasticity is evaluated by USR for one oscillation cycle, not a property determined instantaneously, so the following calculation method is proposed to reconstruct the velocity field. It starts with the Fourier transformed Cauchy's equation

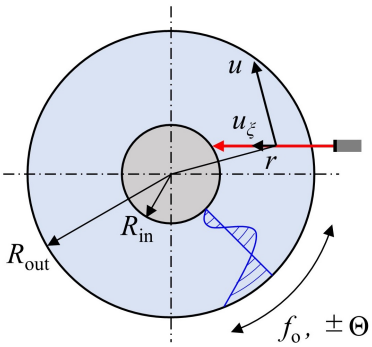


FIGURE 5.1: Schematic of the double concentric cylinders selected for the flow reconstruction. The inner cylinder with radius R_{in} is fixed in the outer cylinder.

and Maxwell model (Eqs. 2.24 and 2.25) as the governing equations. To simplify the expressions, the following definition is introduced as $\hat{u}(r,\omega=\omega_o)=R_u(r)+iI_u(r)$, where R_u and I_u are real and imaginary parts of $\hat{u}(r,\omega=\omega_o)$. Once R_u and I_u are determined, these are converted to the velocity distribution,

$$u(r,t)=A(r)\sin[\omega_o t+\phi(r)], \tag{5.3}$$

where $A(r)$ and $\phi(r)$ are defined as

$$A(r)=\sqrt{R_u^2+I_u^2}, \tag{5.4}$$

$$\phi(r)=\tan^{-1}(I_u/R_u). \tag{5.5}$$

Substituting Eq. 2.27 into Eq. 2.24 yields the following two equations for the real and imaginary parts:

$$-\omega_o\rho I_u=\mu_e\sin^2\delta\left(\frac{d^2}{dr^2}+\frac{1}{r}\frac{d}{dr}-\frac{1}{r^2}\right)(R_u+\cot\delta I_u), \tag{5.6}$$

$$\omega_o\rho R_u=\mu_e\sin^2\delta\left(\frac{d^2}{dr^2}+\frac{1}{r}\frac{d}{dr}-\frac{1}{r^2}\right)(I_u-\cot\delta R_u). \tag{5.7}$$

As μ_e and δ depend on the effective shear rate in the case of non-Newtonian fluids, it is difficult to solve Eq. 5.6 and 5.7 analytically. To solve them numerically, R_u and I_u are discretized as $R_i=R_u(r_i)$ and $I_i=I_u(r_i)$ $(i=0,1,...,N)$ with a spatial resolution Δr, where $r_0=R_{in}$ and $r_N=R_{out}$. The boundary conditions in the discretized form are

$$R_0=0, I_0=0, R_N=U_{wall}, I_N=0. \tag{5.8}$$

Discretizing Eqs. 5.6 and 5.7 with difference equations gives

$$A_{-1}R_{i-1}+A_0R_i+A_1R_{i+1}+B_{-1}I_{i-1}+B_0I_i+B_1I_{i+1}=0, \tag{5.9}$$

$$C_{-1}R_{i-1}+C_0R_i+C_1R_{i+1}+D_{-1}I_{i-1}+D_0I_i+D_1I_{i+1}=0, \tag{5.10}$$

where $i=1,2,...,N-1$. In the above equations, coefficients A_i, B_i, C_i, and D_i $(i=-1,0,1)$ are constants at each radial position r_i including $\mu_i=\mu_e(r_i)$, $\delta_i=\delta(r_i)$, and

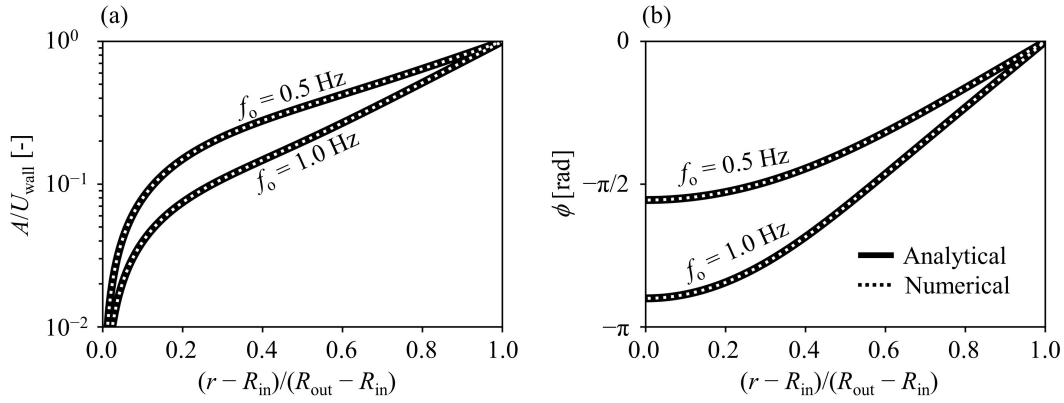


FIGURE 5.2: Comparison of the calculation results and analytical solutions for a Newtonian fluid with a viscosity coefficient of 0.61 Pa · s and density of 997 kg/m^3: spatial profiles of (a) velocity amplitude A normalized by the maximum wall velocity U_{wall} and (b) phase lag ϕ from the outer cylindrical wall.

and defined as follows:

$$A_{-1} = \mu_i \sin^2\delta_i \left(\frac{1}{\Delta r^2} - \frac{1}{2r_i \Delta r} \right), \tag{5.11}$$

$$A_0 = -\mu_i \sin^2\delta_i \left(\frac{2}{\Delta r^2} + \frac{1}{r_i^2} \right), \tag{5.12}$$

$$A_1 = \mu_i \sin^2\delta_i \left(\frac{1}{\Delta r^2} + \frac{1}{2r_i \Delta r} \right), \tag{5.13}$$

$$B_{-1} = \mu_i \sin^2\delta_i \cot\delta_i \left(\frac{1}{\Delta r^2} - \frac{1}{2r_i \Delta r} \right), \tag{5.14}$$

$$B_0 = -\mu_i \sin^2\delta_i \cot\delta_i \left(\frac{2}{\Delta r^2} + \frac{1}{r_i^2} \right) + \omega_o \rho, \tag{5.15}$$

$$B_1 = \mu_i \sin^2\delta_i \cot\delta_i \left(\frac{1}{\Delta r^2} + \frac{1}{2r_i \Delta r} \right), \tag{5.16}$$

$$C_{-1} = -\mu_i \sin^2\delta_i \cot\delta_i \left(\frac{1}{\Delta r^2} - \frac{1}{2r_i \Delta r} \right), \tag{5.17}$$

$$C_0 = \mu_i \sin^2\delta_i \cot\delta_i \left(\frac{2}{\Delta r^2} + \frac{1}{r_i^2} \right) - \omega_o \rho, \tag{5.18}$$

$$C_1 = -\mu_i \sin^2\delta_i \cot\delta_i \left(\frac{1}{\Delta r^2} + \frac{1}{2r_i \Delta r} \right), \tag{5.19}$$

$$D_{-1} = \mu_i \sin^2\delta_i \left(\frac{1}{\Delta r^2} - \frac{1}{2r_i \Delta r} \right), \tag{5.20}$$

$$D_0 = -\mu_i \sin^2\delta_i \left(\frac{2}{\Delta r^2} + \frac{1}{r_i^2} \right), \tag{5.21}$$

$$D_1 = \mu_i \sin^2\delta_i \left(\frac{1}{\Delta r^2} + \frac{1}{2r_i \Delta r} \right). \tag{5.22}$$

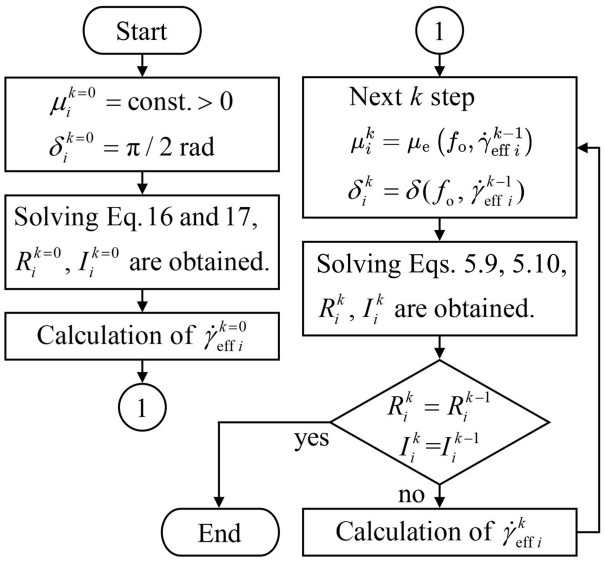


FIGURE 5.3: Flow chart of the convergence calculation method in the frequency domain of the velocity profile based on the comprehensive viscoelasticity data set evaluated vis USR.

Solving Eqs. 5.9 and 5.10 under the boundary conditions in Eq. 5.8 uniquely determines R_i and I_i ($i = 1, 2, ..., N-1$).

A Newtonian fluid is tentatively assumed first to verify whether this calculation scheme in the frequency space works and to grasp the difference error. The viscosity coefficient and density of the fluid are set as $\mu = 0.61$ Pa·s and $\rho = 997$ kg/m^3. The geometric conditions of the double cylinders are $R_{\mathrm{in}} = 26$ mm and $R_{\mathrm{out}} = 77$ mm, and the number of dividing points in the radial direction is $N + 1 = 201$, corresponding to $\Delta r = (R_{\mathrm{out}} - R_{\mathrm{in}})/N = 0.26$ mm. Figure 5.2 shows the calculation results when the oscillation frequency and amplitude are set as $f_o = 0.5$ Hz and $\Theta = 7\pi/6$ rad, $f_o = 1.0$ Hz and $\Theta = 2\pi/3$ rad, where $A(r)$ and $\phi(r)$ represent the velocity intensity and phase lag from the outer cylinder wall defined by Eqs. 5.4 and 5.5. For comparison, the analytically solved distributions are also shown by the solid lines in Fig. 5.2. The derivation of the analytical solutions is specifically explained in § 2.5. The numerically obtained distributions show excellent agreement with the analytical solutions over all the radial positions, indicating that the method works well without any significant difference error.

The flow field of a non-Newtonian fluid is numerically reconstructed as follows along the flow chart in Fig. 5.3. First, R_i and I_i ($i = 1, 2, ..., N-1$) are tentatively calculated with $\mu_i = \mu_i^{k=0} = \text{const.} > 0$ and $\delta_i = \delta_i^{k=0} = \pi/2$ rad ($i = 1, 2, ..., N-1$), and the results are denoted as $R_i^{k=0}$ and $I_i^{k=0}$. The corresponding effective shear rate $\dot{\gamma}_{\mathrm{eff}i}^{k=0}$ ($i = 1, 2, ..., N-1$) is calculated. Then, $\mu_i^{k=0}$ and $\delta_i^{k=0}$ are updated to $\mu_i^{k=1}$ and $\delta_i^{k=1}$ on the basis of the effective shear rate, the viscosity curve $\mu_e(f_o, \dot{\gamma}_{\mathrm{eff}})$, and the delta curve $\delta(f_o, \dot{\gamma}_{\mathrm{eff}})$ extracted from the rheology map. The quantities R_i and I_i are recalculated using this updated spatial distribution of viscoelasticity, and the results are denoted as $R_i^{k=1}$ and $I_i^{k=1}$. This series of operations is repeated until $R_i^k = R_i^{k-1}$ and $I_i^k = I_i^{k-1}$ ($i = 1, 2, ..., N-1$) are satisfied, and the finally obtained R_i^k and I_i^k represent the flow field reconstructed by this method, where the consistency with the experimentally evaluated viscoelasticity is assured.

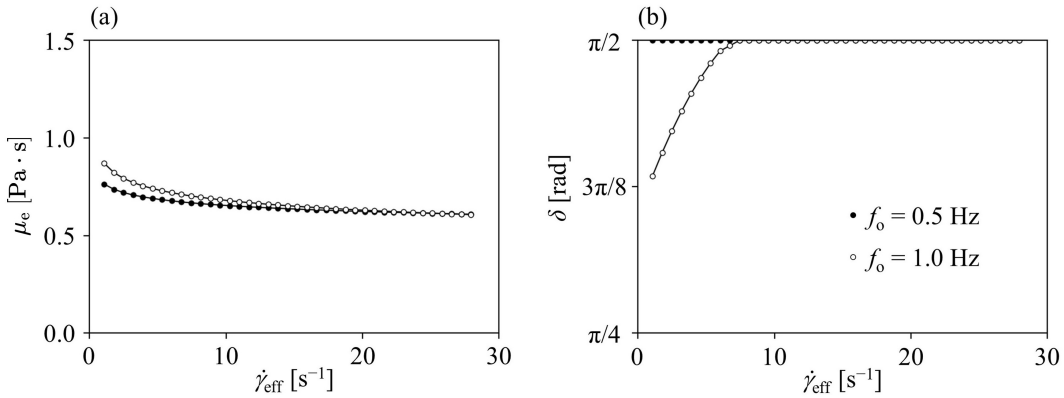


FIGURE 5.4: Viscosity and delta curves extracted from the viscoelasticity data set in Fig. 4.5 for the 12 wt.% PVP solution.

5.1.2 Validation of the reconstruction method

The velocity distributions predicted by the method proposed in the previous section are compared with the experimental results for validation. In USR, the measurement precision at low shear rate $O(10^{-1}\ \mathrm{s}^{-1})$ is lower than that in the region of $O(10^{0}\ \mathrm{s}^{-1})$–$O(10^{1}\ \mathrm{s}^{-1})$ due to the measurement performance of the UVP. In the case of the 8 wt.% PVP solution with viscosity of 0.1 Pa · s, thickness of the viscous layer on the oscillating outer cylinder wall is thin, and shear rate takes $O(10^{-1}\ \mathrm{s}^{-1})$ in a wide range around the inner cylinder. For assuring accurate flow reconstruction, the shear rate range of the reconstructed flow field has to be included in the shear rate range which can be evaluated by USR with high precision. The 12 wt.% PVP solution is therefore used to represent the test fluid with just the suitable viscosity for verification. This is a disadvantage of the current USR, and the extension of the shear rate range is realized by the VPAR as explained in § 2.5.

The oscillation parameters are f_o = 0.5 Hz and $\Theta = 7\pi/6$ rad, f_o = 1.0 Hz and $\Theta = 2\pi/3$ rad. The calculation is performed using the viscosity and delta curves extracted from the rheology maps in Figs. 4.5(b) and 4.5(e) at f_o = 0.5 Hz and f_o = 1.0 Hz. These curves are statistically processed to exclude inaccuracy caused by measurement noise of UVP, and seem to have sufficient smoothness in comparison with the original rheology map. For f_o = 0.5 Hz, the PVP solution is purely viscous, and the dependence of viscosity on shear rate is weaker as shown in Fig. 5.4. However, at f_o = 1.0 Hz, the PVP solution is viscoelastic with a considerable shear rate dependent viscosity at low shear rates.

The velocity distributions reconstructed by the method proposed in the previous section are shown in Fig. 5.5, where $A(r)$ and $\phi(r)$ represent the velocity amplitude and phase lag from the outer cylinder wall defined by Eqs. 5.4 and 5.5. The dotted lines are the experimental results measured through UVP. In these verification experiments, the solution was filled to a height of 215 mm from the bottom of the vessel, and the ultrasonic transducer was horizontally installed 50 mm below the top surface with off-axis Δy = 15 mm. The distribution near the outer cylinder is immeasurable owing to multiple reflection of the ultrasonic waves inside the acrylic wall. In addition, the distribution is not displayed at $(r - R_{in})/(R_{out} - R_{in}) < 0.3$ because measurement accuracy decreases owing to the cylindrical pulses of ultrasonic waves straddling the radial direction. Except for these radial ranges, the predicted and experimental results are in excellent agreement, indicating the validity of the

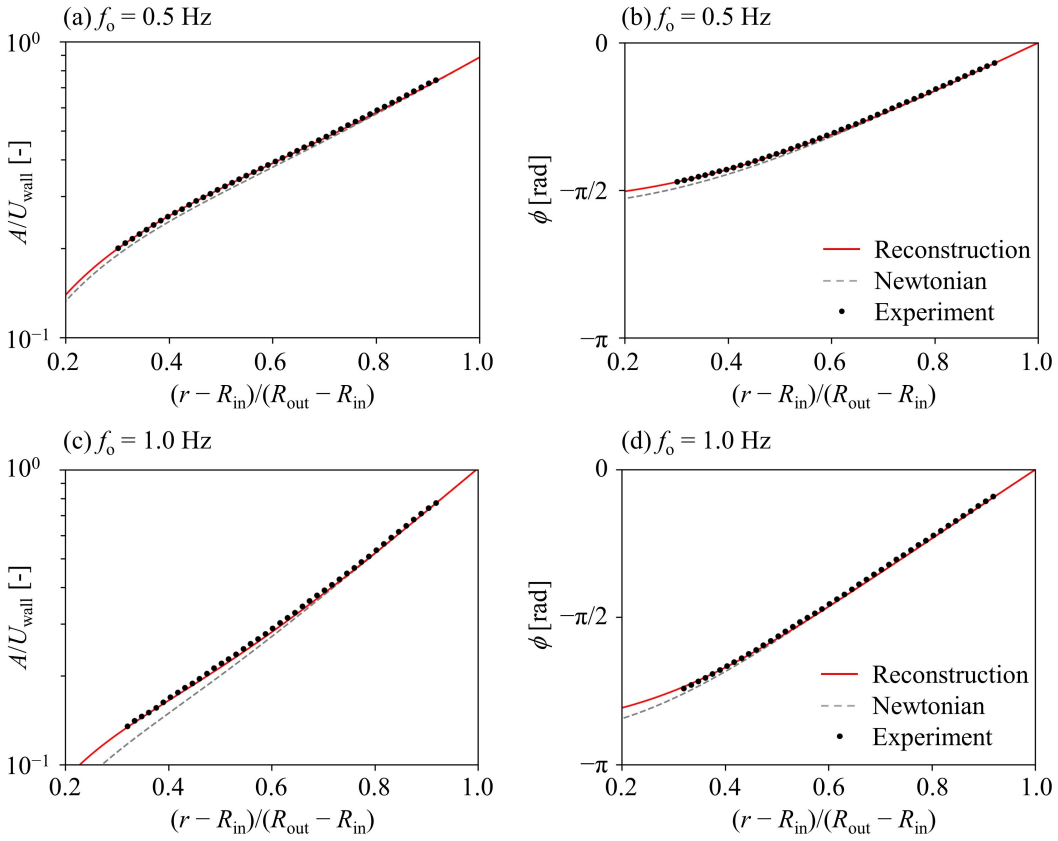


FIGURE 5.5: Comparison of the predicted and experimental velocity profiles: spatial profiles of the velocity amplitude A and phase lag from the outer cylindrical wall ϕ. The oscillation parameters are f_o = 0.5 Hz and $\Theta = 7\pi/6$ rad in figures (a) and (b), and f_o = 1.0 Hz and $\Theta = 2\pi/3$ rad in figures (c) and (d).

proposed method.

The dashed lines in Fig. 5.5 represent the calculated velocity distribution for a Newtonian fluid with a viscosity of 0.61 Pa · s, which is the value at the right ends of the curves in Fig. 5.4(a). These are almost the same as the experimental results near the outer cylinder wall, but they deviate toward the inside. This is because the shear rate for f_o = 0.5 Hz becomes $\dot{\gamma}_{eff}$ = 10 s^{-1} at around $(r - R_{in})/(R_{out} - R_{in})$ = 0.4 and decreases toward the inner cylinder, so the viscosity of the PVP solution becomes dependent on the shear rate. For f_o = 1.0 Hz, the difference from the experimental results is more remarkable than f_o = 0.5 Hz. This is because the shear rate becomes $\dot{\gamma}_{eff}$ = 10 s^{-1} around $(r - R_{in})/(R_{out} - R_{in})$ = 0.4 and decreases further toward the inner cylinder, and viscoelasticity emerges at the same time as the shear rate dependence of the viscosity.

The PVP solutions generally have been assumed to be Newtonian fluids even though they exhibit viscoelasticity in limited conditions of unsteady shear. Understanding these properties requires comprehensive evaluations while varying shear deformation and its timescale, such as with the rheology mapping. It is possible to predict the velocity distributions by directly using the viscoelasticity data as demonstrated here. It has confirmed that when the target fluid is under oscillatory shear flows, the velocity distributions can be reconstructed with high accuracy using a data set and convergence calculation in the frequency domain. As the next step, the

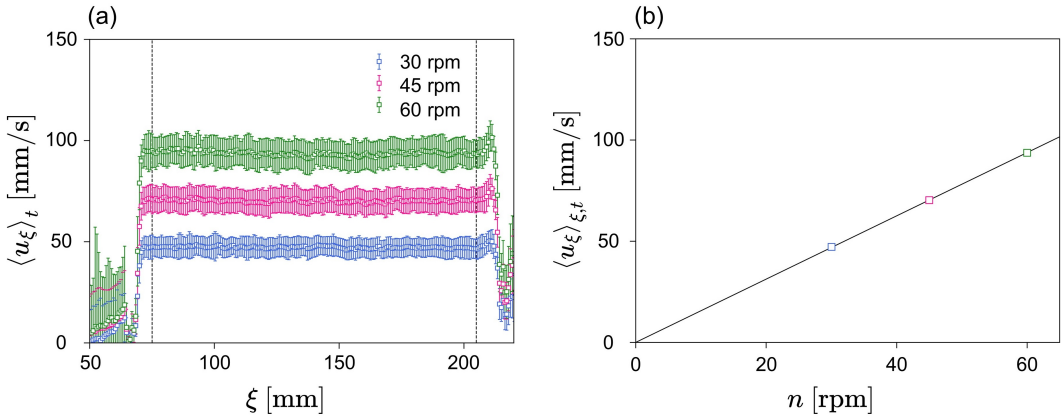


FIGURE 5.6: Velocity profiles of the PVP 12 wt.% aqueous solution under the rigid body rotation with different rotation speeds: (a) Mean velocity profiles $\langle u_\xi \rangle_{\xi}$, and (b) the spatially averaged values of the mean velocity profiles in the range surrounded by dashed lines in figure (a), where the solid line represents a regression curve passing through the origin.

reconstruction scheme established here is advanced to predict pipe flows of non-Newtonian fluids as more practical target in § 5.2 and 5.3.

5.1.3 Technical note and further application to the CMC solution

In the above comparison, it is also important to accurately measure the velocity profile experimentally. Otherwise, the validity of the reconstruction/prediction cannot be truly verified. When measuring the velocity profile in such cylindrical vessel using UVP, it is necessary to correctly determine the off-axis Δy and inner wall positions. Therefore, some methods obtained in the USR development so far are recorded here as technical notes. First, regarding how to determine the off-axis Δy, even if the center of the ultrasonic transducer is get geometrically to $\Delta y = 15$ mm, the measurement line inside the cylinder is not necessarily at that position. This is because the sound speeds of the acrylic and water surrounding the cylinder are different, so refraction first occurs there. Additionally, refraction occurs once again when the ultrasonic waves enter the internal fluid from the acrylic. When the speed of sound of the test fluid is close to that of water, there is almost no off-axis deviation, but care must be taken when there is a significant difference in speed of sound of water such as silicon oil. To determine the off-axis, the inner cylinder is removed and the outer cylinder is rotated with a constant speed. The velocity profiles of the 12 wt.% PVP aqueous solution with different rotation speed n are shown in Fig. 5.6. The velocity profile of the rigid body rotation is given as $u_\theta(r) = 2\pi nr/60$ regardless of the test fluids, and the UVP captures the velocity profile $u_\xi(\xi) = (\Delta y/r)u_\theta = 2\pi n\Delta y/60$, which is a constant regardless of the radial position. Figure 5.6(b) shows the spatially averaged values of the mean velocity profiles at each condition of n, where the average was calculated in the area surrounded by dashed lines in Fig. 5.6(a). These symbols are located on a straight line passing through the origin, and the identified gradient using the least squares method with $\langle u_\xi \rangle_{\xi,t} = an$ is $a = 1.56$ mm/(s rpm). This gradient is also given as $a = 2\pi\Delta y/60$, the off-axis is estimated to be $\Delta y = 14.9$ mm in this measurement.

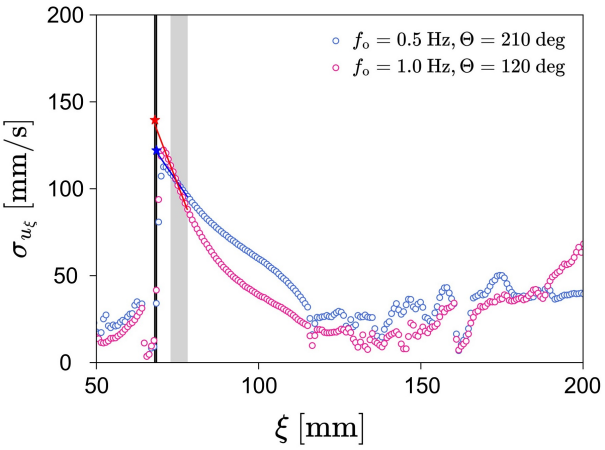


FIGURE 5.7: Velocity profiles of the PVP 12 wt.% aqueous solution captured by UVP in oscillatory shear flows. The oscillation parameters are f_o = 0.5 Hz and Θ = 210 deg for the blue symbols and f_o = 1.0 Hz and Θ = 120 deg for the red symbols. The vertical axis σ_{u_ξ} represents the effective value of $u_\xi(\xi, t)$ in the time direction. The solid lines are the fitting lines of the data in the gray area and the star symbols represent the given wall velocity.

Regarding the position of the inner cylindrical wall, no universal method to determine the position has been established so far, but one possible way is adapting the position of which the velocity distribution is consistent with the given wall velocity. The cylindrical vessel is driven by a stepping motor so that the wall velocity becomes $u_{\text{wall}}(t) = U_{\text{wall}}\sin(\omega_o t)$ with $U_{\text{wall}} = 2\pi f_o R_{\text{out}}\Theta$, and the maximum velocity at the wall captured by UVP is $U_{\text{wall}}\Delta y/R_{\text{out}}$, and its effective value is obtained just by dividing by $\sqrt{2}$ as $U_{\text{wall}}\Delta y/\sqrt{2}R_{\text{out}}$. Figure 5.7 shows the spatial distributions of the effective values of the velocity measured by UVP in oscillatory shear flows, where the inner cylinder is put in the outer cylinder. The average velocity is zero in the oscillatory shear flows, so the standard deviation in the time direction directly corresponds to the effective value. Extrapolating the profiles where the gradient near the wall is constant (shown by gray area in Fig. 5.7), the position where the extrapolated lines intersect with the given velocity $U_{\text{wall}}\Delta y/\sqrt{2}R_{\text{out}}$ (star symbols in Fig. 5.7) is considered to be the wall position. In the case of the experiment using the PVP 12 wt.% solution, the wall position was detected to be around ξ_{wall} = 68 mm as shown by solid line in Fig. 5.7. This method is effective when there is no slip on the wall like PVP solutions. The off-axis is determined in the previous rigid body rotation test, the middle point between the cylindrical wall surfaces on the measurement line is therefore estimated to be $\xi_{\text{wall}} + \sqrt{R_{\text{out}}^2 - \Delta y^2}$.

The velocity reconstruction proposed above was further applied to an aqueous solution with more prominent non-Newtonian properties rather than the PVP solution. The test fluid is the CMC 1.0 wt.% aqueous solution. The viscelastic properties were evaluate by USR, and the viscosity coefficient μ_e and the phase of viscoelasticity δ are shown in Fig.5.8 against the effective shear rate $\dot{\gamma}_{\text{eff}}$. In order to obtain accurate rheology curves, the velocity measurement was conducted under multiple conditions of the oscillation parameters, where the rotation amplitude Θ was varied every 30 deg from 30 to 210 deg under the condition of f_o = 0.5 Hz, and every 15 deg from 15 to 105 deg under the condition of f_o = 1.0 Hz. As explained in § 2.4,

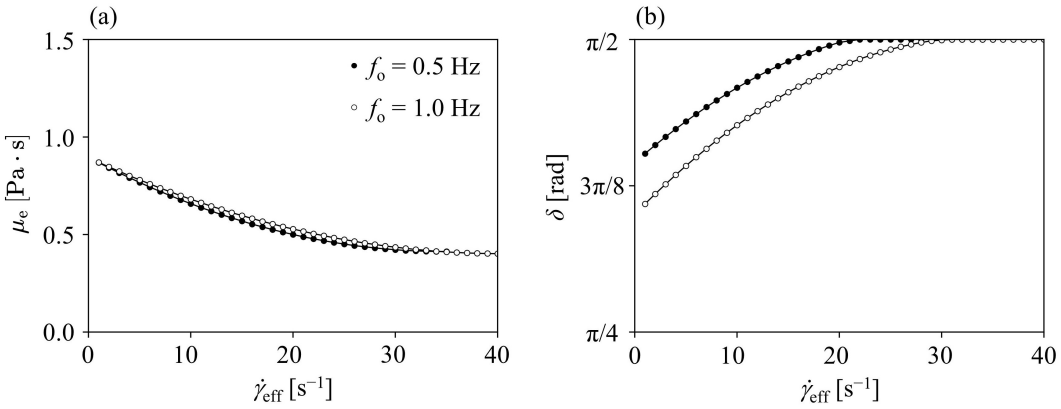


FIGURE 5.8: Viscosity and delta curves of the CMC 1.0 wt.% aqueous solution against the effective shear rate $\dot{\gamma}_{eff}$ evaluated by USR, where the oscillation frequency is f_o = 0.5 Hz for the closed circles and f_o = 1.0 Hz for the open circles.

the velocity distribution obtained under each oscillation parameter was further divided, and the results were summarized on two-dimensional histograms of $\mu_e - \dot{\gamma}_{eff}$ and $\delta - \dot{\gamma}_{eff}$. The statistical values were taken, and the results were smoothed using polynomial fitting, the resulting viscosity and delta curves are shown in Fig. 5.8. This measurement, which changes Θ in small increments, can provide reliable data, but it requires lots of measurement time, so some improvements will be required. As found in § 4.1.2, the CMC solutions have shear-rate-dependent viscosity, the viscosity curves of the current CMC solution also match each other even though the applied oscillation frequency is different. In addition, the CMC solution becomes more elastic as the frequency increases, which is consistent with the rheology mapping in § 4.1.2.

The oscillatory shear flows between double concentric cylinders predicted by these rheological properties evaluated by USR is compared with experimental measurements. To determine the off-axis first, the inner cylinder was removed and the outer cylinder was rotated with a constant speed. The mean velocity profiles under the different rotation speed are shown in Fig. 5.9(a). These profiles were further averaged in the spatial direction and summarized in Fig. 5.9(b). Based on the least squares method, the gradient was evaluated and the resulting off-axis is Δy = 15.2 mm. Figure 5.9(c) shows the spatial distributions of the effective value of the velocity when the oscillatory shear flow was measured by UVP without the inner cylinder. The oscillation frequency is f_o = 0.5 Hz and the rotation amplitude Θ was varied every 30 deg from Θ = 30 deg to Θ = 210 deg, where the profiles in Fig. 5.9(c) correspond to the conditions where Θ is small in order from the bottom. As the flow is axially symmetric, symmetrical profiles are confirmed. The open circles shown in Fig. 5.9(c) are the effective values of the velocity of the wall. Extrapolating the velocity profiles near the wall, it is estimated that the wall positions correspond to around ξ_{wall1} = 58 mm and ξ_{wall2} = 210 mm. The midpoint of these wall positions is indicated by the dash-dotted line in Fig. 5.9(c). The spatial derivative of the effective values of the velocity is shown in Fig. 5.9(d), and the midpoint corresponds to the position where the derivative is zero, showing consistency with the wall positions estimated by the extrapolation. Furthermore, the distance between the walls determined from the cylindrical radius and the off-axis determined earlier is $2\sqrt{R_{out} - \Delta y^2}$ = 151 mm, and this is almost the same as $\xi_{wall2} - \xi_{wall1}$ = 152 mm. As the spatial resolution of

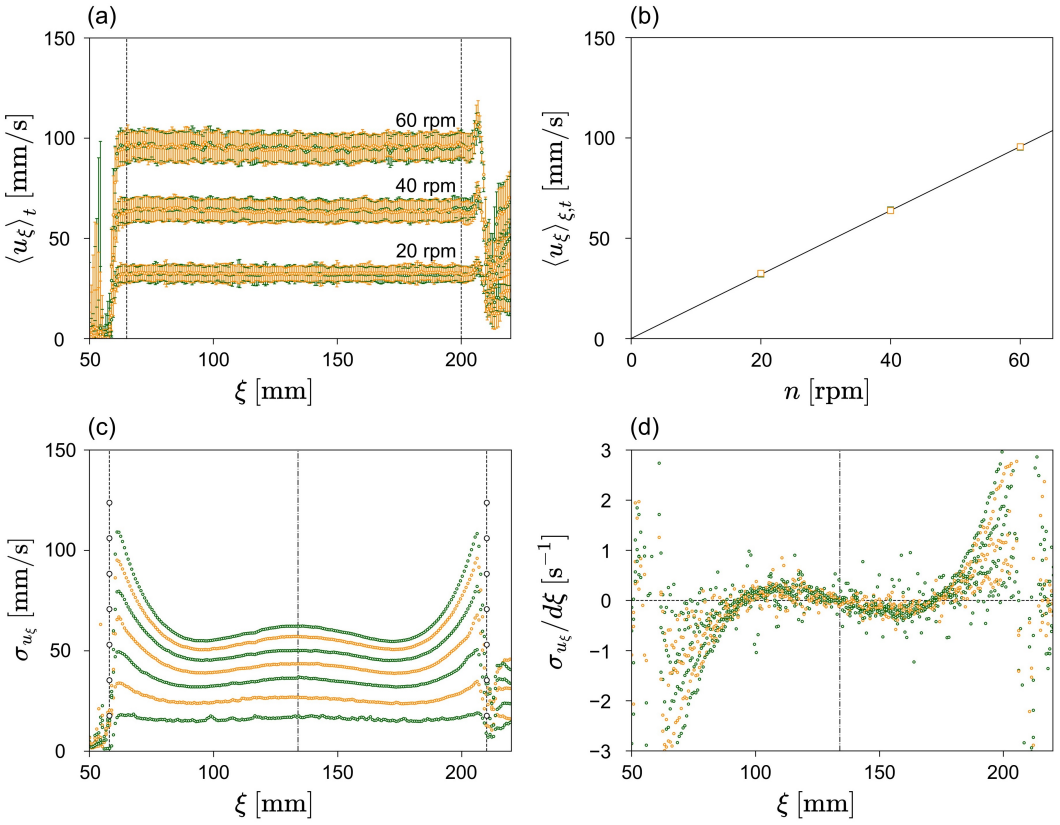


FIGURE 5.9: Velocity profiles of the CMC 1.0 wt.% aqueous solution measured by UVP: (a) mean velocity profiles under different rotation speed n, (b) spatially averaged values of the mean velocity profiles in the range surrounded by dashed lines in figure (a), (c) effective values of the velocity captured by UVP in the time direction ,where the oscillation frequency is f_o = 0.5 Hz and the rotation amplitude Θ was varied every 30 deg from Θ = 30 deg to Θ = 210 deg, and (d) spatial derivative of the effective values of the velocity. The solid line in figure (b) is a regression line passing through the origin to determine the off-axis. The dotted lines in figure (c) indicate the estimated locations of the cylindrical wall, and dashed line in figure (c) and (d) is the middle point of the two wall positions.

UVP is around 1 = mm, this result is considered to be a reasonable agreement and it would be difficult to determine the wall positions more accurately only from the the velocity distribution obtained by UVP.

Figure 5.10 shows comparison of the predicted oscillatory shear flow and experimental results in the double concentric cylinders.The oscillation parameters are f_o = 0.5 Hz and $\Theta = \pi$ rad in Fig 5.10(a) and (b) and f_o = 1.0 Hz and $\Theta = \pi/2$ rad in Fig. 5.10(c) and (d). The solid lines are the predicted results, and the symbols are the experimental results obtained by transforming the original velocity and coordinates $u_\xi(\xi, t)$ using the geometric conditions determined above. Good agreement can be confirmed in both amplitude and phase distributions. These results reinforce the validity of the reconstruction method and the off-axis and wall position determination methods.

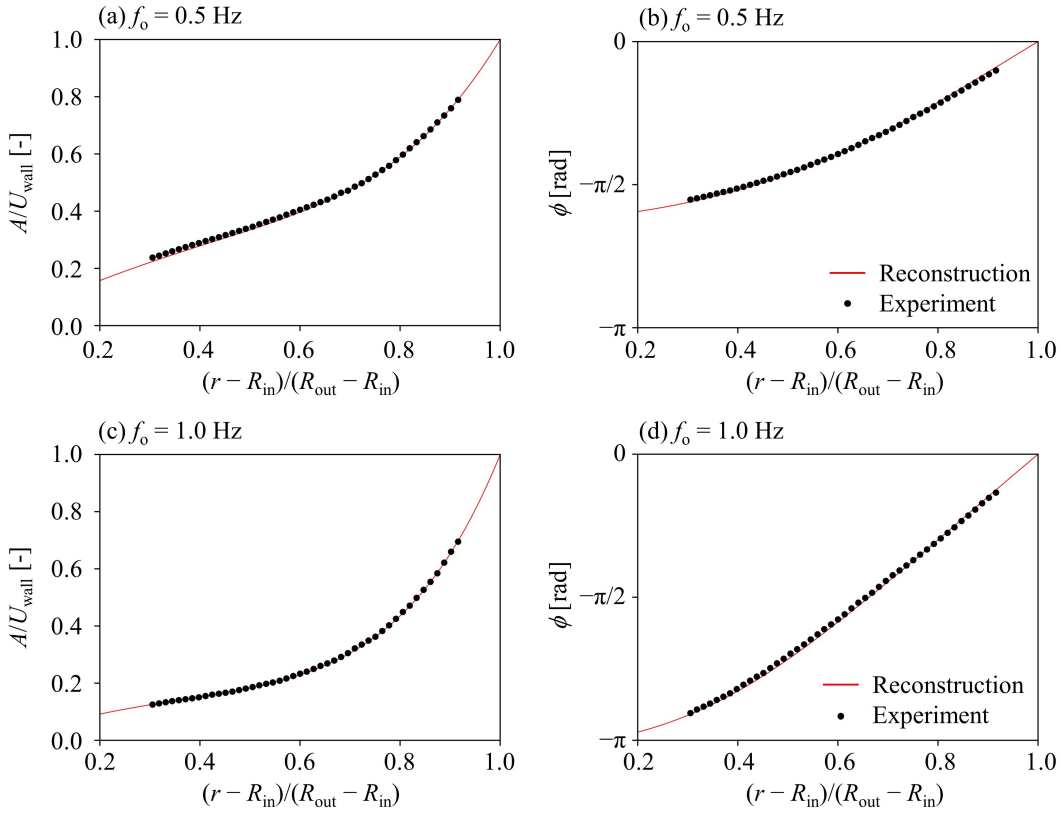


FIGURE 5.10: Comparison of the predicted and experimental velocity profiles of the CMC 1.0 wt.% aqueous solution: spatial profiles of the velocity amplitude A and phase lag from the outer cylindrical wall ϕ, where the oscillation parameters are f_o = 0.5 Hz and $\Theta = \pi$ rad for (a) and (b), f_o = 1.0 Hz and $\Theta = \pi/2$ rad for (c) and (d).

5.2 Steady shear flow in a circular pipe

As fundamental examples of flow prediction based on the rheological data obtained by the velocity-profiling-based rheometry, unidirectional shear flow in a circular pipe is focused here. In the vessel of the proposed rheometry, the rheological properties under steady or oscillatory shear conditions are evaluated. Based on these data, it can be expected that the shear dominant flows in the pipe can be predicted. Flow prediction under steady pressure gradient is examined in this section, and the next section deals with unsteady pulsating pressure conditions. The geometry is relatively simple but the most practical one in industrial applications as almost all the pipeline mainly consists of straight pipe sections.

5.2.1 Test materials and rheological measurement

As application examples, four test fluids were examined using the velocity-profiling-assisted rheometer (see photographs in Fig. 5.11). The first represented a Newtonian fluid: silicon oil (Shin-Etsu Chemical Co., Ltd., Japan) with a viscosity of 0.29 Pa · s. The second was carboxymethyl cellulose (CMC), as 0.8 wt.% aqueous solution (CMC1190, Daicel Miraizu Ltd., Japan; Fig. 5.11(a)) with molecular weight of 8.2×10^5. It has weak shear-thinning properties (Kulicke et al., 1996; Ghannam and Esmail, 1997; Benchabane and Bekkour, 2008) and is used as a thickener for foods

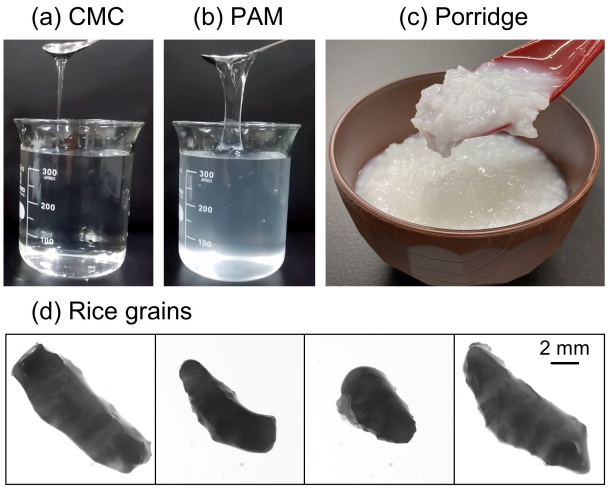


FIGURE 5.11: Photographs of (a) carboxymethyl cellulose (CMC) and (b) polyacrylamide (PAM) aqueous solutions, (c) rice porridge, and (d) photomicrographs of a rice grain in the porridge.

and cosmetics. The third test fluid was polyacrylamide (PAM), used as 0.8 wt.% aqueous solution (Accofloc N-100S, MT AquaPolymer Co., Ltd., Japan; Fig. 5.11(b)) with molecular weight of 1.3×10^7. The PAM solution has strong viscoelasticity and shear-thinning properties (Ghannam and Esmail, 1998; Lewandowska, 2007; Ohie et al., 2022a). These characteristics make it unsuitable for standard torque-type rheometer measurements because of shear-localization problems, so the PAM solution is a challenging target for demonstrating applicability of the velocity-profiling-assisted rheometer. The fourth test fluid was rice porridge, as shown in Fig. 5.11(c). This is a well-known commercial item (TableMark Co., Ltd., Japan) in Japan. The original porridge with 300 mL of pure water added per liter was used in the experiments. Shape of the rice grains is almost ellipsoid having minor axis of 5 mm and major axis of 10 mm at most and they are in wet as shown in Fig. 5.11(d). These rice grains were not separated, so this example represents a complex fluid that may not be measured correctly by a standard rheometer, but for which there is high demand from the food and chemical industries.

A small amount of tracer particles (CL-2507, Sumitomo Seika Chemicals Co., Ltd., Japan) of 0.92 g/mL density and 180 μm mean diameter was added to the silicon oil to serve as ultrasonic reflectors for the UVP measurements. For the CMC and PAM solutions, different particles (CHP20/P120, Mitsubishi Chemical Co. Ltd., Japan) of 1.01 g/mL density and 75 – 150 μm mean diameter were used to satisfy the neutrally buoyant condition. As in the case of the silicon oil, 5 g of the tracer particles were added per 1 L of each solution. There was no need to add particles to the porridge because the rice grains themselves acted as ultrasonic reflectors. Temperature of the test fluids was kept at 25.0 ± 0.5°C in all experiments by use of a thermostatic chamber and air conditioning.

Rheological properties of the four test fluids were examined using the velocity-profiling-assisted rheometer. Rotation speed of the outer cylinder was gradually increased by 2 rpm from 0 rpm to 40 rpm for the CMC and PAM solutions and from 0 rpm to 50 rpm for the porridge. In each condition, axial torque and velocity measurements were conducted a minute after the rotation speed increased for assuring the flow fully developed. The obtained flow curves were statistically analyzed as

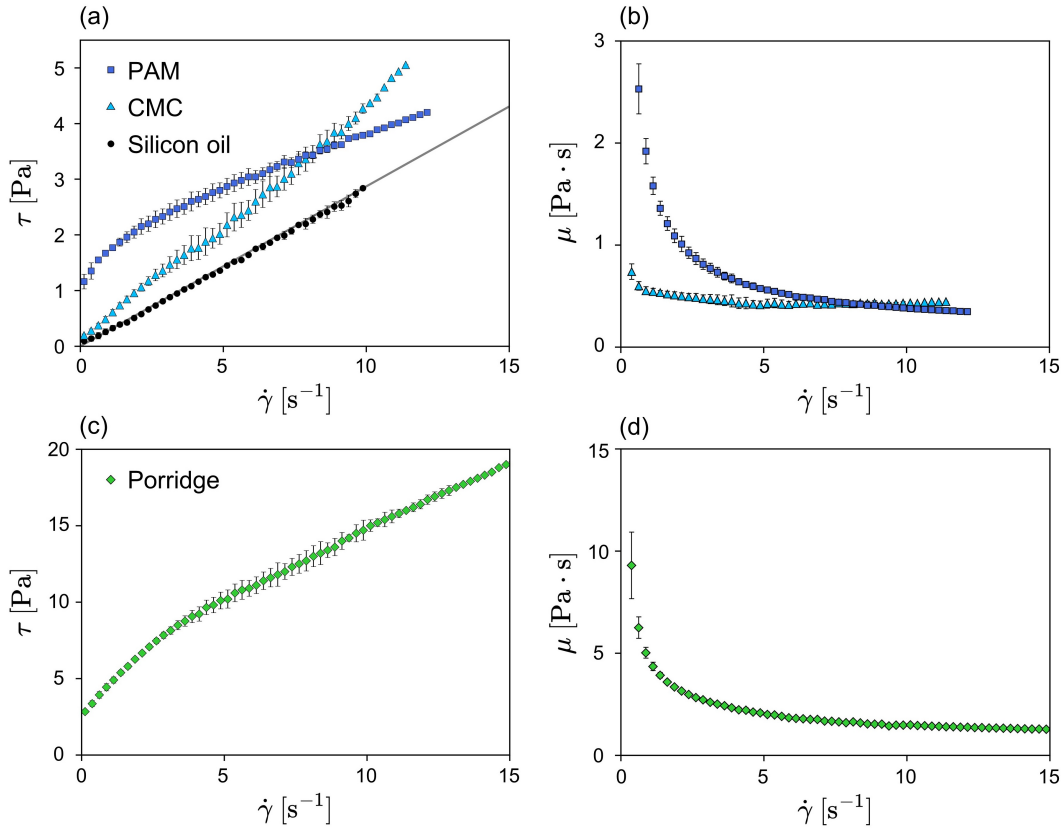


FIGURE 5.12: Rheological properties of test fluids examined by the velocity-profiling-assisted rheometer. (a) Flow curves of silicon oil and CMC and PAM solutions, where the solid line represents the flow curve of a Newtonian fluid with a viscosity coefficient of 0.29 Pa · s. Error bars represent standard deviations. (b) Viscosity curves of CMC and PAM solutions converted from the flow curves. (c) Flow curve and (d) converted viscosity curve of rice porridge.

mentioned previously. Regarding instability limitation of the azimuthal flow between the double cylinders, the maximum Reynolds numbers of the outer and inner cylinders are $Re_{\text{out}} = O(10^0)$ and $Re_{\text{in}} = 0$. The flow is therefore assured as laminar Couette flow according to the flow regime map (Andereck, Liu, and Swinney, 1986).

Flow curves of the silicon oil and CMC and PAM solutions are summarized in Fig. 5.12(a). The solid line represents the flow curve of a Newtonian fluid with a viscosity of 0.29 Pa · s, which corresponds to the catalog value of the silicon oil. The flow curve of the silicon oil is consistent with the solid line, which validates measurements using the torque-rheometer coupled with UVP (see § 2.2). The error bars of the silicon oil were shorter than those of other test fluids. As mentioned previously, the standard deviations also reflect precision of the shear rates calculated from the velocity distribution measured by the UVP. Quality of the velocity date of the silicon oil was better than others because acoustic impedance difference of the solvent and tracer particles for the UVP measurement was the highest in all the test fluids.

In contrast to the silicon oil, the CMC and PAM solutions seemed to have finite values at the lowest shear rate, of 0.20 ± 0.02 (standard deviation) Pa and 1.16 ± 0.13 Pa, respectively. These are attributed to yield stresses; therefore, these fluids hence do not flow until a certain shear stress is applied. These flow curves were

converted to viscosity curves, as shown in Fig. 5.12(b) using the relationship of $\mu = \tau/\dot{\gamma}$. Viscosity of the solutions decreased as shear rate increased, i.e., these fluids exhibited shear-thinning properties. The PAM solution showed remarkable shear-thinning because its molecular weight is much higher than that of the CMC solution. Shear-rate-dependent stress and viscosity of the porridge are shown in Fig. 5.12(c) and (d), respectively. Yield stress and shear-thinning properties are confirmed. The yield stress of 2.83 ± 0.09 (standard deviation) Pa and viscosity were, however, much higher than those of the CMC and PAM solutions because the porridge contained rice grains at a volume fraction close to the packing limit. Flow curves were also obtained by decreasing rotation speed of the outer cylinder, but they matched with those in Fig. 5.12: there are no thixotropic effects in timescale of $O(10\ \mathrm{min})$.

5.2.2 Flow prediction and experimental verification

Prediction protocol

A methodology for predicting a shear flow velocity profile in a circular pipe under a steady pressure gradient is briefly introduced. Assuming the flow is axially symmetric and dominates in one direction, as shown in Fig. 5.13(a), axial velocity u, shear stress τ, and pressure gradient in the axial direction $\alpha(t) = -\partial p/\partial x$ satisfy the following equation (González and Moraga, 2005; Poole and Ridley, 2007; Tasaka, Yoshida, and Murai, 2021):

$$\rho \frac{\partial u(r,t)}{\partial t} = \alpha(t) + \left(\frac{\partial}{\partial r} + \frac{1}{r}\right)\tau(r,t), \tag{5.23}$$

where ρ is fluid density. Under a steady-state condition, i.e., $\partial/\partial t = 0$ and α is constant, the spatial profile of the shear stress $\tau(r)$ is determined from Eq. 5.23 independent of whether the fluid is Newtonian or non-Newtonian (Ouriev and Windhab, 2002; Wiklund, Shahram, and Stading, 2007):

$$\tau(r) = -\frac{\alpha r}{2}. \tag{5.24}$$

The velocity-profiling-assisted rheometer provided the flow curves, as shown in Fig. 5.12(a) and (c), so $\tau(r)$ is uniquely converted to a spatial profile of shear rate $\dot{\gamma}(r)$. In axial flow, shear rate is defined as:

$$\dot{\gamma}(r) = \frac{du}{dr}. \tag{5.25}$$

Therefore, $u(r)$ is obtained by integrating Eq. 5.25 under the boundary conditions of $u(r = R) = 0$, which reflects a non-slip condition on the pipe wall. This assumption is adopted because slip flow was not confirmed in all the velocity data measured in the velocity-profiling-assisted rheometer. In a case that slip condition at the wall is detected by the rheometer, the boundary condition has to be changed. The prediction protocol above assumes laminar shear flow and that the flow curve of the target fluid is unique with respect to applied shear rate.

Experimental setup for verification

A pilot pipeline was built in the laboratory for validation of this proposed prediction protocol. The experimental setup was a circulation circuit that connected a storage tank and rotary lobe pump with stainless pipes with an inner diameter of $2R = 50$ mm. A test fluid in the tank was drawn to the pump through the pipe and

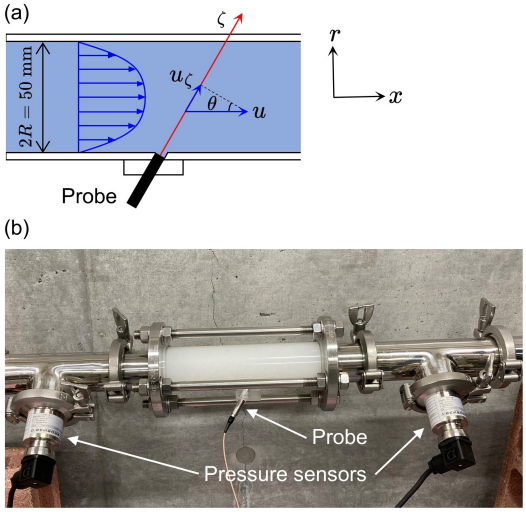


FIGURE 5.13: Pilot pipeline used for verification experiments: (a) schematic of a measurement section attached in pilot pipeline and geometric conditions for UVP measurement, and (b) photograph of measuring unit in the pipeline, showing flow of the porridge as a test fluid.

returned to the tank through another pipe. Flow rate is roughly correlated with rotation speed of the pump. A photograph of a measuring unit attached to the returning pipe is shown in Fig. 5.13(b). The measuring unit was located more than 1.5 m apart from the rotary pump for assuring that the flow is fully developed. Because one of the test fluids was opaque, UVP was suitable for measuring the spatial profile of the axial velocity $u(r,t)$. The ultrasonic transducer was installed at an angle of about $\theta = 30°$ with respect to the direction perpendicular to the axial flow, as shown in Fig. 5.13(a). As there are individual differences in the emission angle of the UVP measurement line, and the angle also changes depending on how the transducer is sealed, the estimation of the angle in the measurement will be denoted at the end of this section. With assumptions of axial symmetry and one-directional flow, the velocity distribution $u_\zeta(\zeta,t)$ captured by the UVP was converted to $u(r,t)$ using the relationship of $u = u_\zeta/\sin\theta$. Synchronously with the velocity measurement, two pressure sensors (DMK351P, BD Sensors GmbH, Germany), installed on each side of the UVP section, were used to measure the pressure gradient. Predictions were compared with experimental results under the same pressure-gradient conditions.

Comparison of predicted and experimental results

Spatial profiles of the axial velocity were predicted under different pressure-gradient conditions based on the rheological properties obtained using the velocity-profiling-assisted rheometer as shown in Fig. 5.12 (a), (b) and (c) with solid lines. As shown in Fig. 5.12(a) and (c), the maximum shear stresses are 5.1 Pa for the CMC solution, 4.2 Pa for the PAM solution, and 19.0 Pa for the porridge, and these correspond to the maximum pressure gradients obtained by Eq. 5.24, 408 Pa/m for the CMC solution, 336 Pa/m for the PAM solution, and 1520 Pa/m for the porridge. For the PAM solution, the flow curve was linearly extrapolated with a constant gradient identified in shear rate range of 6 to 12 s^{-1} for predicting flows in higher pressure

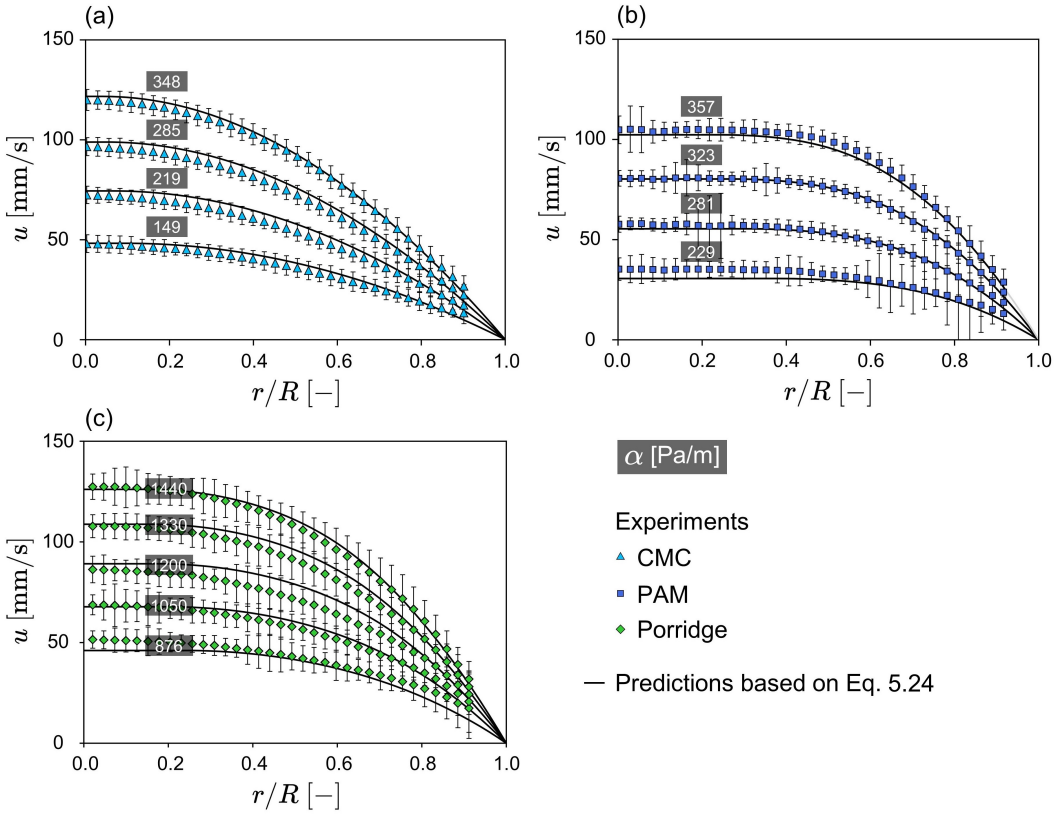


FIGURE 5.14: Comparison of predicted and measured results for (a) CMC, (b) PAM, and (c) porridge. Symbols are measured results obtained by UVP, where the error bars indicate standard deviations. Solid lines are predictions based on the rheological properties evaluated by the velocity-profiling-assisted rheometer. In the graph (b), radial range, where the velocity profile was predicted with the extrapolated flow curve, is shown with gray solid line. The numbers in white on each line indicate the pressure-gradient conditions.

gradient conditions tentatively. Radial range, where velocity profile was predicted with the extrapolated information, is shown with gray solid line in Fig. 5.14(b).

Corresponding experimental results are shown by symbols and error bars in Fig. 5.14. The UVP measurement was conducted for each test fluid with time resolution of 25 ms for 3000 profiles. Average values and standard deviations were calculated at each radial position, which are shown by the symbols and error bars in Fig. 5.14. Velocity information is lost close to the cylinder wall, r/R = 1.0, because this region includes the so-called near field, where the ultrasonic beam is not fully formed. Measurement precision of the porridge was statistically worse than that of the CMC and PAM solutions in the flow curves and velocity profiles in the circular pipe. This is attributed to precision of the UVP measurement. Acoustic impedance difference of solvent and tracer particles is higher in the case of the CMC and PAM solutions, quality of the velocity measurement data obtained by UVP was therefore better than those of the porridge. In addition, quality of the UVP measurement was blurred because of the attenuation of the ultrasonic pulses by the rice grains with a volume fraction close to the packing limit.

The lowest viscosity of the target fluids was $O(0.1\ \mathrm{Pa \cdot s})$, as shown in Fig. 5.12(b), the corresponding velocity intensity in the pipe was $O(100\ \mathrm{mm/s})$, as shown in

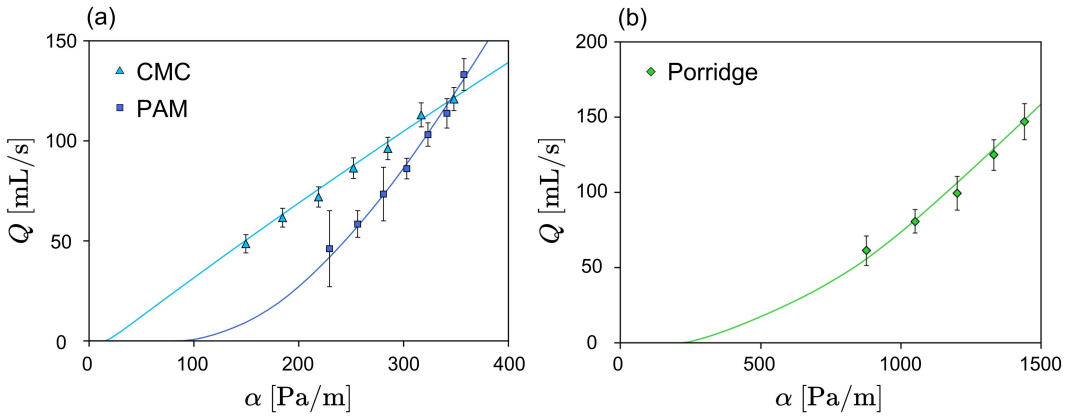


FIGURE 5.15: Pressure loss–flow rate relationships for (a) CMC and PAM solutions and (b) porridge. Solid lines and symbols are the respective predicted and experimental results obtained by integration of the velocity profiles shown in Fig. 5.14. Error bars indicate three times the standard deviation.

Fig. 5.14, and the pipe diameter, which is a representative length scale, was $O(10\,\mathrm{mm})$, so the Reynolds number was $O(10)$. Therefore, use of Eq. 5.23, which assumes laminar flow, holds well. In addition, inlet length estimated with a well-known formula $0.065ReD$ was $O(0.1\,\mathrm{m})$ at most, where D represents diameter $2R = 50$ mm. The flow in the measuring unit was therefore fully developed.

Considering the measurement precision of the experiments, as shown by the error bars in Fig. 5.14, the predictions are in good agreement with the measurement results for all cases of the three test fluids. The CMC solution had the lowest yield stress and weak shear-thinning, so the velocity profiles are similar to parabolic shapes as shown in Fig 5.14 (a), i.e., Poiseuille flows. The PAM solution had relatively higher yield stress and strong shear-thinning, so the profiles are flat near the center of the axis as shown in Fig. 5.14 (b). These characteristic flow shapes were well reproduced by the predictions. More surprisingly, the predictions also worked well for the case of the rice porridge: similar to the PAM solution, this fluid had relatively high yield stress and strong shear-thinning, so the velocity profiles were flat around the axis as shown in Fig. 5.14 (c). In the case of the rice porridge, the difference between the measured and predicted velocity profile is particularly pronounced near the wall under the lowest pressure gradient condition. This may indicate that the assumption of non-slip at the wall is not fully satisfied, and more accurate predictions can be made by performing numerical calculations taking slip characteristics into account.

From the viewpoint of industrial application, it may be more attractive to estimate the relationship between pressure loss and flow rate. The flow rate Q was obtained from the velocity profiles in Fig. 5.14 using the following integral operation:

$$Q = \int_0^R u(r)\, 2\pi r dr. \tag{5.26}$$

Velocity profiles were lost near the wall in the experiments because of the near field, so they were extrapolated in the radial direction using a non-slip assumption. The relationships between pressure gradient and flow rate are shown in Fig. 5.15(a) for the CMC and PAM solutions, where the solid lines and symbols are the predicted and experimental results, respectively. In addition to the four conditions displayed

in Fig. 5.15(a) and (b), the experimental results for another three pressure gradients were added, giving a total of seven conditions plotted in Fig. 5.15(a) for each solution. Based on these performance curves, the CMC and PAM solutions seem to need a certain pressure gradient to initiate flow because they have yield stresses. In particular, the PAM solution needs a higher pressure gradient for flow to start, but the flow rate rapidly increases because this solution has remarkable shear-thinning properties, as shown in 5.12(b). The performance curve of the porridge is shown in Fig. 5.15(b). Similar to the CMC and PAM solutions, this fluid needed a certain pressure gradient for flow to start, following which the flow rate increased nonlinearly with the pressure gradient because of shear-thinning. Relative error was calculated at each pressure-gradient condition. The relative error here is defined as $\epsilon_R = (Q_\mathrm{p} - Q_\mathrm{e})/Q_\mathrm{e} \times 100\%$, where Q_p and Q_e represent flow rates evaluated in the prediction and experiment, respectively. The maximum relative errors are 5.3% at α = 219 Pa/m for the CMC solution and −9.3% at α = 229 Pa/m for the PAM solution. In the case of the porridge, the maximum relative error is −9.4 % at α = 876 Pa/m. Considering that the velocity profiles in the verification experiments were measured by UVP, the precision of which is shown by the error bars in Fig. 5.15, all predictions are considered to fall within acceptable ranges.

Noteworthy here is robustness of the rheological characterization and flow prediction scheme and its high applicability to complex fluids. Multiphase fluids containing O(1 mm) size dispersion, such as the porridge, which can be treated as a continuum approximation for the scale of the UVP measurement volume, are included in application of this rheological characterization and flow prediction. This proposed methodology does not assume any rheological models based on constitutive equations, so the same protocol can immediately be applied to other complex fluids. Engineers involved in numerical simulations of non-Newtonian fluids may have experienced difficulties in selection of rheological models: flow prediction by utilizing the velocity-profiling-assisted rheometer will be a practical tool for use in industrial fields.

Technical note and precision of pressure measurement

As explained in the previous section, making these comparisons requires accurate experimental measurements. When measuring the flow inside a pipe, the actual beam angle of the ultrasonic pulse waves deviates from the ideal one due to errors in machining the TDX holder, how the sealing tape is wrapped, individual differences in the TDX, etc. As shown in Fig. 5.13(a), when the angle between the transducer and one-directional flow is θ, the velocity in the axial direction is obtained as $u = u_\zeta/\sin\theta$. Therefore, the maximum velocity captured by UVP can be increased by reducing θ to a few degrees, but it should be noted that at such a small θ angle, the error in the flow velocity also increases. In UVP-PD (Ouriev and Windhab, 2002) and the pipe flow experiments in this paper, θ is set in the range of 20 to 30 degrees, so the effect of the error in θ on the velocity measurement is only a few percent at most. In this subsection, some effective methods for determining the positions of the pipe wall and the actual angle θ estimated from the velocity and echo distributions obtained by UVP are denoted as technical notes.

Figure 5.16(a)–(c) summarize the velocity distributions of the CMC and PAM solutions, and porridge used in the above experiments under steady pressure gradient conditions. The distributions of CMC and PAM solutions under 4 conditions corresponding to Fig. 5.14(a)–(b) and porridge under 5 conditions corresponding to Fig. 5.14(c) are shown in different colors. The symbols indicate time average values,

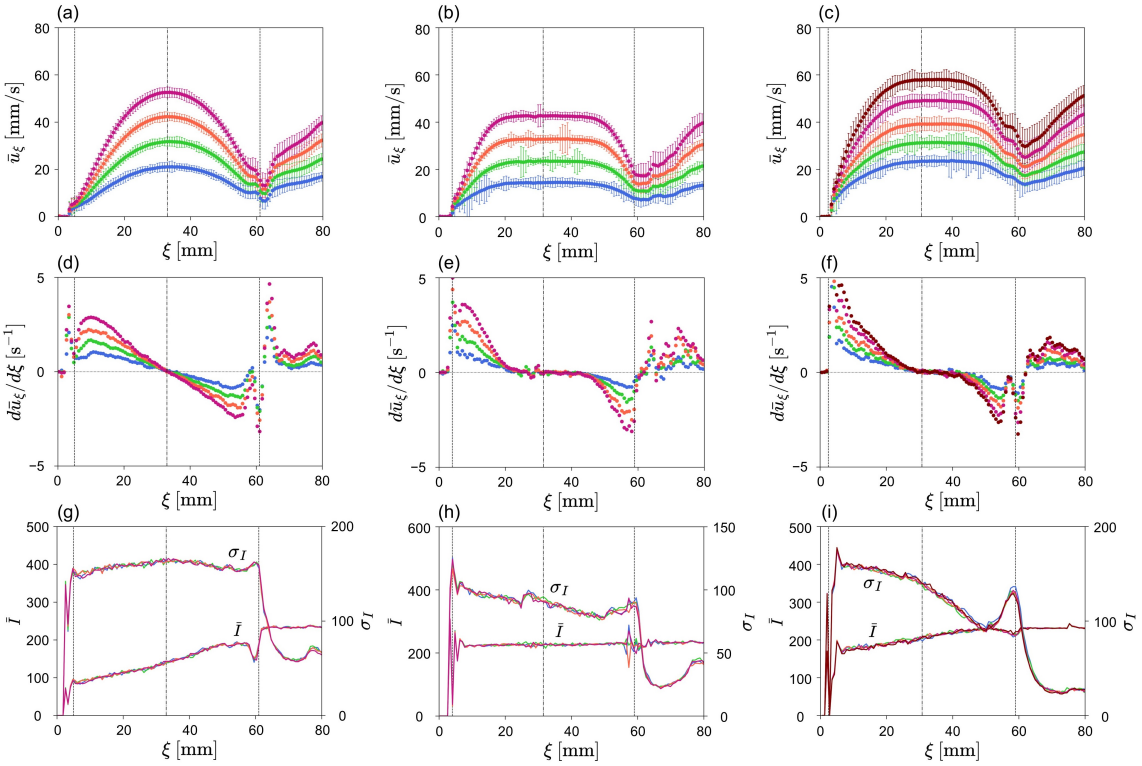


FIGURE 5.16: Velocity and echo distributions obtained by UVP: time averaged velocity distributions $u_{\bar{\xi}}(\xi)$ under different steady pressure gradient conditions for (a) the CMC solution, (b) the PAM solution, and (c) the porridge, where the spatial derivatives of these velocity profiles are shown in the middle row. The graphs in the bottom row indicate spatial distribution of the time averaged values $\bar{I}$ and standard deviations σ_I of the echo signal outputted from the UVP device for each solution.

and error bars represent standard deviations. First, a possible method for determining the position of the front wall is to assume non-slip condition on the surface and extrapolate the velocity distributions to identify the zero-crossing point. The left dashed lines shown in Fig. 5.16(a)–(c) represent the wall position estimated using this method. Accordingly, one possible way for determining the position of the opposite wall is to consider the point where the shear rate is zero as the axial center, and use it as a reference to determine the opposite wall position and angle θ. The radial gradients of the average velocity distributions are shown in Fig. 5.16(d)–(f). This method is effective when the velocity gradient distribution crosses zero neatly as in the CMC solution shown in Fig. 5.16(d), but when the fluid has yield stress such as the PAM and porridge, they have a plug flow at the center, so it is not easy to explicitly determine the center position as shown in Fig. 5.16(e) and (f). Therefore, a method using the UVP echo data is proposed here. Figure 5.16(g)–(i) show the time average values and standard deviations of the spatiotemporal echo information outputted from the UVP device. In all the distributions, sharp changes in the profiles of the mean values and standard deviations can be seen around $\bar{\xi}$ from 59 to 61 mm, and it is expected that the opposite wall exists around here. In the region where the fluid containing tracer particles passes, there are time fluctuations in the echo signal, and the standard deviations should be larger than in the solid wall. Here, the point

where the standard deviation begins to decrease is regarded as the wall position. The wall positions determined according to this method are shown by the dashed lines on the right side in Fig. 5.16, and the resulting center positions are shown by the dotted lines. In the results of the CMC solution, the center position determined by this method matches wit the position where the shear rate is zero, reinforcing the validity of the method. The angle of the transducer estimated from these wall positions θ is between 24.6 and 27.8, assuming the pipe inner diameter is 50 mm. The error in the velocity measurement due to these angle differences is only a few percent and does not essentially affect the conclusions of this thesis, but as pointed out by Yoshida, Wada, and Furuichi (2023), it is important to note that the actual angle of the measurement line is not necessarily the set angle.

This angle θ corresponds to Δy in the cylindrical system used in USR. In the case of the cylindrical vessel, Δy can be identified by measuring the rigid body rotation as explained earlier, but in the case of a pipe flow, there is no equivalent operation. One possible way is to perform the method recently proposed by Yoshida, Wada, and Furuichi (2023) in-site in the acrylic pipe, but the presence of the interface wold be the method much more difficult. Another method, very classic, is to measure flow rate using a scale and stopwatch. The wall positions and the angle θ are determined to be consistent with the flow rate. However, this requires a large amount of test fluid, as it is desirable to keep the liquid level in the tank constant so as not to change the pressure inside the pipe. Therefore, the method proposed above based on the velocity and echo distributions would be the simplest method, and in order to reinforce its validity, verification experiments using a Newtonian fluid were performed and the results are summarized below.

Silicon oil with a catalog kinematic viscosity of ν = 300 cSt was used as the test fluid. The corresponding viscosity coefficient is μ = 2.91 Pa·s with the density of ρ = 967 kg/m^3 and at room temperature 25°C. The outline of the verification way is that the wall positions and θ are estimated using the method based on the velocity and echo distributions obtained by UVP, and then the original velocity distributions are converted to those of the axial velocity. Fitting is performed on these distributions based on Poiseuille flow distribution to estimate the pressure gradient. Then, it is verified whether the estimated pressure gradient matches one actually measured by pressure sensors. Figures 5.17(a) and (b) show the average velocity distributions and echo information obtained under nine conditions of steady pressure gradient. Similarly, for the pulsating condition, the velocity and echo distributions are shown in the lower rows, where the oscillation frequencies are 0.2, 0.3, and 0.5 Hz, respectively. First, by extrapolating the velocity distributions on the near side, the initial wall position is estimated to be around ξ = 4.5 mm. Next, in the distributions of the standard deviations, it is found that the value decreases rapidly at ξ = 59.5 mm in Fig. 5.17(b), (e), (h), and (k), and it is estimated that the other wall position exists around this point. The axis center determined from these two wall positions is indicated by the dotted lines in Fig. 5.17(a), (d), (g), and (j), and corresponds to the maximum points of the parabolas. Also, the angle of the UVP measurement line θ estimated from these wall positions is θ = 25 deg.

The axial velocity distributions transformed with the identified geometric conditions are shown in Fig. 5.17(c), (f), (i), and (l). The pressure gradient is estimated by fitting each velocity distribution with the Poiseuille flow distribution. The velocity distribution of a Newtonian fluid under a steady pressure gradient is

$$u(r) = -\frac{\alpha R^2}{4\mu}\left[1 - \left(\frac{r}{R}\right)^2\right], \tag{5.27}$$

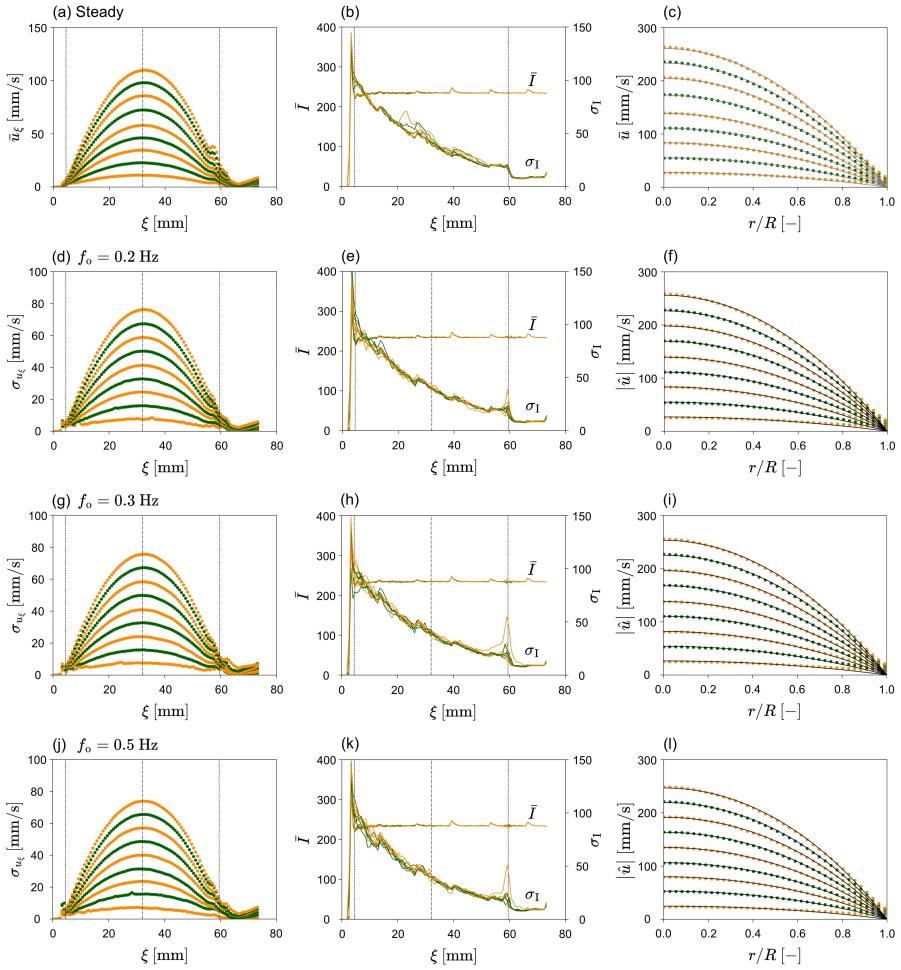


FIGURE 5.17: (a) Time averaged velocity $\bar{u}_\xi$ under steady pressure gradient conditions, (b) time averaged values $\bar{I}$ and standard deviations σ_I of the echo signal, and (c) the converted axial velocity $\bar{u}_\theta$. (g) Effective values of the velocity σ_{u_ξ} under f_o = 0.2 Hz, (h) time averaged values and standard deviations of the echo signal, and (i) the amplitude of the axial velocity $|\hat{u}|$. The graphs in the bottom two rows correspond to those under f_o = 0.3 Hz and 0.5 Hz.

with the pressure gradient α in the axial direction and pipe radius R. When the pressure gradient is given as $\alpha\sin(\omega_o t)$, the velocity amplitude at each radial position is given as

$$u(r) = -\frac{\alpha}{\omega_o \rho}\left(1 - \frac{J_0(\zeta)}{J_0(\zeta)_{r=R}}\right),\ \zeta = (i-1)r\sqrt{\frac{\omega_o}{2\nu}} \tag{5.28}$$

where ν is the kinematic viscosity defined as $\nu = \mu/\rho$ with density of ρ. J_0 is the zero-order Bessel function of the first kind defined as

$$J_0(\zeta) = \sum_{m=0}^{\infty} \frac{(-1)^m}{m!\Gamma(m+1)}\left(\frac{\zeta}{2}\right)^{2m}. \tag{5.29}$$

Using these two equations, fitting was performed to the velocity distributions as shown in Fig. 5.17(c), (f), (i) and (l) with solid lines. It can be seen that under all conditions, the fitting curves closely match the experimental results shown with the

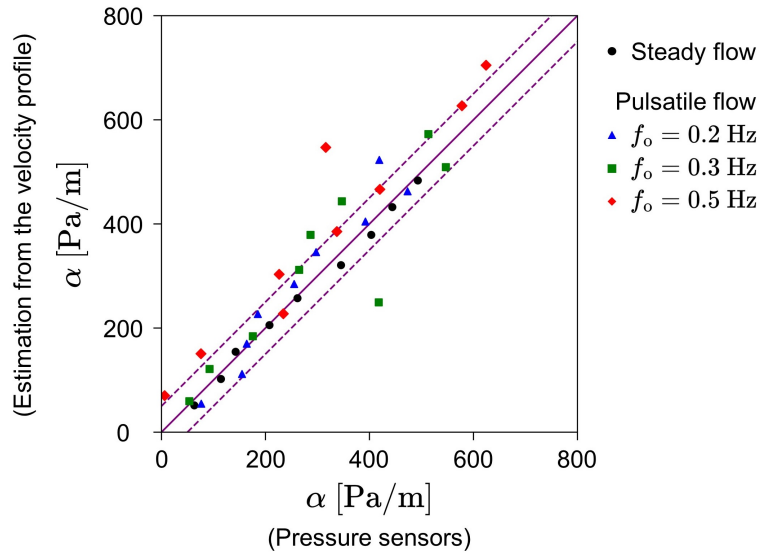


FIGURE 5.18: Comparisons of the measured pressure gradients with the two pressure sensors and those estimated from the velocity profiles obtained by UVP. The solid line shows the state where these values are exactly the same, and the dashed lines show the cases when the solid line is shifted up or down by ±50 Pa/m.

symbols. In parallel with the UVP measurements, pressure sensors were install before and after the UVP measurement section, and the actual pressure gradients were measured. The comparisons of the actual measured values and those estimated from the UVP data are shown in Fig. 5.18. The solid line shows the state where these vales are exactly equal, and the dashed lines show the cases when the line is shifted up or down by ±50 Pa/m, where most symbols are included between these dashed lines. As the pulsation frequency f_o increases, the symbols tend to move away from the solid line, but this is thought to be a problem with the pressure sensors because while the displacement of the symbols increases smoothly along the vertical axis, the amount of the displacement in the horizontal direction is sparse. Under steady pressure gradient conditions, where pressure measurement is most reliable, they are concentrated very close to the solid line, which is a strong evidence that reinforces the validity of the above method for determining the wall positions and angle θ from the velocity and echo distributions.

5.3 Oscillatory shear flow in a circular pipe

In this chapter, an attempt is made to predict pulsatile flow as a representative example of unsteady flow in a circular pipe. It is shown that the unsteady flow in a circular pipe can be reconstructed based on the rheological property information obtained by linear viscoelastic analysis of USR. The flows in USR and circular pipe are dominated by shear deformations in the azimuthal and axial directions, respectively, both are however simple shears from a view point of the principle coordinate. The viscoelasticity evaluated by USR are therefore compatible with the pipe flow prediction. In this section, there are two polymer solutions examined, carboxymethyl cellulose (CMC) and polyacrylamide (PAM) aqueous solutions, which are representations of shear-thinning and viscoelastic fluids, respectively. Under the same condition of the

pulsatile pressure gradient, prediction and experimental result in a circular pipe are compared for evaluating the accuracy of the scheme.

In § 5.3.1, basic characteristics of the two solutions and measurement section attached into the pipe line system are explained. In § 5.3.2, theoretical background of the prediction scheme, which ensures reversibility with the viscoelasticity evaluated by USR, is established. At the beginning of § 5.3.3, the viscoelasticity of the CMC and PAM solutions evaluated by USR are summarized. Under the same condition of pulsatile pressure gradient, predictions based on the scheme are compared with experimental results in the pipe line system for verification of both the rheological measurement and flow reconstruction.

5.3.1 Test fluids and experimental setup

Basic characteristics of the test fluids

There are two kinds of polymer solutions examined. One is carboxymethyl cellulose (CMC) aqueous solution (CMC1190, Daicel Miraizu Ltd., Japan), which is generally known as shear-thinning property (Benchabane and Bekkour, 2008; Kulicke et al., 1996). The other is polyacrylamide (PAM) aqueous solution (Accofloc N-100S, MT AquaPolymer Inc., Japan) as a viscoelastic fluid (Ghannam and Esmail, 1998; Lewandowska, 2007). Viscoelasticity of these solutions have been investigated in detail using USR in previous study (Ohie et al., 2022a). Under oscillatory shear flows, viscosity of the CMC solution strongly depends on the effective shear rate, while that of the PAM solution depends on the effective shear strain (Ohie et al., 2022a). The PAM solution exhibits more remarkable shear-thinning and elasticity than the CMC solution. In the experiments, 0.8 wt.% CMC and PAM aqueous solutions were prepared. As tracer particles for UVP measurement, 30 g of fine spherical particles (MCI GEL CHP20/P120, Mitsubishi Chemical Co. Ltd., Japana) were mixed with 30 L of each solution. Temperature of the solutions was maintained at 25°C by air conditioning and a thermostatic chambers in all the experiments.

Measurement section attached into the circulating system

A circulating pipeline system was prepared to verify the validity of the predictions. The flow is driven by a rotary pump under rotation speed control. For example, a steady shear flow is realized in the circular pipe under a constant rotation speed while a pulsatile flow is generated by changing the rotation speed of the pump with sinusoidal manner over time. Temperature of the test fluid is controlled by air conditioning and a storage tank located on the opposite side of the pump (Figure is not shown.). A flow adapter schematically shown in Fig. 5.19 was attached to a part of the pipeline to measure velocity distribution and pressure gradient, where the radius is $R = 25$ mm. The adapter was located more than 1 m away from the pump and the storage tank, which is long enough entrance length for the sticky test fluids in the experiments.

An ultrasonic probe of UVP is directly inserted to the pipe wall with an angle of about $\theta_1 = 30$ deg to avoid multiple reflections of ultrasonic waves in the acrylic wall. Such an attachment method is also adopted in other literature (Ouriev and Windhab, 2002; Birkhofer et al., 2008), and the effect of a small step around the probe on the mainstream can be sufficiently ignored in the case of relatively high-viscosity fluids appearing in the experiment. Assuming an axial flow, spatial and temporal distribution of the axial velocity $u(r,t)$ is obtained by the relation $u = u_{\tilde{\xi}}/\sin\theta_1$.

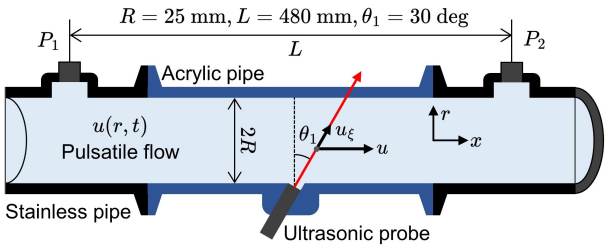


FIGURE 5.19: Schematic diagram of a flow adapter installed in the pipeline system for experiments to verify the validity of the flow prediction. Ultrasonic probe and two pressure sensors are installed to measure time variations of velocity profile $u(r,t)$ and pressure gradient $\alpha(t)$.

Pressure sensors (DMK351P, BD Sensors GmbH, Germany) were installed at a distance $L = 475$ mm to measure the time variation of the pressure gradient inside the pipe synchronously with the velocity measurement as shown in Fig. 5.19. Pressure fluctuations $p_1(t)$ and $p_2(t)$ are recorded with a time resolution of O (1 ms), where p_1 and p_2 are adjusted so that each of these takes zero in the stationary state. In the measurement of pulsatile flow, the negative pressure side cannot be measured due to characteristics of the sensor. As a measurement example, the pressure fluctuation measured under a pulsatile flow with an oscillation frequency $f_o = 0.3$ Hz of a Newtonian fluid with kinematic viscosity of 300 mm^2/s, is shown in Fig. 5.20. In order to determine the amplitude of the pulsatile pressure gradient, the following function is used to fit each $p_1(t)$ and $p_2(t)$,

$$p_i(t) = \alpha_i \frac{1 + \mathrm{sign}[\sin(\omega_o + \phi_i)]}{2} \sin(\omega_o t + \phi_i), \ (i = 1, 2), \tag{5.30}$$

where sign is a function that returns 1 when the valuable is positive, 0 when it is zero, and −1 when it is negative. With this fitting, $p_1(t)$ and $p_2(t)$ are converted to $P_1(t)$ and $P_2(t)$ with the measurement noise removed and the negative pressure side restored,

$$P_i(t) = \alpha_i \sin(\omega_o t + \phi_i), \ (i = 1, 2). \tag{5.31}$$

As shown in Fig. 5.20, the restored signal well matches the original signal in the positive pressure side. Using these P_1 and P_2, time variation of pressure gradient is obtained as,

$$\alpha(t) = -\frac{P_1(t) - P_2(t)}{L} \tag{5.32}$$

Accuracy and precision of the pressure measurement is shown in Fig. 5.18, and it is almost ±50 Pa/m.

5.3.2 Prediction scheme for a circular pipe flow

A prediction scheme for a pulsatile flow in a circular pipe is proposed, which directly utilizes the data set of viscoelasticity evaluated by USR. USR-based flow reconstruction scheme (Ohie et al., 2022c) is extended to a circular pipe geometry. Assuming an axial flow driven by a pressure gradient $\alpha(t)$ changing with time in a sinusoidal

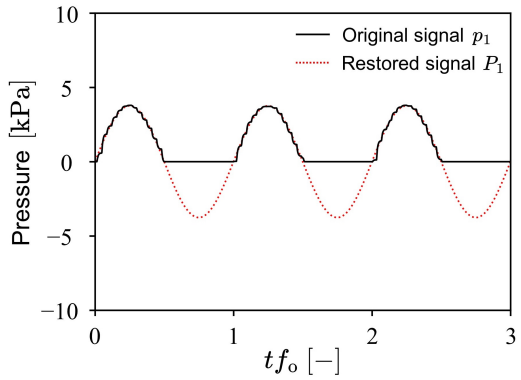


FIGURE 5.20: Measurement example of time variation of pressure values detected by the sensor on the upstream side, where the solid line represents the original signal. The negative pressure side cannot be measured due to the limit of the sensor. The dashed line represents restored signal.

manner with an oscillation frequency f_o, the flow field satisfies the following momentum conservation law (Tasaka, Yoshida, and Murai, 2021),

$$\rho \frac{\partial u}{\partial t} = \alpha(t) + \frac{\partial \tau}{\partial r} + \frac{\tau}{r}. \tag{5.33}$$

As an constitutive equation, Maxwell model is used,

$$\tau + \frac{\mu_e}{E_e}\frac{\partial \tau}{\partial t} = \mu_e \frac{\partial u}{\partial r}. \tag{5.34}$$

For facilitating subsequent mathematical expansion to derive the pulsatile flow, Fourier transform is performed on Eqs. 5.33 and 5.34,

$$i\omega\rho\hat{u} = \hat{\alpha} + \frac{\partial \hat{\tau}}{\partial r} + \frac{\hat{\tau}}{r}, \tag{5.35}$$

$$\hat{\tau} + i\omega\frac{\mu_e}{E_e}\hat{\tau} = \mu_e \frac{\partial \hat{u}}{\partial r}. \tag{5.36}$$

Equation 5.36 is modified with a definition of $\hat{u}(r, \omega = \omega_o) = R_u(r) + iI_u(r)$ to

$$\hat{\tau} = \mu_e \sin^2\delta\left(\frac{\partial R_u}{\partial r} + \cot\delta\frac{\partial I_u}{\partial r}\right) + i\mu_e \sin^2\delta\left(\frac{\partial I_u}{\partial r} - \cot\delta\frac{\partial R_u}{\partial r}\right). \tag{5.37}$$

Substituting Eq. 5.37 to Eq. 5.35, the following equations are obtained for the real and imaginary parts,

$$-\omega\rho I_u = R_\alpha + \mu_e \sin^2\delta\left(\frac{1}{r}\frac{\partial R_u}{\partial r} + \frac{\cot\delta}{r}\frac{\partial I_u}{\partial r} + \frac{\partial^2 R_u}{\partial r^2} + \cot\delta\frac{\partial^2 I_u}{\partial r^2}\right), \tag{5.38}$$

$$\omega\rho R_u = I_\alpha + \mu_e \sin^2\delta\left(-\frac{\cot\delta}{r}\frac{\partial R_u}{\partial r} + \frac{1}{r}\frac{\partial I_u}{\partial r} - \cot\delta\frac{\partial^2 R_u}{\partial r^2} + \frac{\partial^2 I_u}{\partial r^2}\right), \tag{5.39}$$

where $\hat{\alpha} = R_\alpha + iI_\alpha$. Solving Eq. 5.38 and 5.39 for $R_u(r)$ and $I_u(r)$, the spatial and temporal velocity distribution can be obtained as,

$$u(r,t) = A(r)\sin[\omega_o t + \phi(r)], \tag{5.40}$$

where $A(r)$ and $\phi(r)$ are defined as

$$A(r) = \sqrt{R_u^2 + I_u^2}, \tag{5.41}$$

$$\phi(r) = \tan^{-1}(I_u/R_u). \tag{5.42}$$

In the axial flow, shear rate is defined as

$$\dot{\gamma}(r,t) = \frac{\partial u}{\partial r}. \tag{5.43}$$

Substituting Eq. 5.40 to Eq. 5.43, spatial profile of the effective shear rate is derived as

$$\dot{\gamma}_{\text{eff}}(r) = \sqrt{\frac{1}{2}\left[\left(\frac{dA}{dr}\right)^2 + \left(A\frac{d\phi}{dr}\right)^2\right]}. \tag{5.44}$$

The following discretization is performed to numerically solve Eqs. 5.38 and 5.39 for R_u and I_u. The radial position is defined as $r_i = i\Delta r, (i = 0, 1, ..., N)$, where $\Delta r = R/N$. Hereafter, definitions of $R_{u,i} = R_u(r_i)$ and $I_{u,i} = I_u(r_i)$ are introduced to simplify the notation. Using the central difference equations $R'_{u,i} = (R_{u,i+1} - R_{u,i-1})/2\Delta r$ and $R''_{u,i} = (R_{u,i+1} - 2R_{u,i} + R_{u,i-1})/(\Delta r)^2$, similarly for $I'_{u,i}$ and $I''_{u,i}$, Eqs. 5.38 and 5.39 are spatially discretized to

$$a_{-1,i}R_{u,i-1} + a_{0,i}R_{u,i} + a_{1,i}R_{u,i+1} + b_{-1,i}I_{u,i-1} + b_{0,i}I_{u,i} + b_{1,i}I_{u,i+1} = R_{\alpha,i}, \tag{5.45}$$

$$c_{-1,i}R_{u,i-1} + c_{0,i}R_{u,i} + c_{1,i}R_{u,i+1} + d_{-1,i}I_{u,i-1} + d_{0,i}I_{u,i} + d_{1,i}I_{u,i+1} = I_{\alpha,i}, \tag{5.46}$$

where a, b, c and d are coefficients including r_i, Δr, $\mu_i = \mu_e(r_i)$, and $\delta_i = \delta(r_i)$. These coefficients are summarized below.

$$a_{-1,i} = \mu_i \sin^2\delta_i \left(\frac{1}{2r_i\Delta r} - \frac{1}{(\Delta r)^2}\right) \tag{5.47}$$

$$a_{0,i} = \mu_i \sin^2\delta_i \frac{2}{(\Delta r)^2} \tag{5.48}$$

$$a_{1,i} = -\mu_i \sin^2\delta_i \left(\frac{1}{2r_i\Delta r} + \frac{1}{(\Delta r)^2}\right) \tag{5.49}$$

$$b_{-1,i} = \mu_i \sin^2\delta_i \cot\delta_i \left(\frac{1}{2r_i\Delta r} - \frac{1}{(\Delta r)^2}\right) \tag{5.50}$$

$$b_{0,i} = -\omega\rho + \mu_i \sin^2\delta_i \cot\delta_i \frac{2}{(\Delta r)^2} \tag{5.51}$$

$$b_{1,i} = -\mu_i \sin^2\delta_i \cot\delta_i \left(\frac{1}{2r_i\Delta r} + \frac{1}{(\Delta r)^2}\right) \tag{5.52}$$

$$c_{-1,i} = -\mu_i \sin^2\delta_i \cot\delta_i \left(\frac{1}{2r_i\Delta r} - \frac{1}{(\Delta r)^2}\right) \tag{5.53}$$

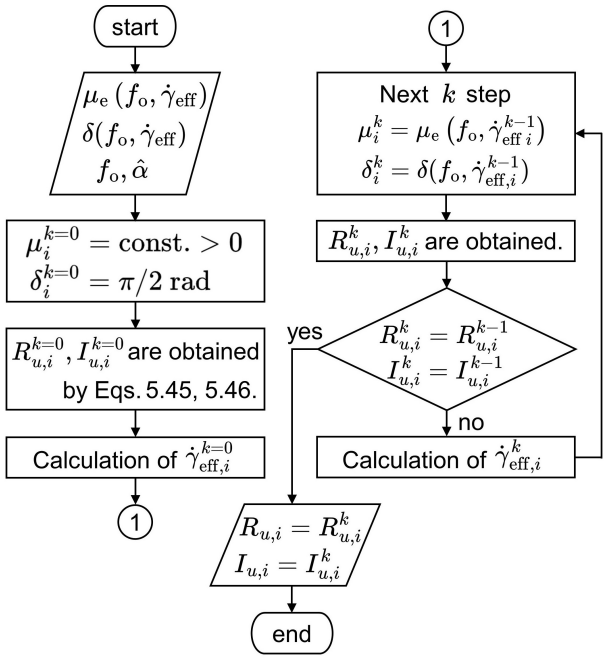


FIGURE 5.21: Flow chart of the convergence calculation method for predicting pulsatile flow in a circular pipe. Viscoelasticity dataset evaluated by USR is given as an input for the calculation.

$$c_{0,i} = \omega\rho - \mu_i \sin^2\delta_i \cot\delta_i \frac{2}{(\Delta r)^2} \tag{5.54}$$

$$c_{1,i} = \mu_i \sin^2\delta_i \cot\delta_i \left(\frac{1}{2r_i\Delta r} + \frac{1}{(\Delta r)^2}\right) \tag{5.55}$$

$$d_{-1,i} = \mu_i \sin^2\delta_i \left(\frac{1}{2r_i\Delta r} - \frac{1}{(\Delta r)^2}\right) \tag{5.56}$$

$$d_{0,i} = \mu_i \sin^2\delta_i \frac{2}{(\Delta r)^2} \tag{5.57}$$

$$d_{1,i} = -\mu_i \sin^2\delta_i \left(\frac{1}{2r_i\Delta r} + \frac{1}{(\Delta r)^2}\right) \tag{5.58}$$

As boundary conditions, zero shear rate at $r_0 = 0$ and non-slip at $r_N = R$ give the following equations,

$$R_{u,0} = R_{u,1}, I_{u,0} = I_{u,1}, \tag{5.59}$$

$$R_{u,N} = 0, I_{u,N} = 0. \tag{5.60}$$

As a closure property of these equations, Eqs. 5.45 and 5.46 are established at r_i, $(i = 1, 2, ..., N-1)$. Therefore, there are $2(N-1)$ equations, being the same number of unknowns $R_{u,i}, I_{u,i}$, $(i = 1, 2, ..., N-1)$, and the solution is uniquely determined. A comparison was made with the analytical solution for the Newtonian fluid to verify whether the series of these calculation in the Fourier space works and to evaluate the error due to the difference formulas. As a result, perfect match between the numerical and exact solutions was confirmed.

In the case of non-Newtonian fluids, the following convergence calculation is introduced with the data set of viscoelasticity evaluated by USR, $\mu_e(f_o, \dot{\gamma}_{eff})$ and

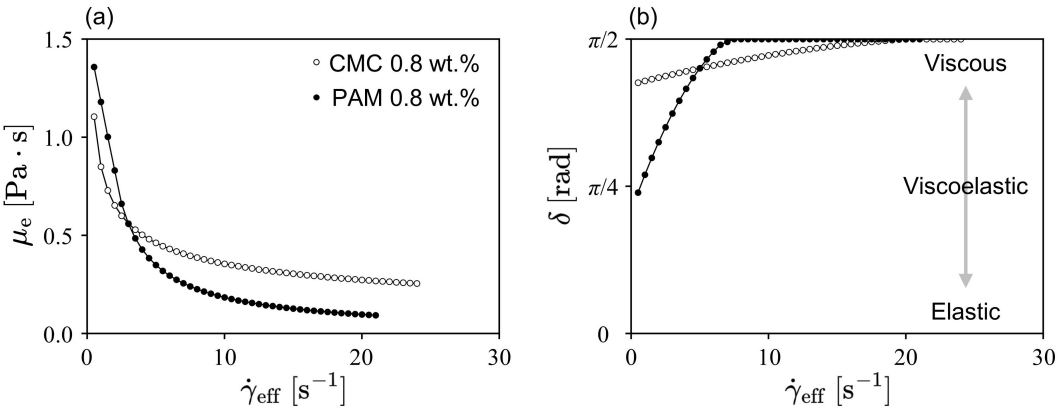


FIGURE 5.22: Viscoelasticity evaluation of the CMC and PAM 0.8 wt.% aqueous solutions by USR: shear rate dependence of (a) viscosity coefficient μ_e and (b) phase lag of viscoelasticity δ, where open and closed circles represent for the CMC and PAM 0.8 wt.% aqueous solutions, respectively.

$\delta(f_o, \dot{\gamma}_{eff})$. Flow chart for the convergence calculation is shown in Fig. 5.21. Viscoelasticity data set obtained via USR, $\mu_e(f_o, \dot{\gamma}_{eff})$ and $\delta(f_o, \dot{\gamma}_{eff})$, are given as inputs of the calculation with f_o and $\hat{\alpha}$. In the first calculation step, $k = 0$, spatial distributions of Fourier coefficients, $R_{u,i}^{k=0}$ and $I_{u,i}^{k=0}$, are tentatively obtained, assuming $\mu_i^{k=0} = \text{const.} > 0$ and $\delta_i^{k=0} = \pi/2$ rad. Then, the effective shear rate $\dot{\gamma}_{eff,i}^{k=0}$ is calculated. Referencing the viscoelasticity data set obtained by USR, spatial variation of viscoelasticity is updated as $\mu_i^{k=1} = \mu_e(f_o, \dot{\gamma}_{eff,i}^{k=0})$ and $\delta_i^{k=1} = \delta(f_o, \dot{\gamma}_{eff,i}^{k=0})$. Based on the renewed spatial distributions of these properties, $R_{u,i}^{k=1}$ and $I_{u,i}^{k=1}$ are calculated by Eq. 5.45 and 5.46 in the next step $k = 1$. When the Fourier coefficients do not match those in the previous calculation step, spatial distribution of the effective shear rate is calculated, and that of the viscoelasticity is updated. Then, the Fourier coefficients are obtained again. This cycle is continued until the following conditions are satisfied, $\left|R_{u,i}^{k} - R_{u,i}^{k-1}\right| < \epsilon$ and $\left|I_{u,i}^{k} - I_{u,i}^{k-1}\right| < \epsilon$, where ϵ is lower limit of the residual set sufficiently small. Finally, the converged solution are obtained as $R_{u,i} = R_{u,i}^{k}$ and $I_{u,i} = I_{u,i}^{k}$, and spatial profiles of the velocity amplitude $A(r)$ and phase lag $\phi(r)$ are obtained by Eqs. 5.41 and 5.42.

5.3.3 Results and discussion

Viscoelasticity evaluated by USR

Viscoelasticity of the CMC and PAM solutions at 25°C were evaluated by USR and summarized in Fig. 5.22, where the oscillation frequency was set at $f_o = 0.3$ Hz. It is confirmed from Fig. 5.22(a) that both solutions have shear-thinning properties, where the PAM solution is more prominent. Viscoelasticity is expressed under the conditions of $\dot{\gamma}_{eff} < 20$ s^{-1} in the CMC solution and $\dot{\gamma}_{eff} < 8$ s^{-1} in the PAM solution as shown in Fig. 5.22(b). The PAM solution develops stronger viscoelasticity than the CMC solution as the shear rate decreases. These viscoelasticity data were directly used in the flow prediction in the following sections, where values between the plots in Fig. 5.22 are linearly interpolated.

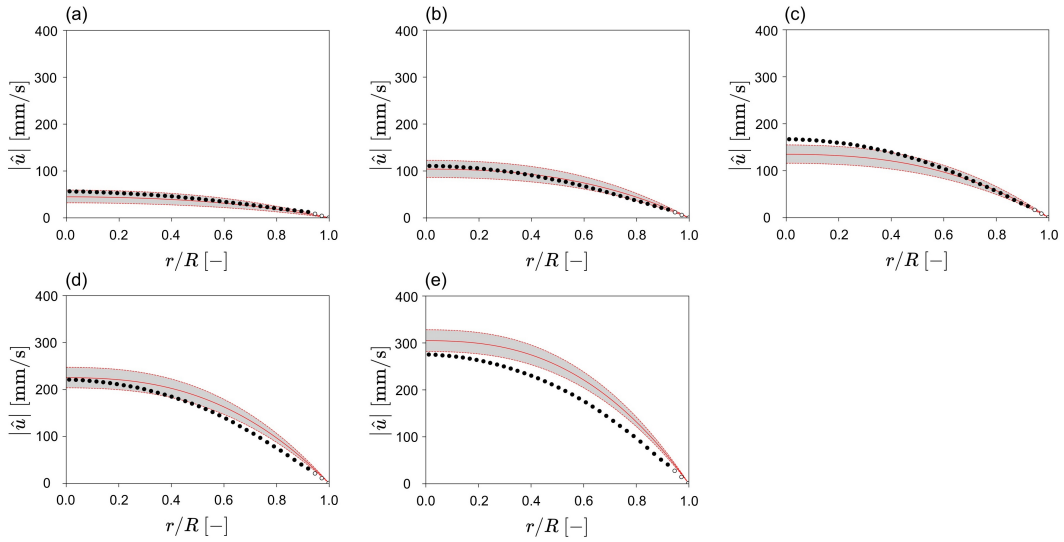


FIGURE 5.23: Comparison of the predicted velocity profiles with the experimental results for the CMC 0.8 wt.% aqueous solution under different pressure gradient $|\hat{\alpha}|$. The solid line shows the prediction result, while the dotted line is the prediction result when ±50 Pa/m is added to the corresponding pressure gradient. Experimental results are represented by symbols.

Validation of the prediction scheme with experimental results

For verifying the validity of the method proposed in the previous section, the experimental results in the pipeline system and the predicted velocity profiles were compared. The CMC solution was prepared in the pipeline and kept at 25°C by air conditioning and thermostatic chamber connected to the storage tank. A pulsatile flow was realized in the circular pipe by varying the rotation speed of the rotary pump in a sinusoidal manner with the oscillation frequency f_o = 0.3 Hz. Using the DFT and Eq. 5.41 for the spatial-temporal velocity distribution obtained by UVP, the spatial distribution of the velocity amplitude $A(r)$ was obtained as shown by plots in Fig. 5.23. By changing the amplitude of the rotation speed of the rotary pump, the experiments were conducted under the different amplitudes of the pressure gradient. In the immediate vicinity of the transducer, velocity cannot be obtained, or there is an effect of the cavity in the holder. Therefore, several points near the wall were removed, and the velocity profile in this range was linearly interpolated with a non-slip condition on the wall.

Based on these f_o, $|\hat{\alpha}|$, and the viscoelasticity dataset obtained by USR as inputs to the prediction scheme, spatial distributions of the velocity were predicted as shown by solid lines in Fig. 5.23, where N = 100 and $\Delta r = R/N$ = 0.25 mm. The dotted lines are the prediction results when ±50 Pa/m is added to the corresponding pressure gradient for considering the precision of the pressure measurement. In the four conditions where the pressure gradient is low, the spatial distributions of the measured velocity amplitude are almost within the range of the predicted velocity distributions, indicating the validity of the predictions. In Fig. 5.23(e), the predicting overall exceed the actual profiles. As explained in § 5.2.2, the precision of the pressure measurement is generally ±50 Pa/m, but there are some cases where measurement results exceed this range. The experimental results and predictions therefore are summarized and compared quantitatively as follows. Here, the bulk quantity Q,

which corresponds to the volumetric flow rate, is defined as

$$Q = \int_0^R 2\pi r A(r) dr. \tag{5.61}$$

In reality, as it is a pulsating flow, the time-averaged amount of fluid transport is zero, but Q is defined here for the comprehensive comparison. It is calculated from the experimental and predicted profiles in Fig. 5.23, and the results are summarized in Fig. 5.25. The error bar in the figure is Q calculated from the velocity amplitude distribution by adding ±50 Pa/m to the average pressure amplitude. The dashed line in the figure indicates a state where the experimental and predicted values are completely equal, and it can be seen that the symbols of the CMC solution generally concentrated around this line, indicating validity of the rheological measurement by USR and its application to flow predictions.

The same comparison was made for the PAM solution as shown in Fig. 5.24. As in the case of the CMC solution, the distributions of the velocity amplitude predicted under the conditions of adding ±50 Pa/m to the average pressure gradient amplitude are also shown as dotted lines, taking into account the precision of the pressure gradient measurement in the system used. The velocity distributions of the PAM solution are blunter near the central axis than those of the CMC solution, which is due to the stronger shear-sinning property of the PAM solution. Except for the pressure condition shown in Fig. 5.24(d), the agreement between the experiment and prediction can be confirmed overall. As in the case of the CMC solution, a comparison when converted to the integral quantity Q is shown in Fig. 5.25 with closed symbols. A good agreement can be confirmed except for one condition, and this abnormal point is considered to be due to a problem in the pressure gradient measurement. The validity of the prediction itself is overall guaranteed. The above comparative verification concludes that the pulsatile flow in a circular pipe can be predictable by the proposed scheme incorporated with viscoelasticity data obtained by USR in the cylindrical geometry.

It has been shown many times in previous sections that determining the wall positions is important when measuring the flow inside a pipe or vessel. The determination and the resulting angle θ in the experiments above are denoted here supplementarily. Figures 5.26(a) and (d) show the spatial distributions of the effective values of the velocity captured by UVP in the CMC and PAM solutions, respectively. Regarding the determination of the first wall position, by extrapolating the velocity distributions near the wall side, it is estimated to be around ξ = 4 mm. Figures 5.26(b) and (e) show the time averaged values and standard deviations of the echo signal obtained from the UVP device. In the distributions of the standard deviation of the CMC solution, the opposite wall position is estimated to be around ξ = 61 mm as it decreases rapidly there. It was also determined that the opposite wall existed at the same location in the case of the PAM solution. The standard deviation sharply decreases a little further to the left, but it is thought to be due to the drop in the average value itself. The resulting angle of the transducer is estimated to be θ = 28.7 deg, and these geometric conditions were used to convert $u_\xi(\xi, t)$ to $u(r, t)$. As the distributions of the averaged echo signal in Figs. 5.16 and 5.17 were relatively gentle, the position of the opposite wall was determined based on the distributions of the standard deviations. When the averaged values also remarkably change at the same time like in Fig. 5.26, it is necessary to identify the geometric conditions comprehensively, including the the symmetry of the velocity distribution.

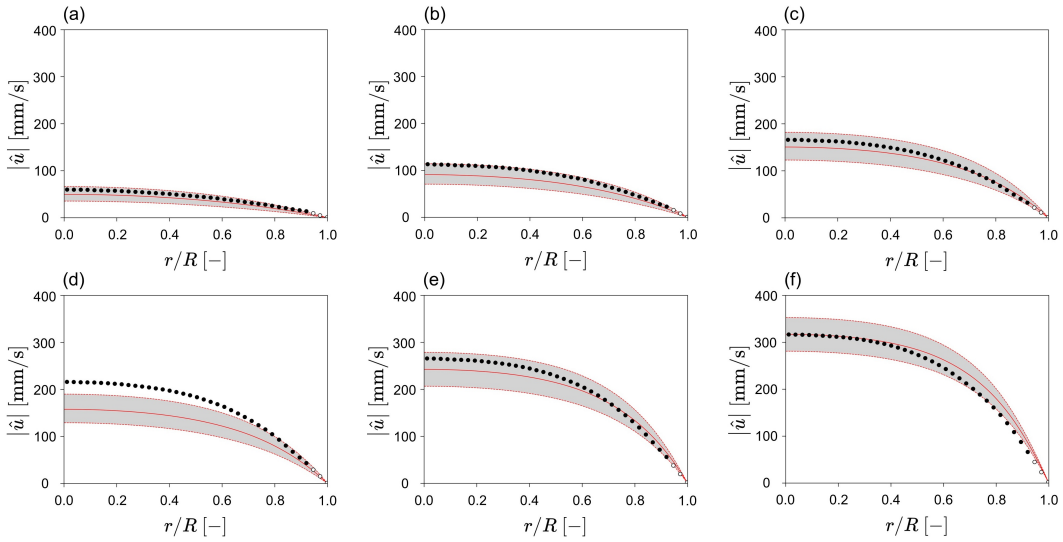


FIGURE 5.24: Comparison of the predicted velocity profiles with the experimental results for the PAM 0.8 wt.% aqueous solution under different pressure gradient $|\hat{\alpha}|$. The solid line shows the prediction result, while the dotted line is the prediction result when ±50 Pa/m is added to the corresponding pressure gradient. Experimental results are represented by symbols.

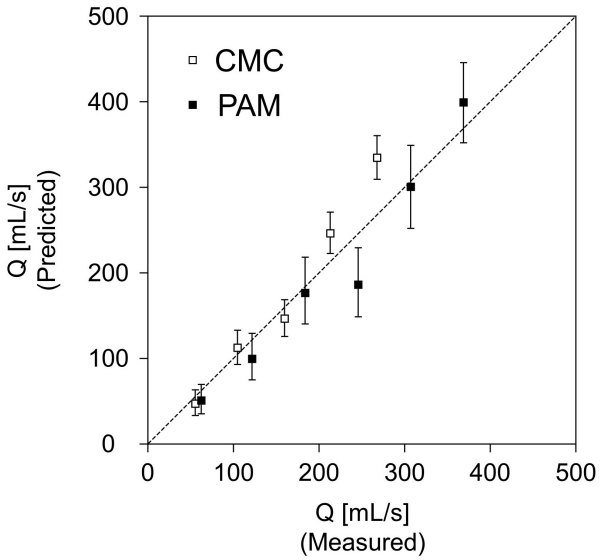


FIGURE 5.25: Comparison of the oscillating flow rate Q obtained by integrating the velocity amplitude profiles in Fig. 5.23 and 5.24. The solid line corresponds to the state where the measured and predicted flow rates are the same. The open and closed symbol correspond to the CMC and PAM solutions, respectively.

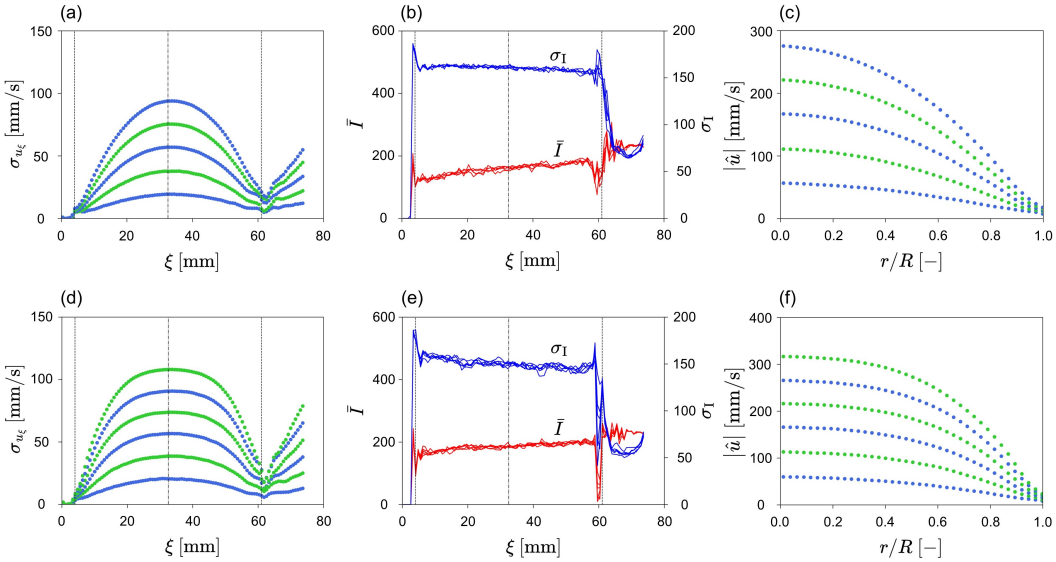


FIGURE 5.26: Detection of wall positions and estimation of the angle of the UVP measurement: (a) Effective values of the velocity captured by UVP σ_{u_ξ} under f_o = 0.3 Hz, (b) time averaged values and standard deviations of the echo signal, and (c) the amplitude of the axial velocity $|\hat{u}|$. The top row corresponds to the CMC solution, and the bottom row the PAM solution.

Chapter 6

Inline rheometry for industrial applications

The basic concept of the rheometry proposed in § 2 is to obtain the velocity information by UVP first and estimate the rheological properties based on the equation of fluid motion. In this chapter, progress in the development of inline rheometry is summarized by utilizing this inverse problem approach. Inline rheometry originally began with capillary rheometer for measuring Newtonian fluids, followed by UVP-PD, which combines pressure and velocity measurement developed by Ouriev and Windhab (2002). Recently, Tasaka, Yoshida, and Murai (2021) developed a method to estimate viscosity only from the velocity measurement. The method is very similar to the rheometry idea in § 2, by measuring the pulsating flow in a circular pipe using UVP and substituting it into the governing equations, the viscosity is inversely estimated. In order to improve the robustness of the analysis against the UVP measurement noise, they took the approach of Fourier analysis and radial integration of the cost function. This approach is effective when the target is a Newtonian fluid, but when trying to extend it to a non-Newtonian fluid, the shear rate amplitude differs at each radial position, the local evaluation is hence required. In principle, it would be possible to solve the cost function at each radial position to determine the local viscosity, but the fact that they took the integral value suggests that it would not robust enough against the measurement noise.

In this chapter, therefore, the phase analysis introduced in § 2.3 is extended to pipe flow. In § 6.1, methodology is specifically explained. Validation of the methodology is denoted in § 6.2 with silicon oil and carboxymethyl cellulose (CMC) aqueous solutions, which are typical Newtonian and shear-thinning fluids. The viscosity curves evaluated by ultrasonic inline rhometry (UIR) are compared with those obtained by USR. As application example, temporally transient food manufacturing process is monitored by UIR. The shear-thinning property is quantified when water, polysaccharide thickener, and amylase are sequentially added to rice porridge flowing in a closed loop.

6.1 Methodology

In the phase analysis of USR, the flow is driven by the sinusoidally oscillating outer cylinder, and the oscillation propagates toward the center with accompanying a phase delay. In the case of the pipe flow, the driving source of the flow is the pressure gradient. Considering an axially symmetric and one-directional flow driven by the pressure fluctuation given as

$$\alpha(t) = \alpha_0 + \alpha_a \sin(\omega_o t), \tag{6.1}$$

the corresponding flow field consists of a steady background and superimposed oscillatory shear flows denoted as

$$u(r,t) = u_0(r) + u_a(r)\sin[\omega_o t + \phi(r)]. \tag{6.2}$$

The definition of the geometry and variables is as same as shown in Figs. 5.13 and 5.19. The key is that the flow profile has the phase lag $\phi(r)$, where the fluid in the viscous layer on the pipe wall responds quickly to the pressure fluctuation, and the fluid around the axis, which is relatively dominated by inertia, accompanies phase delay. When the viscosity is as high as honey, this phase delay becomes relatively small, and conversely, when the viscosity is low, the phase delay increases, so the viscosity should be reflected in $\phi(r)$. As in § 2.3, focusing on its gradient $d\phi/dr$, it is converted to the equivalent Newtonian viscosity.

Momentum balance of the axially symmetric and one-directional flow in a circular pipe is described as

$$\rho\frac{\partial u}{\partial t} = \alpha(t) + \frac{\partial \tau}{\partial r} + \frac{\tau}{r}, \tag{6.3}$$

where ρ is fluid density and the pressure gradient is given as $\alpha(t) = \alpha_a \sin(\omega_o t)$ here. To derive an analytical solution for a Newtonian fluid with a viscosity coefficient of μ, by substituting Newton's law of viscosity $\tau = \mu\partial u/\partial r$ for the shear stress τ, the following equation is derived as

$$\frac{\partial^2 u}{\partial r^2} + \frac{1}{r}\frac{\partial u}{\partial r} - \frac{1}{\nu}\frac{\partial u}{\partial t} = -\frac{\alpha(t)}{\rho\nu}, \tag{6.4}$$

with the kinematic viscosity of ν. The Fourier transform is applied to the above equation to make the mathematical derivation easier, and the following equation is obtained in the Fourier space as

$$\frac{d^2\hat{u}}{dr^2} + \frac{1}{r}\frac{d\hat{u}}{dr} - \frac{i\omega}{\nu}\hat{u} = -\frac{\hat{\alpha}}{\rho\nu}, \tag{6.5}$$

where the hat symbol represents an operation, to which the Fourier transform is applied. By applying the following variable conversion to this equation, a Bessel type equation is obtained as

$$\frac{d^2\hat{u}}{d\zeta^2} + \frac{1}{\zeta}\frac{d\hat{u}}{d\zeta} + \hat{u} = -\frac{\hat{\alpha}}{\rho\omega}, \tag{6.6}$$

$$\zeta = (i-1)r\sqrt{\frac{\omega}{2\nu}}, \tag{6.7}$$

with imaginary unit i. Focusing on the dominant frequency component $\omega = \omega_o$, $\hat{\alpha}$ becomes a constant, and the analytical solution of Eq. 6.6 is obtained as

$$\hat{u}(r) = -\frac{i\hat{\alpha}}{\rho\omega}\left(1 - \frac{J_0(\zeta)}{J_0(\zeta)_{r=R}}\right)_{\omega=\omega_o}. \tag{6.8}$$

The gradient of the phase distribution is therefore given as

$$\phi'_N(r;\nu) = \frac{d}{dr}\arg\left[1 - \frac{J_0(\zeta)}{J_0(\zeta)_{r=R}}\right]. \tag{6.9}$$

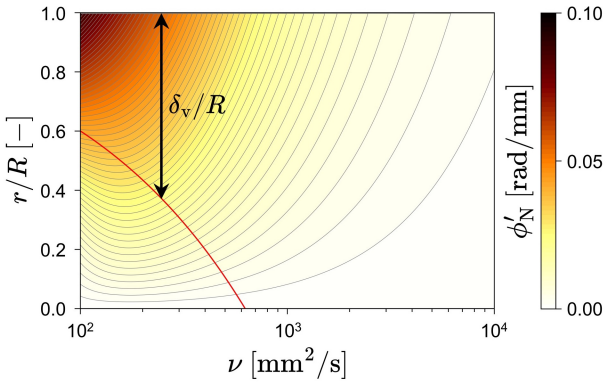


FIGURE 6.1: Relationship between the kinematic viscosity ν and spatial gradient of the phase ϕ'_N at each radial position when the oscillation frequency is f_o = 1.0 Hz. The gray lines represent contour of ϕ'_N and the red line indicates thickness of the viscous layer δ_v.

Just as the phase profile in the cylindrical system of USR does not depend on the velocity amplitude U_{wall}, it also does not depend on the pressure intensity in the pipe flow. The effective viscosity ν_{eff} at a radial position r is therefore defined as the kinematic viscosity satisfying the condition of

$$\frac{d\phi(r)}{dr} = \phi'_N(r; \nu = \nu_{eff}), \tag{6.10}$$

where $\phi(r)$ is the phase profile experimentally obtained. A point to note here is that the effective viscosity evaluated by this phase analysis incorporates all rheological properties such as viscosity and viscoelasticity.

One of the important points in the phase analysis is that the effective viscosity uniquely corresponds to the given gradient $d\phi/dr$. Figure 6.1 shows the relationship between the kinematic viscosity ν and the gradient ϕ'_N at each radial position when the oscillation frequency is given as f_o = 1.0 Hz. The solid line in the figure represent thickness of the viscous layer $\delta_v = \sqrt{\nu/f_o}$. It can be seen that within the viscous layer, ν and ϕ'_N uniquely correspond at each radial position. The phase analysis therefore works well within the viscous layer. Providing a supplemental explanation about outside of the viscous layer, as ν decreases at each radial position, ϕ'_N also decreases, which means that the effective viscosity increases based on the concept. This is because thickness of the viscous layer decrease as the viscosity decreases, causing the relatively inertia dominated fluid near the center to oscillate in the same phase.

6.2 Validation of the method

The validity of the phase analysis is verified in this section. The test fluids are silicon oil and CMC solution, which are typical Newtonian and shear-thinning fluids. The experimental setup is the same one as shown in Figs. 5.13 and 5.19. As a basic step, the pressure gradient is first given as $\alpha(t) = \alpha_a \sin(\omega_o t)$, where the mean velocity is therefore zero, and the fluid oscillates at each radial position with the applied oscillation frequency. The results obtained by the phase analysis are further compared with those obtained by USR.

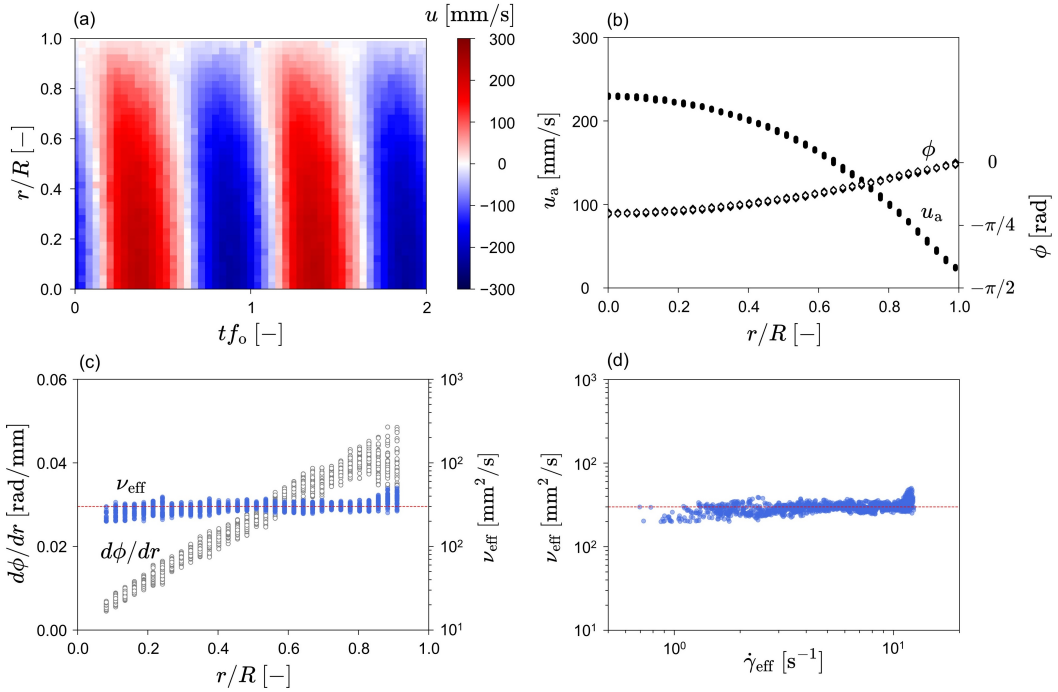


FIGURE 6.2: Application of the phase analysis to the silicon oil with the kinematic viscosity of ν = 300 mm^2/s: (a) spatial and temporal distribution of the axial velocity measured by UVP with the oscillation frequency of f_o = 1.0 Hz, (b) spatial distributions of the velocity amplitude u_a and phase delay of the pulsatile flow ϕ obtained by fitting the velocity distribution in figure (a) with Eq. 6.2, (c) spatial profiles of gradient of the phase $d\phi/dr$ and the effective viscosity ν_{eff} determined along the procedure of the phase analysis, where the dashed line indicates the kinematic viscosity of the silicon oil, (d) the effective viscosity against the effective shear rate $\dot{\gamma}_{eff}$.

6.2.1 Silicon oil

Silicon oil with a catalog kinematic viscosity of ν = 300 mm^2/s was uses as the test fluid. A small amount of tracer particles (CL-2507, Sumitomo Seika Chemicals Co., Ltd., Japan) with 0.92 g/mL density and 180 μm mean diameter was added to the silicon oil to serve as tracer particles for the UVP measurement. The density of the silicon oil is 0.967 g/mL, the particles are almost neutrally buoyant in the relatively high viscous fluid. The fluid in the pipe line is driven by a rotary lobe pump, and its rotation speed was controlled to realize the pulsatile flow with the oscillation frequency of f_o = 1.0 Hz.

Figure 6.2(a) shows two cycles of the spatial and temporal velocity distribution measured by UVP. It can be seen that the striped pattern is slightly tilted from the vertical direction, indicating that the fluid near the wall oscillates first, and the fluid near the center follows it with accompanying a phase delay. The UVP measurement was made for 5,000 profiles at a time resolution of Δt = 40 ms for a total of 200 s. As explained in the technical note in § 2.4, the first 500 profiles were extracted from the entire data, and velocity amplitude $u_a(r)$ and phase $\phi(r)$ were determined by fitting the velocity distribution based on the Eq. 6.2. This operation was repeated multiple times by shifting the window by 100 profiles, and the results are shown in Fig. 6.2(b). Regarding the phase distributions, these are shifted using the gradient near the wall

so that ϕ at the wall becomes zero. As observed from the spatial and temporal velocity distribution in Fig. 6.2(a), it can be seen that ϕ monotonically decreases toward the central axis. The amplitude distributions are parabolic as the fluid is Newtonian, and strictly, these follow those derived in Eq. 6.8. Figure 6.2(c) shows the results of spatial derivatives of phase distributions to evaluate the effective viscosity at each radial position. In calculation of the gradient, linear fitting was performed on a total of seven points, three points before and after the radial position of interest. The kinematic viscosity that satisfies Eq. 6.10 is determined at each radial position, and the resulting effective viscosity is shown with the closed circles in Fig. 6.2(c). The dashed line in the figure shows the catalog value of the silicon oil, and good agreement can be confirmed throughout the entire region.

In the axially symmetric and one-directional flow, shear rate $\dot{\gamma}(r,t)$ is defined as

$$\dot{\gamma}(r,t) = \frac{\partial u(r,t)}{\partial r}. \tag{6.11}$$

Considering the velocity field is given as Eq. 6.2 with $u_0(r) = 0$, the effective shear rate is used as representative one at each radial position, and it is derived as

$$\dot{\gamma}_{\mathrm{eff}}(r) = \sqrt{\frac{1}{2}\left[\left(\frac{du_\mathrm{a}}{dr}\right)^2 + \left(u_\mathrm{a}\frac{d\phi}{dr}\right)^2\right]}. \tag{6.12}$$

The shear rate and viscosity are determined at each radial position, a viscosity curve can be drawn by combining these, and it is shown in Fig. 6.2(d). It is Newtonian, a constant effective viscosity is therefore confirmed regardless of the shear rate, which reinforces the validity of the phase analysis.

6.2.2 Carboxymethyl cellulose aqueous solution

As an application example to non-Newtonian fluid, the same CMC solution used in § 5.3 was measured. The concentration is 0.8 wt.% and it is generally known to have a shear-thinning property. The pulsatile flow was driven with the oscillation frequency of $f_\mathrm{o} = 0.3$ Hz, and Fig. 6.3(a) shows two cycles of the velocity distribution measured by UVP. Although it is not as clear as the silicon oil, it is confirmed that the stripe pattern is slightly tilted with respect to the vertical direction, especially focusing on around the vertical axis. As in the case of the silicon oil, the UVP measurement was made for 5,000 profiles at a time resolution of $\Delta t = 40$ ms for a total of 200 s. The fitting results are shown in Fig. 6.3(b), and spatial gradient of the phase distributions is shown in Fig. 6.3(c). Compared to the silicon oil, the phase delay is clearly smaller and the viscosity is estimated higher. The spatial profiles of the effective viscosity are evaluated by the phase analysis and shown in Fig. 6.3(c) with closed circles. As the range near the wall was not truly measured by UVP, and seven nearby points are used when calculating the spatial gradient, the radial range of $r/R > 0.8$ is ignored. The viscosity monotonically increases toward the central axis. This represents shear-thinning property as the shear rate is zero at the center of the pipe and increases toward the wall. Figure 6.3(d) shows the viscosity curve, and shear-thinning behavior is confirmed. To verify the validity of this result, the same CMC solution was evaluated by the linear viscoelastic analysis of USR. The same oscillation frequency of $f_\mathrm{o} = 0.3$ Hz was applied, and the results are shown in Fig. 5.22 with open circles. As the phase of viscoselasticity δ takes a value close to $\pi/2$ rad at any effective shear rate, the CMC solution is considered as a viscous dominant fluid here, and profile of the viscosity coefficient μ was converted to that

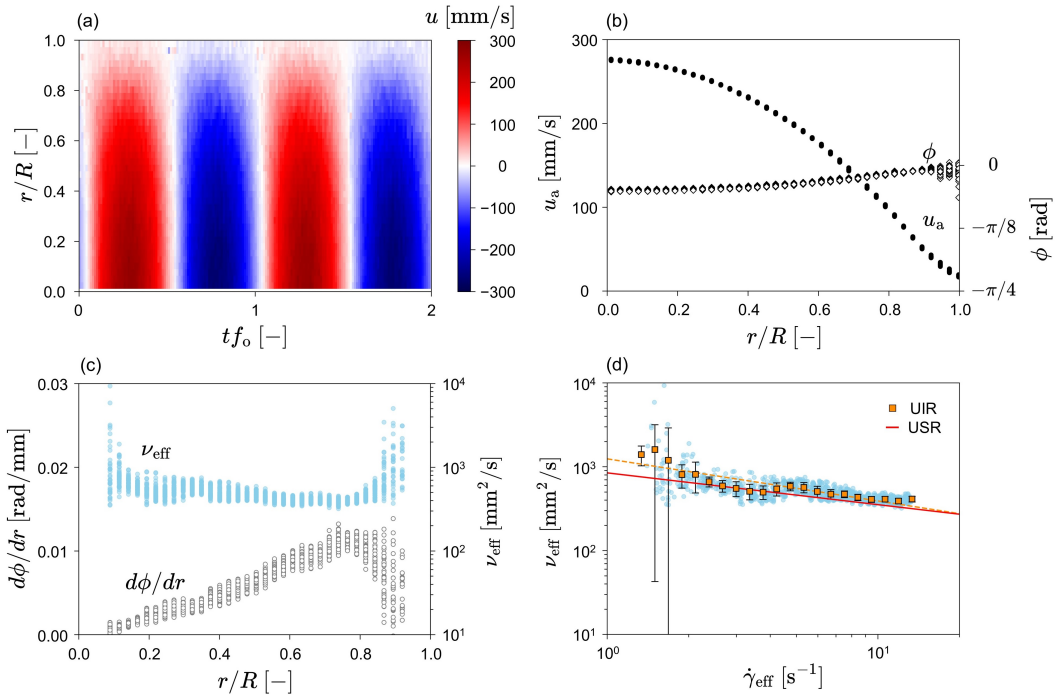


FIGURE 6.3: Application of the phase analysis to the CMC solution: (a) spatial and temporal distribution of the axial velocity measured by UVP with the oscillation frequency of f_o = 0.3 Hz, (b) spatial distributions of the velocity amplitude u_a and phase delay of the pulsatile flow ϕ obtained by fitting the velocity distribution in figure (a) with Eq. 6.2, (c) spatial profiles of gradient of the phase $d\phi/dr$ and the effective viscosity ν_{eff} determined by the phase analysis, (d) the effective viscosity against the effective shear rate $\dot{\gamma}_{eff}$. The square symbols and error bars in figure (d) are average values and standard deviations at each shear rate, where the dashed line is a fitting curve of these symbols with Eq. 6.14. The red solid line is the viscosity curve obtained by the linear viscoelastic analysis of USR with the oscillation frequency of f_o = 0.3 Hz.

of the kinematic viscosity, which is re-plotted as a the solid line in Fig. 6.3(d). In the low shear rate regime, the effective viscosity evaluated by UIR deviates from that evaluated by USR, but overall good agreement was confirmed, further reinforcing the validity of the phase analysis in the pipe flow.

6.3 Application example to food manufacturing processes

As an application example to non-equilibrium and heterogeneous fluid, rice porridge was measured. Totally 25 L of commercially available porridge (Koshihikari Shirogayu, TableMark Co., Ltd., Japan) was prepared in the tank. In addition to the background steady shear flow for transport, pulsatile flow was superimposed by the rotary lobe pump for the phase analysis, where the velocity distribution follows the form of Eq. 6.2. In order to evaluate the original porridge before it was processed, the pulsatile flow with the frequency of f_o = 1.0 Hz was measured by UVP and shown in Fig. 6.4(a). The background steady shear is applied for transportation, and the velocity is always positive. In the UVP measurement, 2,500 profiles at a time resolution of

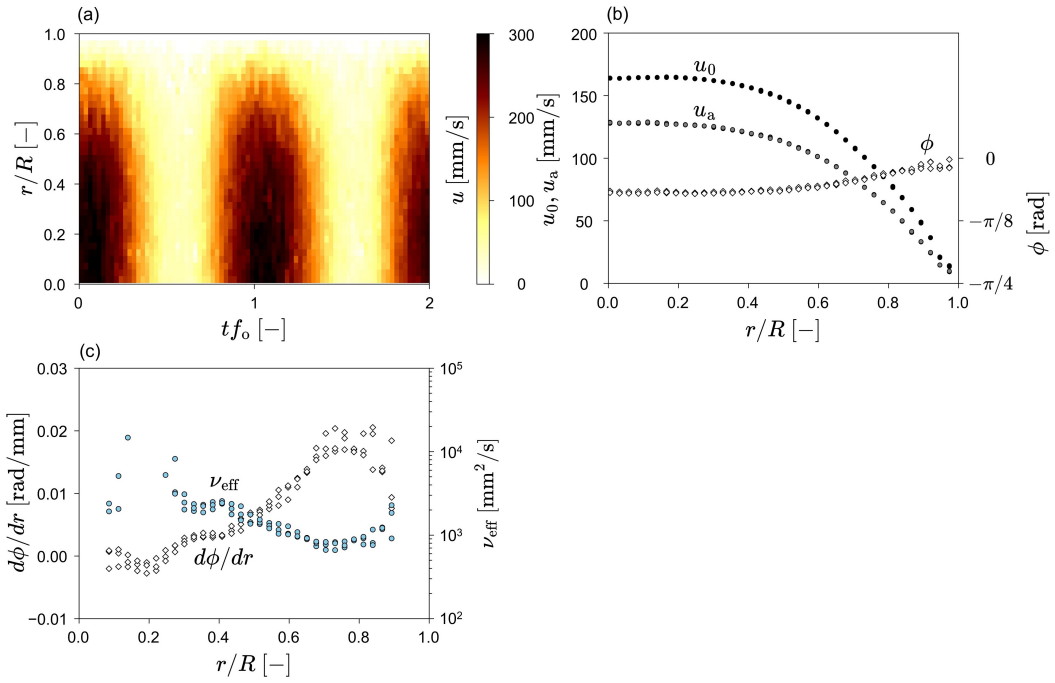


FIGURE 6.4: Application of the phase analysis to the rice porridge: (a) spatial and temporal distribution of the axial velocity measured by UVP with the oscillation frequency of f_o = 1.0 Hz, (b) spatial distributions of the velocity amplitude u_0, u_a and phase delay of the pulsatile flow ϕ obtained by fitting the velocity distribution in figure (a) with Eq. 6.2, (c) spatial profiles of gradient of the phase $d\phi/dr$ and the effective viscosity ν_{eff} determined by the phase analysis.

Δy = 25 ms were obtained for a total of about a minute. The quality of the UVP measurement was not good compared to the silicon oil and CMC solution, the analysis was performed by cutting out 1,200 profiles at a time, and moving the target profiles by 600 profiles. Fitting based on Eq. 6.2 was performed on each divided velocity distribution, and the obtained velocity amplitude and phase profiles are shown in Fig. 6.4(b). The velocity distributions u_0 and u_a are flat near the center rather than parabolic, it is therefore expected to have a yield stress or remarkable shear-thinning property. Regarding the phase distribution, the gradient of the profile is gentler than those of the silicon oil and CMC solution, but it decreases monotonically toward the center, making it possible to apply the phase analysis. Figure 6.4(c) shows the spatial gradient of the phase and corresponding distribution of the effective viscosity. As explained for the CMC solution, the radial range of $r/R > 0.8$ is not subjected to the evaluation in the following. In addition, the gradient becomes almost zero in $r/R < 0.3$, and the symbols of the effective viscosity are also scattered, the radial range from 0.3 to 0.8 was determined to be used for the evaluation.

The viscosity curve of the porridge is shown in Fig. 6.5(a). The shear rate of the steady component is calculated as

$$\dot{\gamma}_0(r) = \frac{du_0}{dr} \tag{6.13}$$

As representative shear rate, $\dot{\gamma}_0 + \dot{\gamma}_{eff}$ is adopted here. Vlastos et al. (1997) have also evaluated the complex viscosity under such shear condition previously, and they

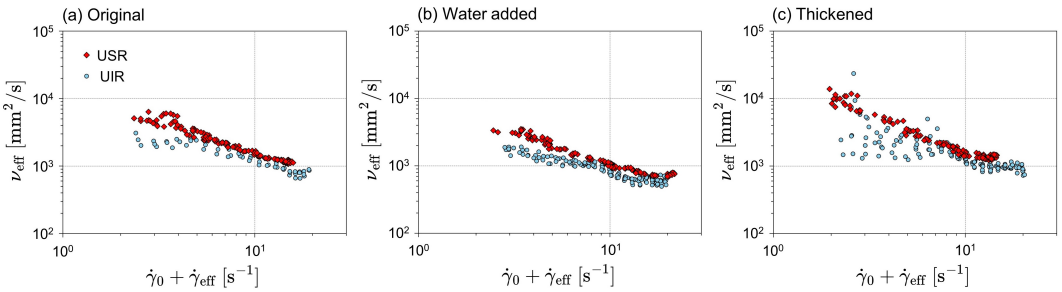


FIGURE 6.5: The effective viscosity curves of (a) original porridge at t = 0 min, (b) water added porridge at t = 15 min, and (c) thickened porridge with the starch at t = 30 min. The light colored symbols are evaluated by the phase analysis of UIR, and the darker symbols are obtained by USR with the oscillation frequency of f_o = 1.0 and the amplitude of $\Theta = \pi/3$ rad.

used similar definition. Strictly, they used the amplitude $\sqrt{2}\dot{\gamma}_{\mathrm{eff}}$, that is, the maximum value of the oscillatory shear rate, instead of the effective value $\dot{\gamma}_{\mathrm{eff}}$. About a liter of the porridge in the tank was sampled and filled in the cylindrical vessel of USR. The oscillatory shear flow under the frequency of f_o = 1.0 Hz and the rotation amplitude of $\Theta = \pi/3$ rad was measured by UVP and analyzed by the phase analysis in the cylindrical coordinate, where the results are shown with darker symbols in Fig. 6.5(a). Strictly, the shear rate conditions applied for UIR and USR are different, but when compared using the representative shear rate $\dot{\gamma}_0 + \dot{\gamma}_{\mathrm{eff}}$, the same trend was confirmed between the two viscosity curves.

As an example of applying the phase analysis to non-equilibrium states, water, polysaccharide thickener, and α-amylase were sequentially added to the tank while circulating the porridge in the closed loop. To explain each process more detail, the first process involved adding pure water to the porridge and examining whether the decrease in viscosity could be monitored by UIR. During the first 6 minutes, water was added to the tank at a rate of 250 mL/min and the inside of the tank was well stirred by an impeller. Subsequently, 15 minutes after the start of the experiment, a starch-based thickener (Tromeline, Nutri Co. Ltd, Japan) was added to the tank at a rate of 15 g/min for a total of 10 minutes. Then, 30 minutes after the start, the α-amylase solution was dripped into the tank over a period of 10 minutes at a rate of 5 mL/min. During these processes, the rotary pump constantly drove the pulsatile flow in the closed loop, and the porridge inside the tank was always mixed with the impeller.

During the above experiments, the pulsatile flow inside the pipe was constantly measured by UVP. Figures 6.5(b) and (c) show the viscosity curves 15 and 30 minutes after the start, where the figure (b) is the viscosity curve after all the water has been added to the original porridge, and (c) is the viscosity curve after all the starch-based thickener has been added to it. The light colored symbols are the effective viscosity evaluated by UIR, and it can be seen that the viscosity curve lowers in all the shear rate range with the water addition. Furthermore, after addition of the thickener, the viscosity curve shifted upward, almost returning to the viscosity of the original porridge. About 1 L of the sample was collected from the tank 15 and 30 minutes after the experiment start, and USR measurements were also done at the same time. Also in the phase analysis of USR, the viscosity curve shifted downward with the water addition, and a thickening effect was confirmed with the starch addition, confirming

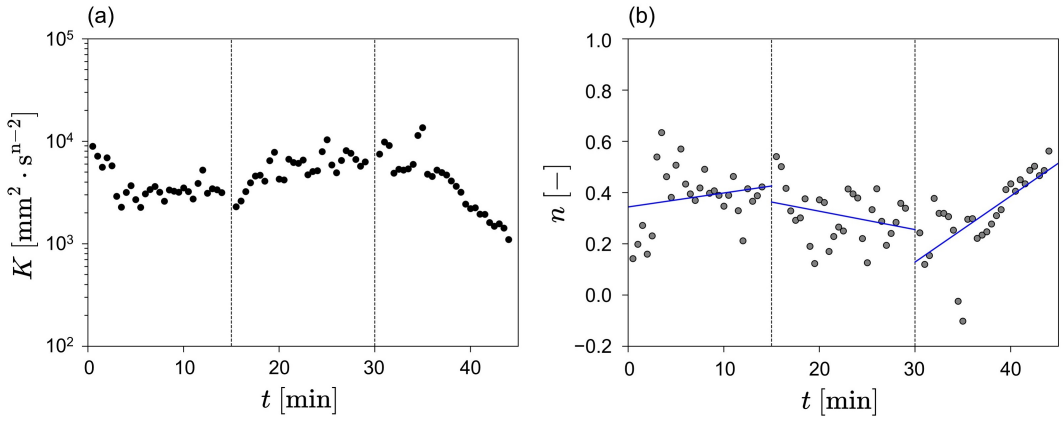


FIGURE 6.6: Time variation of (a) consistency K and (b) power law index n obtained by fitting viscosity curves at each elapsed time with Eq. 6.14. The solid lines in figure (b) are linear fitting results for each process to know the tendency of n over time.

the same trend as with UIR. After the USR measurement was completed, the sample was returned to the tank.

The results of analyzing all the UVP data measured during the 45 minutes experiment are summarized here. The phase analysis of UIR was performed on the velocity distribution for 1 minute, and was performed every 30 seconds. The viscosity curve therefore was output every 30 seconds. The viscosity curve at each time is regarded as approximately a straight line on a log-log scale like as shown in Fig. 6.5, the power law fitting based on

$$\nu_{\text{eff}} = K\left(\dot{\gamma}_0 + \dot{\gamma}_{\text{eff}}\right)^{n-1} \tag{6.14}$$

was applied to extract the consistency K and power law index n, where $n = 1$ indicates Newtonian viscosity, and as n decreases, shear-thinning property becomes more pronounced. Figures 6.6(a) and (b) show temporal variations of these K and n. The water addition started at $t = 0$ min, the dashed line at $t = 15$ min on the left shows the time to start adding the thickener, and the dashed line at $t = 30$ min on the right shows the start time to add the amylase. The range of the shear rate realized in the pipe is at most one order of magnitude or less, as shown in Fig. 6.5, so the n determined by the power law fitting has a large data variance compared with K. In order to know the tendency of n over time, linear fitting was performed for each process, and the results are shown as solid lines in Fig. 6.6(b).

In the first water addition process, it can be seen that K monotonically decreases and confirmed a trend in which n increases. The rice porridge is, so to speak, a particle suspension in which ellipsoids are dispersed at a high volume fraction in the starch-based aqueous solution. Therefore, the volume fraction decreases with the addition of water, which lowers the overall viscosity (K decreases) and reduces the frequency of interactions such as collisions between the particles, weakening the non-Newtonian property (n increases). In the second process t from 15 to 30 min, K increases monotonically and a trend in which n decreases is confirmed. This is because the viscosity of the entire porridge increased with the starch addition (K increases), and the shear-thinning property was enhanced by increasing the solvent concentration. Finally, in the process in which the α-amylase was added, K decreases

and n increases monotonically. The starch has a structure in which the monosaccharide glucose is linked together in a chain, and it is hydrolyzed by the α-amylase into dextrin and maltose. As a result, the thickening effect is lost, and as the solvent approaches water, the shear-thinning property of the porridge is weakened.

Overall, for liquid foods that are even in heterogeneous and non-equilibrium conditions, the phase information of the pulsatile flow can be replaced with the equivalent effective viscosity, and its shear-rate-dependence can be quantitatively evaluated. It is expected that the phase analysis of UIR will be a practical tool for monitoring production processes in food manufacturing and chemical industries.

Chapter 7

Concluding remarks and future perspectives

7.1 Concluding remarks

Toward establishment of multi-time scale rheology of heterogeneous fluids to expand the scope of rheology research regarding more complex fluids, mainly five goals were set in this thesis as described in § 1: (1) Advancement of the velocity-profiling-based rheometry, (2) applications of the rheometry for time-resolved rheology in non-equilibrium conditions, (3) establishment of multi-time scale rheology for comprehensively evaluating viscoelasticity depending on shear strength and its unsteadiness, (4) application of the identified rheological property to flow prediction, and (5) further advancement of the rheometry to in-line rheometry by utilizing the inverse analysis approach, which is the basic concept of the velocity-profiling-base rheometry.

(1) Advancement of the velocity-profiling-based rheometry

As the first chapter of this thesis, the phase analysis and linear viscoelastic analysis of USR are explained, which are respectively for evaluating the effective viscosity and viscoelasticity in oscillatory shear flows. Some techniques and knowledge cultivated during the development of USR to improve its accuracy and precision were summarized as technical notes. In order to further improve the robustness of USR against the UVP measurement noise, vhe velocity-profiling-assisted rheometry (VPAR) coupled with the synchronous torque measurement was developed, and it was confirmed that it has superior robustness to the conventional USR. The results of the carboxymethyl cellulose (CMC) aqueous solution measured by VPAR were consistent with the viscoelastic property evaluated by a standard torque-type rheometer. As an application to rheology of multi-phase fluids, non-colloidal particle suspensions were measured by VPAR, and they were consistent with the theoretical values, indicating high applicability of VPAR to exploring rheology of multi-phase fluids. Although some drawbacks remain, such as the geometry being complicated by the attachment of the inner cylinder, torque sensor, and stepped disk, and the large amount of sample required. Improving these designs, VPAR will become mainstream for rheological measurements of complex fluids.

(2) Time-resolved rheology in non-equilibrium conditions

As representatives of complex fluids whose rheological properties change with time, separating oil-water mixture due to the density difference and fluid foods after adding α-amylase were examined by the rheometry. Regarding the oil-water mixture, it was

found that the shear-thinning property and the effective viscosity decrease as the diameter and volume fraction of the water droplets existing on the UVP measurement line decrease with the passage of time. The result has the same tendency as the theoretical formula proposed by Choi and Schowalter (1975), but the viscosity at the initial time was overestimated. The reasons are considered that the effective volume fraction increased due to the accumulation of the droplets, or it might be an specific issues of the phase analysis, further investigation is required by such as viscoelastic analysis and by carefully controlling the droplet size and dispersing state. Regarding the later liquid foods, three types of commercial thickener aqueous solutions were examined. An effective method for evaluating time-resolved rheological functionalities of swallowed foods is proposed. Demonstrations were conducted with typical thickeners: starch, guar gum, and xanthan gum, with α-amylase as a digestive enzyme. The flow curve of the starch-based solutions lowered with time, and a few minutes after addition of the amylase, the viscosity dropped to one-hundredth of the original value. In contrast, the guar gum-based and xanthan gum-based solutions maintained the original viscosities as generally known. Applying the power law fitting to series of these flow curves, the time variation of the shear-thinning property is quantitatively characterized by the plots on typical $K-n$ space, where K and n are parameters in the model, consistency index and power law exponent. The qualitative characteristics of the thickeners are successfully quantified in the $K-n$ space, and this will be a practical tool for evaluating the time-resolved rheological properties of swallowed foods.

(3) Multi-timescale rheology

Rheological properties represented by viscoelasticity of, for example, polymer solutions change variously depending on the applied shear deformation and its unsteadiness. In order to evaluate it comprehensively, a new expression termed rheology mapping was proposed. Taking advantage of USR to obtain rich rheology information, it has become possible to evaluate the viscoelasticity with respect to changes in the effective shear rate, strain, and the oscillation frequency. As demonstrations, three typical polymer solutions were examined. Polyvinylpyrrolidone (PVP), carboxymethyl cellulose (CMC), and polyacrylamide (PAM) aqueous solutions are generally known as Newtonian, shear-thinning, and viscoelastic fluids, respectively. Regarding the PVP and CMC solutions, it was however revealed that the conditions for the solutions to behave viscoelasticity exist on the map. It was also found that the PAM solution completely loses its elasticity when the effective shear strain exceeds the critical shear strain. Furthermore, the results of the viscosity coefficients of the CMC and PAM solutions are essentially determined by the effective shear rate and shear strain is consistent with the properties predicted in previous studies conducted by other polymer scientist.

As further application of the comprehensive map representation, the viscoelastic property of dilute bubble suspensions is investigated. This is a suitable complex fluid for rheology mapping as the shape of the suspended bubbles with a restoring force originated by surface tension varies depending on the applied shear strength and unsteadiness. These microscopic dynamics appear as macroscopic property, that is, viscoelasticity. The viscoelasticity of dilute bubble suspensions is first theoretically derived from the constitutive equation originally for a dilute emulsion. Non-dimensionalization of the original tensor equation indicates that the viscoelasticity is systematized for a given void fraction by the capillary number Ca and dynamic capillary number Cd, representing the bubble deformability and unsteadiness

of bubble deformation. The comprehensive evaluation by the rheology mapping reveals that whether the viscosity increase or decrease depends on whether Ca or Cd exceeds a common critical value. In addition, it is indicated that the bubble suspension has the most prominent viscoelasticity when the timescale of the shear deformation is as same as the relaxation time of the suspended bubble and when the bubbles keep in spherical shape, that is $Ca \ll 1$ and $Cd = 1$. The effect of parallel combined steady and oscillatory shear on the viscoelasticity is further investigated using the map representation, and more than a century of research on dilute bubble suspension rheology has been fully completed and the next adventurous path to non-dilute regime has opened up.

(4) Application to flow reconstruction and prediction

The greatest advantage of the rheometry is that the flow field can be reconstructed using the identified rheological properties, and this is the most basic and important part for predicting non-Newtonian fluid flows in numerical simulation. As a first attempt, a method was proposed to reconstruct the oscillatory shear flows in the cylindrical coordinate with viscoelasticity evaluated by USR, and their predictions were compared with the experimental results. Verification using the PVP and CMC solutions was performed, and good agreement between the predictions and experiments was confirmed, proving the reversibility of the rheometry. Furthermore, as a fundamental step in predicting the flow of complex fluids, an attempt was made to predict the axially symmetric and one-directional pipe flows. The rheological property evaluated under the simple shear condition has also to be applicable to predict the one-directional flows. As application examples, shear-rate-dependent stress and viscosity of CMC and PAM solutions and rice porridge were evaluated under steady shear conditions in VPAR. The obtained flow curve in shear rate range of $O(10^{-1} - 10^{1}\ \mathrm{s}^{-1})$ was used to predict laminar flow in a pipe under a steady pressure gradient, which is an industrially applicable target. The predicted velocity profiles were in good agreement with experimental results measured in a pilot pipeline, where the maximum relative error of flow rate was less than 10% for all the test fluids. This suggests that the application of the rheological evaluation to flow prediction has high industrial practicality to complex fluids which are out of application of the standard rheometer. Furthermore, it was confirmed that the pulsatile flow of the CMC and PAM solutions in the pipe can be also predicted using the viscoelasticity data obtained by the rheometry. It was proved that the rheology data is reversible under both steady and unsteady conditions and can be used to predict the flow field under the same shear conditions.

(5) Further application to in-line rheometry

Inline rheometry was developed as an application of the inverse analysis approach itself of estimating rhology from velocity fields. This method focuses on the phase profile of pulsatile flow in a circular pipe, and is an application of the idea of the phase analysis in USR. In principle, it would be possible to estimate the effective viscosity by substituting the spatiotemporal velocity distribution in the governing equations, but utilization of the phase delay information enables to increase the robustness against the measurement noise of UVP. The measurement results for silicon oil and CMC solution, which are typical Newtonian and shear-thinning fluids, were compared with those evaluated by the phase analysis and linear viscoelastic analysis of USR, and generally good agreement was confirmed. As an example of

application to monitor transient production processes, a demonstration experiment was conducted in which water, polysaccharide thickeners, and α-amylase were sequentially added to rice porridge. The overall viscosity and shear-thinning property were weakened by the water addition, strengthened by adding the thickener, and finally, the decrease in viscosity and shear-thinning property was confirmed again by the hydrolysis. It is now possible to monitor the rheology at time resolution of $O(10\ \mathrm{s})$, and is expected to be a practical tool in the manufacturing process of fluid products in industry.

7.2 Epilogue and future perspectives

With our experiences of experimental failures and repeated trial and error, it can be said that the development of the rheometry in our lab over the past 10 years has been completed. As the major motivation for the development of this rheometry, the future of application to the rheology of complex fluids is opening. The scope is likely to be far beyond imagination, including not only foods, polymer solutions, and bubble suspensions as demonstrated in this thesis, but also mineral resources, fossil fuels, biofluids, cosmetics, paints, etc. The strength of the rheometry, which can be applied to heterogeneous and nonequilibrium conditions with assuring the reversibility of the evaluated data, will be greatly utilized in the rheological characterization of complex fluids, their flow predictions, and even monitoring their manufacturing processes as well. We may be measuring these complex fluids in our lab one after another. However, it is further desirable that the main characters in these applications are researchers in food and chemical engineering, petroleum and material science, earth and planetary science themselves, rather than the developers. Our final task will be to generalize the rheometer so that it can be used as a tool by a variety of researchers in academia and industry. The time has come for the rheometry to leave the nest and be applied to various fields. In order to see this off, the device geometry optimization and software provision will have to be done in the very near future.

Rather, one of the remaining work, we, fluid engineers must do, is to establish a methodology for predicting flow in more complex channel geometries. In this thesis, predictions of pipe flows driven under steady and pulsatile pressure gradient conditions were performed. When the flow is dominated by steady or oscillatory shear, highly accurate predictions can be made based on the rheological properties identified by the velocity-profiling-based rheometry. As clarified in § 4.3, even when the shear deformation is a parallel combined one in which multiple frequency components are simultaneously included, if one frequency component is predominant, the flow field can be predicted with the rheology data obtained under the oscillatory shear condition with that frequency. This approach is not valid when the channel geometry becomes more complex. For example, if a fluid element passing through a reducer is tracked in a Lagradian manner, the element undergoes a state of constant shear rate, then a transient deformation, and finally another state of constant shear rate. The shear stress response to such shear deformation including multi-frequency components cannot be predicted just from the rheological property evaluated under steady shear or single-frequency oscillatory shear condition, except in special cases such as the CMC solution. There are however two approaches to potentially solve this problem, and one is modeling at the microscale. For example, like the bubble suspension rheology discussed in § 4.2, constitutive equations are created taking into account the dynamics of the dispersion. Very recently, it has become

possible to observe the motion of single polymers (Schroeder, 2018), and it will be possible to construct more accurate constitutive equations incorporating these advanced findings even for polymer solutions. However, if the target fluid changes, it is necessary to create constitutive equations from scratch, so this will likely lead to a more detailed division of rheology. The other of the two approaches is the use of data science, whose application has been rapidly progressing in recent years. VPAR makes it possible to obtain the relationship between strain and stress under various combinations of multi-frequency oscillatory shear flows. One idea would be to select an appropriate constitutive equation based on this big data, or to realize constitutive equation by using an artificial neural network itself. Learning with the reliable data using VPAR enables the realization of more accurate constitutive equations. To do these, cooperation between VPAR developers on experimental side and experts on computational fluid dynamics will be essential.

The rheology is the study of the flow of matter. The response of complex fluids to shear deformation alone is actually insufficient to predict and control their flow. The complex fluids will likely cause slip at the surface, and their elongation property will not be so simple. It is necessary to apply the flow inverse analysis approach to the development of slip measurement tool and stress tensor rheometry, in fact, urgent development of these is desired in various fields such as food and chemical engineering. In parallel with the development of this novel tool set, our important future work is to establish the methodology for predicting complex fluid flows, and a new academic field called engineering of complex fluids will be opened up.

Bibliography

Andereck, C David, SS Liu, and Harry L Swinney (1986). "Flow regimes in a circular Couette system with independently rotating cylinders". In: *Journal of fluid mechanics* 164, pp. 155–183.

Bangyeekhan, Sompong, Vitoon Leelamanit, and Perapong Tekasakul (2013). "Effects of food viscosity on swallowing velocity in pharynx for different groups of age and gender". In: *Journal of Medical and Biological Engineering* 33.3, pp. 343–348.

Banks, Alec, Jonathan Vincent, and Chukwudi Anyakoha (2007). "A review of particle swarm optimization. Part I: background and development". In: *Natural Computing* 6, pp. 467–484.

Benchabane, Adel and Karim Bekkour (2008). "Rheological properties of carboxymethyl cellulose (CMC) solutions". In: *Colloid and Polymer Science* 286.10, pp. 1173–1180.

Benton, E R and A Clark Jr (1974). "Spin-up". In: *Annual Review of Fluid Mechanics* 6.1, pp. 257–280.

Birkhofer, Beat H et al. (2008). "Monitoring of fat crystallization process using UVP–PD technique". In: *Flow Measurement and Instrumentation* 19.3-4, pp. 163–169.

Chang, Chingyi and Robert L Powell (1993). "Dynamic simulation of bimodal suspensions of hydrodynamically interacting spherical particles". In: *Journal of Fluid Mechanics* 253, pp. 1–25.

Chen, Jianshe (2009). "Food oral processing—A review". In: *Food hydrocolloids* 23.1, pp. 1–25.

Choi, Seung Jung and WR Schowalter (1975). "Rheological properties of nondilute suspensions of deformable particles". In: *The Physics of Fluids* 18.4, pp. 420–427.

Cutler, A Norman, Edwin R Morris, and L John Taylor (1983). "Oral perception of viscosity in fluid foods and model systems". In: *Journal of texture studies* 14.4, pp. 377–395.

Derakhshandeh, Babak, Dimitris Vlassopoulos, and Savvas G Hatzikiriakos (2012). "Thixotropy, yielding and ultrasonic Doppler velocimetry in pulp fibre suspensions". In: *Rheologica acta* 51, pp. 201–214.

Dunstan, Dave E, Elisabeth K Hill, and Yalin Wei (2004). "Direct measurement of polymer segment orientation and distortion in shear: semi-dilute solution behavior". In: *Polymer* 45.4, pp. 1261–1266.

Einstein, Albert (1906). "Eine neue bestimung der molekuldimensionen". In: *Annals of Physics* 324, pp. 289–306.

Ewoldt, Randy H, AE Hosoi, and Gareth H McKinley (2008). "New measures for characterizing nonlinear viscoelasticity in large amplitude oscillatory shear". In: *Journal of Rheology* 52.6, pp. 1427–1458.

Ewoldt, Randy H, Anette E Hosoi, and Gareth H McKinley (2007). "Rheological fingerprinting of complex fluids using large amplitude oscillatory shear (LAOS) flow". In: *Annual Transactions-Nordic Rheology Society* 15, p. 3.

Ewoldt, Randy H et al. (2007). "Rheological fingerprinting of gastropod pedal mucus and synthetic complex fluids for biomimicking adhesive locomotion". In: *Soft Matter* 3.5, pp. 634–643.

Fardin, Marc A et al. (2014). "Flow instabilities in large amplitude oscillatory shear: a cautionary tale". In: *Rheologica acta* 53.12, pp. 885–898.

Fischer, Peter, Elizabeth K Wheeler, and Gerald G Fuller (2002). "Shear-banding structure orientated in the vorticity direction observed for equimolar micellar solution". In: *Rheologica Acta* 41.1, pp. 35–44.

Frankel, NA and Andreas Acrivos (1970). "The constitutive equation for a dilute emulsion". In: *Journal of Fluid Mechanics* 44.1, pp. 65–78.

Gallot, Thomas et al. (2013). "Ultrafast ultrasonic imaging coupled to rheometry: Principle and illustration". In: *Review of Scientific Instruments* 84.4.

Gao, Zhihong and Kaoru Kohyama (2014). "Ultrasound Pulsed Wave D oppler Imaging of the Esophagus Illustrates the Effects of Water Volume on Bolus Kinematics". In: *Journal of Texture Studies* 45.5, pp. 335–343.

Ghannam, Mamdouh T and M Nabil Esmail (1997). "Rheological properties of carboxymethyl cellulose". In: *Journal of applied polymer science* 64.2, pp. 289–301.

— (1998). "Rheological properties of aqueous polyacrylamide solutions". In: *Journal of applied polymer science* 69.8, pp. 1587–1597.

González, Hernán A and Nelson O Moraga (2005). "On predicting unsteady non-Newtonian blood flow". In: *Applied mathematics and computation* 170.2, pp. 909–923.

Graessley, William W (1980). "Polymer chain dimensions and the dependence of viscoelastic properties on concentration, molecular weight and solvent power". In: *Polymer* 21.3, pp. 258–262.

Guth, Eugene (1938). "On the hydrodynamical theory of the viscosity of suspensions". In: *Phys. Rev* 53, pp. 322–325.

Hadde, EK and J Chen (2019). "Shear and extensional rheological characterization of thickened fluid for dysphagia management". In: *Journal of Food Engineering* 245, pp. 18–23.

Han, Ch D and RG King (1980). "Measurement of the rheological properties of concentrated emulsions". In: *Journal of Rheology* 24.2, pp. 213–237.

Hart, Abarasi (2014). "A review of technologies for transporting heavy crude oil and bitumen via pipelines". In: *Journal of Petroleum Exploration and Production Technology* 4, pp. 327–336.

Hasan, Shadi W, Mamdouh T Ghannam, and Nabil Esmail (2010). "Heavy crude oil viscosity reduction and rheology for pipeline transportation". In: *Fuel* 89.5, pp. 1095–1100.

Hasegawa, A, F Nakazawa, and H Kumagai (2008). "Measurement of mass dependence of swallowed food velocity in the pharynx by the ultrasonic method". In: *Journal of the Japanese Society for Food Science and Technology* 55, pp. 330–337.

Hasegawa, A et al. (2005). "Velocity of swallowed gel food in the pharynx by ultrasonic method". In: *Journal of the Japanese Society for Food Science and Technology* 52, pp. 441–447.

Houska, M et al. (1998). "Shear rates during oral and nonoral perception of viscosity of fluid foods". In: *Journal of texture studies* 29.6, pp. 603–615.

Hutchings, John B and PJ Lillford (1988). "The perception of food texture-the philosophy of the breakdown path". In: *Journal of Texture Studies* 19.2, pp. 103–115.

Hyun, Kyu et al. (2011). "A review of nonlinear oscillatory shear tests: Analysis and application of large amplitude oscillatory shear (LAOS)". In: *Progress in Polymer Science* 36.12, pp. 1697–1753.

Irgens, Fridtjov (2014). *Rheology and non-newtonian fluids*. Vol. 190. Springer.

Jaishankar, Aditya and Gareth H McKinley (2014). "A fractional K-BKZ constitutive formulation for describing the nonlinear rheology of multiscale complex fluids". In: *Journal of Rheology* 58.6, pp. 1751–1788.

Jarny, S et al. (2005). "Rheological behavior of cement pastes from MRI velocimetry". In: *Cement and concrete research* 35.10, pp. 1873–1881.

Krieger, Irvin M (1968). "Shear rate in the Couette viscometer". In: *Transactions of the Society of Rheology* 12.1, pp. 5–11.

Krishnan, J Murali, Abhijit P Deshpande, and PB Sunil Kumar (2010). *Rheology of complex fluids*. Springer.

Kulicke, W M and RS Porter (1980). "Relation between steady shear flow and dynamic rheology". In: *Rheologica Acta* 19, pp. 601–605.

Kulicke, Werner-Michael et al. (1996). "Characterization of aqueous carboxymethylcellulose solutions in terms of their molecular structure and its influence on rheological behaviour". In: *Polymer* 37.13, pp. 2723–2731.

Kumagai, H and H Kumagai (2009). "Physical properties of foods and effect of water on them V: Rheology and food engineering". In: *Japan Journal of Food Engineering*, 10.3, pp. 137–148.

Kumagai, Hitoshi et al. (2009). "Relationship between flow properties of thickener solutions and their velocity through the pharynx measured by the ultrasonic pulse Doppler method". In: *Food science and technology research* 15.3, pp. 203–210.

Larson, Ronald G and Priyanka S Desai (2015). "Modeling the rheology of polymer melts and solutions". In: *Annual Review of Fluid Mechanics* 47, pp. 47–65.

Lewandowska, Katarzyna (2007). "Comparative studies of rheological properties of polyacrylamide and partially hydrolyzed polyacrylamide solutions". In: *Journal of applied polymer science* 103.4, pp. 2235–2241.

Lewis, TB and LE Nielsen (1968). "Viscosity of dispersed and aggregated suspensions of spheres". In: *Transactions of the Society of Rheology* 12.3, pp. 421–443.

Llewellin, Ed W and M Manga (2005). "Bubble suspension rheology and implications for conduit flow". In: *Journal of Volcanology and Geothermal Research* 143.1-3, pp. 205–217.

Llewellin, EW, HM Mader, and SDR Wilson (2002). "The rheology of a bubbly liquid". In: *Proceedings of the Royal Society of London. Series A: Mathematical, Physical and Engineering Sciences* 458.2020, pp. 987–1016.

Mackenzie, JK0034 (1950). "The elastic constants of a solid containing spherical holes". In: *Proceedings of the Physical Society. Section B* 63.1, p. 2.

Macosko, Christopher W (1994). "Rheology principles". In: *Measurements and Applications*.

Matsumoto, S (1978). "The role of rheology in food science". In: *Journal of the Society of Rheology* 6.2, pp. 39–44.

Matsuo, Taisuke et al. (2020). "Appropriate usage of food thickening agents to prevent non-disintegration of magnesium oxide tablets". In: *Scientific Reports* 10.1, p. 16089.

Mendes, Paulo R de Souza, Alexandra A Alicke, and Roney L Thompson (2014). "Parallel-plate geometry correction for transient rheometric experiments". In: *Applied Rheology* 24.5, pp. 1–10.

Meriem-Benziane, Madjid et al. (2012). "Investigating the rheological properties of light crude oil and the characteristics of its emulsions in order to improve pipeline flow". In: *Fuel* 95, pp. 97–107.

Mitrias, Christos et al. (2017). "Direct numerical simulation of a bubble suspension in small amplitude oscillatory shear flow". In: *Rheologica Acta* 56, pp. 555–565.

Mitrou, Stamatina et al. (2023). "Effect of polydispersity and bubble clustering on the steady shear viscosity of semidilute bubble suspensions in Newtonian media". In: *Journal of Rheology* 67.3, pp. 635–646.

Mooney, Melvin (1951). "The viscosity of a concentrated suspension of spherical particles". In: *Journal of colloid science* 6.2, pp. 162–170.

Morini, Romain et al. (2019). "Steady shear viscosity of semi-dilute bubbly suspensions". In: *Journal of Non-Newtonian Fluid Mechanics* 264, pp. 19–24.

Moritaka, Hatsue and Fumiko Nakazawa (2009). "The rheological and swallowing properties of rice starch". In: *Food science and technology research* 15.2, pp. 133–140.

Murai, Yuichi and Hiroshi Oiwa (2008). "Increase of effective viscosity in bubbly liquids from transient bubble deformation". In: *Fluid dynamics research* 40.7-8, p. 565.

Nagatoshi, A et al. (2001). "Comparison of the passage velocity of various foods in the human pharynx by ultrasonic measurement". In: *Journal of Home Economics of Japan* 52.4, pp. 343–350.

Nakauma, Makoto et al. (2011). "Swallowing profiles of food polysaccharide solutions with different flow behaviors". In: *Food Hydrocolloids* 25.5, pp. 1165–1173.

Nishinari, K et al. (2011). "Effect of shear thinning on aspiration–Toward making solutions for judging the risk of aspiration". In: *Food Hydrocolloids* 25.7, pp. 1737–1743.

Nishinari, Katsuyoshi (2003). "Rheology in food and eating". In: *JOURNAL-SOCIETY OF RHEOLOGY JAPAN* 31.1, pp. 41–50.

Nishinari, Katsuyoshi et al. (2019). "Role of fluid cohesiveness in safe swallowing". In: *NPJ Science of Food* 3.1.

Noto, Daisuke et al. (2023). "Optical spinning rheometry test on viscosity curves of less viscous fluids at low shear rate range". In: *Experiments in Fluids* 64.1, p. 18.

Ohie, Kohei et al. (2020). "Evaluation on time variation of effective viscosity by ultrasonic spinning rheometry (Application to separating oil-water mixture)". In: *Transactions of the JSME (in Japanese)* 86.890.

Ohie, Kohei et al. (2022a). "Effective rheology mapping for characterizing polymer solutions utilizing ultrasonic spinning rheometry". In: *Experiments in fluids* 63.2, p. 40.

— (2022b). "Flow Prediction of Complex Fluids in a Circular Pipe by Utilizing a Velocity-Profiling-Assisted Rheometer". In: *Industrial & Engineering Chemistry Research* 61.49, pp. 18157–18164.

Ohie, Kohei et al. (2022c). "Rheological characterization and flow reconstruction of polyvinylpyrrolidone aqueous solutions by means of velocity profiling-based rheometry". In: *Experiments in Fluids* 63.8, p. 135.

Ouriev, B and EJ Windhab (2002). "Rheological study of concentrated suspensions in pressure-driven shear flow using a novel in-line ultrasound Doppler method". In: *Experiments in fluids* 32.2, pp. 204–211.

Pal, Rajinder (2001). "Evaluation of theoretical viscosity models for concentrated emulsions at low capillary numbers". In: *Chemical Engineering Journal* 81.1-3, pp. 15–21.

— (2003). "Rheological behavior of bubble-bearing magmas". In: *Earth and Planetary Science Letters* 207.1-4, pp. 165–179.

Palmer, Jeffrey B and Karen M Hiiemae (1997). "Integration of oral and pharyngeal bolus propulsion: a new model for the physiology of swallowing". In: *The Japanese Journal of Dysphagia Rehabilitation* 1.1, pp. 15–30.

Phan-Thien, Nhan and Nam Mai-Duy (2013). *Understanding viscoelasticity: an introduction to rheology*. Springer.

Pipkin, Allen C (2012). *Lectures on viscoelasticity theory*. Vol. 7. Springer Science & Business Media.

Poole, RJ and BS Ridley (2007). "Development-length requirements for fully developed laminar pipe flow of inelastic non-Newtonian liquids". In.

Qazi, Waqas M et al. (2020). "Simultaneous X-ray video-fluoroscopy and pulsed ultrasound velocimetry analyses of the pharyngeal phase of swallowing of boluses with different rheological properties". In: *Dysphagia* 35, pp. 898–906.

Rao, M Anandha (2013). *Rheology of fluid, semisolid, and solid foods: principles and applications*. Springer Science & Business Media.

Reiner, Markus (1964). "The deborah number". In: *Physics today* 17.1, pp. 62–62.

Rodríguez-González, Francisco et al. (2010). "Rheo-PIV analysis of the slip flow of a metallocene linear low-density polyethylene melt". In: *Rheologica Acta* 49, pp. 145–154.

Rønningsen, Hans Petter (1992). "Rheological behaviour of gelled, waxy North Sea crude oils". In: *Journal of Petroleum Science and Engineering* 7.3-4, pp. 177–213.

Ross, Alexander IV et al. (2019). "Relationships between shear rheology and sensory attributes of hydrocolloid-thickened fluids designed to compensate for impairments in oral manipulation and swallowing". In: *Journal of Food Engineering* 263, pp. 123–131.

Rust, AC and Michael Manga (2002). "Effects of bubble deformation on the viscosity of dilute suspensions". In: *Journal of non-newtonian fluid mechanics* 104.1, pp. 53–63.

Saint-Michel, Brice et al. (2016). "Local oscillatory rheology from echography". In: *Physical Review Applied* 5.3, p. 034014.

Sakurai, K, Y Tasaka, and Y Murai (2013). "Modification of effective viscosity on bubbly flows due to transient bubble deformations". In: *Transactions of the Japan Society of Mechanical Engineers. B* 79.797, pp. 1–11.

Schramm, Gebhard et al. (1994). *A practical approach to rheology and rheometry*. Haake Karlsruhe.

Schroeder, Charles M (2018). "Single polymer dynamics for molecular rheology". In: *Journal of Rheology* 62.1, pp. 371–403.

Seo, Kyung Won, Yang Jun Kang, and Sang Joon Lee (2014). "Lateral migration and focusing of microspheres in a microchannel flow of viscoelastic fluids". In: *Physics of Fluids* 26.6.

Shama, F and P Sherman (1973). "Identification of stimuli controlling the sensory evaluation of viscosity II. Oral methods". In: *Journal of texture studies* 4.1, pp. 111–118.

Shiratori, Takahisa, Yuji Tasaka, and Yuichi Murai (2016). "Rapid rheological characterization of a viscoelastic fluid based on spatiotemporal flow velocimetry". In: *Experimental Thermal and Fluid Science* 71, pp. 1–13.

Shiratori, Takahisa et al. (2013). "Development of ultrasonic visualizer for capturing the characteristics of viscoelastic fluids". In: *Journal of visualization* 16, pp. 275–286.

Shiratori, Takahisa et al. (2015). "Ultrasonic velocity profiling rheometry based on a widened circular Couette flow". In: *Measurement Science and Technology* 26.8, p. 085302.

Sui, Changping and Gregory B McKenna (2007). "Instability of entangled polymers in cone and plate rheometry". In: *Rheologica acta* 46, pp. 877–888.

Takahashi, Tomoko et al. (2002). "Effects of physical properties and oral perception on transit speed and passing time of semiliquid foods from the mid-pharynx to the hypopharynx". In: *Journal of texture studies* 33.6, pp. 585–598.

Takeda, Yasushi (1986). "Velocity profile measurement by ultrasound Doppler shift method". In: *International journal of heat and fluid flow* 7.4, pp. 313–318.
— (1995). "Velocity profile measurement by ultrasonic Doppler method". In: *Experimental thermal and fluid science* 10.4, pp. 444–453.
— (2012). *Ultrasonic Doppler velocity profiler for fluid flow*. Springer Science & Business Media.
Tan, Chao et al. (2021). "Ultrasonic Doppler technique for application to multiphase flows: A review". In: *International Journal of Multiphase Flow* 144, p. 103811.
Tapia, Franco et al. (2022). "Viscous to inertial transition in dense granular suspension". In: *Physical Review Letters* 129.7, p. 078001.
Tasaka, Y., T. Kimura, and Y. Murai (2015). "Estimating the effective viscosity of bubble suspensions in oscillatory shear flows by means of ultrasonic spinning rheometry". In: *Experiments in fluids* 56.1, pp. 1–13.
Tasaka, Y et al. (2021). "Ultrasonic spinning rheometry test of food rheology for better swallowing". In: *Fine Chemicals* 50.2, pp. 41–47.
Tasaka, Yuji, Taiki Yoshida, and Yuichi Murai (2021). "Nonintrusive in-line rheometry using ultrasonic velocity profiling". In: *Industrial & engineering chemistry research* 60.30, pp. 11535–11543.
Tasaka, Yuji et al. (2018). "Linear viscoelastic analysis using frequency-domain algorithm on oscillating circular shear flows for bubble suspensions". In: *Rheologica Acta* 57, pp. 229–240.
Tashiro, Akiko et al. (2010). "Relationship between the rheological properties of thickener solutions and their velocity through the pharynx as measured by the ultrasonic pulse Doppler method". In: *Bioscience, biotechnology, and biochemistry* 74.8, pp. 1598–1605.
Taylor, Geoffrey Ingram (1932). "The viscosity of a fluid containing small drops of another fluid". In: *Proceedings of the Royal Society of London. Series A, Containing Papers of a Mathematical and Physical Character* 138.834, pp. 41–48.
Tobin, Aarti Ben et al. (2020). "Bolus rheology and ease of swallowing of particulated semi-solid foods as evaluated by an elderly panel". In: *Food & function* 11.10, pp. 8648–8658.
Ueha, R et al. (2014). "Appropriate thickener usage in the management of dysphagia". In: *Deglutition* 3, pp. 279–287.
Vlastos, Georgios et al. (1997). "The effect of parallel combined steady and oscillatory shear flows on blood and polymer solutions". In: *Rheologica Acta* 36, pp. 160–172.
Wagner, Caroline E et al. (2017). "Quantifying the consistency and rheology of liquid foods using fractional calculus". In: *Food Hydrocolloids* 69, pp. 242–254.
Wiklund, Johan, Iman Shahram, and Mats Stading (2007). "Methodology for in-line rheology by ultrasound Doppler velocity profiling and pressure difference techniques". In: *Chemical Engineering Science* 62.16, pp. 4277–4293.
Wood, FW (1968). "Psychophysical studies on the consistency of liquid foods". In: *Rheology and texture of foodstuffs* 27, pp. 40–49.
Yoshida, T et al. (2018a). "Rheological properties of montmorillonite dispersions in dilute NaCl concentration investigated by ultrasonic spinning rheometry". In: *Applied Clay Science* 161, pp. 513–523.
Yoshida, Taiki, Kohei Ohie, and Yuji Tasaka (2022). "In situ measurement of instantaneous viscosity curve of fluids in a reserve tank". In: *Industrial & Engineering Chemistry Research* 61.31, pp. 11579–11588.
Yoshida, Taiki, Yuji Tasaka, and Peter Fischer (2019). "Ultrasonic spinning rheometry test on the rheology of gelled food for making better tasting desserts". In: *Physics of Fluids* 31.11.

Yoshida, Taiki, Yuji Tasaka, and Yuichi Murai (2017). "Rheological evaluation of complex fluids using ultrasonic spinning rheometry in an open container". In: *Journal of rheology* 61.3, pp. 537–549.

— (2019a). "Effective viscoelasticity of non-Newtonian fluids modulated by large-spherical particles aligned under unsteady shear". In: *Physics of Fluids* 31.10.

— (2019b). "Efficacy assessments in ultrasonic spinning rheometry: Linear viscoelastic analysis on non-Newtonian fluids". In: *Journal of Rheology* 63.4, pp. 503–517.

Yoshida, Taiki, Sanehiro Wada, and Noriyuki Furuichi (2023). "A calibration methodology of ultrasonic transducers: Evaluation of spatial propagation characteristics of pulse-echo". In: *Measurement* 214, p. 112783.

Yoshida, Taiki et al. (2018b). "Accuracy and robustness evaluations on algorithms of ultrasonic spinning rheometry". In: *Proceedings of 11th International Symposium on Ultrasonic Doppler Methods for Fluid Mechanics and Fluid Engineering (2018b)*, pp. 56–59.

Zhu, JF, H Mizunuma, and Y Michiwaki (2014). "Determination of characteristic shear rate of a liquid bolus through the pharynx during swallowing". In: *Journal of Texture Studies* 45.6, pp. 430–439.